

**NASA
Technical
Paper
2879**

November 1989

**Laser Anemometer
Measurements in a
Transonic Axial-Flow
Fan Rotor**

Anthony J. Strazisar,
Jerry R. Wood,
Michael D. Hathaway,
and Kenneth L. Suder



(NASA-TP-2879) LASER ANEMOMETER
MEASUREMENTS IN A TRANSONIC AXIAL-FLOW FAN
ROTOR (NASA) 216 D USCL 200

79-11245

Unclass

41/34 0187353

**NASA
Technical
Paper
2879**

1989

Laser Anemometer
Measurements in a
Transonic Axial-Flow
Fan Rotor

Anthony J. Strazisar,
Jerry R. Wood,
Michael D. Hathaway,
and Kenneth L. Suder
*Lewis Research Center
Cleveland, Ohio*

NASA

National Aeronautics and
Space Administration
Office of Management
Scientific and Technical
Information Division

Summary

A laser fringe anemometer has been used to survey the flowfield upstream, within, and downstream of NASA rotor 67, a low-aspect-ratio transonic axial-flow fan rotor. Laser anemometer surveys were made of the flowfield for operating conditions near peak efficiency and near stall.

The fan tip relative Mach number was 1.38. The rotor was designed for axial inflow and therefore did not require inlet guide vanes. In addition, the fan was operated without stators. The resulting rotor-only configuration enables comparison of the laser anemometer data with results from numerical flow analysis codes that assume the flow is steady in the reference frame of the rotor.

Each laser anemometer survey consists of axial and tangential velocity component measurements acquired at 50 points from blade to blade at a fixed axial and radial location. Surveys were acquired at approximately 30 axial locations on each of 9 surfaces of revolution spaced approximately every 10 percent of span from hub to tip. The laser anemometer survey data are presented in the form of plots of relative Mach number and relative flow angle. Two types of plots are presented for each spanwise location: (1) blade-to-blade plots at fixed chord locations; and (2) streamwise plots at fixed pitch locations. In addition, contour plots of relative Mach number are presented at 10-, 30-, and 70-percent span locations.

Radial surveys of total and static pressure, total temperature, and flow angle were also acquired at stations upstream and downstream of the rotor. The radial survey data are used to calculate the rotor overall aerodynamic performance. The radial survey and overall performance data are included in tabular form and can be used to set boundary conditions for computational codes.

A detailed description of the blade and flowpath geometry is provided in tabular form so that the experimental results reported herein can be used as a test case for three-dimensional turbomachinery flow analysis codes.

The blade and flowpath geometry as well as a complete set of the laser anemometer survey data are available on magnetic media upon request.

Introduction

In recent years, several investigators have presented comparisons between detailed laser anemometer (LA) flowfield

measurements acquired in transonic axial-flow compressors and predictions from numerical flow analysis codes (refs. 1 to 4). These early comparison efforts utilized quasi- and fully three-dimensional inviscid analysis codes with simple corrections for viscous flow effects.

The need for detailed flowfield measurements continues as computational methods evolve toward fully three-dimensional, viscous solution schemes. To meet the need for turbomachinery data test cases for use in validating computational methods, the NASA Lewis Research Center has undertaken a program aimed at obtaining detailed measurements within transonic turbomachinery blade rows using laser anemometry. Test case results obtained in an axial-flow turbine vane are presented in reference 5. Test case results obtained within a low-aspect-ratio axial-flow fan rotor are the subject of this report. The NASA designation for the test rotor is rotor 67.

The results reported herein were obtained from a 1.56-aspect-ratio fan rotor with a design tip relative Mach number of 1.38. The fan was designed for axial inflow and did not require an inlet guide vane. The fan was also operated without a stator. The resulting rotor-only configuration eliminates circumferential variations in the flowfield induced by stationary blade rows and thus allows comparison of the measurements with numerical analyses which assume a steady flow relative to the rotor blade row.

Results of radial surveys of total and static pressure, total temperature, and flow angle acquired at stations upstream and downstream of the rotor are reported. The radial survey data are used to calculate the rotor overall aerodynamic performance.

A detailed description of the blade and flowpath geometry is provided in tabular form so that the experimental results reported herein can be used as a test case for three-dimensional turbomachinery flow analysis codes.

To keep the size of this report manageable, all LA data are presented in plotted form. Plots of the relative Mach number and relative flow angle distributions are presented for blade-to-blade surfaces of revolution at nine spanwise locations corresponding to the design streamline locations. Data are presented for two design speed operating conditions—one near peak efficiency and one near stall. The complete LA data set consists of axial and tangential velocity component measurements at 50 points from blade to blade at each of approximately 270 measurement locations (30 axial locations at each of 9 spanwise locations). The complete LA data set as well as the blade and flowpath geometry are available on magnetic

media upon request. A description of the data format is given in appendix B. (Symbols used in this report are defined in appendix A.)

We anticipate that many users of these data will be comparing the data to results obtained from three-dimensional flow analysis codes. It is important to note that only the axial and tangential components of velocity were measured in this investigation. We have studied the effect of neglecting the radial velocity components when comparing three-dimensional computed results to the data presented herein. Results from Denton's three-dimensional Euler code (ref. 6) were used to calculate the Mach number with and without the radial velocity included, and the effect was found to be minimal. However, this effect should be checked for each individual code.

The results reported herein are only suitable for comparison to results from three-dimensional codes which have some viscous losses included. The data could also be compared to results from an S1-S2 calculation procedure if an S2 code capable of giving reasonable streamsheet thickness distributions through the rotor is used.

This report presents a detailed description of the blade and flowpath geometry, presents the data, and discusses measurement uncertainty. No attempt is made to compare the data to computational results or to use the data to study detailed flow physics. Comparisons between the data and Denton's three-dimensional Euler code can be found in references 7 and 8. Flow physical details which have been studied using these data include (1) flowfield variations from passage to passage, passage shock structure, strength, and steadiness, and (2) vortex shedding from the blade trailing edge. Discussions of these flow features can be found in references 8 to 10.

Apparatus

Axial Compressor Facility

A schematic diagram of the NASA Lewis single-stage axial-flow compressor test facility is shown in figure 1. The drive system consists of a 3000-hp electric motor with a variable-frequency power supply. Motor speed is controllable from 400 to 3600 rpm. The motor is coupled to a 5.25 gear ratio speed increaser gear box that in turn drives the rotor. The facility is sized for a maximum airflow of 45 kg/sec with atmospheric air as the working fluid.

Air is drawn into the facility from an inlet located on the roof of the building. The air first passes through a filter to removed large particles. It then passes through a flow measuring station consisting of a thin-plate orifice, through inlet butterfly valves, and into a plenum chamber. The air is not dried before entering the plenum. The air is accelerated into the compressor test section through a nozzle, passes through the test rotor,

and then passes through a sleeve throttle valve into a collector before it is exhausted back into the atmosphere. The airflow is controlled through the collector valve.

Test rotor.—The test rotor, NASA rotor 67, is shown in figure 2. It is an undamped low-aspect-ratio design rotor and is the first-stage rotor of a two-stage fan. Inlet and exit velocity vector diagrams are shown at the design condition at 10-percent span in figure 3. (All spanwise locations discussed in this report are measured from the tip.) A complete description of the aerodynamic design of the full two-stage fan is given in references 11 and 12.

The rotor design pressure ratio is 1.63 at a mass flow of 33.25 kg/sec. The design rotational speed is 16 043 rpm, which yields a tip speed of 429 m/sec and an inlet tip relative Mach number of 1.38. The rotor has 22 blades and an aspect ratio of 1.56 (based on average span/root axial chord). The rotor solidity varies from 3.11 at the hub to 1.29 at the tip. The inlet and exit tip diameters are 51.4 and 48.5 cm, respectively, and the inlet and exit hub/tip radius ratios are 0.375 and 0.478, respectively. A fillet radius of 1.78 mm is used at the airfoil-hub juncture. The square root of the mean square of the airfoil surface finish is 0.8 μm or better, the airfoil surface tolerance is ± 0.04 mm, and the running tip clearance is approximately 1.0 mm.

Two features of the rotor blading which can be seen in figure 2 are a strain gauge mounted on the suction surface of one blade and a nick in the leading edge of another blade. The leading edge nick occurred after the laser anemometer flowfield measurements were completed. The blade with the strain gauge was included in the blades surveyed with the laser anemometer. The impact of the strain gauge on the flowfield is discussed in reference 9. The impact on the results presented in this report is considered to be minimal because the blade with the strain gauge affects only 1 of the 17 blade passages surveyed with the laser anemometer and the results reported here are averaged across all 17 blade passages.

Blade coordinates at the design speed operating condition are given in table I for surfaces of revolution for 14 blade sections. The nomenclature used in table I is shown in figure 4. The origin of all blade geometry Z-coordinates is the intersection of the blade leading edge with the hub. The blade surface coordinates are given at 35 points for each blade section. These coordinates describe a blunt-edge blade with the Z-coordinates for points 1 and 35 corresponding to the minimum and maximum axial extents of the blade leading and trailing edge circles. Coordinates which describe the blade leading and trailing edge circles precede the blade surface coordinates for each blade section. The blade edge circles fit into the blade surfaces in a meridional (along an R,Z -line) and radius \times angular coordinate system. The blade edge circles are tangent to both blade surfaces and to the Z-coordinate of points 1 and 35 listed in the blade surface table.

The blade sections run from the hub of the rotor to the shroud. Blade section 14 lies outside the physical blade tip. The R, Z -location of the actual tip of the blade under design speed operating conditions can be obtained by subtracting 1.0 mm from blade section 14 in a direction which is normal to the annulus shroud contour.

The rotor geometry under design speed operating conditions is normally determined by applying deflections calculated by the NASTRAN finite-element computer code to the blade manufacturing coordinates. However, in the present work the actual blade tip geometry was measured at design speed with the laser anemometer by focussing the LA probe volume on the blade tip. During the analysis of these blade tip position data it became apparent that the actual blade untwist was slightly less than that predicted by the NASTRAN code. The NASTRAN-derived geometry was therefore corrected to yield a *best match* with the laser measurements at the blade tip. This correction amounts to a 1.4° restagger toward the closed position at the planar manufacturing section located 25.4 cm along the stacking axis from the rotor centerline. This correction is faired to 0° at the planar manufacturing section located 20.32 cm along the stacking axis from the rotor centerline, which is the location where the NASTRAN-predicted deflections begin to deviate from a simple beam deflection analysis. The blade geometry listed in table I has resulted from this process and is considered to be an accurate representation of the actual blade geometry under design speed operating conditions.

Annulus.—The nomenclature used to define the hub and shroud contours is also shown in figure 4. The hub and shroud contours are given in table II. The origin of the Z -coordinate corresponds to the origin of the Z -coordinate used to define the blade geometry—i.e., $Z = 0$ corresponds to the intersection of the blade leading edge with the hub flowpath.

Laser Anemometer System

The laser anemometer system used in the present investigation is a single-channel fringe anemometer which is described in detail in references 13 to 15. Optical access to the flowfield is provided by a 3-mm-thick glass window which conforms to the flowpath contour in both the circumferential and streamwise directions. Liquid fluorescent seed particles are injected into the flow through a 6-mm-diameter tube 35 cm upstream of the rotor. Recent measurements made with aerosol sizing instrumentation indicate that the mean particle size is approximately $0.5 \mu\text{m}$. Measurements reported in reference 15 indicate a particle size of 1.0 to $1.4 \mu\text{m}$ based on particle lag across the rotor passage shock. These measurements were made on a different transonic rotor with a tip speed similar to that of the rotor used in the present work. Particle lag measurements repeated during the present investigation yielded

similar results. Therefore, although the seed particles are actually of the order of $0.5 \mu\text{m}$ in diameter, only particles which are of the order of 1.0 to $1.4 \mu\text{m}$ in diameter scatter enough light to be detected by the laser anemometer optical system.

Test Procedure

Aerodynamic Performance Measurements

The plenum total temperature is measured by two thermocouples located in the plenum. The rotor mass flow is determined from the measured pressure differential across the calibrated orifice plate. Radial surveys of total and static pressure, total temperature, and flow angle are made at survey stations 1 and 2 located upstream and downstream of the rotor as shown in figure 5. The total pressure, total temperature, and flow angle are measured by a single self-nulling combination (cobra + thermocouple) probe, while the static pressure is measured by a single self-nulling 18° wedge-angle probe. Drawings of the combination and wedge-angle probe are shown in figure 6. At stations 1 and 2 measurements were acquired at nine radial locations across the annulus. Additional measurements were made in the endwall regions at station 1 to obtain good resolution of the annulus wall boundary layers. Inner- and outer-wall static pressures are also measured at stations 1 and 2.

The overall pressure ratio and efficiency are calculated based on appropriate averages of the radial distributions of total pressure and total temperature measured at survey stations 1 and 2. Details of the averaging procedures used are given in the subsequent **Calculation Procedures** section.

Laser Anemometer Measurements

The laser anemometer measurement location in the stationary reference frame is specified by the parameters AP , RP , and CP . As shown schematically in figure 7, AP is the axial position, RP the radial position measured from the compressor axis of rotation, and CP the circumferential position measured relative to the Z - θ -plane. Velocity measurements occur along the circumferential measurement line which is swept through the LA measurement location as the blades rotate past the measurement location.

Since an LA measurement is a random event triggered by the presence of a seed particle in the probe volume, the blade row rotational position must be measured each time a velocity measurement occurs. The method used to determine the blade row rotational position is shown schematically in figure 8. A once-per-revolution (OPR) pulse, which originates from the face of the fan rotor disk, provides rotor speed information

to an electronic shaft angle encoder. The shaft angle encoder uses the elapsed time between the last two OPR pulses to calculate the output pulse frequency required to generate a given number of pulses per rotor revolution. The output pulse frequency is adjusted by the encoder for each new OPR signal to maintain a fixed number of pulses for each rotor revolution as the rotor speed drifts. For each new OPR signal, the encoder also initializes an internal counter and then starts to count the pulses generated during the current rotor revolution. Each time a velocity measurement occurs, the data acquisition computer records the measured velocity along with the current shaft angle encoder pulse count. Measurements which occur anywhere between two adjacent pulses are thus assigned to the same *measurement window*.

The distribution of measurement windows along a circumferential measurement line is specified by the following parameters:

- (1) Number of blade passages measured, *NP*
- (2) Number of measurement windows per blade passage, *NWN*
- (3) Value of the first measurement window in which measurements are recorded, *WNBEG*

The width of a window defines the minimum spatial resolution of the data in the circumferential direction. It is therefore advantageous to select the smallest window width possible while maintaining a reasonable total number of windows. All measurements reported herein were acquired with $NP = 17$ and $NW = 50$. The 17 measured blade passages form a contiguous segment on the rotor, which has a total of 22 blades. In other words, we do not measure a few blade passages, skip one passage, and then measure more blade passages.

At a given axial and radial location the first measurement window in which data are recorded *WNBEG* is chosen such that the window lies on the suction surface of a blade. The value of *WNBEG* is a function of the axial and radial location of the measurement line. The variation of *WNBEG* with axial location is shown schematically in figure 9. For clarity, only 15 measurement windows are shown from blade to blade in this figure. As shown in figure 9, *WNBEG* is chosen so as to lie on a straight-line extension of the blade mean camber line upstream and downstream of the blade. In practice, the blade geometry is used to calculate the value of *WNBEG* for each axial and radial measurement location. Because of blade untwist under varying speed and aerodynamic loading conditions, the accuracy of the calculation of *WNBEG* is of the order of one or two measurement windows.

The measurement windows in a blade passage are evenly distributed along the blade pitch, not along the gap between adjacent blade surfaces. In the blade-to-blade data plots presented in this report, the first point (at the left edge of the plot) is on the suction side of the blade passage. The blade appears near the right edge of the plot as a region of zero data since no measurements are acquired when the blade is in a

measurement window. The average value of all velocity measurements that occur in each window is plotted at a point located at the center of the window. These features of the data plots are shown schematically in figure 10.

Since the NASA Lewis LA system is a single-channel system, only one velocity component is measured during a given LA data acquisition run. The axial and tangential velocity components could be directly measured by orienting the probe volume fringe pattern normal to the axial and tangential directions, respectively. However, large measurement errors can occur (see ref. 15) if the fringe orientation is more than 30° from the absolute flow angle. Such errors are minimized by first determining the circumferentially averaged absolute flow angle at each measurement location from a preliminary survey of the flowfield. Two different fringe orientations which are within 20° of the circumferentially averaged flow angle are then specified for each axial, radial measurement location. For example, if the circumferentially averaged flow angle along a measurement line is 40° , the operator would collect data at fringe orientations of 20° and 60° during two runs made on the circumferential measurement line. The axial and tangential velocity components are then calculated using data from these two runs following the procedure outlined in the **Calculation Procedures** section.

In practice, the LA operator specifies the total number of measurements required for each run. For the present rotor the number of measurements requested was generally 60 000. For 17 surveyed blade passages with 50 measurement windows per blade passage, this yields approximately 70 measurements in each measurement window for each fringe orientation if the measurements are evenly distributed. As will be discussed in the **Calculation Procedures** section, all measurements which occur within a given measurement window are averaged together to obtain a mean velocity which is assigned to the center of the window.

Flowfield surveys are performed by collecting data at varying *AP, RP* locations. LA measurements are acquired along conical measurement surfaces which approximate the location of the rotor design streamsurfaces. The radial coordinates of the design streamlines are known at stations 1 and 2 (which are the locations of conventional pressure and temperature surveys), at the rotor blade leading and trailing edges, and at the stator leading edge location. The measurement surfaces are created using straight-line interpolation between these points as shown in figure 11. A meridional view of all the measurement surfaces showing the axial, radial coordinates of the measurement points is shown in figure 5.

Calculation Procedures

Aerodynamic Performance Data

The values of total and static pressure and total temperature measured at survey stations 1 and 2 are first corrected for Mach

number and streamline slope. These corrections are based on a calibration of each probe used and on the design streamline slope. All measurements are corrected to NACA standard-day sea-level conditions (temperature, 288.2 K; pressure, 101 325 N/m²) at the rotor inlet. The rotor overall performance is based on orifice mass flow and the aerodynamic survey measurements acquired at stations 1 and 2 upstream and downstream of the rotor, respectively. The orifice mass flow is corrected to standard-day conditions at the rotor inlet. The radial distributions of total temperature are mass averaged across the annulus. The radial distributions of total pressure are energy averaged by converting them to their enthalpy equivalents and then mass averaging them across the annulus. The formulas used are

$$\left. \begin{aligned} \frac{\bar{P}_j}{P_o} &= \left[\frac{\sum_{i=1}^{NR} \left(\frac{P_j}{P_o}\right)^{(\gamma-1)/\gamma} \rho_{j,i} (V_z)_{j,i} (\Delta A_{an})_{j,i}}{\sum_{i=1}^{NR} \rho_{j,i} (V_z)_{j,i} (\Delta A_{an})_{j,i}} \right]^{\gamma/\gamma-1} \\ \bar{T}_j &= \frac{\sum_{i=1}^{NR} T_{j,i} \rho_{j,i} (V_z)_{j,i} (\Delta A_{an})_{j,i}}{\sum_{i=1}^{NR} \rho_{j,i} (V_z)_{j,i} (\Delta A_{an})_{j,i}} \\ \eta_{AP} &= \frac{\left(\frac{\bar{P}_2}{\bar{P}_1}\right)^{(\gamma-1)/\gamma} - 1}{\frac{\bar{T}_2}{\bar{T}_1} - 1} \end{aligned} \right\} (1)$$

Subscript i refers to the i^{th} radial measurement location, subscript j to the station number, ΔA_{an} is the incremental annulus area, and NR the number of survey locations across the annulus. Standard practice is to use nine survey locations from tip to hub. In the present investigation, additional survey locations were used at station 1 at the peak efficiency and near stall operating conditions to obtain increased resolution of the inlet boundary layers for use in comparing measured performance to that predicted by numerical analysis codes. These additional stations were not included in the overall performance results because they were not used for all rotor operating conditions.

Laser Anemometer Measurements

The laser anemometer velocity measurements acquired along a measurement line which passes through a given axial, radial location can be represented by the following array:

$$V(i,j) \quad i = 1, NM(j) \quad j = 1, NWN \times NP \quad (2)$$

where $V(i,j)$ is the i^{th} measurement in window j and $NM(j)$ the number of measurements acquired in window j . The total number of measurement windows is $NWN \times NP$, where NWN is the number of measurement windows across one rotor pitch, and NP the number of rotor blade passages which are surveyed. As mentioned previously, all of the data reported herein were acquired with $NWN = 50$, $NP = 17$.

The velocities are corrected to standard day conditions using the relation

$$V_c(i,j) = V(i,j) \sqrt{\frac{T_s}{T_o}} \quad (3)$$

where V and V_c are the uncorrected and corrected velocities, respectively, and T_s and T_o the standard day and plenum total temperatures, respectively. The c subscript notation will be dropped in the following discussion for simplicity—all velocities should be understood to be standard day corrected.

The mean and standard deviation of the velocity measurements acquired within each measurement window are calculated as follows:

$$\bar{V}(j) = \frac{1}{NM(j)} \sum_{i=1}^{NM(j)} V(i,j) \quad j = 1, NWN \times NP \quad (4)$$

$$V'(j) = \left\{ \frac{1}{NM(j) - 1} \sum_{i=1}^{NM(j)} [\bar{V}(j) - V(i,j)]^2 \right\}^{1/2} \\ j = 1, NWN \times NP \quad (5)$$

where $\bar{V}(j)$ is the circumferential distribution of the ensemble-averaged velocity component in the fringe normal direction across each of the NP blade passages which were surveyed. The ensemble averaging period is one rotor revolution.

As mentioned in the previous **Test Procedure** section, measurements acquired at two different fringe orientations are required to calculate the axial and tangential components of velocity. This calculation is performed as the simultaneous solution of the following two equations for the two unknowns V_z and V_θ :

$$\bar{V}_{z\theta_1}(j) = \bar{V}_z(j) \cos Z\theta_1 + \bar{V}_\theta(j) \sin Z\theta_1$$

$$j = 1, NWN \times NP \quad (6)$$

$$\bar{V}_{z\theta_2}(j) = \bar{V}_z(j) \cos Z\theta_2 + \bar{V}_\theta(j) \sin Z\theta_2$$

$$j = 1, NWN \times NP \quad (7)$$

where $Z\theta_1$ and $Z\theta_2$ are the fringe orientation angles for the two separate runs, $\bar{V}_{z\theta_1}$ and $\bar{V}_{z\theta_2}$ the ensemble average velocity distributions calculated from equation (4) for the two separate runs, and \bar{V}_z and \bar{V}_θ the ensemble-averaged distributions of the axial and tangential velocity, respectively.

The circumferential distribution of \bar{V}_z and \bar{V}_θ across each blade passage can be used to assess the passage-to-passage variations in the ensemble average flowfield. However, the data set is quite large, since there are $NWN \times NP = 50 \times 17 = 850$ data points along the measurement line through each (AP, RP) point shown in figure 5. NASA Lewis can provide the data in this *spatially unaveraged* form on magnetic tape upon request.

To provide a more compact data set which should meet the needs of most users, the measurements acquired in each of the NP blade passages surveyed are spatially averaged across all the measured blade passages to yield a passage-averaged circumferential velocity distribution. The spatial average is formed as follows:

$$\bar{\bar{V}}_z(k) = \frac{1}{NP - NZ} \sum_{j=1}^{NP} \bar{V}_z[k + (j-1)NWN]$$

$$k = 1, NWN \quad (8)$$

$$\bar{\bar{V}}_\theta(k) = \frac{1}{NP - NZ} \sum_{j=1}^{NP} \bar{V}_\theta[k + (j-1)NWN]$$

$$k = 1, NWN \quad (9)$$

where NZ is the number of blade passages in which no measurements were acquired in window number k .

Values of $\bar{\bar{V}}_z(k)$ and $\bar{\bar{V}}_\theta(k)$ are used to calculate the passage-averaged relative flow angle as follows:

$$\beta_{REL}(k) = \text{ARCTAN} \left[\frac{\bar{\bar{V}}_\theta(k) - R\omega}{\bar{\bar{V}}_z(k)} \right] \quad k = 1, NWN \quad (10)$$

where R is the radius and ω the rotor rotational speed in radians per second.

The local speed of sound in each window in the averaged blade passage is calculated as follows:

$$\bar{\bar{V}}(k) = \left\{ \left[\bar{\bar{V}}_z(k) \right]^2 + \left[\bar{\bar{V}}_\theta(k) \right]^2 \right\}^{1/2}$$

$$c_p T_o = c_p t(k) + \left[\frac{\bar{\bar{V}}(k)}{2} \right]^2 - \omega R \bar{\bar{V}}_\theta(k)$$

$$VSOUND(k) = \sqrt{(\gamma - 1)c_p t(k)} =$$

$$\left((\gamma - 1) \left\{ c_p T_o + \omega R \bar{\bar{V}}_\theta(k) - \frac{[\bar{\bar{V}}(k)]^2}{2} \right\} \right)^{1/2}$$

where T_o is the plenum total temperature, $t(k)$ the local static temperature, $V(k)$ the absolute velocity calculated from $V_z(k)$ and $V_\theta(k)$, R the radius, and ω the rotational speed.

The relative Mach number is then calculated from the relative velocity and the local speed of sound:

$$M_{REL}(k) = \frac{\bar{\bar{W}}(k)}{VSOUND(k)} \quad k = 1, NWN \quad (11)$$

where

$$\bar{\bar{W}}(k) = \left\{ \left[\bar{\bar{V}}_z(k) \right]^2 + \left[\bar{\bar{V}}_\theta(k) - R\omega \right]^2 \right\}^{1/2} \quad (12)$$

Results and Discussion

Aerodynamic Performance Measurements

Aerodynamic performance data and laser anemometer flowfield measurements are presented for two design-speed operating conditions—one near peak efficiency and one near stall. The location of these two points on the rotor design speed operating line is shown in figure 12 along with additional aerodynamic performance measurements which are not reported in detail here. The data shown in figure 12 are based on orifice mass flow and the aerodynamic survey measurements acquired at survey stations 1 and 2 upstream and downstream of the rotor.

The aerodynamic radial survey results obtained at survey stations 1 and 2 at the near peak efficiency and the near stall conditions are presented in tables III(a) and (b). The overall rotor aerodynamic performance based on the energy-averaged total pressure ratio and mass-averaged total temperature ratio at station 2 is included in each table just ahead of the station 2 radial survey results.

The station 1 survey data from tables III(a) and (b) are plotted in figures 13 and 14 in the form of the total velocity

distribution normalized with respect to the critical velocity at standard-day conditions. The static pressure gradient near the casing wall for the peak efficiency condition does not match well with the measured wall static pressure. Since the near wall pressure measurements were made with a standard aerodynamic probe, it is possible that the probe access hole or probe stem affected the measurements near the casing. To check this effect, the static pressure distribution from 64-percent span from the hub to the casing was changed to give a linear distribution to the measured value of the casing static pressure. The modified velocity distribution which results from this process is plotted along with the measured velocity distribution in figure 13. The mass flow corresponding to each velocity distribution was calculated using a cubic spline. The measured pressure distribution yields a mass flow of 34.62 kg/sec (76.32 lbm/sec), while the modified distribution yields a mass flow of 34.78 kg/sec (76.66 lbm/sec). This difference is within the measurement accuracy of the orifice.

Also shown in figures 13 and 14 is the velocity distribution obtained from a radial survey performed at station 1 with the laser anemometer. Agreement between the velocities calculated from the survey probe pressure measurements and those measured with the laser anemometer is within 8 percent at all spanwise locations. This level of agreement is considered to be reasonable for several reasons. First, the flowfield at station 1 is affected by the potential flow which propagates upstream of the rotor, particularly near the hub. The absolute velocity and flow angle therefore vary slightly across the blade pitch. The range between the maximum and minimum velocity measured across the blade pitch is shown by the flags in figures 13 and 14. Second, although the laser anemometer system measures the pitchwise distribution of velocity at station 1, the pitchwise density distribution is not known. Therefore the LA data cannot be mass averaged. The LA data shown in figures 13 and 14 were arithmetically averaged across the blade pitch. Finally, the aerodynamic survey probes respond to the pitchwise varying velocity and pressure field in some unknown manner. The time-averaged probe measurements are then mass averaged to yield the results shown in figures 13 and 14.

The integrated mass flow at stations 1 and 2 was calculated from the survey data listed in tables III(a) and (b) using the measurement radii and annular area elements listed in table IV. The results are presented in table V. Note that when calculating the mass flow from an integration of the radial distribution of flow parameters across the annulus, the result is dependent on the number of annular elements used in the integration and on the location of the element centers. Therefore, when comparing mass- and energy-averaged conditions predicted by computational results to the measured values shown in table V, one should take care to use computed conditions at the radii shown in table IV and to use the annular area elements shown in table IV to obtain accurate comparisons.

Measurements made with a hot-wire anemometer 8 cm upstream of the rotor hub leading edge plane indicate a free-stream turbulence level of about 1.5 percent.

Laser Anemometer Measurements

Two features of the velocity measurements should be kept in mind when interpreting the LA data. First, the average of all velocity measurements which occur in a given window is often considered as a single velocity measured at a point located at the center of the measurement window. It is important to remember that the measurements do not actually occur at a single point but rather occur in a region centered around the plotted point. Second, although each individual velocity measurement provides an instantaneous measurement of the unsteady velocity field, the measurements acquired in each measurement window are acquired over thousands of separate rotor revolutions. The average of all velocity measurements acquired in a given window is therefore the ensemble average (with the averaging period being one rotor revolution) velocity at the window location.

The location of each laser anemometer measurement is listed in table VI. The absolute angular location of the first measurement window is given by the parameter *WNBEG*. Since the rotor has 22 blades and there are 50 measurement windows across each blade passage, there are a total of 1100 measurement windows around the rotor wheel. The absolute angular location which corresponds to a given value of *WNBEG* can therefore be obtained from

$$\theta(\text{radians}) = \frac{2\pi WNBEG}{1100}$$

The origin of the *AP*-coordinate shown in figure 5 (which defines the laser anemometer measurement axial location as well as the axial location of aerodynamic survey stations 1 and 2) is different from the origin of the *Z*-coordinate shown in figure 4 (which defines the blade sections and the annulus geometry). The conversion factor between the two *Z*-coordinates is given by

$$AP_{\text{laser and aerodata}} = Z_{\text{blade}} - 2.159 \text{ cm}$$

The absolute axial locations listed in table VI are dependent on the rotor axial deflection, which varies with operating condition from day to day. The axial locations listed in table VI for 0- and 100-percent chord may therefore not agree with those listed in the blade geometry data in table I. Consequently, when comparing laser anemometer measurements to computed results, one should use the percent chord locations listed in table VI as a method of placing the axial measurement location relative to the blade.

The radial measurement locations listed in table VI in terms of percent span from the tip (i.e., 10- through 90-percent span) define LA measurement surfaces as shown in figure 11 which follow the design streamlines that pass through the rotor trailing edge at 10 through 90 percent of mass flow fraction as measured from the blade tip. As a result, the measurement locations listed for 10-percent span, for example, do not in general lie at 10 percent of geometric span from the tip. The radial location of each measurement point relative to the inner and outer flowpath radius at a given axial location should therefore be determined by calculating the percent span location based on the absolute axial, radial measurement locations given in table VI along with the flowpath coordinates listed in table II.

The laser anemometer data are presented in the form of relative Mach number and relative flow angle distributions along the surfaces of revolution which are shown schematically in figures 15 and 16.

Figure 15 illustrates the constant pitch lines along which the LA data are presented in the form of *streamwise* plots for each immersion. The data are plotted in the streamwise direction from approximately one chord upstream of the rotor, through the rotor, and approximately one chord downstream of the rotor along nine constant-pitch lines. The pitch is measured relative to the blade suction surface—0-percent pitch is the suction surface of one blade, 100-percent pitch is the suction surface of the adjacent blade.

Figure 16 illustrates the constant chord lines along which the LA data are presented in the form of blade-to-blade plots for each immersion. At 10-, 30-, and 70-percent span, blade-to-blade plots of the data are presented for each chordwise measurement location. To limit the number of plots in this report, blade-to-blade plots at the remaining immersions are presented at only six chordwise locations upstream and downstream of the blade. These chordwise locations were chosen because the Mach number and flow angle distributions at these locations define the bow wave system and the blade wake. The blade-to-blade distributions of Mach number and flow angle within the blade at immersions other than 10-, 30-, and 70-percent span can be determined at nine points across the blade pitch from the nine streamwise plots presented herein for each immersion or can be obtained from the complete LA data set which is available upon request on magnetic media.

Contour plots of the relative Mach number distribution along the LA measurement surfaces at 10-, 30-, and 70-percent span are shown in figure 17 for both the near peak efficiency and the near stall operating conditions. These contour plots are from reference 7. They were generated from the data by applying data enhancement procedures such as smoothing and interpolation in the direction of the steepest Mach number gradient. These procedures, which are fully described in reference 7, do not affect the overall characteristics of the contour plots. The contour plots formed from the data without using enhancement procedures are compared to the enhanced contour plots in reference 7.

The streamwise and blade-to-blade plots of relative Mach number and relative flow angle are presented in the following figures:

Near peak efficiency		Near stall	
Figure	Percent span	Figure	Percent span
18,19	10	34,35	10
20,21	20	36,37	20
22,23	30	48,49	30
24,25	40	40,41	40
26,27	50	42,43	50
28,29	60	44,45	60
30,31	70	46,47	70
32,33	80	48,49	80
		50,51	90

Data are not presented at 90-percent span for the peak efficiency condition because of a high degree of scatter in the data. The interpretation of the *uncertainty interval* drawn for each LA measurement in figures 18 to 51 is discussed in the next section.

Data Uncertainty and Reproducibility

The rotor speed is constant to within 0.3 percent of design speed. The orifice mass flow is maintained constant to within 0.14 kg/sec.

Aerodynamic probe measurements.—The aerodynamic survey probes were calibrated before starting the test program. Pressure probes are calibrated for streamline pitch angle sensitivity. Temperature probes are calibrated to determine recovery factors for the Mach number range encountered during testing. The estimated uncertainties in the individual aerodynamic survey measurements are as follows:

Flow angle, deg	1
Temperature, K	0.6
Total pressure at station 1, N/cm ²	0.1
Static pressure at station 1, N/cm ²	0.4
Total pressure at station 2, N/cm ²	0.10
Static pressures at station 2, N/cm ²	0.07

The uncertainty in overall performance is affected by two additional factors. First, the combination probe and the static pressure probe were located at a single circumferential location. Therefore, any effects due to asymmetries in the flowfield are not included in the measurements reported here. Second, only nine radial survey locations were used at the rotor exit (survey station 2); this introduces uncertainty in the spanwise-averaged quantities at station 2 because of a lack of resolution within the endwall boundary layers.

Laser anemometer measurements.—The estimated uncertainty for the laser anemometer data is nominally 1.0 percent on velocity and 1° on flow angle. This uncertainty is dependent

on many factors, including local turbulence intensity, through-flow unsteadiness, velocity bias errors, and rotor speed drift during each individual rotor revolution. Uncertainties due to rotor speed drift are minimized by not recording measurements from rotor revolutions during which the rotor speed drifted by more than 0.4 percent. The measurement uncertainty is higher in regions of high-velocity gradients which occur across the rotor passage shock and across the blades wakes. In these regions the accuracy of the laser anemometer measurements is controlled by the ability of the seed particles to follow the flow. A more complete discussion of measurement uncertainties and seed particle tracking error across a typical transonic rotor passage shock can be found in reference 15.

The statistical uncertainty in the relative Mach number and flow angle is estimated by first determining the statistical uncertainty in \bar{V}_1 and \bar{V}_2 in each individual measurement window using equation (5). These statistical uncertainties are then combined by applying propagation of uncertainty methods (ref. 16) to equations (6) to (9) to determine the uncertainty in \bar{V}_c and \bar{V}_θ . Finally, the uncertainty in Mach number and flow angle is determined by applying propagation of uncertainty methods to equations (10) and (11).

The magnitude of the uncertainty in Mach number and flow angle is indicated by the *uncertainty interval* drawn on each data point in figures 18 to 51. These uncertainty intervals indicate a 95-percent confidence level that the true mean lies within the uncertainty interval.

Summary of Results

A laser anemometer has been used to provide detailed flowfield surveys within a low-aspect-ratio axial-flow transonic fan rotor operating in a rotor-only configuration. Both laser anemometer and aerodynamic performance data were acquired at operating conditions near peak efficiency and near stall.

Flowpath coordinates and detailed blade geometry are presented in tabular form. The aerodynamic performance is presented in tabular form as well as in plots of the radial distribution of velocity upstream of the rotor. The laser anemometer data are presented in the form of pitchwise and streamwise plots of the distribution of relative Mach number and relative flow angle on blade-to-blade streamsurfaces located at nine equally spaced spanwise locations from hub to tip.

Appendix A—Symbols

ΔA_{an}	incremental annulus area (eq. (1))	$TNPC$	blade thickness normal to the mean camber line, cm (fig. 4)
AP	laser anemometer axial measurement location (fig. 7)	U	blade velocity, m/sec (fig. 3)
$BETA$	angle of blade mean camber line from meridional direction (table I)	V	velocity, m/sec
$BETA1$	angle of blade surface 1 from meridional direction (fig. 4)	$VSOUND$	sonic velocity, m/sec
$BETA2$	angle of blade surface 2 from meridional direction (fig. 4)	W	relative velocity, m/sec
c_p	coefficient of specific heat at constant pressure (eq. (11))	$WNBEG$	starting window number for laser anemometer survey
M_{REL}	relative Mach number	Z	axial coordinate used to define blade and flowpath geometry (fig. 4)
NM	number of LA measurements in each measurement window	$Z\theta$	laser anemometer fringe angle relative to axial direction, deg
NP	number of blade passages surveyed with laser anemometer	β_{REL}	relative flow angle, deg
NR	number of points in aerodynamic performance radial survey (eq. (1))	γ	ratio of specific heats (eq. (11))
NWN	number of laser anemometer measurement windows in blade passage	η_{AD}	adiabatic efficiency (eq. (1))
NZ	number of blade passages for which no LA measurements occurred in given measurement window	θ	circumferential coordinate (fig. 8)
OPR	once-per-revolution timing mark (fig. 8)	ρ	static density (eq. (1))
P	total pressure (eq. (1))	ω	rotational speed, radians/sec
R	radial coordinate used to define blade and flowpath geometry (fig. 4)		
RP	laser anemometer radial measurement location (fig. 7)		
T	total temperature (eq. (1))		
T_s	NACA standard day temperature, 288.2 K		
t	static temperature		
$THSP1$	angular coordinate of blade surface 1, radians (table I)		
$THSP2$	angular coordinate of blade surface 2, radians (table I)		
		Subscripts:	
		c	corrected to standard day conditions
		z	axial velocity component
		θ	tangential velocity component
		0	plenum conditions
		1	aerodynamic survey station upstream of rotor
		2	aerodynamic survey station downstream of rotor
		Superscripts:	
		—	ensemble-averaged quantity
		=	passage-averaged quantity
		'	standard deviation

Appendix B—Description of Data Available on Magnetic Media

Blade and flowpath geometry as well as the complete set of laser anemometer measurements acquired at peak efficiency and near stall operating conditions are available on magnetic media as formatted ASCII files. The contents of the blade and flowpath geometry files are exactly as shown in tables I and II, respectively. The contents of the laser anemometer data files are now described.

Types of Laser Anemometer Data Files

The laser anemometer data are acquired on surfaces of revolution called *measurement surfaces* which approximate streamsurfaces through the rotor at the design operating condition. A measurement surface is shown schematically in figure 11. The nine measurement surfaces used in the present investigation are shown in figure 5. All the LA data acquired at a given axial and radial location under a given operating condition are contained in a *scan*. Two types of data files are used to describe the scan data—a scan background information file and a scan data file.

Background Information File

The background information file is essentially a catalog by scan number of all the data acquired on a measurement surface at a given operating condition. This file contains information on the measurement location, fan operating condition, and number of measurements acquired at each point along the measurement surface. There is one background information file for each measurement surface for each fan operating condition. An example of a background information file is shown in table B-I. The file contents are now described.

SCAN

Scan number. This is a unique number used to identify the scan data file which contains the LA data acquired at the measurement location and fan operating condition listed in the background information file.

PERCENT CHORD

Measurement location in terms of percent chord. This value is calculated from the absolute measurement location and the axial location of the blade leading and trailing edge during the acquisition of data on the measurement surface. As discussed in the **Results and Discussion** section of the report, the axial location of the blade changes from day to day. The percent chord location of the data should therefore be used to place the data at the proper location relative to the blade and flowpath geometry.

AP,RP,CP

Absolute axial, radial, and circumferential measurement locations, respectively. In the present work the value of *CP* is fixed and is not important. Recall that the origin of the axial coordinate which describes the LA measurement location *AP* is different from the origin of the blade and flowpath coordinates. The relationship between the two coordinate systems is given by

$$AP_{laser\ data} = Z_{blade} - 2.159\ cm$$

RT

Most LA measurements were acquired with the LA optical axis aligned in the radial direction. However, to minimize optical blockage due to blade twist the LA optical axis can be tilted away from the radial direction. The angular deflection of the LA optical axis, measured in the *R-θ*-plane shown in figure 7, is given by the angle *RT*. When $RT \neq 0$, the measured velocity components lie in the *Z-θ'*-plane shown in figure B-1 rather than in the *Z-θ*-plane. In these cases, the circumferential component of absolute velocity is given by $V_{\theta} = V_{\theta'} \cos RT$. This correction is small since most of the off-radial deflections used in this investigation were less than 10° and the cosine of 10° is 0.985.

PERCENT SPD

Rotor speed, corrected to standard day conditions, as a percentage of the design value of 16 043 rpm.

PR

Total pressure ratio as determined by rakes located far downstream of the rotor. The rake-measured pressure ratio is only used to reset the rig operating conditions from day to day. A more accurate measure of the rotor total pressure rise is provided by the total pressure ratios listed in tables III(a) and (b).

CWF

Nominal mass flow as measured by the orifice during data acquisition, corrected to standard day conditions.

T01

Plenum total temperature. This temperature is used to correct measured conditions to standard day conditions.

RUN NUMBERS

Run numbers of the two individual laser anemometer runs which were combined using equations (3) to (9) of the **Calculation Procedures** section to calculate the axial and tangential velocity components.

NP

Number of blade passages surveyed with the laser anemometer.

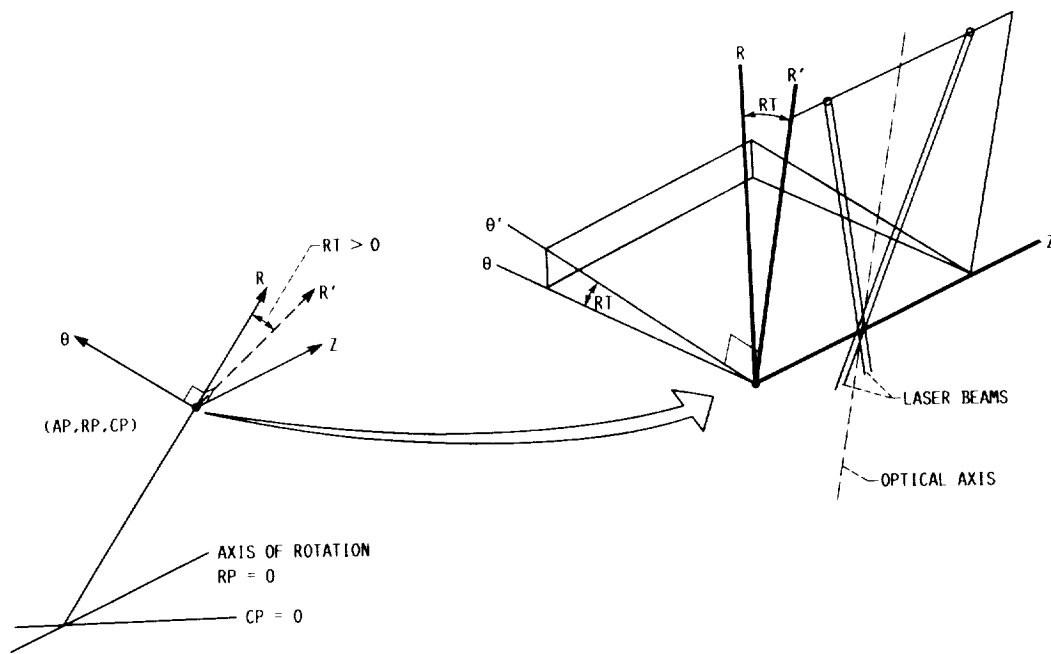


Figure B-1.—Definition of off-radial beam deflection angle RT . As shown, RT is positive.

NWN

Number of measurement windows across each blade passage surveyed.

WNBEG

Starting measurement window number for the scan data. The measurement windows are numbered relative to a once-per-revolution marker which is fixed to the rotor disk. In the present investigation there are 1100 windows around the rotor, 50 windows in each of the 22 blade passages. The value of *WNBEG* for each scan is set such that the first measurement window in the scan data file lies on the blade suction surface as shown in figure 9.

NMEAS

Total number of measurements acquired in each of the two laser anemometer runs which comprise a scan.

NREJ

Number of measurements flagged for rejection. Each LA run consists of two parts. During the initial part, $NMEAS/2$ measurements are acquired and a mean velocity is calculated for each measurement window based on the average of all measurements acquired within the window. During the second part of the run, additional $NMEAS/2$ measurements are acquired, and each measurement is compared to the mean velocity previously calculated for the window in which the measurement occurred. If a measurement deviates by more than 25 percent from the mean, the *data rejected* counter *NREJ* is incremented. The measurement is recorded or discarded depending on the setting of a reject/save flag. A detailed comparison of data acquired under identical flow

conditions with both flag settings indicates that rejected data usually occur in regions of high velocity gradients such as near the blade surfaces and in the edges of wakes. *Saved* data in these regions are generally well behaved but display higher scatter between measurements due to the large velocity gradients. During the present investigation the reject/save flag was always set to save the data. Since no measurements were rejected, the value of *NREJ* merely serves as an indicator of the scatter in the data.

Scan Data File

There is one scan data file for each scan listed in the background information file. Each scan data file contains information on the measurement location, the measured velocity components, measurement uncertainty intervals, passage-to-passage flowfield variations, and the total unsteadiness for each of the 50 measurement windows across the blade pitch. An example scan data file is shown in table B-II. The file contents are now described.

AXIAL POSITION

Absolute axial location of the LA measurement *AP*. The conversion to percent chord is based on the leading and trailing edge axial positions which are also listed in the scan data file. As discussed in the **Results and Discussion** section of the report, the blade axial location shifts from day to day. The percent chord location of the data should therefore be used to properly orient the data relative to the blade and flowpath geometry.

RADIAL POSITION

Absolute radial location of the LA measurements. The percent span value is based on the radial location of the measurement *RP* and the flowpath hub and tip radius at the axial location of the measurement *AP*.

CIRCUMFERENTIAL POSITION

Absolute circumferential location of the LA measurements.

BEAM DEFLECTION

Off-radial measurement angle *RT* as defined previously for the background information file.

CORR SPEED

Rotor rotational speed, corrected to standard day conditions.

PRESSURE RATIO, CORR MASS FLOW, TOTAL TEMPERATURE

These variables are identical to those defined previously for the background information file.

LEADING/TRAILING EDGE AXIAL POS

Absolute axial location of the blade leading and trailing edge during LA data acquisition on the measurement surface. These locations are determined by reflecting the laser beams off the blade leading and trailing edges at the measurement surface radial immersion. Since the blade edge axial locations vary slightly from day to day, these locations are used to convert the absolute measurement axial location *AP* into a percent chord value.

BEGINNING WINDOW NUMBER

Value of *WNBEG* as defined previously for the background information file.

WINDOW NO.

Window number relative to the blade suction surface. There are 1100 actual measurement windows, 50 windows in each of 22 blade passages. Since only 17 blade passages were surveyed, measurements were recorded in only 850 of these windows. The results presented in the scan data file are the spatially ensemble-averaged data which result from applying equations (3) to (9) to the data. The window number in the scan data file is therefore the window number in the averaged blade passage that results from spatially ensemble-averaging measurements, which occurred in the 17 measured blade passages. Values listed in window 1, for example, are the average of measurements, which occurred in windows 1, 51, 101, 151, . . . , 801, relative to the starting window number *WNBEG*. When combining data from several different scans, as would be required when constructing a blade-to-blade contour plot for example, the value of *WNBEG* for each scan gives the absolute circumferential measurement location of the windows for that scan in the averaged blade passage. This feature of the data is shown in figure 9.

NO. MEAS.

Total number of measurements acquired in the measurement window number across the *NP* measured blade passages. This number is the average of the number of measurements acquired in each of the two laser anemometer runs which comprise the scan.

AVG PASS VEL

Spatially ensemble-averaged axial and tangential velocity components (in m/sec) as calculated by equations (8) and (9). *AVZ* corresponds to $\bar{\bar{V}}_z$, and *AVT* corresponds to $\bar{\bar{V}}_\theta$.

UNCERTAINTY OF AVG

Uncertainty intervals for the velocity components (m/sec). *UVZ* and *UNT* are the uncertainty intervals for the axial and tangential velocity components, respectively. The odds are 20:1 that the true mean velocity components $\bar{\bar{V}}_z$ and $\bar{\bar{V}}_\theta$ lie in the intervals $AVZ - UVZ < \bar{\bar{V}}_z < AVZ + UVZ$ and $AVT - UNT < \bar{\bar{V}}_\theta < AVT + UNT$.

SDVZ,SDVT

Spatially ensemble-averaged velocity components $\bar{\bar{V}}_z$ and $\bar{\bar{V}}_\theta$ do not provide any information on the degree of flowfield variation from passage to passage. A measure of the passage-to-passage flowfield variations is provided by the parameters *SDVZ* and *SDVT*, which are the standard deviation between the spatially ensemble-averaged velocity components and the velocity components measured in each of the *NP* blade passages that were surveyed. *SDVZ* and *SDVT* are calculated as follows, where *j* is the blade passage number and $k = 1, NWN$:

$$SDVZ(k) = \left(\frac{1}{NP - NZ - 1} \sum_{j=1}^{NP} \left\{ \bar{\bar{V}}_z(k) - \bar{V}_z[k + (j - 1)NWN] \right\}^2 \right)^{1/2}$$

$$SDVT(k) = \left(\frac{1}{NP - NZ - 1} \sum_{j=1}^{NP} \left\{ \bar{\bar{V}}_\theta(k) - \bar{V}_\theta[k + (j - 1)NWN] \right\}^2 \right)^{1/2}$$

AVZ', AVT'

Axial and tangential components of the unresolved unsteadiness are denoted by *AVZ'* and *AVT'*, respectively. The unresolved unsteadiness is defined as the sum of all flow fluctuations which are not correlated to the rotor blade passing frequency. Such fluctuations include rotor speed drift, through-flow fluctuations, vortex streets shed from the blade trailing edge, and turbulence.

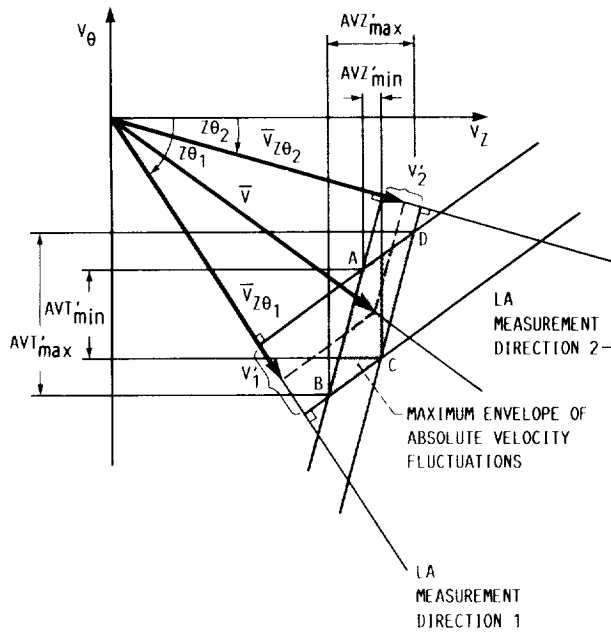


Figure B-2.—Schematic representation of bounds on unresolved unsteadiness.

The laser anemometer system used in the present investigation is a single-channel system and therefore measures only the component of unresolved unsteadiness which is in the fringe orientation direction. Measurements acquired with a single-channel LA system cannot be used to calculate values of the unresolved unsteadiness in the axial and tangential directions unless the measurements are acquired with the fringes oriented in the axial and tangential directions, which was not done in the present work. It is, however, possible to calculate upper and lower bounds for the unsteadiness components using measurements acquired at arbitrary fringe orientations.

As shown in figure B-2, measurements acquired in measurement directions 1 and 2 at a given axial and radial location enable the calculation of $\bar{V}_{z\theta_1}$, V'_1 , $\bar{V}_{z\theta_2}$, and V'_2 in the directions 1 and 2, respectively. V'_1 and V'_2 represent one standard deviation of the velocity from $\bar{V}_{z\theta_1}$ and $\bar{V}_{z\theta_2}$. The parallelogram ABCD can be defined in figure B-2 by projecting the range of possible velocities defined by V'_1 and V'_2 perpendicular to the 1 and 2 directions. This parallelogram defines the locii of all possible velocity fluctuations which are one standard deviation from the mean absolute velocity \bar{V} . The extremes of this parallelogram in the Z- and θ -directions define the bounds AVZ' and AVT' included in each scan data file.

TABLE B-I.—EXAMPLE OF A BACKGROUND INFORMATION FILE

31-OCT-88

***** LASER VELOCIMETER SCAN DATA BACKGROUND INFORMATION *****

ROTOR 67, NEAR STALL

AP, RP, CP - AXIAL, RADIAL, AND CIRCUMFERENTIAL POSITIONS
 T01, PR, CWF - TOTAL TEMP., PRESSURE RATIO AND CORR. MASS FLOW
 WNBEQ - BEGINNING WINDOW NUMBER (STARTS WHEN ROTOR SUCTION SURFACE ALIGNS WITH LFA PROBE VOLUME)

NMEAS, NREJ - # MEASUREMENTS/RUN, MAX # REJECTED
 NP - NUMBER OF ROTOR PASSAGES SURVEYED
 NWN - NUMBER OF MEASUREMENT WINDOWS
 RT - OFF RADIAL BEAM-DEFLECTION ANGLE

SEQ. SCAN	% CHORD	AP CM	RP CM	CP (DEG)	RT (DEG)	% SPD	PR (KG/S)	CWF (KG/S)	T01 (R)	RUN NO.S	NP	NWN	WNBEQ	NMEAS	NREJ
1	100.00	-4.674	24.235	20.00	0.00	100.4	1.680	32.50	496.1	2161/ 2162	17	50	123.5	60000	522
2	1001	-99.14	-4.633	24.234	20.00	0.00	100.4	32.50	496.1	2163/ 2164	17	50	124.2	60000	473
3	1002	-80.00	-3.729	24.223	20.00	0.00	100.5	32.50	496.1	2165/ 2166	17	50	138.7	60000	510
4	1003	-60.00	-2.784	24.211	20.00	0.00	100.5	32.50	496.1	2167/ 2168	17	50	153.2	60000	552
5	1004	-40.00	-1.839	24.192	20.00	0.00	100.5	32.50	496.1	2169/ 2170	17	50	167.2	60000	694
6	1005	-20.00	-0.894	24.169	20.00	0.00	100.6	32.50	496.1	2171/ 2172	17	50	180.8	60000	551
7	1006	-10.00	-0.422	24.157	20.00	0.00	100.4	32.50	495.6	2173/ 2174	17	50	187.4	60000	396
8	1007	-5.00	-0.185	24.151	20.00	0.00	100.7	32.50	495.6	2175/ 2176	17	50	190.8	60000	910
9	1008	-2.50	-0.067	24.148	20.00	0.00	100.7	32.50	495.6	2177/ 2178	17	50	192.4	60000	617
10	1009	0.00	0.051	24.145	20.00	0.00	100.6	32.50	495.6	2179/ 2180	17	50	194.3	60000	437
11	1010	2.50	0.169	24.128	20.00	0.00	100.5	32.50	495.6	2181/ 2182	17	50	195.2	60000	319
12	1011	5.00	0.287	24.111	20.00	6.00	100.5	32.50	495.6	2183/ 2184	17	50	197.1	60000	248
13	1012	7.50	0.405	24.094	20.00	12.00	100.5	32.50	495.6	2185/ 2186	17	50	198.9	60000	360
14	1013	10.00	0.523	24.077	20.00	14.00	100.5	32.50	495.6	2187/ 2188	17	50	200.7	60000	470
15	1014	20.00	0.996	24.010	20.00	14.00	100.3	32.50	495.6	2189/ 2190	17	50	207.9	60000	914
16	1015	30.00	1.468	23.942	20.00	9.16	100.7	32.50	496.5	2211/ 2212	17	50	214.7	60000	***
17	1016	40.00	1.941	23.874	20.00	5.91	100.7	32.50	495.6	2193/ 2194	17	50	221.2	60000	686
18	1017	50.00	2.413	23.806	20.00	1.09	100.8	32.50	495.6	2195/ 2196	17	50	227.6	60000	128
19	1018	60.00	2.885	23.738	20.00	-4.09	100.7	32.50	495.6	2197/ 2198	17	50	233.7	60000	42
20	1019	70.00	3.358	23.670	20.00	-8.97	100.5	32.50	495.6	2209/ 2210	17	50	239.3	60000	18
21	1020	80.00	3.830	23.603	20.00	-14.00	100.5	32.50	495.6	2201/ 2202	17	50	244.3	60000	89
22	1021	90.00	4.303	23.535	20.00	-10.00	100.7	32.50	495.6	2203/ 2204	17	50	248.8	60000	54
23	1022	100.00	4.775	23.467	20.00	0.00	100.6	32.50	496.5	2205/ 2206	16	50	252.5	60000	72
24	1023	123.61	5.891	23.401	20.00	0.00	100.7	32.50	496.5	2207/ 2208	16	50	263.8	60000	251

References

1. Dunker, R.J.; Strinning, P.E.; and Weyer, H.B.: Experimental Study of the Flow Field Within a Transonic Axial Compressor Rotor by Laser Velocimetry and Comparison with Through-flow Calculations. *J. Eng. Power*, vol. 100, no. 2, Apr. 1978, pp. 279-286.
2. Chima, R.V.; and Strazisar, A.J.: Comparison of Two- and Three-Dimensional Flow Computations with Laser Anemometer Measurements in a Transonic Compressor Rotor. *J. Eng. Power*, vol. 105, no. 3, July 1983, pp. 596-605.
3. Sarathy, K.P.: Computation of Three-Dimensional Flow Fields Through Rotating Blade Rows and Comparison with Experiment. *J. Eng. Power*, vol. 104, no. 2, Apr. 1982, pp. 394-402.
4. Singh, U.K.: A Computation and Comparison with Measurements of Transonic Flow in an Axial Compressor Stage with Shock and Boundary Layer Interaction. *J. Eng. Power*, vol. 104, no. 2, Apr. 1982, pp. 510-515.
5. Goldman, L.J.; and Seasholtz, R.G.: Laser Anemometer Measurements in an Annular Cascade of Core Turbine Vanes and Comparison with Theory. NASA TP-2018, 1982.
6. Denton, J.D.: An Improved Time Marching Method for Turbomachinery Calculation. ASME Paper 82-GT-239, Apr. 1982.
7. Pierzga, M.J.; and Wood, J.R.: Investigation of the Three-Dimensional Flow Field Within a Transonic Fan Rotor: Experiment and Analysis. *J. Eng. Gas Turbines Power*, vol. 107, no. 2, Apr. 1985, pp. 436-449.
8. Wood, J.R.; Strazisar, A.J.; and Simonyi, P.S.: Shock Structure Measured in a Transonic Fan Using Laser Anemometry. Transonic and Supersonic Phenomena in Turbomachines, AGARD CP-401, AGARD, Neuilly-Sur-Seine, France, 1986, pp. 2-1 to 2-14.
9. Strazisar, A.J.: Investigation of Flow Phenomena in a Transonic Fan Rotor Using Laser Anemometry. *J. Eng. Gas Turbines Power*, vol. 107, no. 2, Apr. 1985, pp. 427-435.
10. Hathaway, M.D.; Gertz, J.B.; Epstein, A.H.; and Strazisar, A.J.: Rotor Wake Characteristics of a Transonic Axial-Flow Fan. *AIAA J.*, vol. 24, no. 11, Nov. 1986, pp. 1802-1810.
11. Cunnan, W.S.; Stevens, W.; and Urasek, D.C.: Design and Performance of a 427-Meter-per-Second-Tip-Speed Two-Stage Fan Having a 2.40 Pressure Ratio. NASA TP-1314, 1978.
12. Urasek, D.C.; Gorrell, W.T.; and Cunnan, W.S.: Performance of Two-Stage Fan Having Low-Aspect-Ratio, First-Stage Rotor Blading. NASA TP-1493, 1979.
13. Powell, J.A.; Strazisar, A.J.; and Seasholtz, R.G.: High-Speed Laser Anemometer System for Intra-Rotor Flow Mapping in Turbomachinery. NASA TP-1663, 1982.
14. Powell, J.A.; Strazisar, A.J.; and Seasholtz, R.G.: Efficient Laser Anemometer for Intra-Rotor Flow Mapping in Turbomachinery. *J. Eng. Gas Turbines Power*, vol. 103, no. 2, Apr. 1981, pp. 424-429.
15. Strazisar, A.J.; and Powell, J.A.: Laser Anemometer Measurements in a Transonic Axial Flow Compressor Rotor. *J. Eng. Gas Turbines Power*, vol. 103, no. 2, Apr. 1981, pp. 430-437.
16. Kline, S.J.: The Purpose of Uncertainty Analysis. *J. Fluids Eng.* vol. 107, no. 2, June 1985, pp. 153-160.

TABLE I.—Continued.

SURFACE NUMBER 1 FROM THE HUB

LEADING EDGE AND TRAILING EDGE CIRCLE DATA

	LEADING EDGE	TRAILING EDGE
CIRCLE RADIUS	0.04498	0.04232
CIRCLE CENTER COORDINATES		
RADIAL	9.57171	11.80840
AXIAL	0.04391	8.98787
MERIDIONAL	0.04498	9.28088
ANGULAR	0.00666	0.18351

COORDINATES FOR TANGENCY POINTS ON BLADE SURFACE 1

MERIDIONAL	0.01370	9.30333
ANGULAR	0.01004	0.18655

COORDINATES FOR TANGENCY POINTS ON BLADE SURFACE 2

MERIDIONAL	0.06864	9.27058
ANGULAR	0.00266	0.18003

K	Z	R	THSP1	THSP2	TNPC	BETA	BETA1	BETA2
1	0.00000	9.56278	0.00865	-0.00178	0.07810	38.47	44.11	31.80
2	0.27160	9.62407	0.03618	0.01613	0.15315	37.49	42.66	31.50
3	0.54378	9.68852	0.06189	0.03360	0.22232	35.78	40.43	30.52
4	0.81570	9.75592	0.08533	0.04974	0.29163	32.86	37.69	27.43
5	1.08754	9.82631	0.10657	0.06354	0.36437	30.51	35.77	24.61
6	1.35921	9.89964	0.12681	0.07647	0.43233	29.83	34.83	24.29
7	1.63072	9.97588	0.14576	0.08907	0.50011	27.83	32.10	23.21
8	1.90194	10.05495	0.16218	0.10056	0.56154	25.01	28.58	21.21
9	2.17294	10.13684	0.17671	0.11102	0.61248	23.10	26.27	19.78
10	2.44372	10.22147	0.18984	0.12075	0.65702	21.51	24.15	18.77
11	2.71419	10.30831	0.20160	0.12989	0.69534	19.83	21.87	17.73
12	2.98434	10.39669	0.21199	0.13834	0.72800	18.05	19.60	16.48
13	3.25408	10.48583	0.22112	0.14608	0.75476	16.41	17.52	15.29
14	3.52334	10.57497	0.22913	0.15318	0.77604	14.95	15.64	14.25
15	3.79207	10.66334	0.23613	0.15971	0.79224	13.54	13.76	13.32
16	4.06023	10.75022	0.24212	0.16572	0.80290	12.15	11.91	12.40
17	4.32773	10.83489	0.24719	0.17121	0.80863	10.80	10.17	11.44
18	4.59453	10.91671	0.25139	0.17618	0.80984	9.44	8.38	10.50
19	4.86060	10.99513	0.25470	0.18066	0.80601	8.06	6.56	9.56
20	5.12594	11.06985	0.25718	0.18465	0.79753	6.68	4.79	8.55
21	5.39054	11.14095	0.25887	0.18814	0.78469	5.28	3.00	7.55
22	5.65443	11.20855	0.25975	0.19115	0.76714	3.84	1.12	6.55
23	5.91761	11.27275	0.25981	0.19369	0.74472	2.33	-0.83	5.47
24	6.18010	11.33364	0.25905	0.19574	0.71748	0.76	-2.83	4.34
25	6.44192	11.39136	0.25746	0.19728	0.68542	-0.90	-4.92	3.12
26	6.70311	11.44597	0.25500	0.19830	0.64831	-2.67	-7.13	1.83
27	6.96369	11.49759	0.25164	0.19876	0.60604	-4.50	-9.40	0.47
28	7.22368	11.54628	0.24736	0.19867	0.55865	-6.41	-11.74	-0.96
29	7.48312	11.59217	0.24211	0.19799	0.50596	-8.43	-14.21	-2.47
30	7.74204	11.63531	0.23584	0.19670	0.44757	-10.62	-16.87	-4.09
31	8.00045	11.67577	0.22844	0.19475	0.38343	-12.88	-19.56	-5.84
32	8.25840	11.71363	0.21996	0.19211	0.31491	-15.15	-22.08	-7.72
33	8.51592	11.74899	0.21024	0.18866	0.24091	-18.20	-25.59	-10.12
34	8.77309	11.78190	0.19869	0.18420	0.15866	-21.60	-29.58	-12.65
35	9.02991	11.81262	0.18550	0.17891	0.07122	-23.85	-32.17	-14.33

TABLE I.—Continued.

SURFACE NUMBER 2 FROM THE HUB

LEADING EDGE AND TRAILING EDGE CIRCLE DATA		
	LEADING EDGE	TRAILING EDGE
CIRCLE RADIUS	0.04772	0.04384
CIRCLE CENTER COORDINATES		
RADIAL	10.80878	12.82506
AXIAL	0.17245	8.94385
MERIDIONAL	0.04772	9.06074
ANGULAR	0.00301	0.22916
COORDINATES FOR TANGENCY POINTS ON BLADE SURFACE 1		
MERIDIONAL	0.01354	9.07648
ANGULAR	0.00609	0.23235
COORDINATES FOR TANGENCY POINTS ON BLADE SURFACE 2		
MERIDIONAL	0.07393	9.05888
ANGULAR	-0.00068	0.22574

K	Z	R	THSP1	THSP2	TNPC	BETA	BETA1	BETA2
1	0.12564	10.80027	0.00481	-0.00520	0.08251	40.23	45.80	33.56
2	0.39540	10.85464	0.03035	0.01132	0.16099	38.80	44.28	32.32
3	0.66593	10.91191	0.05422	0.02689	0.23869	36.82	42.09	30.71
4	0.93607	10.97189	0.07635	0.04163	0.30974	35.60	40.49	30.03
5	1.20601	11.03465	0.09725	0.05600	0.37716	34.04	38.55	29.00
6	1.47591	11.10010	0.11607	0.06915	0.44794	30.69	34.96	26.01
7	1.74533	11.16827	0.13256	0.08062	0.51030	28.41	32.56	23.90
8	2.01436	11.23908	0.14818	0.09153	0.56356	27.74	31.62	23.57
9	2.28303	11.31249	0.16285	0.10220	0.61444	26.41	29.55	23.09
10	2.55120	11.38846	0.17605	0.11244	0.65859	24.60	27.01	22.09
11	2.81881	11.46653	0.18788	0.12203	0.69581	22.83	24.75	20.86
12	3.08578	11.54604	0.19852	0.13100	0.72638	21.29	22.74	19.81
13	3.35199	11.62632	0.20814	0.13944	0.75065	19.97	20.96	18.98
14	3.61736	11.70666	0.21684	0.14745	0.76918	18.77	19.26	18.27
15	3.88181	11.78639	0.22467	0.15504	0.78244	17.54	17.54	17.53
16	4.14529	11.86481	0.23164	0.16222	0.79042	16.33	15.89	16.78
17	4.40775	11.94128	0.23784	0.16899	0.79339	15.21	14.34	16.08
18	4.66919	12.01521	0.24332	0.17539	0.79160	14.12	12.79	15.42
19	4.92955	12.08609	0.24809	0.18143	0.78498	13.02	11.26	14.76
20	5.18890	12.15366	0.25219	0.18710	0.77400	11.91	9.74	14.04
21	5.44726	12.21795	0.25563	0.19241	0.75885	10.74	8.15	13.29
22	5.70471	12.27911	0.25841	0.19736	0.73921	9.54	6.52	12.52
23	5.96128	12.33722	0.26055	0.20195	0.71530	8.34	4.92	11.71
24	6.21702	12.39241	0.26206	0.20618	0.68728	7.09	3.24	10.88
25	6.47196	12.44475	0.26293	0.21004	0.65484	5.76	1.46	10.00
26	6.72618	12.49433	0.26313	0.21353	0.61793	4.37	-0.37	9.05
27	6.97971	12.54124	0.26266	0.21663	0.57659	2.94	-2.23	8.07
28	7.23257	12.58554	0.26153	0.21934	0.53079	1.45	-4.16	7.03
29	7.48483	12.62734	0.25969	0.22164	0.48051	-0.15	-6.20	5.89
30	7.73650	12.66667	0.25712	0.22351	0.42546	-1.86	-8.41	4.73
31	7.98764	12.70363	0.25376	0.22496	0.36514	-3.56	-10.56	3.56
32	8.23827	12.73826	0.24970	0.22598	0.30095	-5.23	-12.52	2.23
33	8.48842	12.77066	0.24484	0.22646	0.23257	-7.64	-15.45	0.47
34	8.73813	12.80087	0.23872	0.22629	0.15648	-10.41	-18.95	-1.39
35	8.98742	12.82913	0.23151	0.22559	0.07423	-12.24	-21.23	-2.59

TABLE I.—Continued.

SURFACE NUMBER 3 FROM THE HUB

LEADING EDGE AND TRAILING EDGE CIRCLE DATA

	LEADING EDGE	TRAILING EDGE
CIRCLE RADIUS	0.04439	0.04365
CIRCLE CENTER COORDINATES		
RADIAL	12.04077	13.83842
AXIAL	0.33876	8.84911
MERIDIONAL	0.04439	8.75311
ANGULAR	-0.00051	0.26877

COORDINATES FOR TANGENCY POINTS ON BLADE SURFACE 1

MERIDIONAL	0.01116	8.76006
ANGULAR	0.00194	0.27188

COORDINATES FOR TANGENCY POINTS ON BLADE SURFACE 2

MERIDIONAL	0.06904	8.75976
ANGULAR	-0.00357	0.26565

K	Z	R	THSP1	THSP2	TNPC	BETA	BETA1	BETA2
1	0.29502	12.03391	0.00089	-0.00741	0.07426	42.02	48.52	33.85
2	0.56195	12.08119	0.02568	0.00752	0.16623	40.72	46.82	33.25
3	0.82913	12.13123	0.04861	0.02203	0.25090	38.91	44.32	32.52
4	1.09539	12.18389	0.06948	0.03600	0.32582	36.98	41.86	31.39
5	1.36100	12.23917	0.08865	0.04916	0.39500	35.18	39.78	29.98
6	1.62605	12.29704	0.10650	0.06167	0.45793	33.83	38.10	29.10
7	1.89031	12.35745	0.12319	0.07371	0.51657	32.34	36.12	28.22
8	2.15377	12.42035	0.13847	0.08518	0.56990	30.57	33.78	27.12
9	2.41639	12.48572	0.15244	0.09607	0.61547	29.03	31.77	26.14
10	2.67815	12.55347	0.16535	0.10647	0.65448	27.69	29.94	25.34
11	2.93896	12.62319	0.17725	0.11648	0.68696	26.43	28.13	24.69
12	3.19875	12.69428	0.18822	0.12612	0.71299	25.26	26.44	24.06
13	3.45743	12.76609	0.19834	0.13540	0.73331	24.13	24.82	23.44
14	3.71492	12.83802	0.20765	0.14432	0.74817	23.04	23.24	22.84
15	3.97115	12.90941	0.21621	0.15291	0.75732	22.07	21.81	22.33
16	4.22611	12.97968	0.22411	0.16120	0.76144	21.17	20.48	21.86
17	4.47980	13.04820	0.23139	0.16920	0.76111	20.27	19.14	21.38
18	4.73222	13.11445	0.23806	0.17692	0.75629	19.39	17.84	20.91
19	4.98342	13.17792	0.24416	0.18436	0.74724	18.53	16.58	20.43
20	5.23348	13.23841	0.24973	0.19152	0.73430	17.67	15.33	19.95
21	5.48244	13.29594	0.25478	0.19842	0.71744	16.78	14.02	19.47
22	5.73041	13.35065	0.25930	0.20506	0.69655	15.87	12.70	18.94
23	5.97748	13.40262	0.26334	0.21143	0.67217	14.94	11.43	18.34
24	6.22369	13.45194	0.26689	0.21752	0.64436	13.99	10.06	17.79
25	6.46912	13.49873	0.26994	0.22338	0.61244	12.99	8.61	17.22
26	6.71383	13.54304	0.27249	0.22896	0.57673	11.94	7.17	16.55
27	6.95791	13.58497	0.27455	0.23426	0.53744	10.86	5.68	15.86
28	7.20138	13.62455	0.27610	0.23930	0.49423	9.73	4.12	15.17
29	7.44429	13.66188	0.27715	0.24405	0.44709	8.54	2.49	14.40
30	7.68672	13.69703	0.27766	0.24852	0.39594	7.27	0.77	13.59
31	7.92869	13.73005	0.27763	0.25269	0.34053	6.02	-0.92	12.79
32	8.17023	13.76099	0.27710	0.25658	0.28139	4.80	-2.52	11.96
33	8.41137	13.78993	0.27600	0.26014	0.21837	3.03	-4.84	10.80
34	8.65213	13.81693	0.27408	0.26328	0.14923	1.00	-7.55	9.50
35	8.89254	13.84220	0.27145	0.26606	0.07468	-0.35	-9.34	8.66

TABLE I.—Continued.

SURFACE NUMBER 4 FROM THE HUB

LEADING EDGE AND TRAILING EDGE CIRCLE DATA

	LEADING EDGE	TRAILING EDGE
CIRCLE RADIUS	0.04430	0.04098
CIRCLE CENTER COORDINATES		
RADIAL	13.26832	14.84445
AXIAL	0.54243	8.69667
MERIDIONAL	0.04430	8.35879
ANGULAR	-0.00303	0.30012

COORDINATES FOR TANGENCY POINTS ON BLADE SURFACE 1

MERIDIONAL	0.01028	8.35729
ANGULAR	-0.00089	0.30288

COORDINATES FOR TANGENCY POINTS ON BLADE SURFACE 2

MERIDIONAL	0.06948	8.37222
ANGULAR	-0.00578	0.29751

K	Z	R	THSP1	THSP2	TNPC	BETA	BETA1	BETA2
1	0.49865	13.26223	-0.00182	-0.00940	0.07301	43.42	50.21	34.69
2	0.75827	13.30321	0.02138	0.00423	0.16874	42.31	48.65	34.37
3	1.01760	13.34677	0.04294	0.01763	0.25592	40.76	46.37	34.01
4	1.27559	13.39281	0.06273	0.03076	0.33138	39.31	44.27	33.54
5	1.53254	13.44131	0.08113	0.04350	0.39903	37.91	42.39	32.82
6	1.78852	13.49221	0.09820	0.05583	0.46014	36.40	40.29	32.09
7	2.04330	13.54548	0.11395	0.06771	0.51325	34.97	38.39	31.24
8	2.29694	13.60105	0.12871	0.07912	0.56047	33.81	36.94	30.44
9	2.54940	13.65888	0.14263	0.09020	0.60143	32.89	35.46	30.15
10	2.80063	13.71888	0.15565	0.10112	0.63579	31.81	33.69	29.86
11	3.05057	13.78067	0.16769	0.11173	0.66429	30.52	31.80	29.21
12	3.29915	13.84365	0.17885	0.12198	0.68554	29.46	30.30	28.60
13	3.54635	13.90730	0.18934	0.13190	0.70123	28.61	29.07	28.14
14	3.79214	13.97099	0.19921	0.14158	0.71202	27.84	27.87	27.82
15	4.03649	14.03416	0.20852	0.15103	0.71806	27.12	26.73	27.51
16	4.27945	14.09626	0.21728	0.16026	0.71989	26.41	25.59	27.22
17	4.52108	14.15672	0.22551	0.16928	0.71716	25.73	24.46	26.97
18	4.76143	14.21508	0.23325	0.17809	0.71015	25.08	23.45	26.66
19	5.00059	14.27089	0.24056	0.18669	0.69993	24.44	22.48	26.34
20	5.23868	14.32393	0.24744	0.19508	0.68625	23.78	21.42	26.07
21	5.47581	14.37431	0.25388	0.20330	0.66879	23.12	20.36	25.76
22	5.71206	14.42209	0.25993	0.21131	0.64803	22.45	19.36	25.41
23	5.94752	14.46741	0.26560	0.21914	0.62415	21.78	18.32	25.07
24	6.18229	14.51036	0.27088	0.22678	0.59709	21.06	17.21	24.71
25	6.41644	14.55104	0.27577	0.23424	0.56668	20.30	16.07	24.31
26	6.65004	14.58951	0.28028	0.24151	0.53303	19.54	14.95	23.88
27	6.88319	14.62586	0.28441	0.24859	0.49619	18.74	13.74	23.45
28	7.11590	14.66012	0.28815	0.25548	0.45581	17.90	12.49	22.99
29	7.34826	14.69239	0.29152	0.26218	0.41207	17.04	11.27	22.48
30	7.58034	14.72273	0.29450	0.26868	0.36519	16.13	9.93	21.95
31	7.81217	14.75120	0.29708	0.27499	0.31447	15.20	8.56	21.44
32	8.04376	14.77785	0.29928	0.28110	0.26025	14.30	7.30	20.89
33	8.27518	14.80276	0.30107	0.28701	0.20275	13.08	5.52	20.21
34	8.50642	14.82596	0.30228	0.29267	0.13948	11.68	3.37	19.53
35	8.73748	14.84767	0.30298	0.29815	0.07043	10.74	1.89	19.10

TABLE I.—Continued.

SURFACE NUMBER 5 FROM THE HUB

LEADING EDGE AND TRAILING EDGE CIRCLE DATA

	LEADING EDGE	TRAILING EDGE
CIRCLE RADIUS	0.04139	0.03837
CIRCLE CENTER COORDINATES		
RADIAL	14.49509	15.83104
AXIAL	0.74862	8.44629
MERIDIONAL	0.04139	7.86299
ANGULAR	-0.00769	0.32026

COORDINATES FOR TANGENCY POINTS ON BLADE SURFACE 1

MERIDIONAL	0.00867	7.85543
ANGULAR	-0.00594	0.32264

COORDINATES FOR TANGENCY POINTS ON BLADE SURFACE 2

MERIDIONAL	0.06627	7.88079
ANGULAR	-0.00997	0.31811

K	Z	R	THSP1	THSP2	TNPC	BETA	BETA1	BETA2
1	0.70763	14.48984	-0.00671	-0.01341	0.06790	45.64	52.27	36.97
2	0.95455	14.52551	0.01500	-0.00049	0.16016	44.63	50.77	36.85
3	1.20097	14.56348	0.03522	0.01232	0.24293	43.25	48.62	36.72
4	1.44588	14.60361	0.05389	0.02497	0.31362	42.03	46.76	36.48
5	1.68954	14.64591	0.07138	0.03739	0.37614	40.93	45.14	36.10
6	1.93207	14.69027	0.08776	0.04957	0.43130	39.77	43.37	35.75
7	2.17324	14.73669	0.10310	0.06148	0.47857	38.70	41.86	35.24
8	2.41305	14.78510	0.11763	0.07307	0.52075	37.78	40.62	34.71
9	2.65149	14.83545	0.13141	0.08440	0.55763	36.92	39.26	34.43
10	2.88849	14.88764	0.14443	0.09553	0.58877	36.02	37.84	34.11
11	3.12401	14.94133	0.15671	0.10642	0.61449	35.13	36.51	33.71
12	3.35798	14.99600	0.16832	0.11706	0.63466	34.35	35.29	33.39
13	3.59039	15.05112	0.17934	0.12749	0.64950	33.67	34.18	33.16
14	3.82126	15.10620	0.18983	0.13774	0.65939	33.07	33.16	32.98
15	4.05057	15.16071	0.19982	0.14781	0.66526	32.47	32.18	32.75
16	4.27842	15.21415	0.20933	0.15768	0.66720	31.90	31.22	32.57
17	4.50490	15.26601	0.21841	0.16740	0.66468	31.40	30.32	32.47
18	4.73011	15.31585	0.22709	0.17696	0.65858	30.92	29.52	32.28
19	4.95420	15.36329	0.23541	0.18636	0.64977	30.43	28.70	32.10
20	5.17734	15.40813	0.24335	0.19562	0.63733	29.94	27.77	32.01
21	5.39969	15.45047	0.25093	0.20476	0.62143	29.42	26.92	31.80
22	5.62138	15.49041	0.25820	0.21374	0.60305	28.88	26.08	31.54
23	5.84249	15.52807	0.26513	0.22258	0.58147	28.34	25.12	31.37
24	6.06317	15.56356	0.27172	0.23131	0.55653	27.76	24.17	31.12
25	6.28351	15.59698	0.27800	0.23989	0.52881	27.16	23.25	30.82
26	6.50360	15.62840	0.28398	0.24835	0.49800	26.57	22.27	30.58
27	6.72351	15.65790	0.28964	0.25669	0.46399	25.93	21.22	30.30
28	6.94332	15.68554	0.29497	0.26489	0.42672	25.26	20.15	29.97
29	7.16313	15.71142	0.30001	0.27297	0.38624	24.60	19.13	29.63
30	7.38302	15.73560	0.30473	0.28092	0.34271	23.88	17.98	29.29
31	7.60299	15.75815	0.30913	0.28874	0.29548	23.14	16.80	28.94
32	7.82309	15.77913	0.31322	0.29643	0.24482	22.45	15.74	28.57
33	8.04339	15.79863	0.31699	0.30400	0.19093	21.56	14.27	28.19
34	8.26389	15.81669	0.32031	0.31145	0.13136	20.54	12.45	27.85
35	8.48456	15.83352	0.32322	0.31879	0.06591	19.82	11.17	27.62

TABLE 1.—Continued.

SURFACE NUMBER 6 FROM THE HUB

LEADING EDGE AND TRAILING EDGE CIRCLE DATA

	LEADING EDGE	TRAILING EDGE
CIRCLE RADIUS	0.03858	0.03696
CIRCLE CENTER COORDINATES		
RADIAL	15.72494	16.80092
AXIAL	0.93490	8.13866
MERIDIONAL	0.03858	7.33092
ANGULAR	-0.01482	0.33133

COORDINATES FOR TANGENCY POINTS ON BLADE SURFACE 1

MERIDIONAL	0.00731	7.31886
ANGULAR	-0.01338	0.33341

COORDINATES FOR TANGENCY POINTS ON BLADE SURFACE 2

MERIDIONAL	0.06422	7.35172
ANGULAR	-0.01665	0.32951

K	Z	R	THSP1	THSP2	TNPC	BETA	BETA1	BETA2
1	0.89664	15.72039	-0.01402	-0.02029	0.06502	48.69	54.16	41.70
2	1.12823	15.75080	0.00611	-0.00710	0.13980	47.80	52.88	41.50
3	1.35908	15.78316	0.02504	0.00592	0.20715	46.65	51.14	41.27
4	1.58806	15.81740	0.04272	0.01873	0.26541	45.63	49.62	40.99
5	1.81552	15.85348	0.05944	0.03128	0.31723	44.72	48.33	40.59
6	2.04155	15.89128	0.07531	0.04356	0.36389	43.85	47.10	40.20
7	2.26598	15.93078	0.09041	0.05559	0.40553	43.03	45.93	39.84
8	2.48884	15.97189	0.10480	0.06736	0.44268	42.25	44.81	39.45
9	2.71014	16.01453	0.11854	0.07887	0.47618	41.46	43.74	39.00
10	2.92991	16.05862	0.13169	0.09010	0.50600	40.75	42.77	38.59
11	3.14814	16.10381	0.14431	0.10109	0.53230	40.11	41.88	38.25
12	3.36488	16.14964	0.15644	0.11186	0.55540	39.51	40.98	37.96
13	3.58017	16.19563	0.16807	0.12245	0.57467	38.94	40.02	37.82
14	3.79410	16.24138	0.17919	0.13292	0.58887	38.41	39.00	37.81
15	4.00676	16.28641	0.18984	0.14328	0.59822	37.92	38.13	37.71
16	4.21829	16.33029	0.20009	0.15350	0.60397	37.47	37.33	37.61
17	4.42880	16.37260	0.20995	0.16361	0.60556	37.05	36.47	37.61
18	4.63844	16.41299	0.21943	0.17364	0.60336	36.61	35.67	37.53
19	4.84737	16.45111	0.22858	0.18354	0.59816	36.17	34.90	37.41
20	5.05573	16.48683	0.23740	0.19335	0.58948	35.75	34.08	37.35
21	5.26363	16.52023	0.24590	0.20307	0.57734	35.31	33.26	37.27
22	5.47121	16.55145	0.25410	0.21271	0.56219	34.84	32.42	37.13
23	5.67854	16.58061	0.26199	0.22225	0.54402	34.34	31.53	36.97
24	5.88574	16.60785	0.26958	0.23170	0.52259	33.83	30.64	36.79
25	6.09285	16.63324	0.27689	0.24106	0.49791	33.32	29.75	36.63
26	6.29997	16.65686	0.28391	0.25035	0.46992	32.80	28.80	36.47
27	6.50718	16.67880	0.29065	0.25955	0.43872	32.24	27.86	36.23
28	6.71457	16.69913	0.29712	0.26865	0.40464	31.66	26.91	35.96
29	6.92218	16.71791	0.30331	0.27767	0.36706	31.10	25.89	35.79
30	7.13011	16.73526	0.30923	0.28663	0.32585	30.48	24.81	35.55
31	7.33835	16.75119	0.31485	0.29549	0.28131	29.83	23.76	35.24
32	7.54697	16.76581	0.32021	0.30427	0.23321	29.24	22.74	35.02
33	7.75604	16.77919	0.32530	0.31299	0.18146	28.53	21.45	34.77
34	7.96559	16.79141	0.33002	0.32162	0.12492	27.68	19.95	34.46
35	8.17558	16.80261	0.33442	0.33017	0.06355	27.07	18.87	34.23

TABLE I.—Continued.

SURFACE NUMBER 7 FROM THE HUB

LEADING EDGE AND TRAILING EDGE CIRCLE DATA

	LEADING EDGE	TRAILING EDGE
CIRCLE RADIUS	0.03590	0.03445
CIRCLE CENTER COORDINATES		
RADIAL	16.95374	17.78734
AXIAL	1.13008	7.88870
MERIDIONAL	0.03590	6.85362
ANGULAR	-0.01871	0.33918

COORDINATES FOR TANGENCY POINTS ON BLADE SURFACE 1

MERIDIONAL	0.00625	6.83849
ANGULAR	-0.01751	0.34093

COORDINATES FOR TANGENCY POINTS ON BLADE SURFACE 2

MERIDIONAL	0.06176	6.87571
ANGULAR	-0.02018	0.33770

K	Z	R	THSP1	THSP2	TNPC	BETA	BETA1	BETA2
1	1.09442	16.94980	-0.01805	-0.02397	0.06251	51.41	55.68	46.16
2	1.30927	16.97540	0.00034	-0.01074	0.11912	50.71	54.72	45.88
3	1.52340	17.00253	0.01788	0.00228	0.17103	49.83	53.45	45.57
4	1.73591	17.03111	0.03454	0.01507	0.21718	49.07	52.39	45.25
5	1.94712	17.06108	0.05051	0.02761	0.25960	48.37	51.46	44.85
6	2.15715	17.09238	0.06587	0.03989	0.29900	47.66	50.53	44.45
7	2.36587	17.12495	0.08063	0.05192	0.33531	47.00	49.66	44.04
8	2.57333	17.15871	0.09486	0.06370	0.36892	46.38	48.86	43.66
9	2.77957	17.19360	0.10861	0.07525	0.39994	45.80	48.08	43.32
10	2.98460	17.22957	0.12190	0.08659	0.42850	45.24	47.33	42.99
11	3.18843	17.26630	0.13476	0.09771	0.45475	44.69	46.59	42.66
12	3.39108	17.30339	0.14720	0.10864	0.47861	44.16	45.84	42.39
13	3.59260	17.34047	0.15922	0.11941	0.49908	43.70	45.07	42.27
14	3.79304	17.37717	0.17083	0.13008	0.51517	43.32	44.32	42.30
15	3.99245	17.41312	0.18205	0.14067	0.52797	42.88	43.52	42.24
16	4.19095	17.44795	0.19288	0.15115	0.53727	42.43	42.69	42.17
17	4.38862	17.48131	0.20332	0.16156	0.54206	42.05	41.89	42.21
18	4.58558	17.51288	0.21341	0.17190	0.54292	41.67	41.12	42.22
19	4.78196	17.54240	0.22316	0.18218	0.54032	41.27	40.33	42.19
20	4.97787	17.56976	0.23259	0.19238	0.53421	40.86	39.52	42.15
21	5.17344	17.59505	0.24172	0.20252	0.52481	40.45	38.79	42.04
22	5.36878	17.61839	0.25058	0.21257	0.51262	40.05	38.04	41.94
23	5.56397	17.63992	0.25916	0.22258	0.49711	39.62	37.17	41.91
24	5.75911	17.65976	0.26746	0.23253	0.47833	39.16	36.35	41.75
25	5.95427	17.67802	0.27551	0.24240	0.45699	38.68	35.55	41.56
26	6.14955	17.69473	0.28330	0.25221	0.43222	38.23	34.66	41.49
27	6.34504	17.71001	0.29083	0.26198	0.40400	37.75	33.78	41.34
28	6.54078	17.72389	0.29813	0.27169	0.37308	37.24	32.93	41.11
29	6.73685	17.73647	0.30518	0.28133	0.33893	36.75	32.02	40.97
30	6.93331	17.74779	0.31199	0.29094	0.30128	36.23	31.03	40.82
31	7.13020	17.75795	0.31854	0.30050	0.26015	35.69	30.06	40.62
32	7.32759	17.76698	0.32486	0.31001	0.21563	35.18	29.16	40.43
33	7.52553	17.77499	0.33095	0.31947	0.16792	34.60	28.08	40.24
34	7.72406	17.78204	0.33675	0.32890	0.11590	33.93	26.80	40.04
35	7.92314	17.78827	0.34228	0.33828	0.05945	33.44	25.87	39.89

TABLE I.—Continued.

SURFACE NUMBER 8 FROM THE HUB

LEADING EDGE AND TRAILING EDGE CIRCLE DATA		
	LEADING EDGE	TRAILING EDGE
CIRCLE RADIUS	0.03239	0.03113
CIRCLE CENTER COORDINATES		
RADIAL	18.17931	18.77914
AXIAL	1.34211	7.66226
MERIDIONAL	0.03239	6.38807
ANGULAR	-0.01742	0.34319
COORDINATES FOR TANGENCY POINTS ON BLADE SURFACE 1		
MERIDIONAL	0.00513	6.37154
ANGULAR	-0.01645	0.34460
COORDINATES FOR TANGENCY POINTS ON BLADE SURFACE 2		
MERIDIONAL	0.05689	6.40994
ANGULAR	-0.01858	0.34201

K	Z	R	THSP1	THSP2	TNPC	BETA	BETA1	BETA2
1	1.30989	18.17612	-0.01689	-0.02221	0.05723	53.64	57.31	49.20
2	1.50799	18.19705	-0.00003	-0.00957	0.10422	53.10	56.59	48.93
3	1.70553	18.21909	0.01623	0.00289	0.14808	52.45	55.67	48.67
4	1.90164	18.24214	0.03185	0.01517	0.18770	51.91	54.88	48.49
5	2.09661	18.26619	0.04694	0.02729	0.22409	51.38	54.13	48.26
6	2.29064	18.29114	0.06155	0.03923	0.25770	50.87	53.41	48.00
7	2.48358	18.31697	0.07570	0.05099	0.28865	50.37	52.72	47.77
8	2.67548	18.34360	0.08941	0.06258	0.31711	49.88	52.03	47.51
9	2.86641	18.37100	0.10272	0.07400	0.34329	49.41	51.41	47.24
10	3.05636	18.39909	0.11567	0.08525	0.36736	48.99	50.82	47.01
11	3.24537	18.42761	0.12828	0.09635	0.38929	48.59	50.24	46.82
12	3.43347	18.45622	0.14056	0.10730	0.40921	48.19	49.67	46.61
13	3.62070	18.48460	0.15252	0.11811	0.42734	47.80	49.13	46.39
14	3.80712	18.51250	0.16418	0.12877	0.44365	47.42	48.58	46.20
15	3.99279	18.53960	0.17556	0.13930	0.45748	47.11	48.08	46.10
16	4.17783	18.56558	0.18666	0.14978	0.46878	46.80	47.44	46.15
17	4.36231	18.59019	0.19741	0.16023	0.47657	46.42	46.57	46.27
18	4.54633	18.61314	0.20779	0.17065	0.47990	46.03	45.78	46.28
19	4.73004	18.63426	0.21788	0.18102	0.48000	45.66	45.10	46.21
20	4.91351	18.65344	0.22768	0.19133	0.47715	45.27	44.35	46.16
21	5.09686	18.67081	0.23720	0.20160	0.47092	44.89	43.60	46.12
22	5.28019	18.68646	0.24646	0.21184	0.46133	44.52	42.88	46.07
23	5.46359	18.70058	0.25549	0.22204	0.44889	44.15	42.18	45.99
24	5.64712	18.71326	0.26428	0.23220	0.43373	43.73	41.36	45.92
25	5.83084	18.72461	0.27280	0.24235	0.41506	43.30	40.52	45.84
26	6.01484	18.73468	0.28111	0.25245	0.39324	42.90	39.83	45.70
27	6.19921	18.74358	0.28921	0.26252	0.36891	42.48	39.03	45.60
28	6.38399	18.75133	0.29708	0.27259	0.34111	42.04	38.13	45.52
29	6.56925	18.75801	0.30473	0.28263	0.30987	41.61	37.33	45.39
30	6.75502	18.76367	0.31217	0.29265	0.27584	41.16	36.50	45.23
31	6.94138	18.76842	0.31940	0.30264	0.23865	40.68	35.61	45.09
32	7.12836	18.77229	0.32643	0.31261	0.19794	40.25	34.75	44.98
33	7.31600	18.77534	0.33325	0.32258	0.15385	39.78	33.79	44.87
34	7.50436	18.77766	0.33982	0.33255	0.10582	39.24	32.73	44.73
35	7.69339	18.77939	0.34619	0.34250	0.05391	38.84	31.94	44.62

TABLE I.—Continued.

SURFACE NUMBER 9 FROM THE HUB

LEADING EDGE AND TRAILING EDGE CIRCLE DATA

	LEADING EDGE	TRAILING EDGE
CIRCLE RADIUS	0.02884	0.02806
CIRCLE CENTER COORDINATES		
RADIAL	19.40833	19.77011
AXIAL	1.53291	7.43266
MERIDIONAL	0.02884	5.94595
ANGULAR	-0.01457	0.34435

COORDINATES FOR TANGENCY POINTS ON BLADE SURFACE 1

MERIDIONAL	0.00414	5.92888
ANGULAR	-0.01380	0.34548

COORDINATES FOR TANGENCY POINTS ON BLADE SURFACE 2

MERIDIONAL	0.05156	5.96709
ANGULAR	-0.01548	0.34342

K	Z	R	THSP1	THSP2	TNPC	BETA	BETA1	BETA2
1	1.50418	19.40593	-0.01415	-0.01888	0.05163	55.79	58.93	52.05
2	1.68586	19.42188	0.00129	-0.00687	0.09006	55.38	58.37	51.86
3	1.86715	19.43849	0.01629	0.00501	0.12599	54.99	57.67	51.69
4	2.04737	19.45572	0.03082	0.01677	0.15877	54.48	57.04	51.55
5	2.22680	19.47353	0.04494	0.02840	0.18914	54.04	56.43	51.34
6	2.40555	19.49185	0.05868	0.03988	0.21726	53.63	55.85	51.14
7	2.58352	19.51067	0.07207	0.05124	0.24330	53.24	55.31	50.95
8	2.76076	19.52991	0.08514	0.06246	0.26740	52.88	54.80	50.77
9	2.93729	19.54953	0.09791	0.07356	0.28966	52.53	54.31	50.59
10	3.11312	19.56949	0.11039	0.08454	0.31020	52.19	53.81	50.44
11	3.28830	19.58957	0.12259	0.09541	0.32883	51.87	53.33	50.30
12	3.46285	19.60948	0.13454	0.10618	0.34579	51.56	52.91	50.13
13	3.63680	19.62900	0.14627	0.11682	0.36150	51.29	52.56	49.94
14	3.81022	19.64793	0.15780	0.12736	0.37605	51.04	52.22	49.80
15	3.98315	19.66602	0.16912	0.13781	0.38942	50.77	51.75	49.74
16	4.15568	19.68304	0.18019	0.14820	0.40089	50.44	51.21	49.65
17	4.32787	19.69881	0.19102	0.15852	0.41042	50.13	50.73	49.52
18	4.49981	19.71307	0.20162	0.16877	0.41754	49.86	50.16	49.55
19	4.67160	19.72572	0.21196	0.17904	0.42118	49.57	49.45	49.68
20	4.84334	19.73669	0.22203	0.18933	0.42137	49.23	48.72	49.74
21	5.01509	19.74609	0.23183	0.19962	0.41815	48.89	48.02	49.73
22	5.18695	19.75406	0.24140	0.20989	0.41201	48.55	47.37	49.68
23	5.35899	19.76073	0.25076	0.22015	0.40313	48.20	46.69	49.62
24	5.53127	19.76622	0.25989	0.23040	0.39121	47.85	45.96	49.61
25	5.70388	19.77069	0.26881	0.24067	0.37586	47.50	45.22	49.60
26	5.87685	19.77411	0.27752	0.25094	0.35748	47.14	44.52	49.53
27	6.05027	19.77660	0.28603	0.26120	0.33643	46.77	43.79	49.45
28	6.22422	19.77818	0.29435	0.27147	0.31218	46.39	43.00	49.40
29	6.39873	19.77895	0.30247	0.28176	0.28442	46.03	42.24	49.37
30	6.57387	19.77893	0.31040	0.29207	0.25346	45.67	41.49	49.30
31	6.74968	19.77821	0.31816	0.30238	0.21957	45.27	40.69	49.20
32	6.92625	19.77689	0.32572	0.31271	0.18234	44.86	39.84	49.13
33	7.10356	19.77493	0.33308	0.32307	0.14144	44.43	38.93	49.07
34	7.28174	19.77251	0.34024	0.33344	0.09679	43.98	38.01	48.96
35	7.46073	19.76970	0.34723	0.34382	0.04874	43.65	37.34	48.86

TABLE I.—Continued.

SURFACE NUMBER 10 FROM THE HUB

LEADING EDGE AND TRAILING EDGE CIRCLE DATA

	LEADING EDGE	TRAILING EDGE
CIRCLE RADIUS	0.02551	0.02504
CIRCLE CENTER COORDINATES		
RADIAL	20.63824	20.76767
AXIAL	1.71889	7.23209
MERIDIONAL	0.02551	5.54547
ANGULAR	-0.01099	0.34448

COORDINATES FOR TANGENCY POINTS ON BLADE SURFACE 1

MERIDIONAL	0.00332	5.52864
ANGULAR	-0.01038	0.34537

COORDINATES FOR TANGENCY POINTS ON BLADE SURFACE 2

MERIDIONAL	0.04627	5.56533
ANGULAR	-0.01171	0.34374

K	Z	R	THSP1	THSP2	TNPC	BETA	BETA1	BETA2
1	1.69343	20.63673	-0.01066	-0.01485	0.04614	57.72	60.45	54.49
2	1.86159	20.64726	0.00363	-0.00343	0.07852	57.40	60.01	54.35
3	2.02959	20.65810	0.01760	0.00791	0.10882	57.06	59.49	54.27
4	2.19675	20.66920	0.03123	0.01918	0.13650	56.79	59.05	54.22
5	2.36335	20.68054	0.04458	0.03036	0.16244	56.49	58.62	54.10
6	2.52945	20.69208	0.05767	0.04146	0.18658	56.21	58.18	54.01
7	2.69496	20.70375	0.07048	0.05248	0.20880	55.93	57.76	53.91
8	2.85994	20.71555	0.08305	0.06340	0.22952	55.66	57.38	53.78
9	3.02438	20.72740	0.09538	0.07425	0.24861	55.42	56.99	53.72
10	3.18829	20.73929	0.10749	0.08504	0.26592	55.18	56.62	53.64
11	3.35172	20.75104	0.11940	0.09574	0.28215	54.94	56.29	53.49
12	3.51466	20.76241	0.13112	0.10635	0.29727	54.69	55.91	53.40
13	3.67715	20.77324	0.14263	0.11689	0.31045	54.50	55.60	53.34
14	3.83922	20.78342	0.15400	0.12738	0.32244	54.35	55.38	53.27
15	4.00093	20.79277	0.16521	0.13781	0.33389	54.12	54.97	53.23
16	4.16234	20.80113	0.17620	0.14820	0.34388	53.81	54.51	53.09
17	4.32349	20.80835	0.18701	0.15847	0.35310	53.52	54.21	52.81
18	4.48445	20.81427	0.19769	0.16864	0.36099	53.33	53.89	52.76
19	4.64530	20.81882	0.20819	0.17884	0.36638	53.16	53.39	52.92
20	4.80613	20.82195	0.21847	0.18909	0.36910	52.88	52.71	53.06
21	4.96699	20.82378	0.22848	0.19937	0.36896	52.50	51.95	53.04
22	5.12794	20.82443	0.23822	0.20962	0.36585	52.10	51.22	52.95
23	5.28908	20.82408	0.24774	0.21987	0.35907	51.77	50.54	52.94
24	5.45046	20.82281	0.25704	0.23013	0.34922	51.45	49.88	52.91
25	5.61212	20.82077	0.26615	0.24039	0.33683	51.10	49.21	52.84
26	5.77414	20.81795	0.27506	0.25065	0.32152	50.74	48.50	52.79
27	5.93657	20.81442	0.28377	0.26092	0.30308	50.40	47.79	52.76
28	6.09945	20.81021	0.29230	0.27121	0.28158	50.07	47.09	52.72
29	6.26286	20.80539	0.30064	0.28153	0.25707	49.73	46.37	52.68
30	6.42685	20.80002	0.30881	0.29186	0.22948	49.38	45.65	52.62
31	6.59145	20.79413	0.31681	0.30222	0.19888	49.05	44.94	52.57
32	6.75672	20.78780	0.32465	0.31261	0.16512	48.73	44.21	52.56
33	6.92273	20.78104	0.33232	0.32305	0.12797	48.40	43.44	52.56
34	7.08952	20.77396	0.33983	0.33354	0.08736	48.07	42.67	52.53
35	7.25711	20.76666	0.34719	0.34407	0.04362	47.82	42.11	52.49

TABLE I.—Continued.

SURFACE NUMBER 11 FROM THE HUB

LEADING EDGE AND TRAILING EDGE CIRCLE DATA

	LEADING EDGE	TRAILING EDGE
CIRCLE RADIUS	0.02261	0.02213
CIRCLE CENTER COORDINATES		
RADIAL	21.86462	21.77237
AXIAL	1.92608	7.07234
MERIDIONAL	0.02261	5.17386
ANGULAR	-0.00572	0.34408

COORDINATES FOR TANGENCY POINTS ON BLADE SURFACE 1

MERIDIONAL	0.00259	5.15805
ANGULAR	-0.00524	0.34479

COORDINATES FOR TANGENCY POINTS ON BLADE SURFACE 2

MERIDIONAL	0.04153	5.19196
ANGULAR	-0.00629	0.34350

K	Z	R	THSP1	THSP2	TNPC	BETA	BETA1	BETA2
1	1.90349	21.86391	-0.00546	-0.00919	0.04099	59.79	62.31	56.83
2	2.05877	21.86906	0.00798	0.00166	0.07006	59.54	61.94	56.74
3	2.21409	21.87419	0.02119	0.01249	0.09716	59.31	61.54	56.75
4	2.36862	21.87927	0.03415	0.02328	0.12187	59.16	61.24	56.79
5	2.52262	21.88432	0.04689	0.03403	0.14520	58.95	60.90	56.74
6	2.67632	21.88921	0.05942	0.04474	0.16676	58.75	60.54	56.74
7	2.82955	21.89395	0.07174	0.05542	0.18644	58.55	60.22	56.71
8	2.98230	21.89850	0.08386	0.06602	0.20502	58.34	59.91	56.61
9	3.13472	21.90282	0.09579	0.07658	0.22193	58.16	59.58	56.63
10	3.28676	21.90686	0.10754	0.08713	0.23697	58.00	59.28	56.62
11	3.43843	21.91051	0.11914	0.09762	0.25122	57.80	59.00	56.51
12	3.58981	21.91357	0.13056	0.10805	0.26436	57.59	58.66	56.46
13	3.74090	21.91595	0.14181	0.11845	0.27564	57.42	58.36	56.44
14	3.89172	21.91762	0.15293	0.12881	0.28581	57.27	58.12	56.37
15	4.04237	21.91847	0.16392	0.13913	0.29518	57.08	57.81	56.33
16	4.19286	21.91841	0.17475	0.14943	0.30332	56.87	57.49	56.24
17	4.34325	21.91736	0.18546	0.15966	0.31067	56.67	57.23	56.09
18	4.49360	21.91519	0.19607	0.16986	0.31673	56.53	56.96	56.09
19	4.64396	21.91190	0.20654	0.18008	0.32146	56.33	56.54	56.11
20	4.79441	21.90747	0.21683	0.19029	0.32518	55.98	55.95	56.02
21	4.94500	21.90202	0.22688	0.20048	0.32656	55.62	55.32	55.92
22	5.09576	21.89568	0.23673	0.21065	0.32506	55.29	54.67	55.89
23	5.24679	21.88861	0.24634	0.22086	0.32005	54.98	53.96	55.95
24	5.39811	21.88092	0.25573	0.23111	0.31184	54.64	53.26	55.92
25	5.54977	21.87274	0.26492	0.24135	0.30130	54.25	52.58	55.79
26	5.70181	21.86406	0.27391	0.25157	0.28813	53.86	51.88	55.67
27	5.85430	21.85495	0.28270	0.26178	0.27198	53.50	51.16	55.61
28	6.00723	21.84540	0.29130	0.27202	0.25267	53.14	50.42	55.55
29	6.16069	21.83549	0.29971	0.28226	0.23063	52.74	49.69	55.42
30	6.31471	21.82526	0.30793	0.29249	0.20610	52.31	48.92	55.25
31	6.46934	21.81477	0.31597	0.30270	0.17859	51.90	48.15	55.12
32	6.62456	21.80402	0.32384	0.31292	0.14792	51.58	47.48	55.06
33	6.78049	21.79309	0.33156	0.32317	0.11446	51.26	46.78	55.00
34	6.93709	21.78201	0.33913	0.33345	0.07804	50.91	46.05	54.94
35	7.09442	21.77090	0.34657	0.34376	0.03878	50.66	45.52	54.89

TABLE I.—Continued.

SURFACE NUMBER 12 FROM THE HUB

LEADING EDGE AND TRAILING EDGE CIRCLE DATA

	LEADING EDGE	TRAILING EDGE
CIRCLE RADIUS	0.02044	0.01989
CIRCLE CENTER COORDINATES		
RADIAL	23.09180	22.77913
AXIAL	2.13039	6.92447
MERIDIONAL	0.02044	4.82790
ANGULAR	0.00031	0.34246

COORDINATES FOR TANGENCY POINTS ON BLADE SURFACE 1

MERIDIONAL	0.00205	4.81321
ANGULAR	0.00070	0.34305

COORDINATES FOR TANGENCY POINTS ON BLADE SURFACE 2

MERIDIONAL	0.03795	4.84444
ANGULAR	-0.00015	0.34197

K	Z	R	THSP1	THSP2	TNPC	BETA	BETA1	BETA2
1	2.10996	23.09181	0.00051	-0.00288	0.03704	61.78	64.15	58.97
2	2.25221	23.09166	0.01316	0.00736	0.06377	61.60	63.88	58.93
3	2.39458	23.09111	0.02565	0.01759	0.08885	61.47	63.59	59.00
4	2.53637	23.09021	0.03796	0.02784	0.11183	61.39	63.37	59.13
5	2.67780	23.08891	0.05010	0.03810	0.13341	61.24	63.09	59.14
6	2.81908	23.08714	0.06208	0.04834	0.15353	61.07	62.79	59.14
7	2.96006	23.08490	0.07389	0.05856	0.17191	60.93	62.51	59.18
8	3.10076	23.08214	0.08554	0.06879	0.18854	60.81	62.24	59.23
9	3.24129	23.07883	0.09705	0.07902	0.20372	60.68	62.00	59.24
10	3.38162	23.07494	0.10843	0.08924	0.21781	60.54	61.74	59.23
11	3.52183	23.07039	0.11968	0.09946	0.23052	60.39	61.46	59.24
12	3.66190	23.06505	0.13079	0.10966	0.24189	60.24	61.20	59.21
13	3.80190	23.05891	0.14178	0.11985	0.25208	60.10	60.96	59.19
14	3.94185	23.05199	0.15268	0.13005	0.26100	59.98	60.72	59.20
15	4.08181	23.04428	0.16346	0.14025	0.26908	59.80	60.41	59.17
16	4.22181	23.03574	0.17412	0.15043	0.27584	59.64	60.17	59.09
17	4.36190	23.02632	0.18472	0.16060	0.28152	59.54	60.03	59.04
18	4.50212	23.01605	0.19525	0.17079	0.28645	59.42	59.71	59.12
19	4.64252	23.00488	0.20564	0.18104	0.28991	59.18	59.27	59.10
20	4.78316	22.99290	0.21589	0.19124	0.29292	58.88	58.90	58.85
21	4.92404	22.98018	0.22601	0.20139	0.29448	58.63	58.48	58.78
22	5.06525	22.96689	0.23597	0.21160	0.29353	58.37	57.89	58.84
23	5.20680	22.95317	0.24569	0.22184	0.29040	57.97	57.10	58.80
24	5.34871	22.93912	0.25514	0.23208	0.28436	57.49	56.21	58.68
25	5.49105	22.92491	0.26431	0.24229	0.27507	56.98	55.37	58.47
26	5.63381	22.91046	0.27325	0.25244	0.26304	56.51	54.62	58.22
27	5.77708	22.89587	0.28198	0.26255	0.24856	56.05	53.87	58.00
28	5.92083	22.88112	0.29051	0.27262	0.23121	55.60	53.08	57.84
29	6.06517	22.86630	0.29883	0.28267	0.21104	55.17	52.31	57.67
30	6.21006	22.85141	0.30696	0.29270	0.18838	54.68	51.47	57.45
31	6.35557	22.83649	0.31487	0.30268	0.16300	54.15	50.58	57.20
32	6.50172	22.82159	0.32259	0.31263	0.13465	53.70	49.80	56.98
33	6.64854	22.80670	0.33014	0.32253	0.10394	53.20	48.98	56.72
34	6.79606	22.79193	0.33750	0.33238	0.07075	52.66	48.12	56.43
35	6.94427	22.77728	0.34471	0.34219	0.03503	52.29	47.51	56.23

TABLE I.—Continued.

SURFACE NUMBER 13 FROM THE HUB

LEADING EDGE AND TRAILING EDGE CIRCLE DATA

	LEADING EDGE	TRAILING EDGE
CIRCLE RADIUS	0.01909	0.01826
CIRCLE CENTER COORDINATES		
RADIAL	24.32150	23.78459
AXIAL	2.31965	6.77260
MERIDIONAL	0.01909	4.50683
ANGULAR	0.00482	0.33888

COORDINATES FOR TANGENCY POINTS ON BLADE SURFACE 1

MERIDIONAL	0.00166	4.49319
ANGULAR	0.00514	0.33939

COORDINATES FOR TANGENCY POINTS ON BLADE SURFACE 2

MERIDIONAL	0.03578	4.52212
ANGULAR	0.00443	0.33846

K	Z	R	THSP1	THSP2	TNPC	BETA	BETA1	BETA2
1	2.30058	24.32231	0.00498	0.00178	0.03451	63.69	65.95	60.99
2	2.42980	24.31662	0.01685	0.01137	0.05926	63.56	65.74	61.00
3	2.55904	24.31026	0.02859	0.02100	0.08239	63.50	65.53	61.14
4	2.68777	24.30322	0.04020	0.03065	0.10369	63.47	65.37	61.27
5	2.81622	24.29546	0.05170	0.04032	0.12395	63.37	65.17	61.31
6	2.94454	24.28690	0.06309	0.05002	0.14269	63.30	64.96	61.43
7	3.07271	24.27759	0.07437	0.05976	0.15962	63.25	64.77	61.55
8	3.20079	24.26741	0.08555	0.06954	0.17534	63.18	64.59	61.61
9	3.32881	24.25641	0.09665	0.07936	0.18985	63.09	64.36	61.69
10	3.45682	24.24451	0.10763	0.08921	0.20296	62.98	64.13	61.72
11	3.58495	24.23166	0.11855	0.09908	0.21499	62.88	63.96	61.72
12	3.71319	24.21780	0.12941	0.10899	0.22590	62.81	63.78	61.78
13	3.84160	24.20300	0.14019	0.11895	0.23569	62.71	63.55	61.82
14	3.97031	24.18735	0.15091	0.12896	0.24437	62.60	63.32	61.84
15	4.09933	24.17091	0.16156	0.13901	0.25172	62.50	63.09	61.88
16	4.22868	24.15369	0.17215	0.14912	0.25796	62.37	62.85	61.88
17	4.35848	24.13576	0.18268	0.15926	0.26350	62.21	62.61	61.80
18	4.48873	24.11713	0.19314	0.16941	0.26840	62.03	62.34	61.72
19	4.61948	24.09789	0.20357	0.17959	0.27151	61.97	62.24	61.69
20	4.75076	24.07809	0.21405	0.18984	0.27351	62.01	62.26	61.77
21	4.88261	24.05789	0.22451	0.20020	0.27555	61.88	61.75	62.01
22	5.01502	24.03741	0.23469	0.21072	0.27476	61.52	60.95	62.06
23	5.14801	24.01683	0.24465	0.22121	0.27267	61.02	60.31	61.70
24	5.28159	23.99625	0.25433	0.23160	0.26964	60.37	59.20	61.47
25	5.41575	23.97581	0.26356	0.24198	0.26167	59.63	57.86	61.23
26	5.55048	23.95546	0.27244	0.25221	0.25043	58.88	56.91	60.64
27	5.68580	23.93527	0.28105	0.26225	0.23745	58.15	55.92	60.13
28	5.82174	23.91525	0.28937	0.27219	0.22095	57.47	54.82	59.78
29	5.95829	23.89545	0.29741	0.28202	0.20125	56.83	53.88	59.38
30	6.09545	23.87585	0.30523	0.29174	0.17934	56.16	52.91	58.95
31	6.23324	23.85655	0.31279	0.30134	0.15490	55.47	51.87	58.52
32	6.37166	23.83752	0.32013	0.31083	0.12762	54.85	50.93	58.13
33	6.51070	23.81879	0.32726	0.32022	0.09813	54.17	49.94	57.68
34	6.65039	23.80042	0.33417	0.32949	0.06630	53.47	48.92	57.21
35	6.79072	23.78241	0.34090	0.33866	0.03212	52.98	48.22	56.88

TABLE I.—Concluded.

SURFACE NUMBER 14 FROM THE HUB

LEADING EDGE AND TRAILING EDGE CIRCLE DATA

	LEADING EDGE	TRAILING EDGE
CIRCLE RADIUS	0.01891	0.01874
CIRCLE CENTER COORDINATES		
RADIAL	25.55194	24.78156
AXIAL	2.50380	6.56211
MERIDIONAL	0.01891	4.15251
ANGULAR	0.00683	0.33427

COORDINATES FOR TANGENCY POINTS ON BLADE SURFACE 1

MERIDIONAL	0.00137	4.13841
ANGULAR	0.00711	0.33476

COORDINATES FOR TANGENCY POINTS ON BLADE SURFACE 2

MERIDIONAL	0.03579	4.16856
ANGULAR	0.00650	0.33388

K	Z	R	THSP1	THSP2	TNPC	BETA	BETA1	BETA2
1	2.48498	25.55368	0.00698	0.00373	0.03399	65.83	68.02	63.19
2	2.59766	25.54294	0.01790	0.01250	0.05680	65.72	67.83	63.21
3	2.71030	25.53110	0.02873	0.02130	0.07810	65.70	67.67	63.37
4	2.82239	25.51820	0.03947	0.03016	0.09773	65.72	67.58	63.55
5	2.93420	25.50421	0.05014	0.03905	0.11658	65.66	67.43	63.61
6	3.04601	25.48901	0.06074	0.04800	0.13408	65.63	67.26	63.76
7	3.15778	25.47263	0.07128	0.05702	0.14999	65.60	67.11	63.90
8	3.26951	25.45497	0.08176	0.06610	0.16516	65.54	66.96	63.93
9	3.38148	25.43610	0.09221	0.07523	0.17935	65.47	66.79	64.00
10	3.49375	25.41592	0.10263	0.08445	0.19223	65.42	66.62	64.09
11	3.60635	25.39445	0.11303	0.09375	0.20441	65.33	66.44	64.11
12	3.71944	25.37167	0.12339	0.10311	0.21575	65.21	66.20	64.14
13	3.83314	25.34776	0.13373	0.11257	0.22567	65.11	66.00	64.16
14	3.94753	25.32285	0.14407	0.12211	0.23482	65.02	65.86	64.14
15	4.06271	25.29713	0.15443	0.13173	0.24354	64.91	65.64	64.14
16	4.17870	25.27066	0.16475	0.14144	0.25090	64.79	65.38	64.18
17	4.29564	25.24361	0.17507	0.15127	0.25671	64.71	65.19	64.21
18	4.41358	25.21605	0.18541	0.16120	0.26189	64.59	64.98	64.19
19	4.53252	25.18811	0.19575	0.17122	0.26612	64.49	64.80	64.17
20	4.65254	25.15993	0.20613	0.18135	0.26882	64.46	64.69	64.23
21	4.77368	25.13164	0.21653	0.19160	0.27160	64.31	64.37	64.25
22	4.89591	25.10341	0.22686	0.20193	0.27331	64.11	64.14	64.07
23	5.01924	25.07538	0.23729	0.21224	0.27511	64.03	64.23	63.82
24	5.14374	25.04776	0.24774	0.22267	0.27512	64.01	63.59	64.43
25	5.26933	25.02060	0.25778	0.23358	0.26843	63.68	62.31	64.93
26	5.39601	24.99390	0.26741	0.24452	0.26154	62.81	61.20	64.25
27	5.52374	24.96770	0.27666	0.25514	0.25402	61.79	59.80	63.55
28	5.65253	24.94203	0.28540	0.26564	0.24031	60.82	58.08	63.15
29	5.78232	24.91689	0.29366	0.27598	0.22140	59.82	56.57	62.54
30	5.91310	24.89233	0.30154	0.28612	0.19872	58.84	55.18	61.86
31	6.04486	24.86839	0.30909	0.29604	0.17237	57.90	53.82	61.23
32	6.17751	24.84505	0.31632	0.30579	0.14239	57.02	52.52	60.65
33	6.31105	24.82231	0.32327	0.31538	0.10910	56.11	51.12	60.08
34	6.44543	24.80022	0.32990	0.32480	0.07220	55.15	49.68	59.45
35	6.58063	24.77884	0.33627	0.33406	0.03197	54.42	48.63	58.94

TABLE II.—INNER AND OUTER FLOWPATH COORDINATES

K	Z	R HUB	R SHROUD	K	Z	R HUB	R SHROUD
1	-18.05981	9.16263	25.69380	41	9.02989	11.81286	24.51726
2	-17.38257	9.13694	25.69502	42	9.70713	11.88601	24.47249
3	-16.70532	9.11110	25.69606	43	10.38437	11.95076	24.43715
4	-16.02809	9.08530	25.69690	44	11.06161	12.01159	24.41084
5	-15.35085	9.05977	25.69756	45	11.73885	12.07301	24.39322
6	-14.67361	9.03473	25.69798	46	12.41610	12.13859	24.38387
7	-13.99637	9.01039	25.69821	47	13.09333	12.20953	24.38176
8	-13.31913	8.98698	25.69824	48	13.77056	12.28665	24.38327
9	-12.64188	8.96473	25.69804	49	14.44781	12.37076	24.38435
10	-11.96464	8.94385	25.69763	50	15.12507	12.46268	24.38408
11	-11.28739	8.92453	25.69701	51	15.80229	12.56321	24.38383
12	-10.61015	8.90693	25.69615	52	16.47954	12.67077	24.38394
13	-9.93291	8.89121	25.69508	53	17.15677	12.77743	24.38408
14	-9.25567	8.87769	25.69377	54	17.83401	12.87424	24.38414
15	-8.57843	8.86747	25.69223	55	18.51125	12.95222	24.38414
16	-7.90118	8.86182	25.69044	56	19.18851	13.00243	24.38409
17	-7.22394	8.86201	25.68843	57	19.86575	13.02487	24.38399
18	-6.54670	8.86932	25.68617	58	20.54298	13.03990	24.38382
19	-5.86946	8.88502	25.68367	59	21.22025	13.05056	24.38364
20	-5.19221	8.91040	25.68091	60	21.89746	13.05828	24.38345
21	-4.51497	8.94672	25.67789	61	22.57472	13.06386	24.38329
22	-3.83773	8.99527	25.67462	62	23.25197	13.06740	24.38315
23	-3.16048	9.05731	25.67108	63	23.92920	13.06903	24.38306
24	-2.48324	9.13414	25.66730	64	24.60646	13.06884	24.38303
25	-1.80600	9.22699	25.66324	65	25.28368	13.06695	24.38301
26	-1.12875	9.33708	25.65891	66	25.96094	13.06346	24.38303
27	-0.45151	9.46554	25.65430	67	26.63817	13.05847	24.38307
28	0.22573	9.61263	25.64807	68	27.31541	13.05209	24.38310
29	0.90297	9.77807	25.63542	69	27.99268	13.04443	24.38315
30	1.58021	9.96160	25.61099	70	28.66989	13.03558	24.38319
31	2.25746	10.16295	25.56900	71	29.34715	13.02566	24.38321
32	2.93470	10.37995	25.50014	72	30.02438	13.01477	24.38321
33	3.61194	10.60335	25.39339	73	30.70163	13.00301	24.38321
34	4.28918	10.82219	25.24631	74	31.37886	12.99049	24.38321
35	4.96643	11.02556	25.08638	75	32.05611	12.97732	24.38321
36	5.64367	11.20660	24.94333	76	32.73337	12.96361	24.38319
37	6.32091	11.36588	24.82292	77	33.41060	12.94945	24.38319
38	6.99816	11.50476	24.72263	78	34.08784	12.93495	24.38319
39	7.67540	11.62462	24.63994	79	34.76508	12.92022	24.38319
40	8.35264	11.72681	24.57231	80	35.44234	12.90536	24.38319

TABLE III.—AERODYNAMIC SURVEY DATA

(a) Near stall operating point

STATION 1 (UPSTREAM OF ROTOR)

P REF. = 101325 NT/METER SQUARED; T REF. = 288.15 K
 FLOW ANGLE IS FROM THE MERIDIONAL DIRECTION

RADIUS OF SHROUD	25.654 CENTIMETERS
RADIUS OF HUB	9.1465 CENTIMETERS
AXIAL DISTANCE FROM ROTOR HUB LEADING EDGE	-2.473 CENTIMETERS
MASS FLOW RATE MEASURED WITH ORIFICE	32.305 KG/SECOND
STATIC PRESSURE ON THE SHROUD	0.8390 * P REF.
STATIC PRESSURE ON THE HUB	0.8764 * P REF.

RADIUS (CENTIMETERS)	P TOTAL/ P REF.	T TOTAL/ T REF.	P STATIC/ P REF.	FLOW ANGLE (DEGREES)
25.5194	0.9223	1.0089	0.8543	1.7
25.3848	0.9454	0.9956	0.8563	1.5
25.2501	0.9610	1.0015	0.8543	0.0
25.1130	0.9745	1.0035	0.8543	1.1
24.9758	0.9813	1.0041	0.8543	0.6
24.2570	0.9908	1.0050	0.8509	-0.1
23.4798	0.9942	1.0054	0.8462	0.0
22.6873	0.9955	1.0042	0.8401	0.0
21.1988	1.0016	0.9994	0.8247	0.0
19.6469	1.0016	0.9992	0.8213	0.0
18.0645	1.0016	0.9987	0.8206	0.0
16.4414	1.0010	0.9990	0.8234	0.0
14.7396	1.0023	0.9987	0.8315	0.1
12.9591	1.0023	0.9992	0.8417	0.0
11.0084	1.0016	0.9985	0.8581	0.0
10.0736	0.9969	0.9998	0.8750	1.3
9.8882	0.9908	1.0008	0.8777	0.8
9.7028	0.9779	1.0013	0.8790	0.7
9.5174	0.9582	1.0006	0.8784	0.9

STATION 2 (DOWNSTREAM OF ROTOR)

RADIUS OF SHROUD	24.4043 CENTIMETERS
RADIUS OF HUB	12.0167 CENTIMETERS
AXIAL DISTANCE FROM ROTOR HUB LEADING EDGE	11.011 CENTIMETERS
ENERGY AVERAGED TOTAL PRESSURE RATIO ACROSS ROTOR	1.728
MASS AVERAGED TOTAL TEMPERATURE RATIO ACROSS ROTOR	1.188
ROTOR ADIABATIC EFFICIENCY	0.901
STATIC PRESSURE ON THE SHROUD	1.3630 * P REF.
STATIC PRESSURE ON THE HUB	1.0336 * P REF.

RADIUS (CENTIMETERS)	P TOTAL/ P REF.	T TOTAL/ T REF.	P STATIC/ P REF.	FLOW ANGLE (DEGREES)
23.2258	1.7937	1.2269	1.3691	45.2
22.0320	1.7665	1.2059	1.3242	43.6
20.8280	1.7433	1.1936	1.2997	43.3
19.6164	1.7243	1.1754	1.2752	41.8
18.3947	1.7011	1.1737	1.2493	43.8
17.1526	1.6821	1.1689	1.2235	45.1
15.8902	1.6991	1.1716	1.1922	47.6
14.6126	1.6889	1.1708	1.1500	50.2
13.3299	1.6773	1.1641	1.1017	51.5

TABLE III.—Concluded.

(b) Near peak efficiency operating point

STATION 1 (UPSTREAM OF THE ROTOR)

P REF. = 101325 NT/METER SQUARED; T REF. = 288.15 K
 FLOW ANGLE IS FROM THE MERIDIONAL DIRECTION

RADIUS OF SHROUD	25.654 CENTIMETERS
RADIUS OF HUB	9.1465 CENTIMETERS
AXIAL DISTANCE FROM ROTOR HUB LEADING EDGE	-2.473 CENTIMETERS
MASS FLOW RATE MEASURED WITH ORIFICE	34.573 KG/SECOND
STATIC PRESSURE ON THE SHROUD	0.8077 * P REF.
STATIC PRESSURE ON THE HUB	0.8513 * P REF.

RADIUS (CENTIMETERS)	P TOTAL/ P REF.	T TOTAL/ T REF.	P STATIC/ P REF.	FLOW ANGLE (DEGREES)
25.5194	0.9094	1.0012	0.8226	1.3
25.3848	0.9338	0.9990	0.8219	0.5
25.2501	0.9569	1.0013	0.8205	0.3
25.1130	0.9704	1.0010	0.8205	0.4
24.9758	0.9806	1.0012	0.8185	0.7
24.2570	0.9982	1.0010	0.8158	0.9
23.4798	0.9996	1.0008	0.8083	0.3
22.6873	1.0003	1.0010	0.7995	0.0
21.1988	1.0003	1.0000	0.7941	0.0
19.6469	1.0003	0.9994	0.7921	0.0
18.0645	1.0010	0.9994	0.7914	0.0
16.4414	1.0003	0.9994	0.7921	0.0
14.7396	1.0010	1.0004	0.7982	0.0
12.9591	1.0010	0.9996	0.8084	0.0
11.0084	1.0003	0.9994	0.8274	0.0
10.0736	0.9948	1.0013	0.8383	1.0
9.8882	0.9853	1.0019	0.8410	0.6
9.7028	0.9690	1.0013	0.8430	0.6
9.5174	0.9459	1.0013	0.8444	1.1

STATION 2 (DOWNSTREAM OF ROTOR)

RADIUS OF SHROUD	24.4043 CENTIMETERS
RADIUS OF HUB	12.0167 CENTIMETERS
AXIAL DISTANCE FROM ROTOR HUB LEADING EDGE	11.011 CENTIMETERS
ENERGY AVERAGED TOTAL PRESSURE RATIO ACROSS ROTOR	1.642
MASS AVERAGED TOTAL TEMPERATURE RATIO ACROSS ROTOR	1.164
ROTOR ADIABATIC EFFICIENCY	0.93
STATIC PRESSURE ON THE SHROUD	1.2589 * P REF.
STATIC PRESSURE ON THE HUB	1.0023 * P REF.

RADIUS (CENTIMETERS)	P TOTAL/ P REF.	T TOTAL/ T REF.	P STATIC/ P REF.	FLOW ANGLE (DEGREES)
23.2258	1.6664	1.1903	1.2691	37.0
22.0320	1.6549	1.1664	1.2378	34.9
20.8280	1.6501	1.1612	1.2180	36.0
19.6164	1.6426	1.1575	1.2024	35.7
18.3947	1.6277	1.1556	1.1826	37.8
17.1526	1.6202	1.1529	1.1609	39.6
15.8902	1.6372	1.1556	1.1343	41.4
14.6126	1.6406	1.1585	1.0962	44.5
13.3299	1.6086	1.1535	1.0588	48.1

TABLE IV.—GEOMETRIC PARAMETERS USED IN PERFORMANCE CALCULATIONS

[Areas used cover only a portion of the span. Approximately 1.5-percent blockage at the hub and 1.26-percent blockage at the tip were assumed to account for aerodynamic blockage of endwall layers. At station 1 only values of measured conditions from tables III(a) and (b) corresponding to radii herein should be used.]

DESIGN STREAMLINE	RADIUS (CM)		AREA, ΔA_{2n} (SQ. CM)		STREAMLINE SLOPE (DEGREES)	
	STATION 1	STATION 2	STATION 1	STATION 2	STATION 1	STATION 2
1	24.2570	23.2258	324.789	241.362	-0.508	-1.467
2	22.6873	22.0320	216.650	165.832	-0.587	-0.771
3	21.1988	20.8280	205.222	158.120	-0.288	0.052
4	19.6469	19.6164	193.331	150.038	0.327	0.963
5	18.0645	18.3947	181.811	142.327	1.176	1.936
6	16.4414	17.1526	171.592	134.895	2.225	2.952
7	14.7396	15.8902	161.001	126.813	3.501	3.933
8	12.9591	14.6126	151.339	117.615	4.969	4.865
9	11.0084	13.3299	177.631	138.240	6.932	5.341

TABLE V.—COMPARISON OF INTEGRATED FLOW RATES AT STATIONS 1 AND 2 TO THE ORIFICE FLOW

[Mass flow rates for station 1 differ from those given in figs. 13 and 14 because only the 9 positions given in table IV were used to calculate the flow rates herein whereas all radial positions listed in tables III(a) and (b) were used to calculate the flow rates shown in the figures.]

STATION	NEAR PEAK EFFICIENCY		NEAR STALL	
	FLOW RATE (kg/sec)	RATIO	FLOW RATE (kg/sec)	RATIO
ORIFICE	34.57	1.000	32.31	1.000
1	35.00	1.012	32.75	1.014
2	35.53	1.028	33.20	1.028

TABLE VI.—LASER ANEMOMETER MEASUREMENT LOCATIONS

[Axial distance in rotor geometry table (table I) is $AP + 2.159$ cm.]

10% SPAN, PEAK EFFICIENCY				20% SPAN, PEAK EFFICIENCY			
% CHORD	AP cm	RP cm	WNBEG	% CHORD	AP cm	RP cm	WNBEG
-100.49	-4.633	24.234	92.5	-100.00	-4.978	22.728	87.1
-75.54	-3.467	24.220	101.7	-88.76	-4.427	22.717	96.4
-57.99	-2.647	24.209	117.0	-80.00	-3.998	22.693	103.6
-40.43	-1.826	24.195	131.7	-60.00	-3.018	22.640	119.2
-22.88	-1.006	24.178	145.9	-40.00	-2.037	22.621	134.2
-5.33	-0.185	24.162	159.6	-20.00	-1.057	22.664	148.6
3.45	0.225	24.154	166.4	-10.00	-0.566	22.686	155.7
7.84	0.430	24.149	169.7	-5.00	-0.321	22.697	159.2
10.00	0.531	24.077	172.8	-2.50	-0.199	22.702	161.0
12.50	0.648	24.060	174.7	0.00	-0.076	22.708	163.0
15.00	0.765	24.044	176.5	2.50	0.046	22.694	164.9
17.50	0.881	24.027	178.3	5.00	0.169	22.681	166.8
20.00	0.998	24.010	180.1	7.50	0.291	22.668	168.7
22.50	1.115	23.993	181.8	10.00	0.414	22.654	170.6
25.00	1.232	23.976	183.6	12.50	0.537	22.641	172.5
27.50	1.349	23.959	185.3	15.00	0.659	22.628	174.3
30.00	1.466	23.942	187.0	17.50	0.782	22.614	176.1
32.50	1.582	23.925	188.7	20.00	0.904	22.601	177.9
35.00	1.699	23.908	190.3	22.50	1.027	22.588	179.7
37.50	1.816	23.891	192.0	25.00	1.149	22.574	181.4
40.00	1.933	23.874	193.6	27.50	1.272	22.561	183.1
42.50	2.050	23.857	195.3	30.00	1.394	22.548	184.8
45.00	2.167	23.840	196.9	32.50	1.517	22.534	186.5
47.50	2.283	23.823	198.5	35.00	1.640	22.521	188.2
50.00	2.400	23.806	200.1	37.50	1.762	22.508	189.8
52.50	2.517	23.789	201.7	40.00	1.885	22.494	191.5
55.00	2.634	23.772	203.2	42.50	2.007	22.481	193.1
57.50	2.751	23.755	204.8	45.00	2.130	22.468	194.7
60.00	2.868	23.738	206.3	47.50	2.252	22.454	196.3
62.50	2.984	23.721	207.8	50.00	2.375	22.441	197.8
65.00	3.101	23.704	209.3	52.50	2.497	22.428	199.4
67.50	3.218	23.687	210.7	55.00	2.620	22.414	200.9
70.00	3.335	23.671	212.0	57.50	2.743	22.401	202.4
75.00	3.569	23.637	214.7	60.00	2.865	22.388	203.8
77.70	3.695	23.618	216.0	62.50	2.988	22.374	205.3
80.00	3.802	23.603	217.1	65.00	3.110	22.361	206.7
91.22	4.327	23.535	221.7	70.00	3.355	22.334	209.4
100.00	4.737	23.467	225.5	72.50	3.478	22.321	210.7
124.68	5.891	23.399	237.9	75.00	3.600	22.308	212.0
149.10	7.032	23.332	249.5	100.00	4.826	22.174	223.0
173.51	8.173	23.266	261.4	121.39	5.875	22.137	233.6
188.04	8.852	23.226	268.6	141.29	6.850	22.103	243.3
197.92	9.314	23.218	273.6	161.19	7.826	22.068	253.2
222.34	10.455	23.198	286.3	175.37	8.521	22.044	260.4
234.46	11.021	23.197	292.8	182.12	8.852	22.032	263.3
				200.99	9.777	22.026	273.7

TABLE VI.—Continued.

30% SPAN, PEAK EFFICIENCY				40% SPAN, PEAK EFFICIENCY			
% CHORD	AP cm	RP cm	WNBEG	% CHORD	AP cm	RP cm	WNBEG
-100.00	-6.071	21.202	81.1	-100.00	-6.629	19.641	97.8
-80.00	-4.940	21.200	99.0	-80.00	-5.431	19.645	117.9
-74.56	-4.633	21.199	100.6	-66.69	-4.633	19.647	129.5
-60.00	-3.810	21.203	115.9	-60.00	-4.232	19.654	136.7
-40.00	-2.680	21.208	132.0	-40.00	-3.033	19.674	154.5
-20.00	-1.549	21.224	147.5	-20.00	-1.834	19.708	171.6
-10.00	-0.984	21.234	155.2	-10.00	-1.234	19.733	180.0
-5.00	-0.702	21.239	158.9	-5.00	-0.935	19.746	184.1
-2.50	-0.560	21.242	160.8	-2.50	-0.785	19.752	186.2
0.00	-0.419	21.245	163.0	0.00	-0.635	19.759	188.6
2.50	-0.278	21.235	165.1	2.50	-0.485	19.754	190.9
5.00	-0.137	21.226	167.1	5.00	-0.335	19.750	193.2
7.50	0.005	21.217	169.2	7.50	-0.185	19.746	195.4
10.00	0.146	21.208	171.2	10.00	-0.036	19.742	197.6
12.50	0.287	21.199	173.1	20.00	0.564	19.725	206.0
15.00	0.429	21.190	175.1	30.00	1.163	19.708	213.9
22.50	0.852	21.163	180.7	40.00	1.763	19.691	221.2
25.00	0.994	21.154	182.5	50.00	2.362	19.674	228.1
30.00	1.276	21.136	186.1	60.00	2.962	19.657	234.3
32.50	1.418	21.126	187.9	70.00	3.561	19.640	240.0
35.00	1.559	21.117	189.6	80.00	4.161	19.623	245.3
40.00	1.841	21.099	193.0	90.00	4.760	19.605	250.1
42.50	1.983	21.090	194.7	100.00	5.359	19.588	254.0
45.00	2.124	21.081	196.3	117.38	6.401	19.597	263.1
50.00	2.407	21.063	199.5	134.47	7.425	19.605	271.8
50.00	2.407	21.063	199.5	151.55	8.450	19.613	280.7
55.00	2.689	21.045	202.6	158.26	8.852	19.616	284.3
60.00	2.972	21.027	205.6	168.64	9.474	19.629	289.8
65.00	3.254	21.008	208.4	185.81	10.503	19.649	308.3
70.00	3.537	20.990	211.2				
80.00	4.102	20.954	216.3				
90.00	4.667	20.918	221.1				
100.00	5.232	20.881	225.0				
117.07	6.197	20.867	235.2				
136.03	7.268	20.851	245.0				

TABLE VI.—Continued.

50% SPAN, PEAK EFFICIENCY				60% SPAN, PEAK EFFICIENCY			
% CHORD	AP cm	RP cm	WNBEG	% CHORD	AP cm	RP cm	WNBEG
-100.00	-7.341	17.997	91.5	-100.00	-8.128	16.331	127.7
-80.00	-6.041	18.029	113.2	-80.00	-6.716	16.376	152.6
-60.00	-4.741	18.062	133.1	-60.00	-5.304	16.420	174.3
-58.34	-4.633	18.064	134.6	-50.50	-4.633	16.441	185.6
-40.00	-3.441	18.089	151.8	-40.00	-3.891	16.464	194.7
-20.00	-2.141	18.132	169.7	-20.00	-2.479	16.507	215.2
-10.00	-1.491	18.190	178.3	-10.00	-1.773	16.593	223.8
-5.00	-1.166	18.219	182.6	-5.00	-1.420	16.640	229.3
-2.50	-1.003	18.233	184.8	-2.50	-1.243	16.664	231.5
0.00	-0.841	18.247	187.3	2.50	-0.890	16.696	236.8
2.50	-0.678	18.249	189.8	5.00	-0.714	16.704	239.3
5.00	-0.516	18.250	192.2	7.50	-0.537	16.711	241.8
7.50	-0.353	18.251	194.5	20.00	0.345	16.751	254.0
10.00	-0.191	18.252	196.8	30.00	1.052	16.782	262.9
20.00	0.459	18.257	205.5	40.00	1.758	16.814	270.8
50.00	2.409	18.271	227.3	50.00	2.464	16.845	276.9
60.00	3.059	18.276	233.1	60.00	3.170	16.877	283.1
70.00	3.709	18.281	238.4	70.00	3.876	16.908	288.7
80.00	4.359	18.286	243.1	80.00	4.582	16.940	292.6
90.00	5.009	18.291	247.3	90.00	5.288	16.971	297.0
100.00	5.659	18.296	250.8	100.00	5.994	17.003	300.5
115.14	6.643	18.326	257.6	112.88	6.904	17.050	305.3
130.04	7.612	18.356	264.5	125.76	7.813	17.098	311.2
144.95	8.581	18.386	271.4	138.63	8.722	17.146	317.2
149.12	8.852	18.395	273.4	140.47	8.852	17.153	317.9
159.85	9.549	18.420	278.5	151.51	9.632	17.196	323.3
174.76	10.518	18.456	285.8	164.39	10.541	17.247	329.7
183.35	11.077	18.478	290.1				

TABLE VI.—Continued.

70% SPAN, PEAK EFFICIENCY				80% SPAN, PEAK EFFICIENCY			
% CHORD	AP cm	RP cm	WNBEG	% CHORD	AP cm	RP cm	WNBEG
-100.00	-9.111	14.518	117.0	-100.00	-9.952	12.540	99.6
-80.00	-7.563	14.595	143.9	-80.00	-8.291	12.671	132.7
-60.00	-6.015	14.671	168.1	-60.00	-6.630	12.802	160.7
-42.14	-4.633	14.740	187.7	-40.00	-4.970	12.933	185.8
-40.00	-4.467	14.748	189.8	-35.94	-4.633	12.959	191.3
-20.00	-2.919	14.831	211.4	-20.00	-3.309	13.061	210.5
-10.00	-2.146	14.905	221.8	-10.00	-2.479	13.125	221.9
-5.00	-1.759	14.979	227.4	-5.00	-2.064	13.224	226.9
-2.50	-1.565	15.015	229.7	-2.50	-1.856	13.283	230.3
0.00	-1.372	15.052	232.4	0.00	-1.648	13.343	233.3
2.50	-1.178	15.068	235.3	2.50	-1.441	13.369	236.5
7.50	-0.791	15.101	241.8	5.00	-1.233	13.396	239.4
10.00	-0.598	15.118	244.2	7.50	-1.026	13.423	243.3
20.00	0.176	15.184	254.5	10.00	-0.818	13.450	246.0
30.00	0.950	15.249	263.3	20.00	0.012	13.558	258.6
50.00	2.498	15.381	277.4	30.00	0.843	13.665	266.4
60.00	3.272	15.447	283.1	40.00	1.673	13.772	272.5
70.00	4.046	15.513	288.0	50.00	2.503	13.880	277.5
80.00	4.820	15.578	291.2	60.00	3.333	13.987	284.3
90.00	5.594	15.644	294.8	70.00	4.164	14.095	288.1
100.00	6.368	15.710	297.2	80.00	4.994	14.202	291.0
110.95	7.216	15.771	301.3	90.00	5.824	14.310	293.1
121.78	8.053	15.832	305.6	100.00	6.655	14.417	293.8
132.10	8.852	15.890	309.9	109.56	7.448	14.488	297.3
132.60	8.891	15.893	310.1	119.02	8.234	14.558	300.0
				126.46	8.852	14.613	302.5
				128.50	9.022	14.629	302.9
				137.95	9.806	14.703	306.1
				147.42	10.592	14.778	309.5

TABLE VI.—Continued.

10% SPAN, NEAR STALL				20% SPAN, NEAR STALL			
% CHORD	AP cm	RP cm	WNBEG	% CHORD	AP cm	RP cm	WNBEG
-100.00	-4.674	24.235	123.5	-100.00	-5.385	22.729	117.1
-99.14	-4.633	24.234	124.2	-88.76	-4.802	22.728	126.4
-80.00	-3.729	24.223	138.7	-80.00	-4.348	22.712	133.6
-60.00	-2.784	24.211	153.2	-60.00	-3.312	22.656	149.2
-40.00	-1.839	24.192	167.2	-40.00	-2.276	22.611	164.2
-20.00	-0.894	24.169	180.8	-20.00	-1.240	22.659	178.6
-10.00	-0.422	24.157	187.4	-10.00	-0.721	22.683	185.7
-5.00	-0.185	24.151	190.8	-10.00	-0.721	22.683	185.7
-2.50	-0.067	24.148	192.4	-5.00	-0.462	22.696	189.2
0.00	0.051	24.145	194.3	-2.50	-0.333	22.702	191.0
2.50	0.169	24.128	195.2	0.00	-0.203	22.708	193.0
5.00	0.287	24.111	197.1	2.50	-0.074	22.694	194.9
7.50	0.405	24.094	198.9	5.00	0.056	22.681	196.8
10.00	0.523	24.077	200.7	7.50	0.185	22.668	198.7
20.00	0.996	24.010	207.9	10.00	0.315	22.654	200.6
30.00	1.468	23.942	214.7	20.00	0.833	22.601	207.9
40.00	1.941	23.874	221.2	30.00	1.351	22.548	214.8
50.00	2.413	23.806	227.6	40.00	1.869	22.494	221.5
60.00	2.885	23.738	233.7	50.00	2.388	22.441	227.8
70.00	3.358	23.670	239.3	60.00	2.906	22.388	233.8
80.00	3.830	23.603	244.3	70.00	3.424	22.334	239.4
90.00	4.303	23.535	248.8	80.00	3.942	22.281	244.4
100.00	4.775	23.467	252.5	90.00	4.460	22.228	249.1
123.61	5.891	23.401	263.8	100.00	4.978	22.174	253.0
				121.39	6.087	22.133	263.6
				141.29	7.118	22.096	273.3
				161.19	8.149	22.058	283.2
				175.37	8.884	22.032	290.4
				181.09	9.180	22.030	293.3
				200.99	10.212	22.023	303.7

TABLE VI.—Continued.

30% SPAN, NEAR STALL				40% SPAN, NEAR STALL			
% CHORD	AP cm	RP cm	WNBEG	% CHORD	AP cm	RP cm	WNBEG
-100.00	-5.969	21.202	111.1	-100.00	-6.452	19.641	52.2
-80.00	-4.856	21.199	128.8	-80.00	-5.263	19.645	71.9
-75.98	-4.633	21.199	131.0	-69.40	-4.633	19.647	83.9
-60.00	-3.744	21.203	145.5	-60.00	-4.074	19.656	90.3
-40.00	-2.631	21.208	161.4	-40.00	-2.885	19.677	107.8
-20.00	-1.519	21.225	176.7	-20.00	-1.697	19.712	124.5
-10.00	-0.963	21.235	184.3	-10.00	-1.102	19.735	132.7
-5.00	-0.685	21.240	188.0	-5.00	-0.805	19.747	136.7
-2.50	-0.545	21.242	189.8	-2.50	-0.657	19.753	138.7
0.00	-0.406	21.245	192.0	0.00	-0.508	19.759	141.1
2.50	-0.267	21.235	194.0	2.50	-0.359	19.754	143.3
5.00	-0.128	21.226	196.1	5.00	-0.211	19.750	145.6
7.50	0.011	21.217	198.1	7.50	-0.062	19.746	147.8
10.00	0.150	21.208	200.1	10.00	0.086	19.742	149.9
20.00	0.706	21.172	207.7	20.00	0.681	19.725	158.1
30.00	1.262	21.136	214.8	30.00	1.275	19.708	165.8
40.00	1.819	21.099	221.7	40.00	1.869	19.691	173.0
50.00	2.375	21.063	228.2	50.00	2.464	19.674	179.6
60.00	2.931	21.027	234.3	60.00	3.058	19.657	185.7
70.00	3.487	20.990	239.9	90.00	4.841	19.605	200.9
80.00	4.044	20.954	245.0	116.25	6.401	19.596	213.3
90.00	4.600	20.918	249.8	133.46	7.424	19.604	221.7
100.00	5.156	20.881	253.7	150.73	8.451	19.614	230.3
118.71	6.197	20.866	263.9				
137.97	7.268	20.851	273.7				
157.23	8.340	20.835	283.3				
166.44	8.852	20.828	288.0				
176.49	9.411	20.831	293.2				
195.75	10.483	20.836	302.9				
205.89	11.046	20.847	308.5				

TABLE VI.—Continued.

50% SPAN, NEAR STALL				60% SPAN, NEAR STALL			
% CHORD	AP cm	RP cm	WNBEG	% CHORD	AP cm	RP cm	WNBEG
-100.00	-7.264	17.999	93.9	-100.00	-8.090	16.332	7.7
-80.00	-5.969	18.031	115.4	-80.00	-6.680	16.377	31.1
-60.00	-4.674	18.063	135.1	-60.00	-5.270	16.421	52.3
-59.37	-4.633	18.064	136.7	-50.95	-4.633	16.441	62.8
-40.00	-3.378	18.090	153.6	-40.00	-3.861	16.465	72.2
-10.00	-1.435	18.192	179.9	-20.00	-2.451	16.508	91.2
-5.00	-1.111	18.220	184.2	-10.00	-1.746	16.595	100.1
-2.50	-0.949	18.233	186.3	-5.00	-1.394	16.641	104.6
0.00	-0.787	18.247	188.8	-2.50	-1.218	16.665	106.9
2.50	-0.625	18.249	191.3	2.50	-0.865	16.696	112.3
5.00	-0.464	18.250	193.6	5.00	-0.689	16.704	114.9
7.50	-0.302	18.251	196.0	7.50	-0.513	16.711	117.5
10.00	-0.140	18.252	198.2	10.00	-0.337	16.719	119.9
20.00	0.508	18.257	206.8	20.00	0.368	16.751	129.0
30.00	1.156	18.262	214.7	30.00	1.073	16.782	137.2
40.00	1.803	18.267	221.9	40.00	1.778	16.814	144.3
50.00	2.451	18.271	228.3	50.00	2.483	16.845	150.6
60.00	3.099	18.276	234.1	60.00	3.188	16.877	156.1
70.00	3.746	18.281	239.2	70.00	3.893	16.908	160.9
80.00	4.394	18.286	243.9	80.00	4.597	16.940	165.1
90.00	5.042	18.291	248.0	90.00	5.302	16.971	168.8
100.00	5.690	18.296	251.4	100.00	6.007	17.003	171.5
114.72	6.643	18.325	258.1	112.72	6.904	17.050	176.6
129.68	7.612	18.356	264.8	125.62	7.813	17.098	181.8
148.82	8.852	18.395	273.5	140.23	8.852	17.153	187.9
159.59	9.549	18.420	278.6	151.30	9.632	17.196	192.6
				164.20	10.541	17.247	198.3
				172.10	11.097	17.277	201.8

TABLE VI.—Continued.

70% SPAN, NEAR STALL				80% SPAN, NEAR STALL			
% CHORD	AP cm	RP cm	WNBEG	% CHORD	AP cm	RP cm	WNBEG
-100.00	-8.951	14.526	53.6	-100.00	-9.754	12.556	39.7
-80.00	-7.416	14.602	79.0	-80.00	-8.113	12.685	69.9
-60.00	-5.882	14.678	101.3	-60.00	-6.472	12.814	96.1
-43.73	-4.633	14.740	112.8	-40.00	-4.831	12.943	119.4
-40.00	-4.347	14.755	122.2	-37.59	-4.633	12.959	122.6
-20.00	-2.812	14.836	142.2	-20.00	-3.190	13.070	141.3
-10.00	-2.045	14.919	152.1	-10.00	-2.370	13.136	151.8
-5.00	-1.661	14.985	156.6	-5.00	-1.960	13.239	156.8
-2.50	-1.469	15.019	157.0	-2.50	-1.755	13.291	159.3
0.00	-1.278	15.052	159.6	0.00	-1.549	13.343	162.3
2.50	-1.086	15.068	162.2	2.50	-1.344	13.369	165.5
5.00	-0.894	15.085	164.6	5.00	-1.139	13.396	168.5
7.50	-0.702	15.101	167.0	7.50	-0.934	13.423	171.4
10.00	-0.510	15.118	169.3	10.00	-0.729	13.450	174.1
20.00	0.257	15.184	178.8	20.00	0.091	13.558	183.8
33.30	1.278	15.291	190.0	30.00	0.912	13.665	191.7
40.00	1.792	15.315	193.9	40.00	1.732	13.772	197.9
50.00	2.559	15.381	200.6	50.00	2.553	13.880	203.0
60.00	3.326	15.447	206.5	60.00	3.373	13.987	206.9
70.00	4.094	15.513	210.7	80.00	5.014	14.202	211.8
80.00	4.861	15.578	215.3	90.00	5.834	14.310	213.0
90.00	5.628	15.644	219.4	100.00	6.655	14.417	212.8
100.00	6.396	15.710	221.5	109.67	7.448	14.488	214.4
110.69	7.216	15.770	227.0	119.25	8.234	14.558	216.2
				126.78	8.852	14.613	217.8
				128.85	9.022	14.629	218.2

TABLE VI.—Concluded.

90% SPAN, NEAR STALL

% CHORD	AP cm	RP cm	WNBEG
-80.00	-8.700	10.635	92.4
-60.00	-6.985	10.792	126.8
-40.00	-5.270	10.950	155.9
-32.56	-4.633	11.008	168.6
-20.00	-3.556	11.162	183.2
-10.00	-2.699	11.284	196.1
-5.00	-2.270	11.361	202.9
-2.50	-2.056	11.419	205.7
0.00	-1.841	11.478	209.1
2.50	-1.627	11.519	213.7
5.00	-1.413	11.561	216.9
7.50	-1.199	11.602	220.1
10.00	-0.984	11.643	223.0
20.00	-0.127	11.807	234.1
30.00	0.730	11.972	242.9
40.00	1.587	12.137	249.6
50.00	2.445	12.301	253.6
60.00	3.302	12.466	257.3
70.00	4.159	12.630	259.5
80.00	5.016	12.795	260.4
90.00	5.874	12.960	260.3
109.93	7.582	13.207	258.9
118.79	8.341	13.280	259.7
124.74	8.852	13.330	259.8
127.64	9.101	13.356	260.9

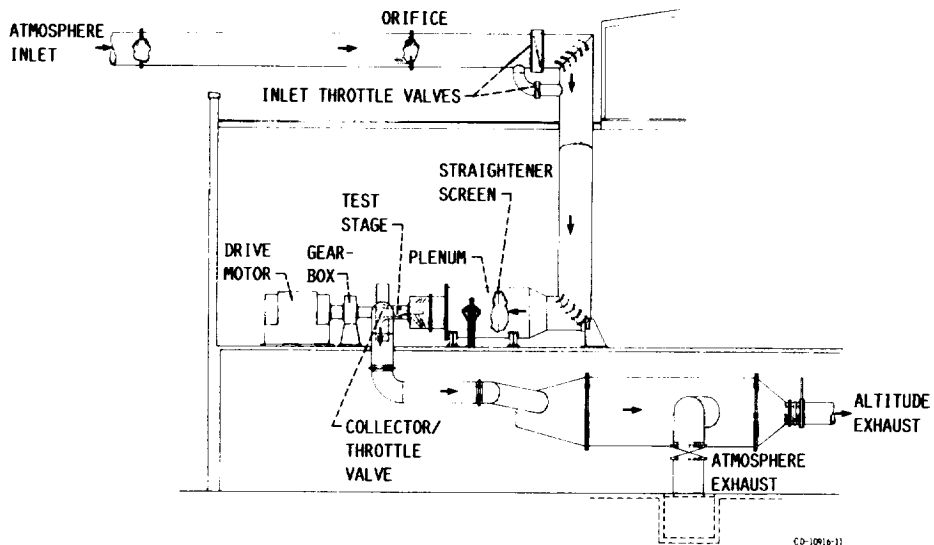


Figure 1.—Schematic diagram of NASA Lewis single-stage compressor test facility.

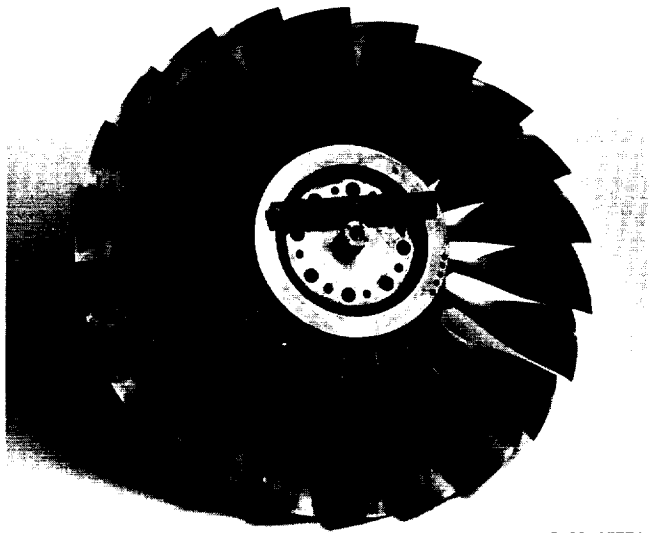


Figure 2.—Test rotor.

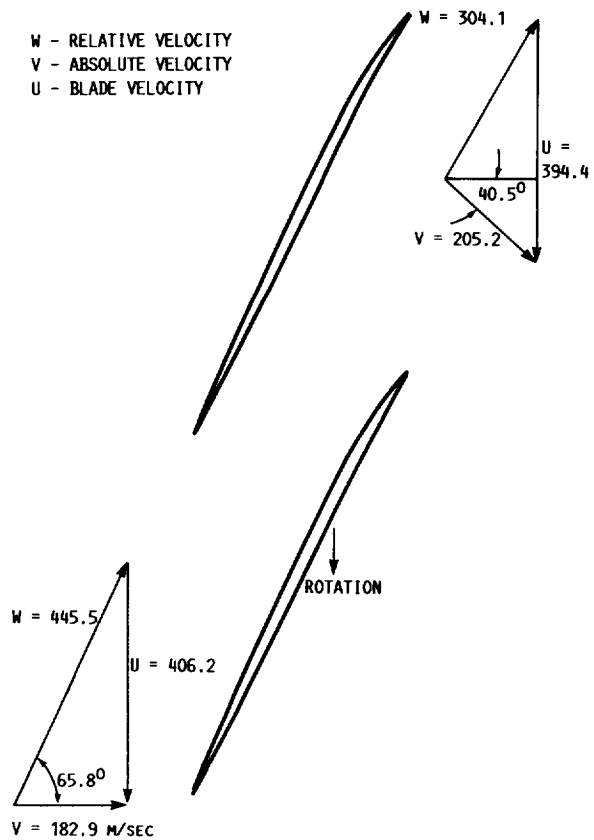
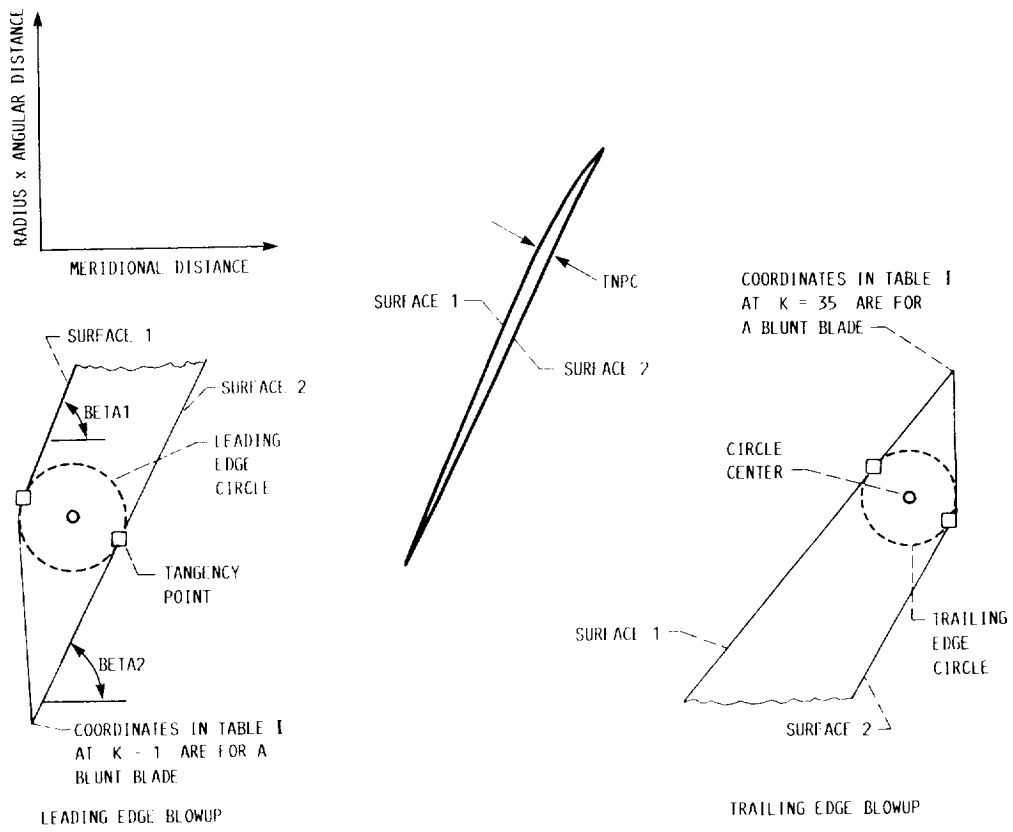
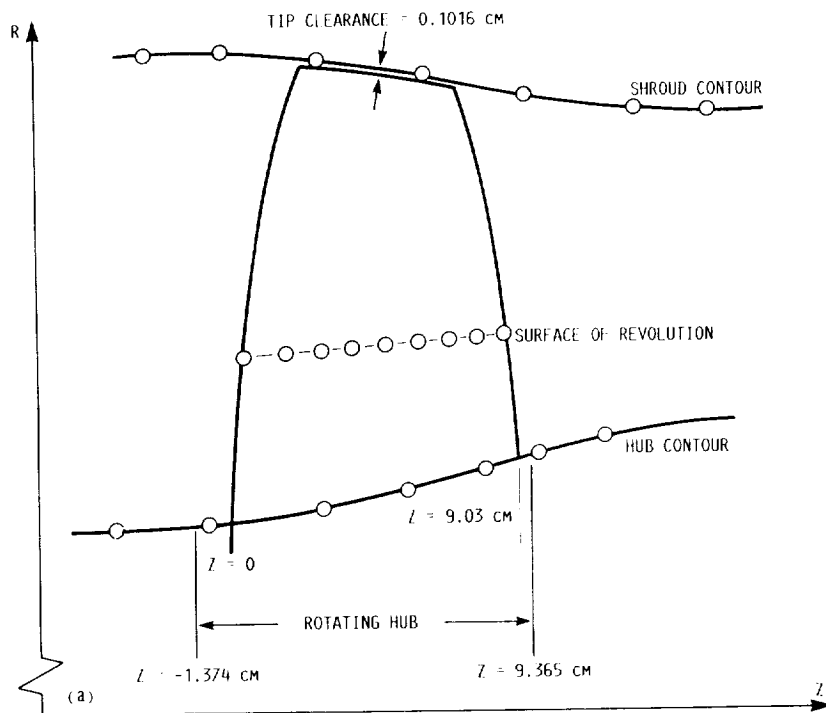


Figure 3.—Velocity diagrams at design conditions at 10-percent span from tip.



(a) Meridional projection.
 (b) Blade-to-blade surface.

Figure 4.—Definition of blade and flowpath geometry nomenclature used in tables I and II.

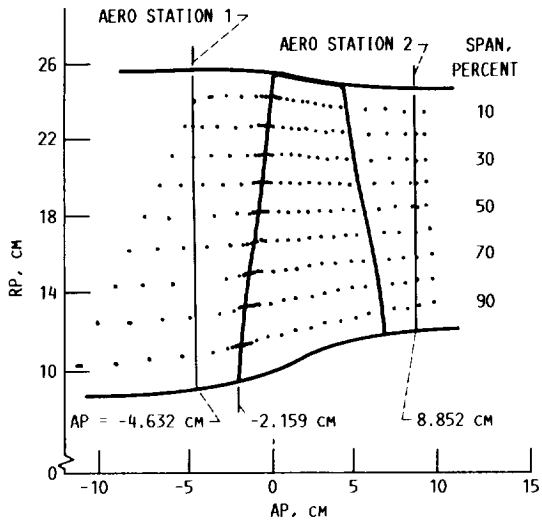


Figure 5.—Meridional view of test fan rotor showing laser anemometer and aerodynamic survey locations.

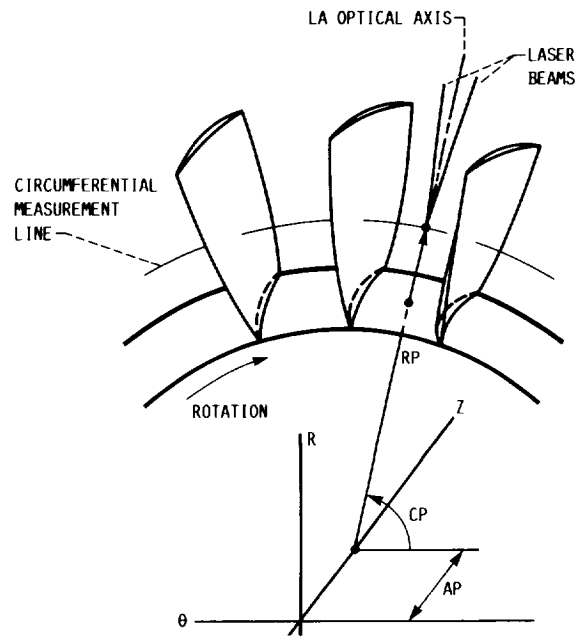
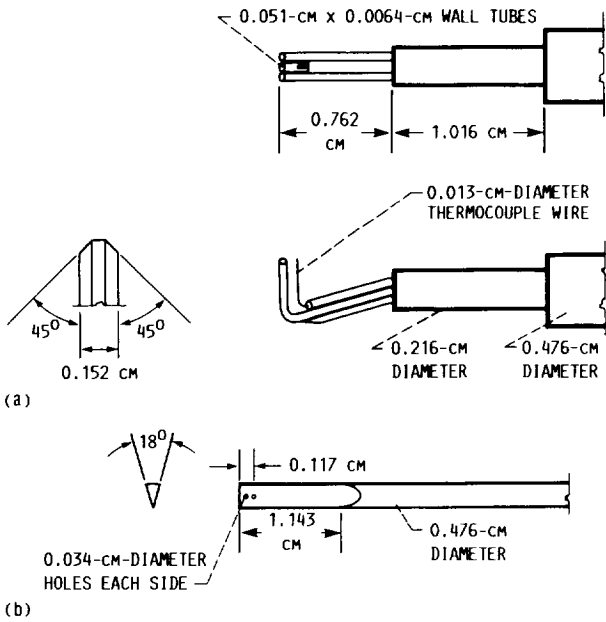


Figure 7.—Definition of circumferential measurement line.



(a) Cobra probe for total pressure, total temperature, and angle measurements.
 (b) Wedge probe for static pressure measurements.

Figure 6.—Aerodynamic survey probes.

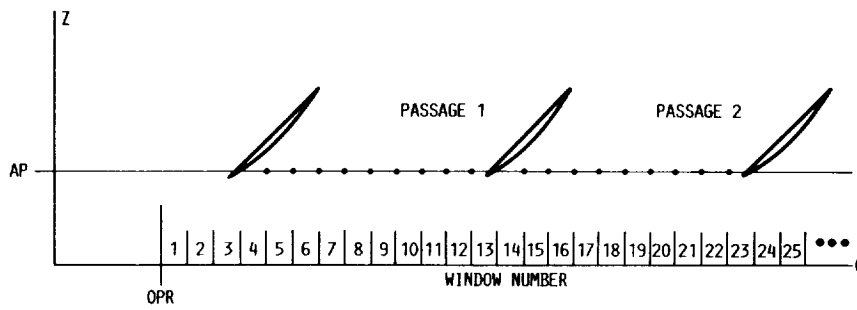


Figure 8.—Generation of measurement windows using shaft angle encoder pulses.

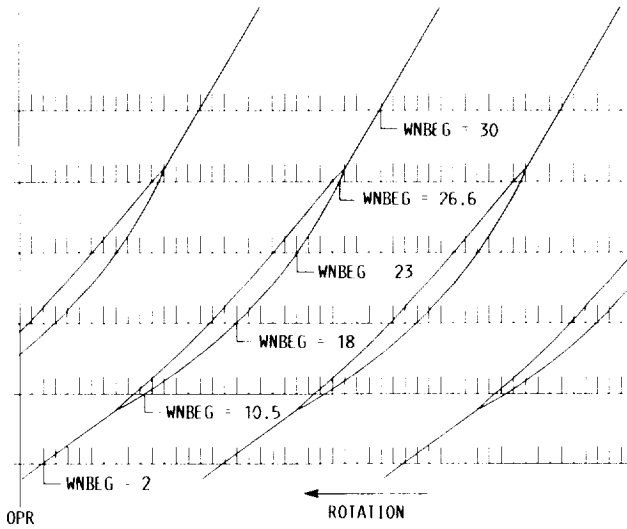


Figure 9.—Definition of LA beginning measurement window WNBEG through rotor.

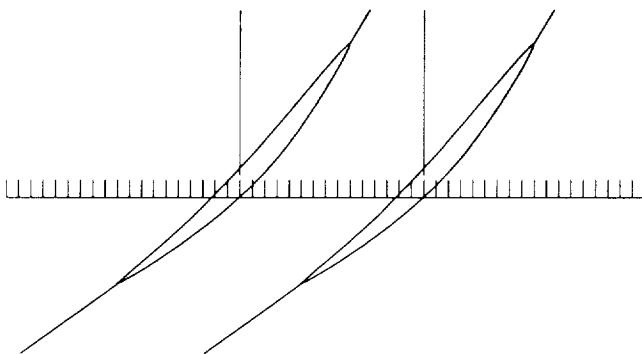
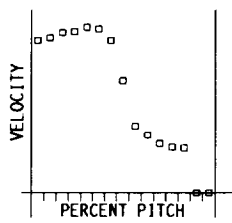


Figure 10.—Schematic representation of LA blade-to-blade data plot showing location of zero-data region caused by blade metal blockage.

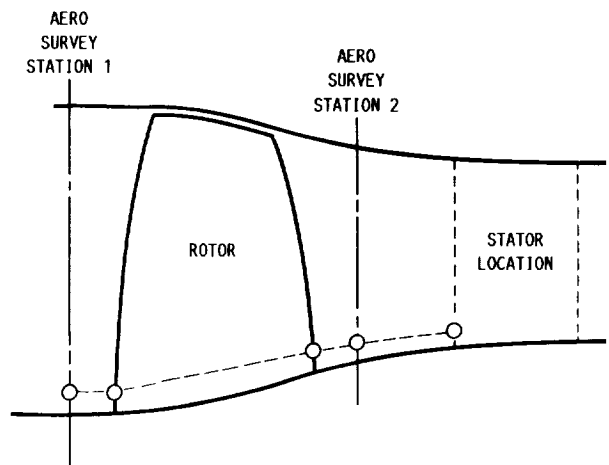


Figure 11.—Meridional view of measurement surface constructed from straight-line interpolation between known design streamline coordinates.

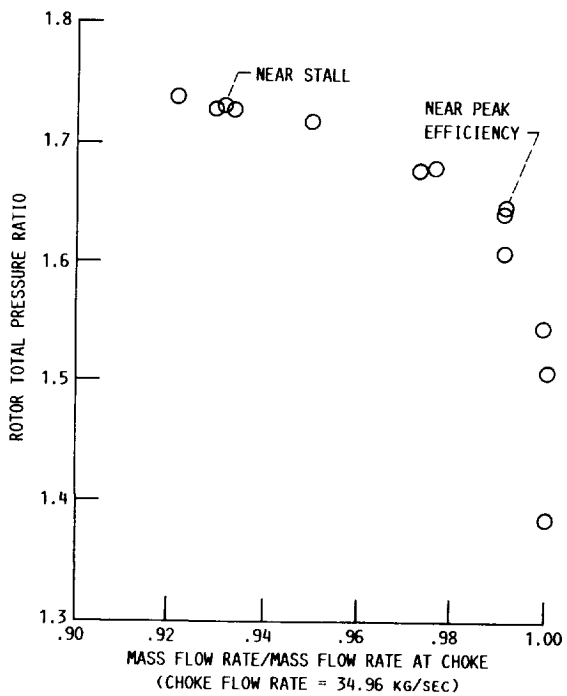
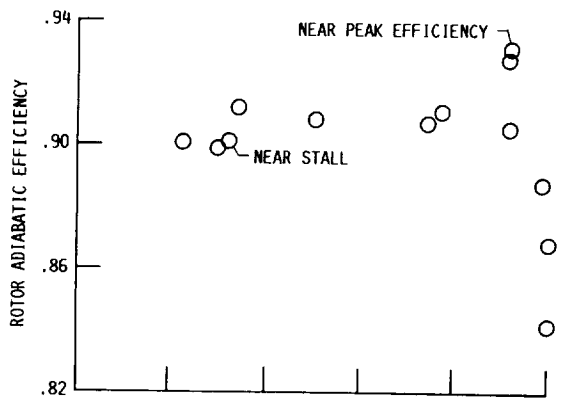


Figure 12.—Fan rotor design speed operating characteristic.

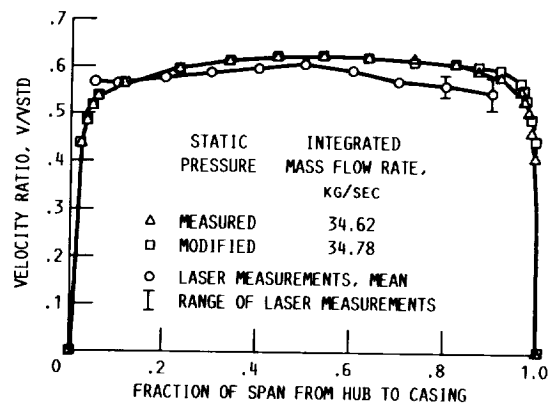


Figure 13.—Axial velocity distribution at inlet survey station at near peak efficiency flow rate. Flow rate from orifice, 34.57 kg/sec; critical velocity at standard-day conditions, VSTD, 310.63 m/sec.

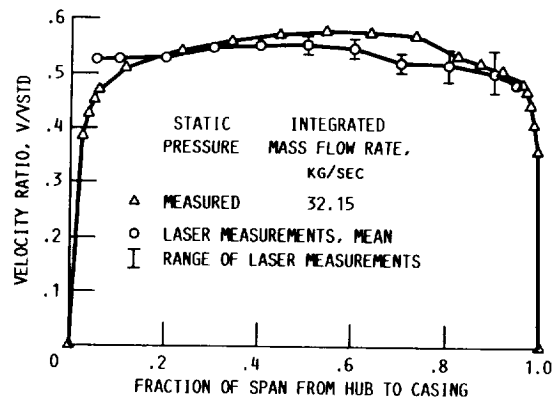


Figure 14.—Axial velocity distribution at inlet survey station at near stall flow rate. Flow rate from orifice, 32.31 kg/sec; critical velocity at standard-day conditions, VSTD, 310.63 m/sec.

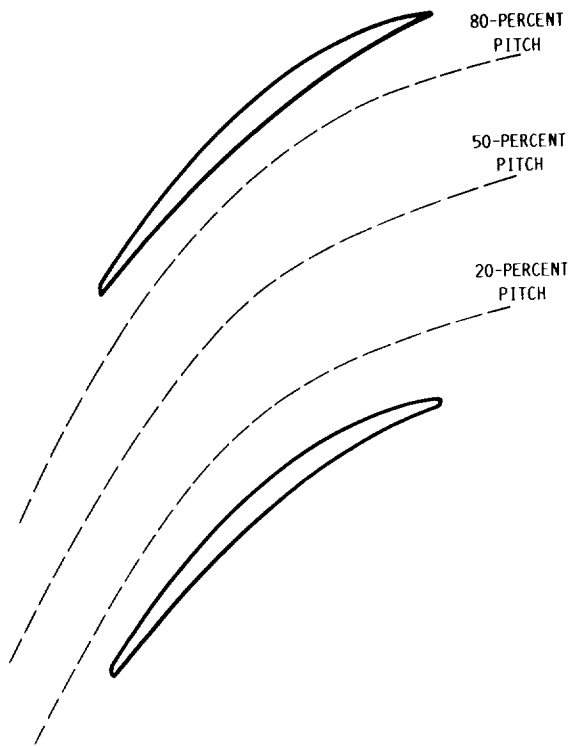


Figure 15.—Schematic representation of constant pitch lines used to plot LA data in streamwise direction through rotor.

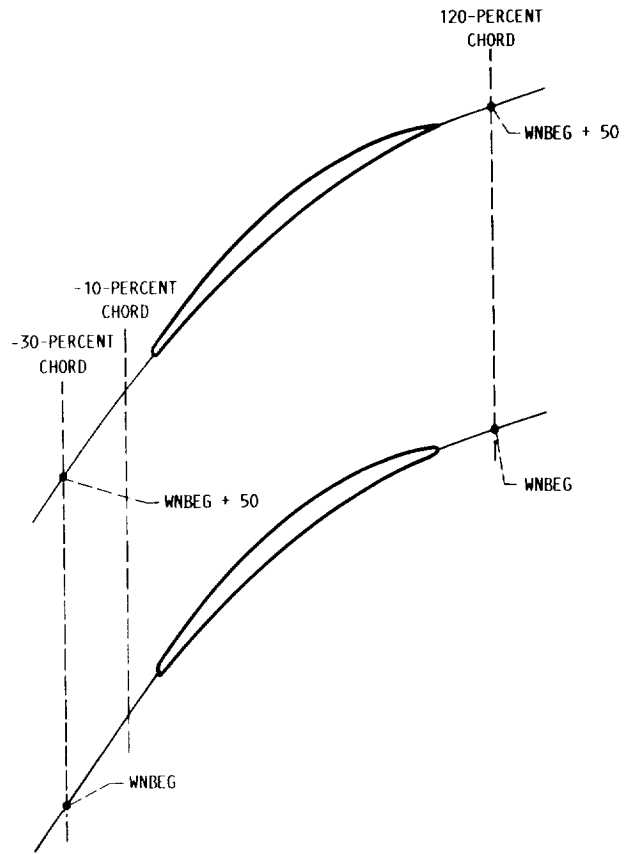


Figure 16.—Schematic representation of constant chord lines used to plot LA data in blade-to-blade direction upstream and downstream of rotor.

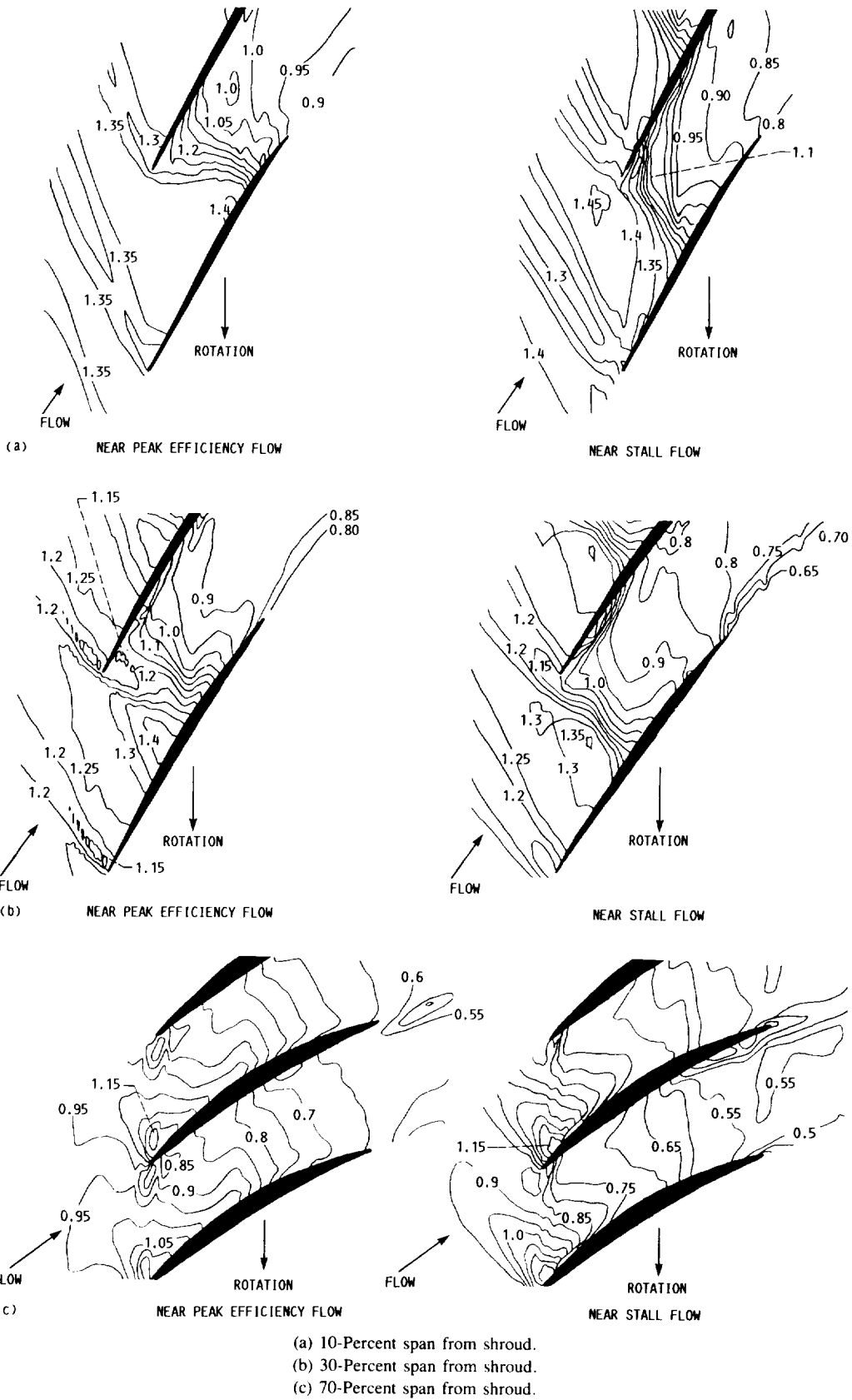


Figure 17.—Contour plots of relative Mach numbers at flows near peak efficiency and near stall.

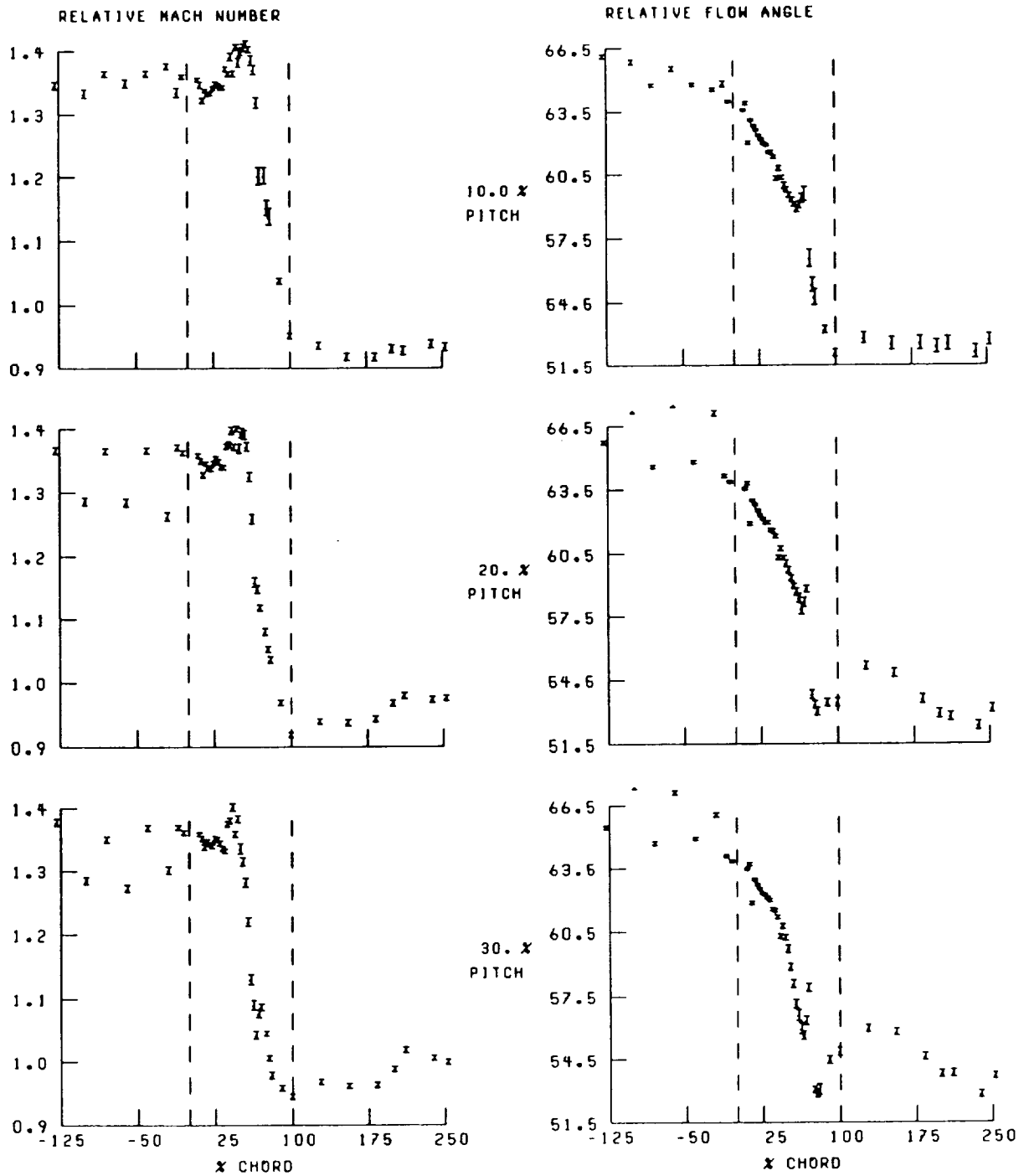


Figure 18.—Streamwise distribution of relative Mach number and flow angle for 10-percent span and near peak efficiency. Broken lines denote location of blade leading and trailing edges.

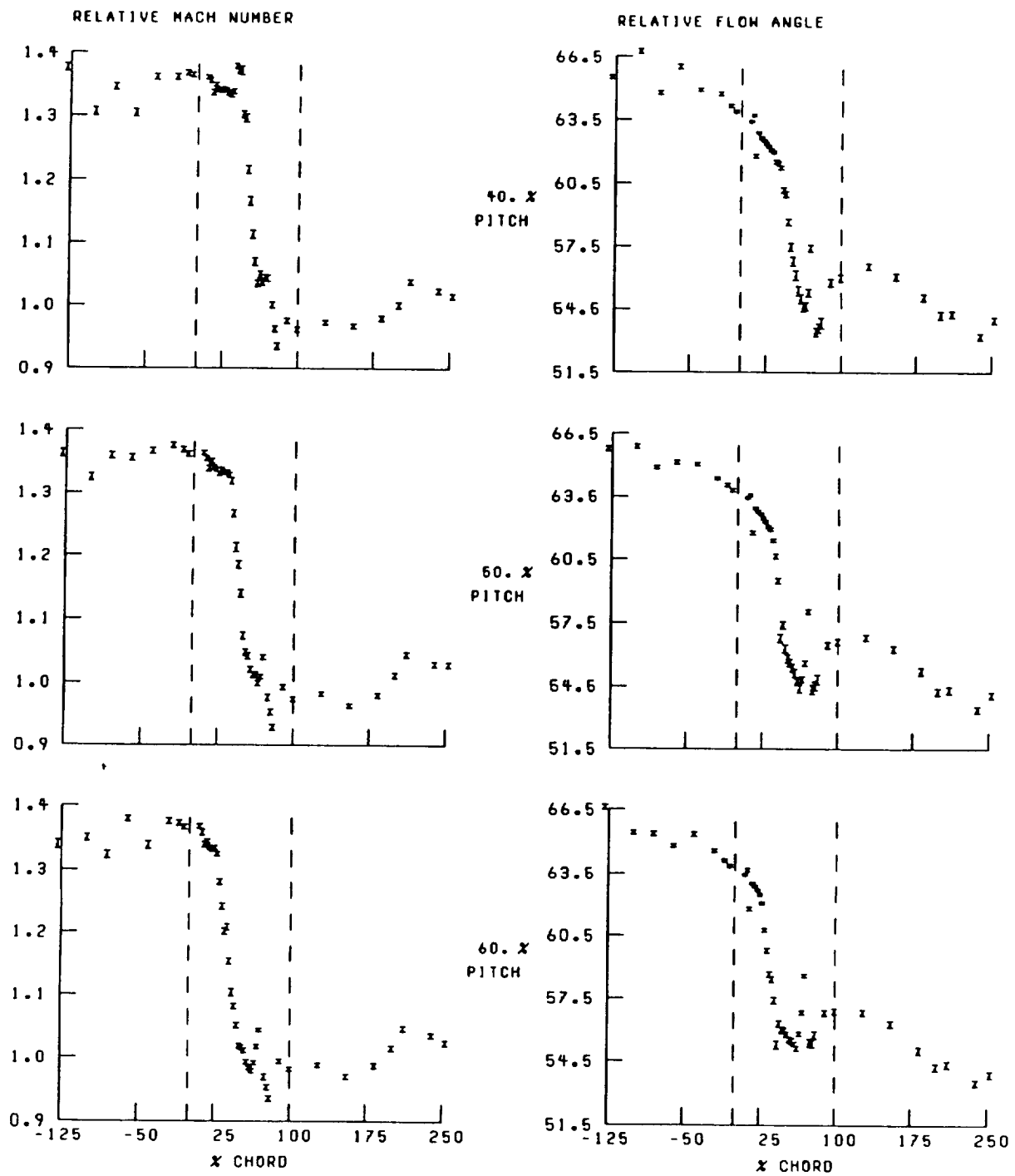


Figure 18.—Continued.

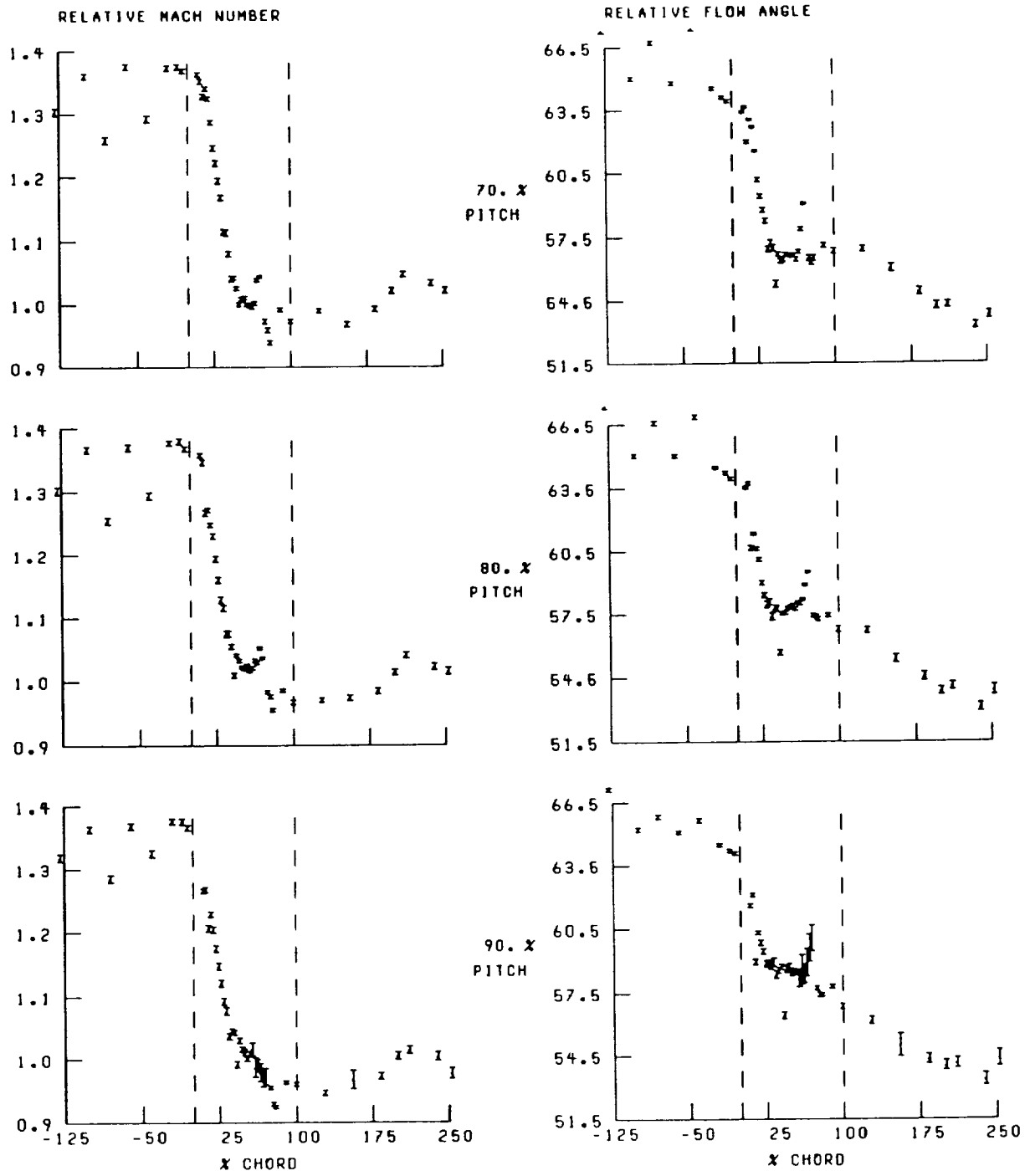


Figure 18.—Concluded.

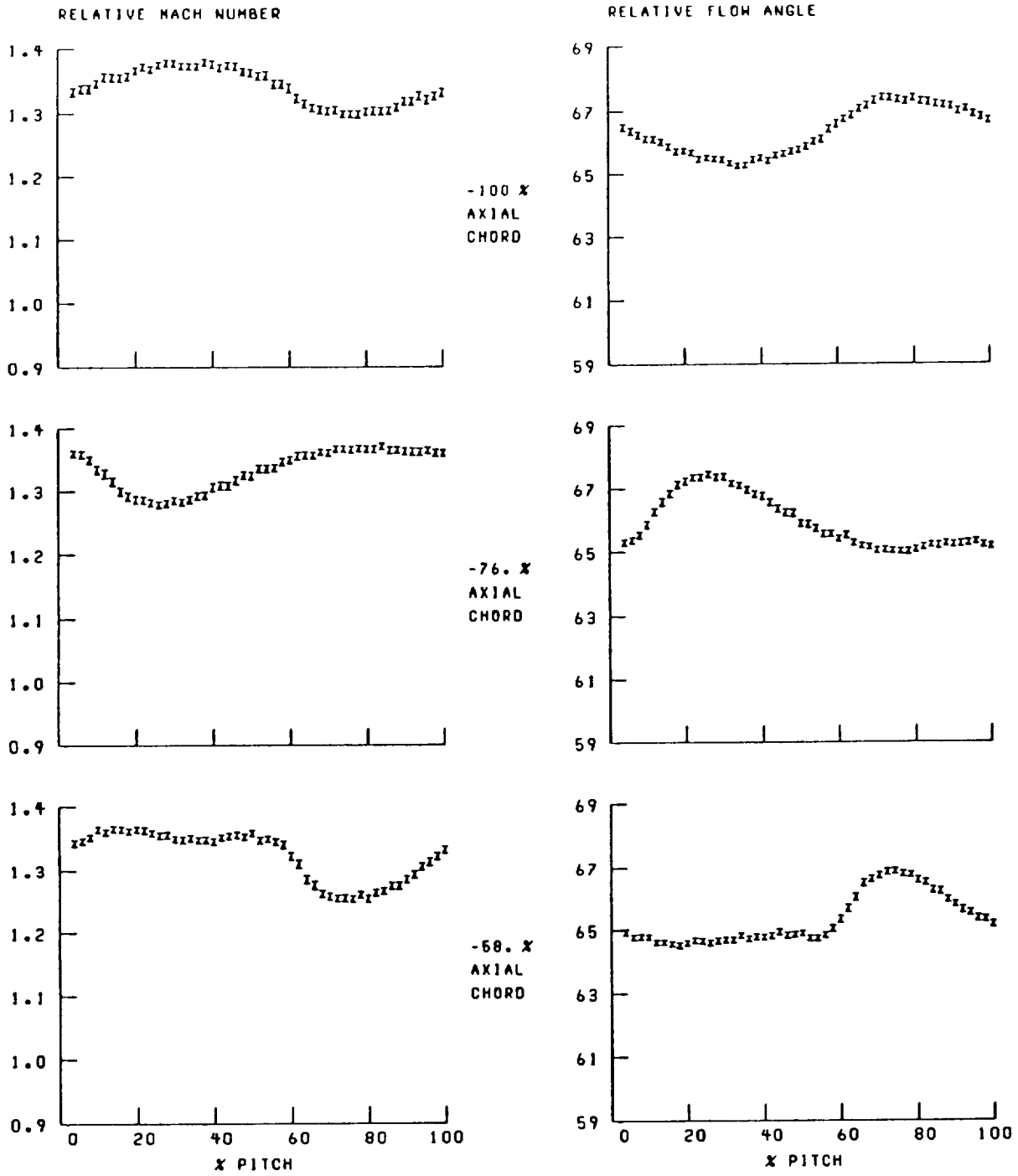


Figure 19.—Blade-to-blade distribution of relative Mach number and flow angle at 10-percent span and near peak efficiency.

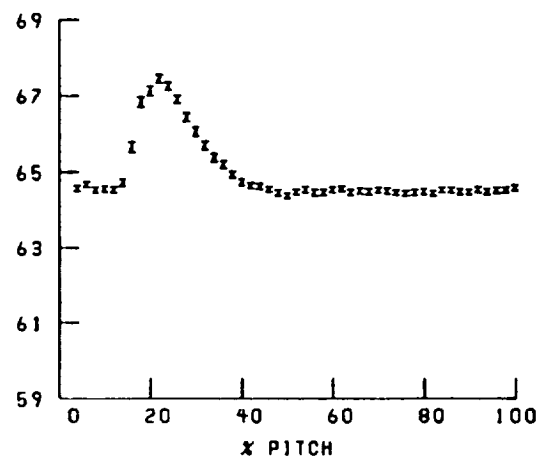
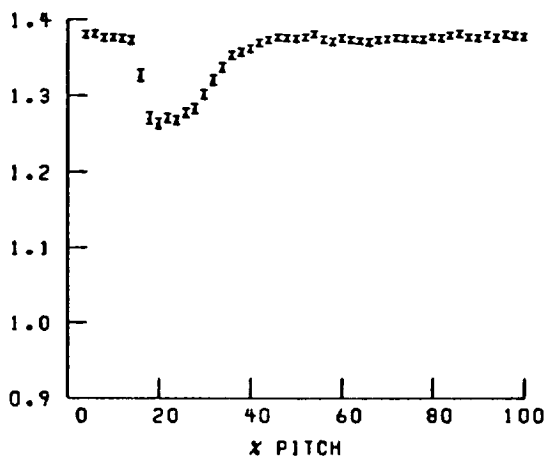
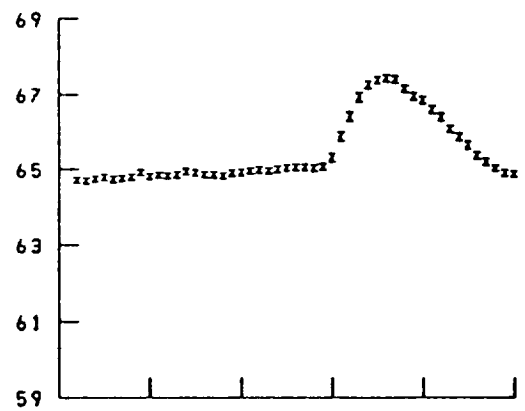
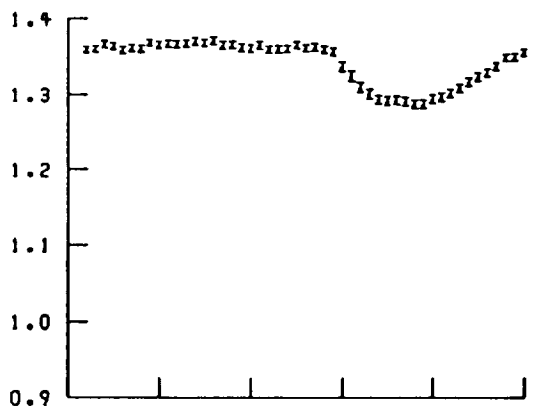
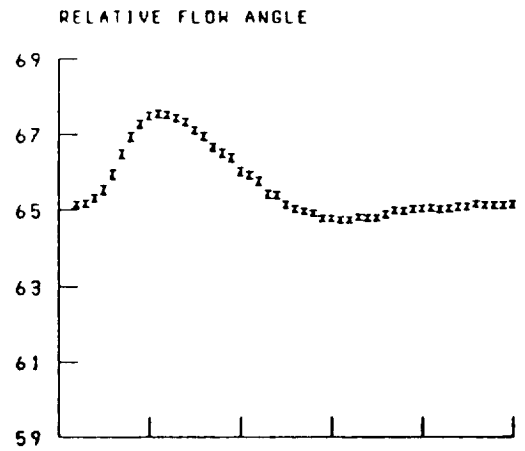
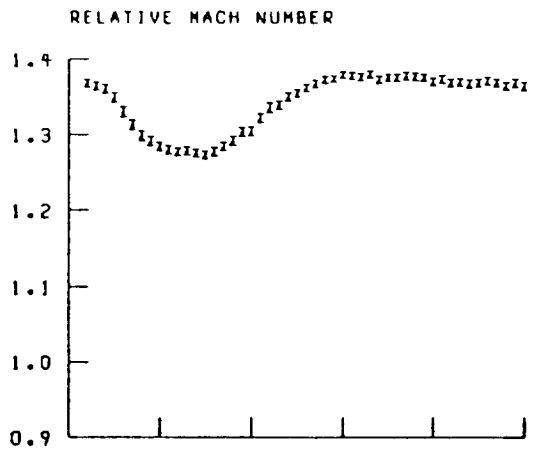


Figure 19.—Continued.

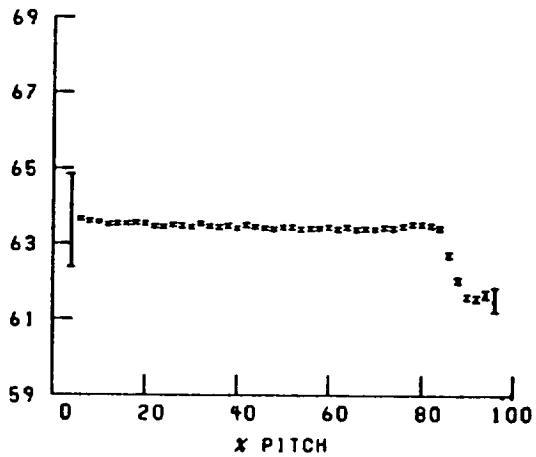
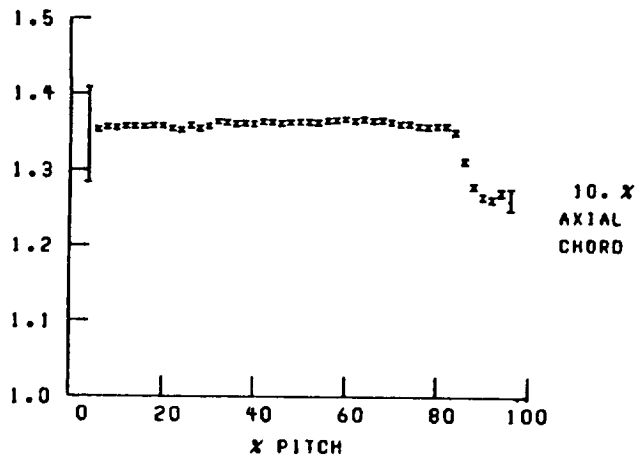
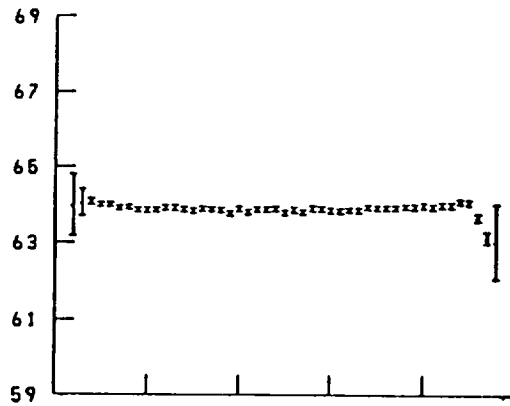
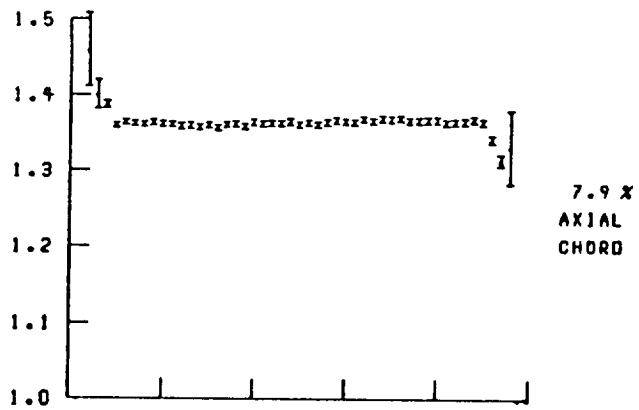
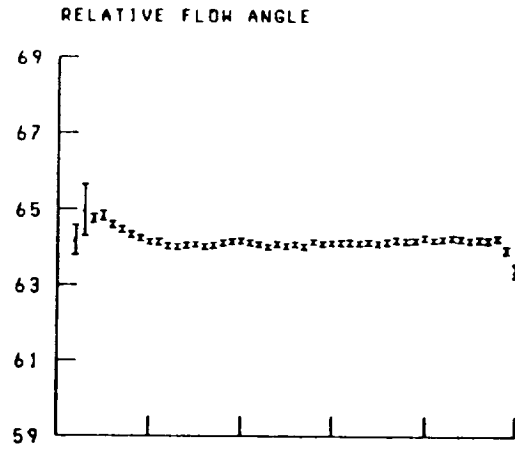
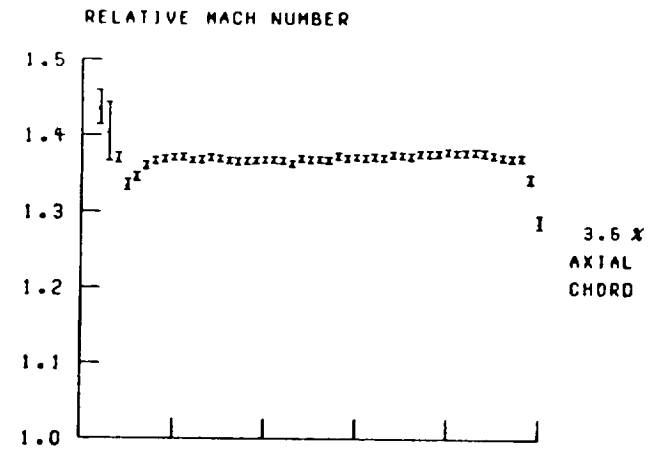


Figure 19.—Continued.

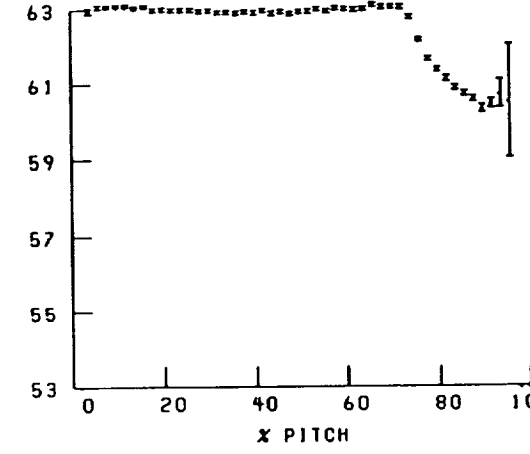
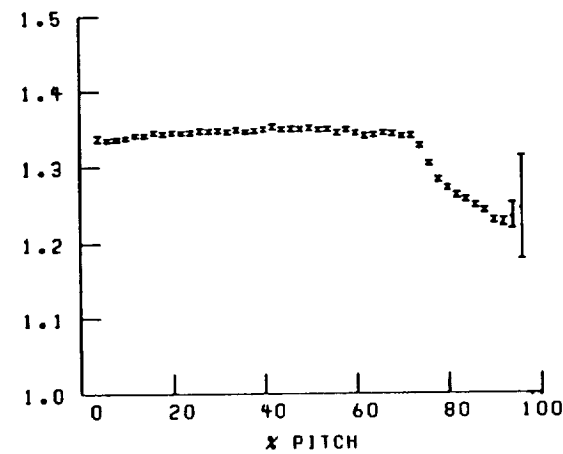
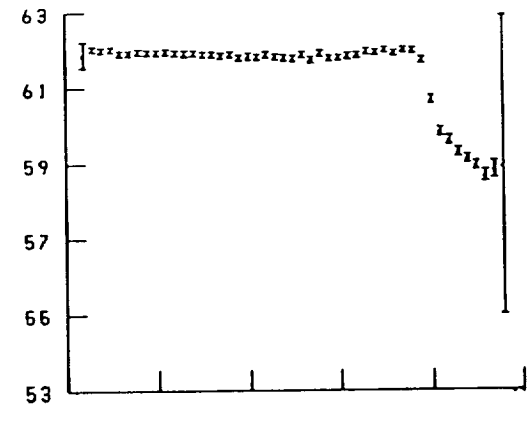
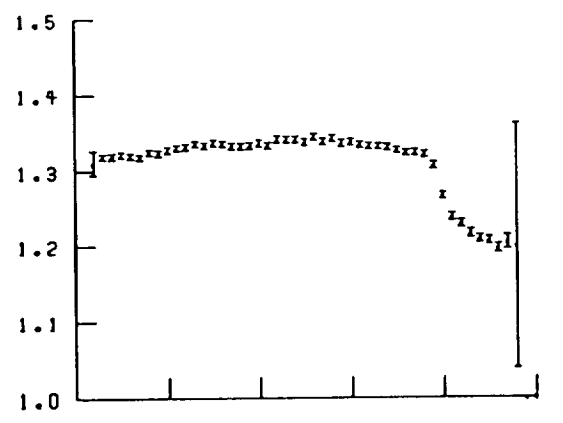
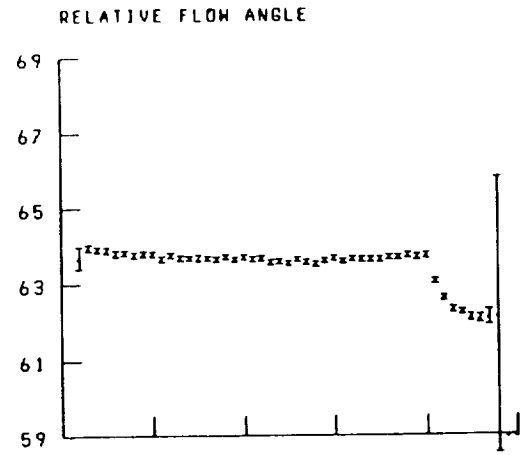
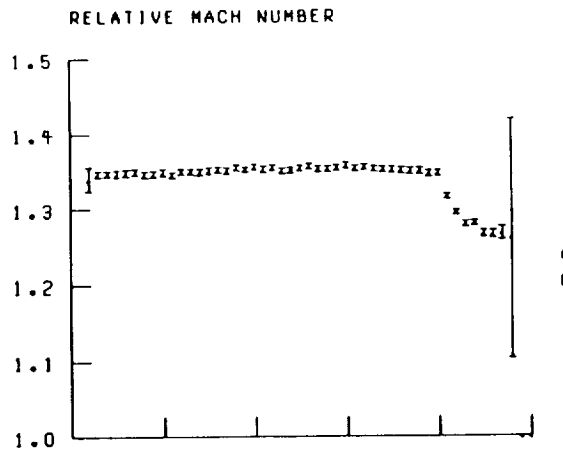


Figure 19.—Continued.

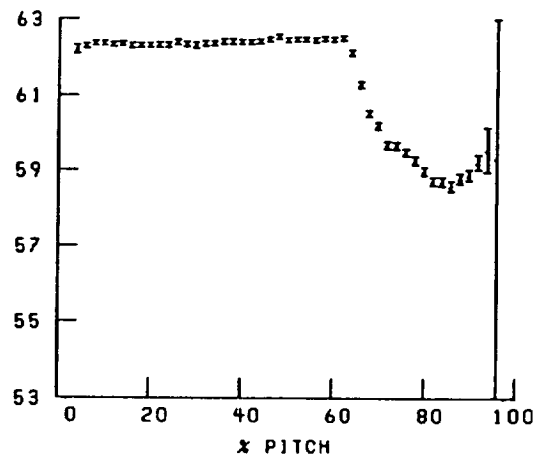
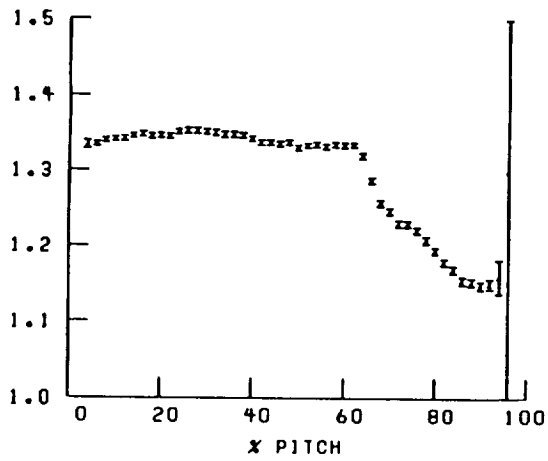
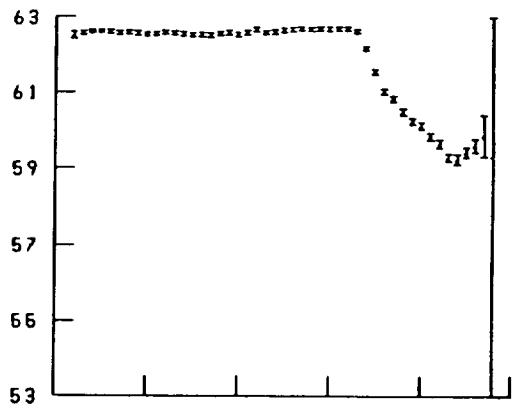
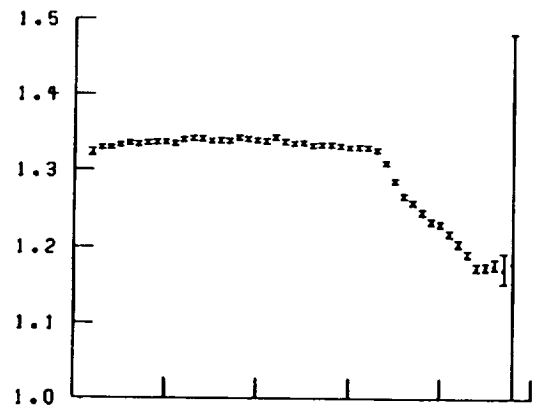
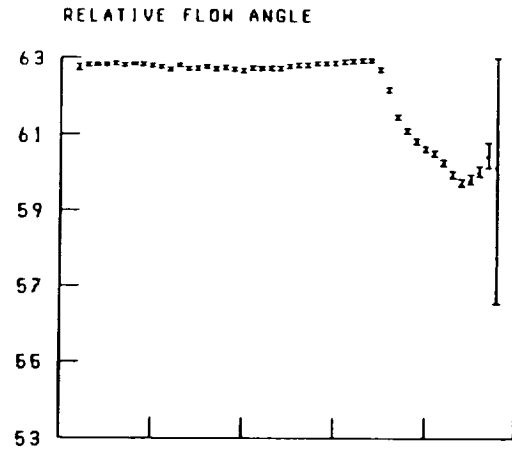
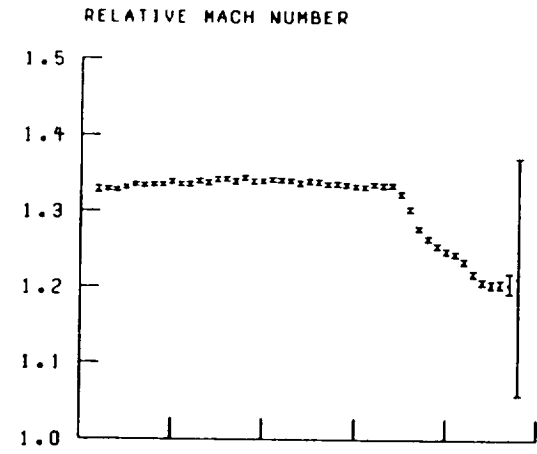


Figure 19.—Continued.

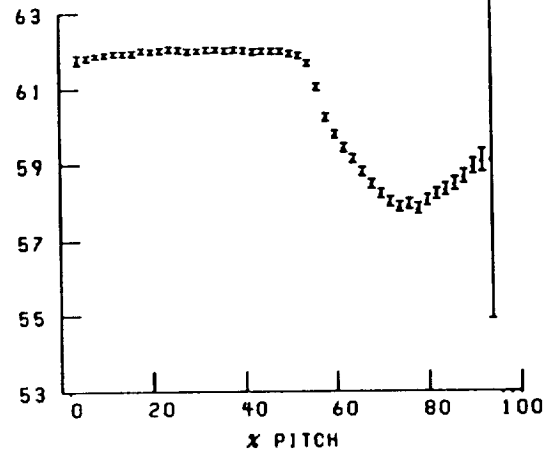
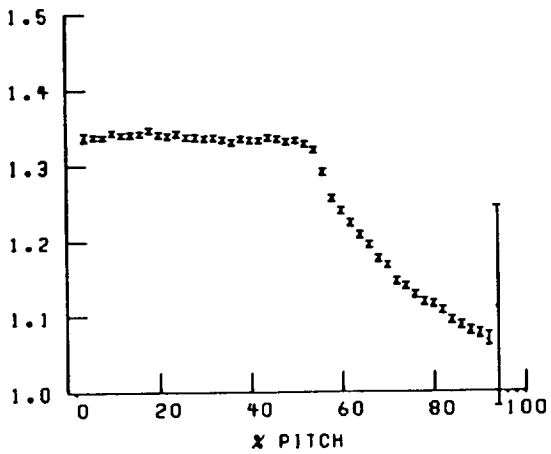
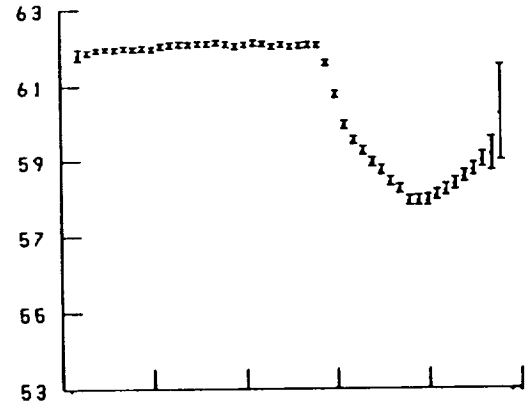
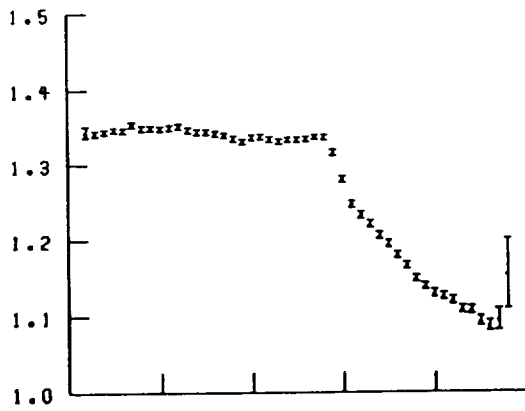
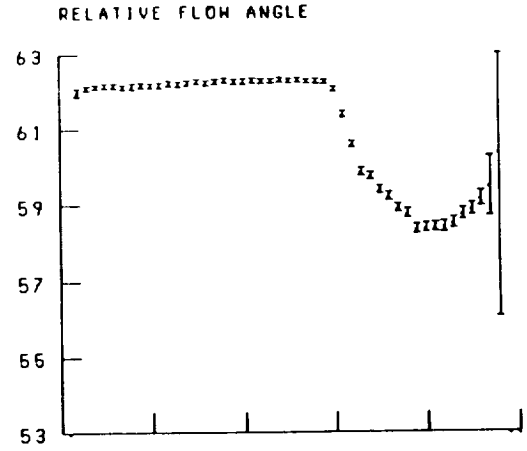
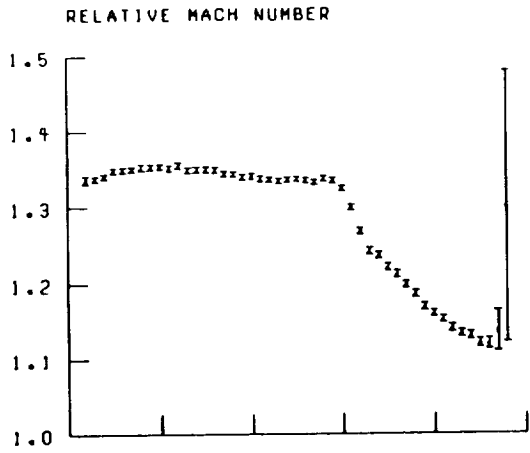


Figure 19.—Continued.

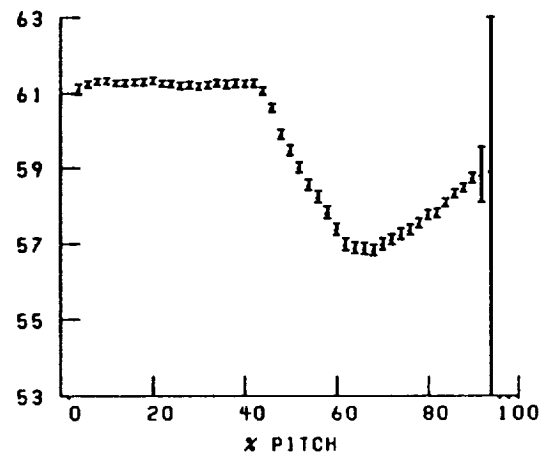
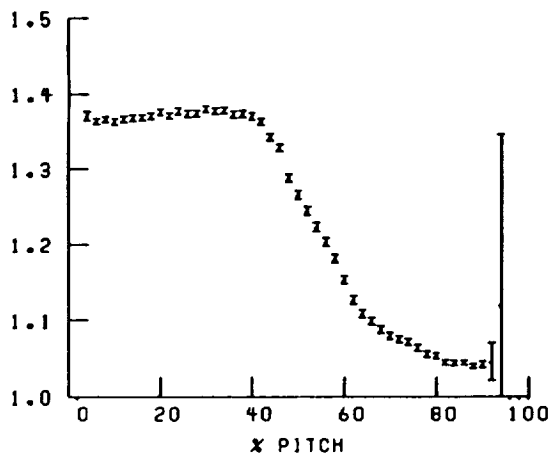
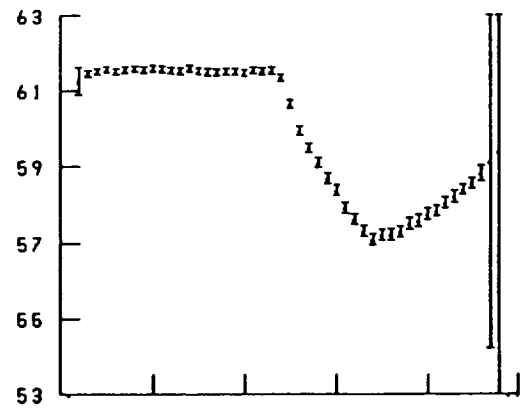
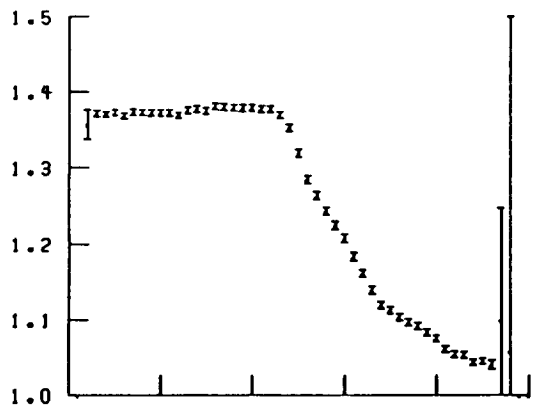
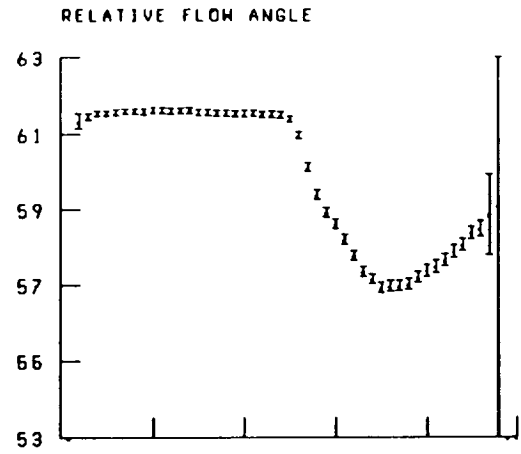
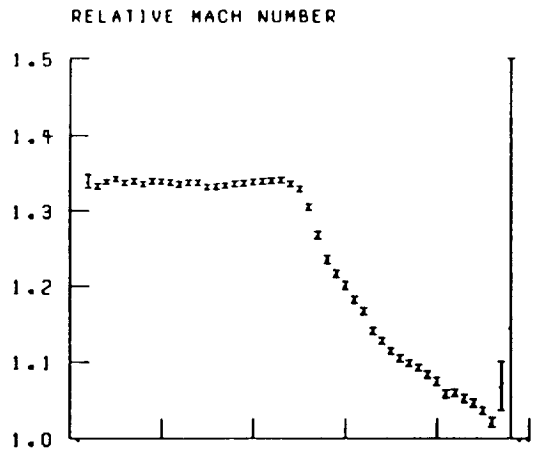


Figure 19.—Continued.

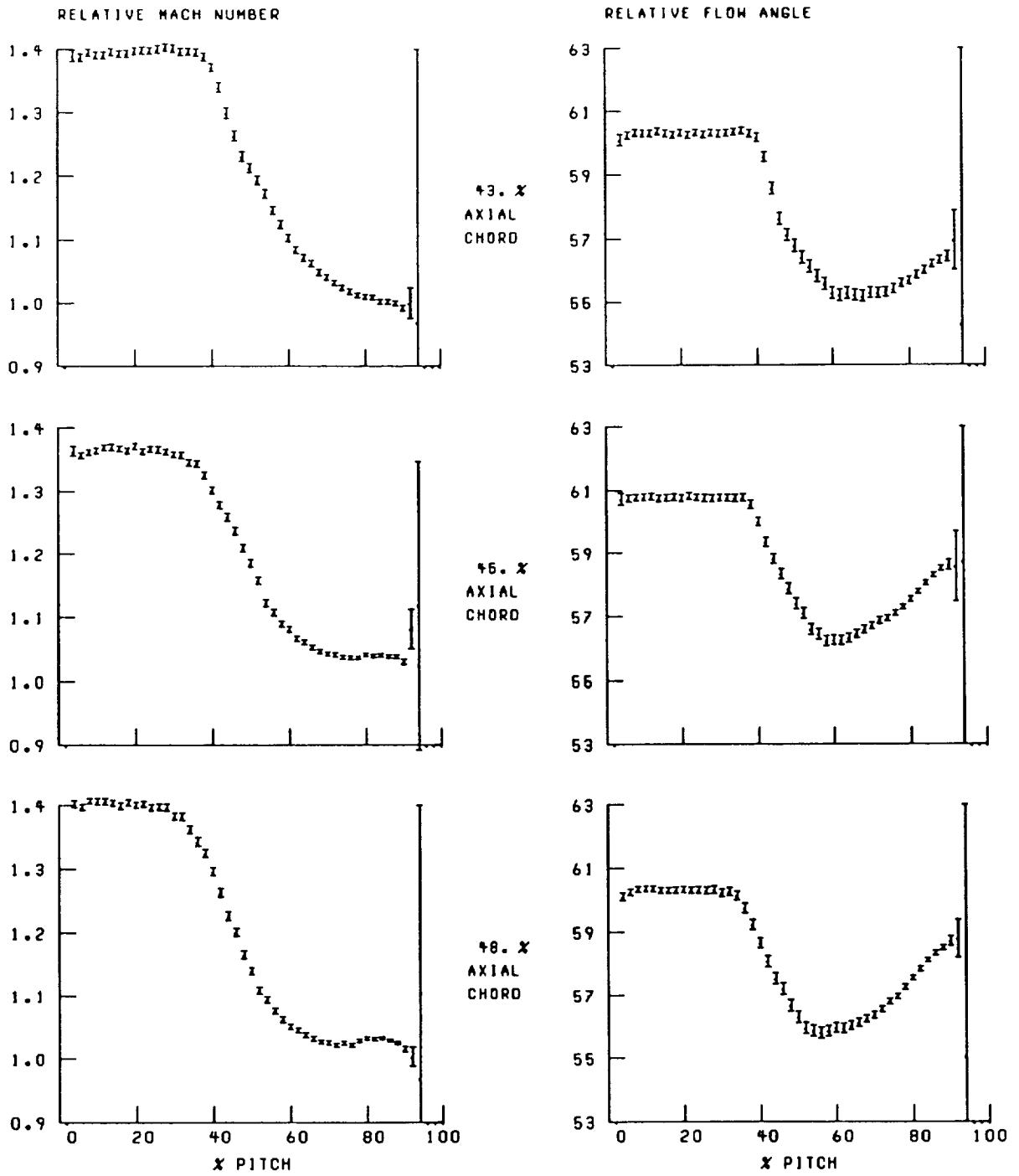


Figure 19.—Continued.

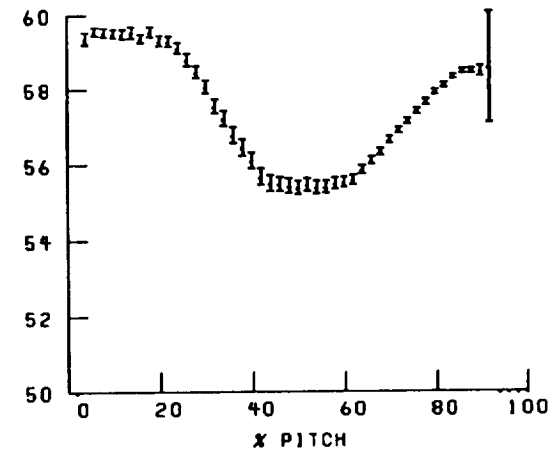
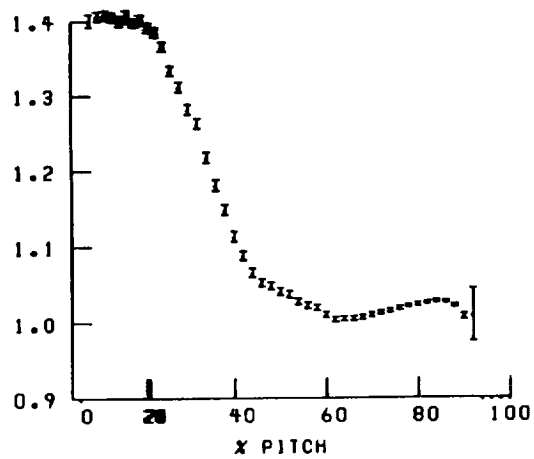
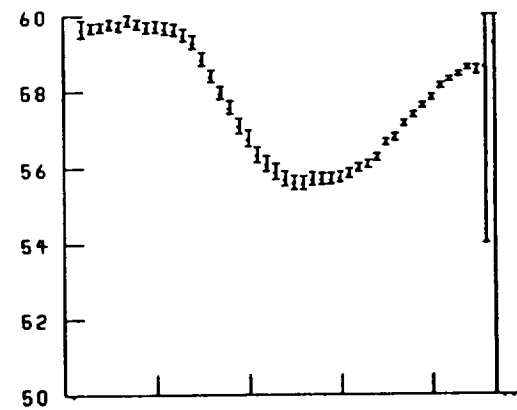
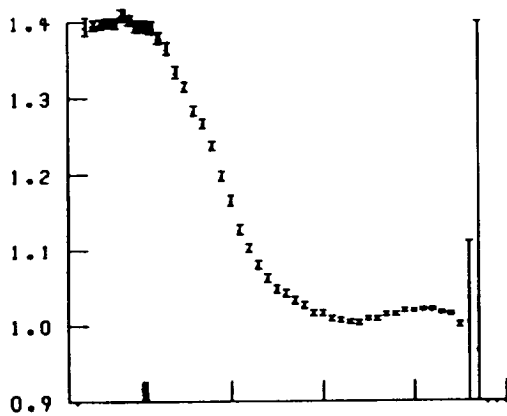
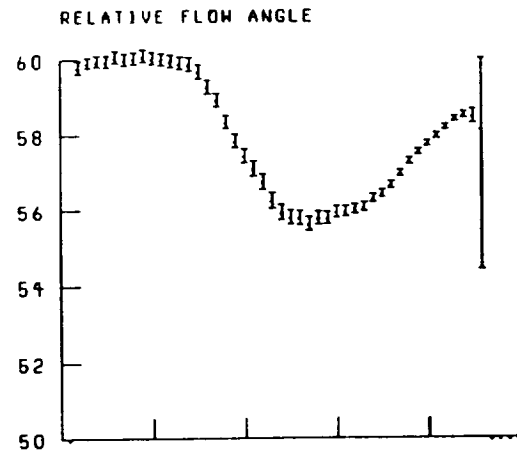
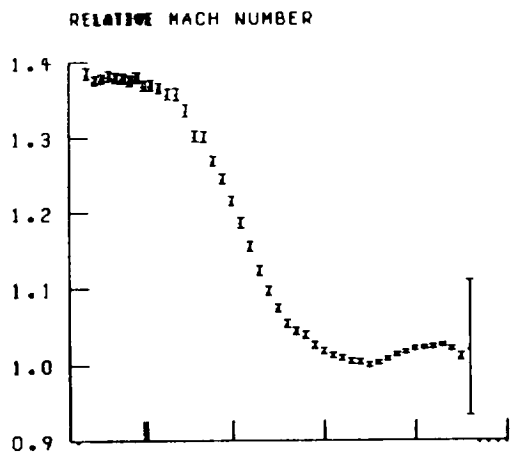


Figure 19.—Continued.

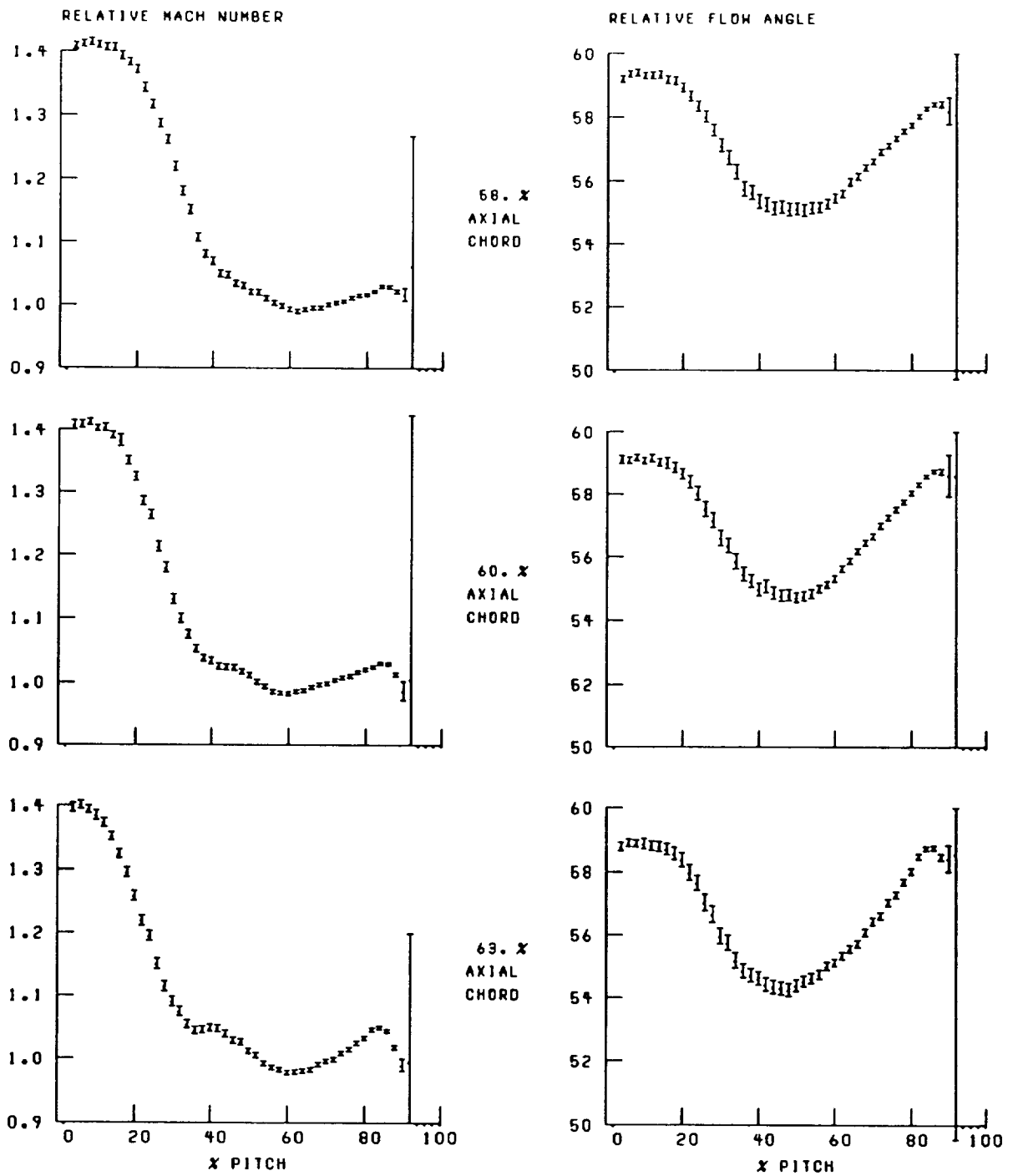


Figure 19.—Continued.

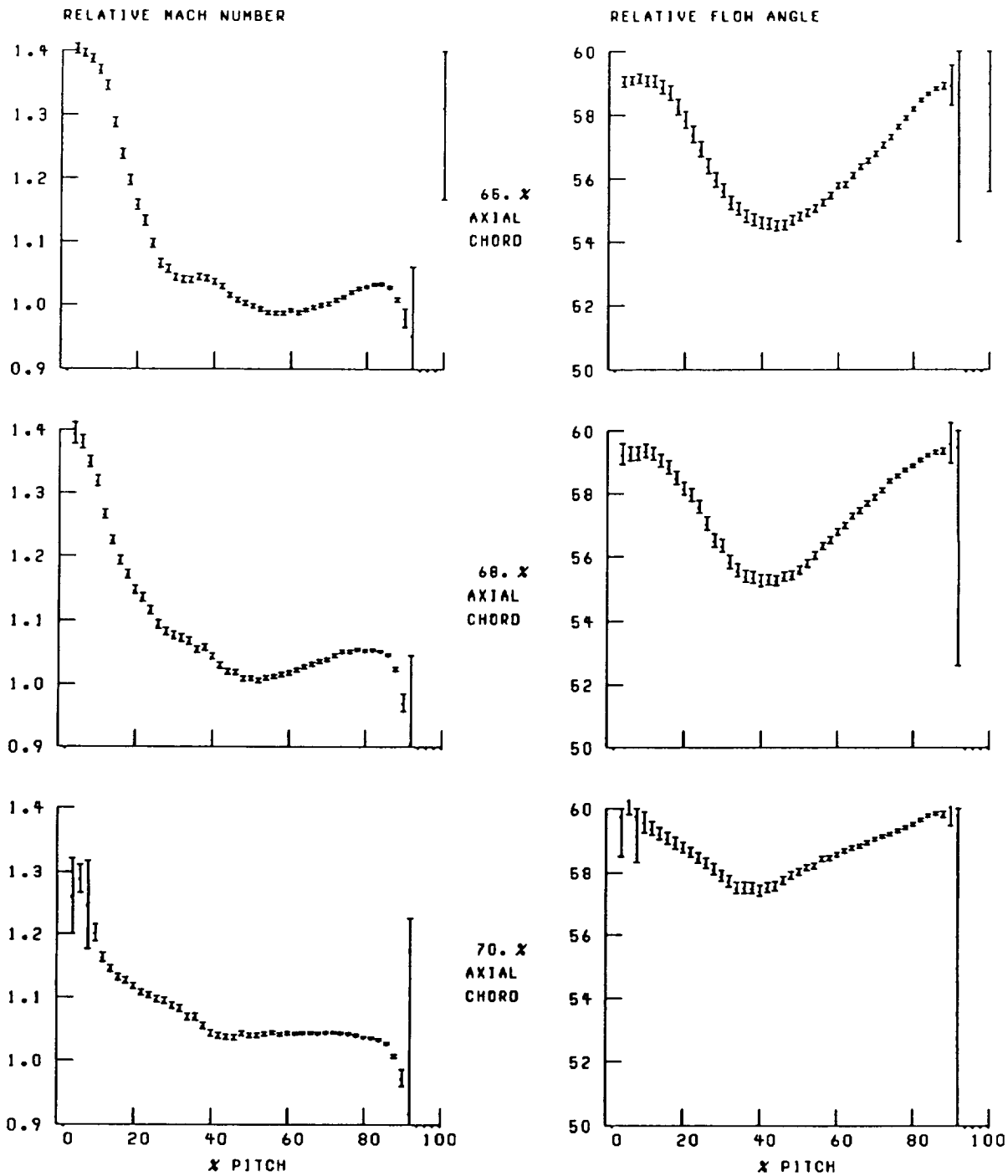


Figure 19.—Continued.

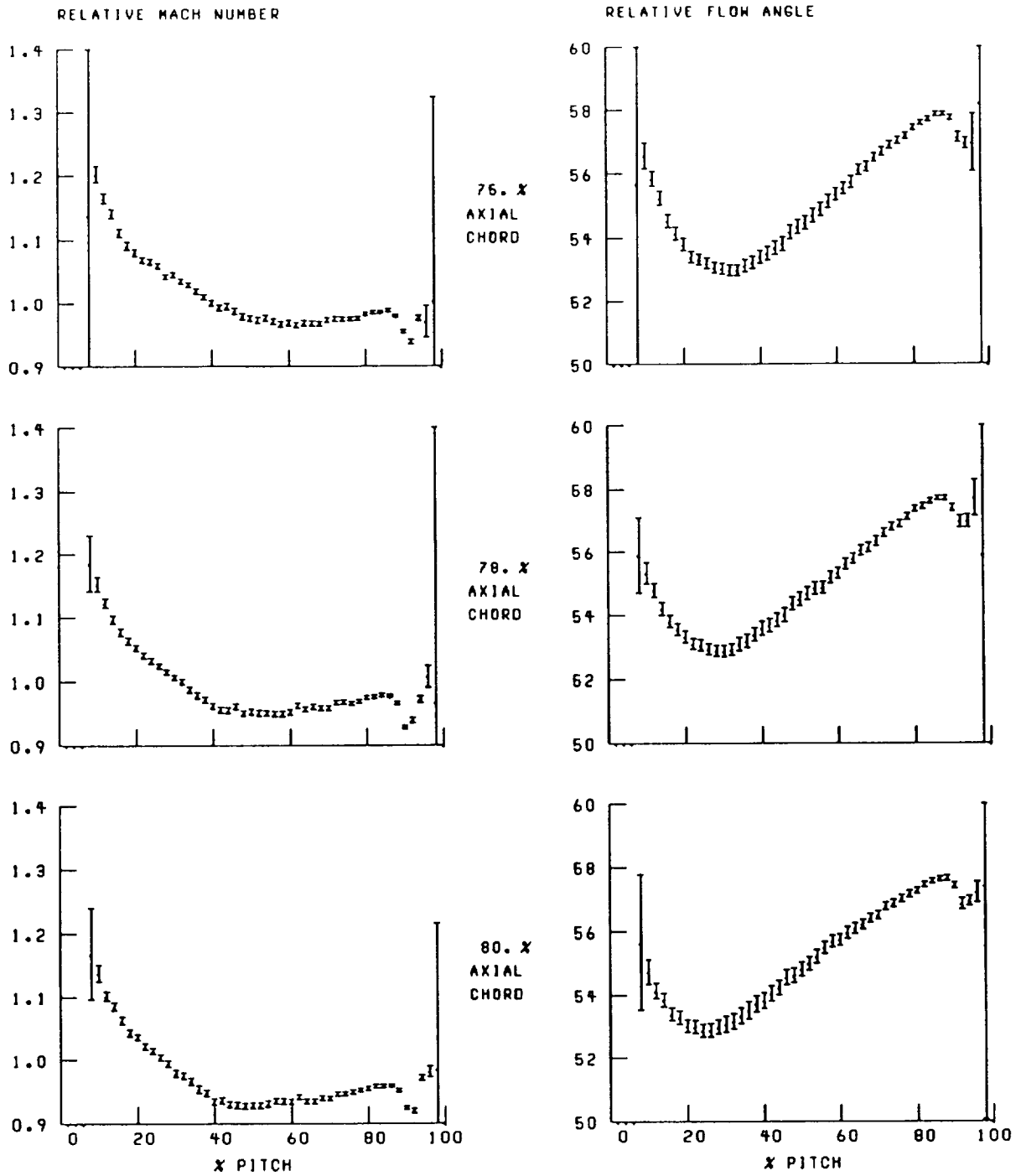


Figure 19.—Continued.

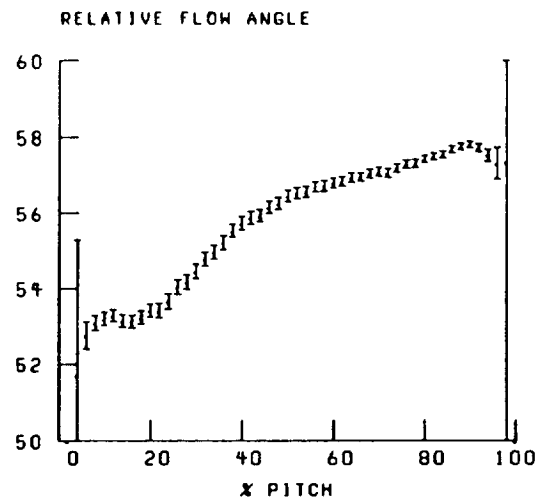
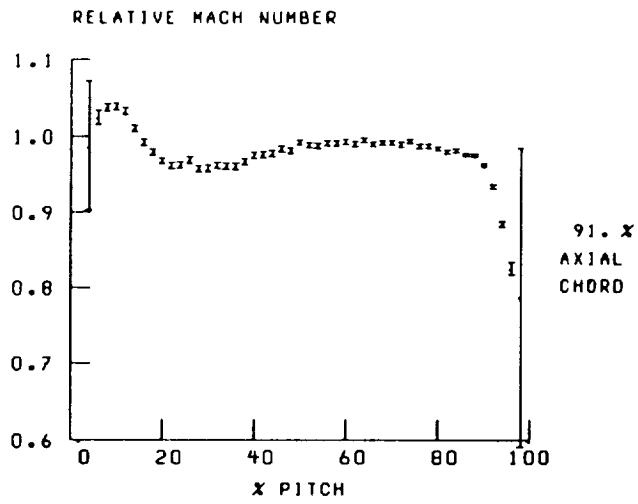


Figure 19.—Continued.

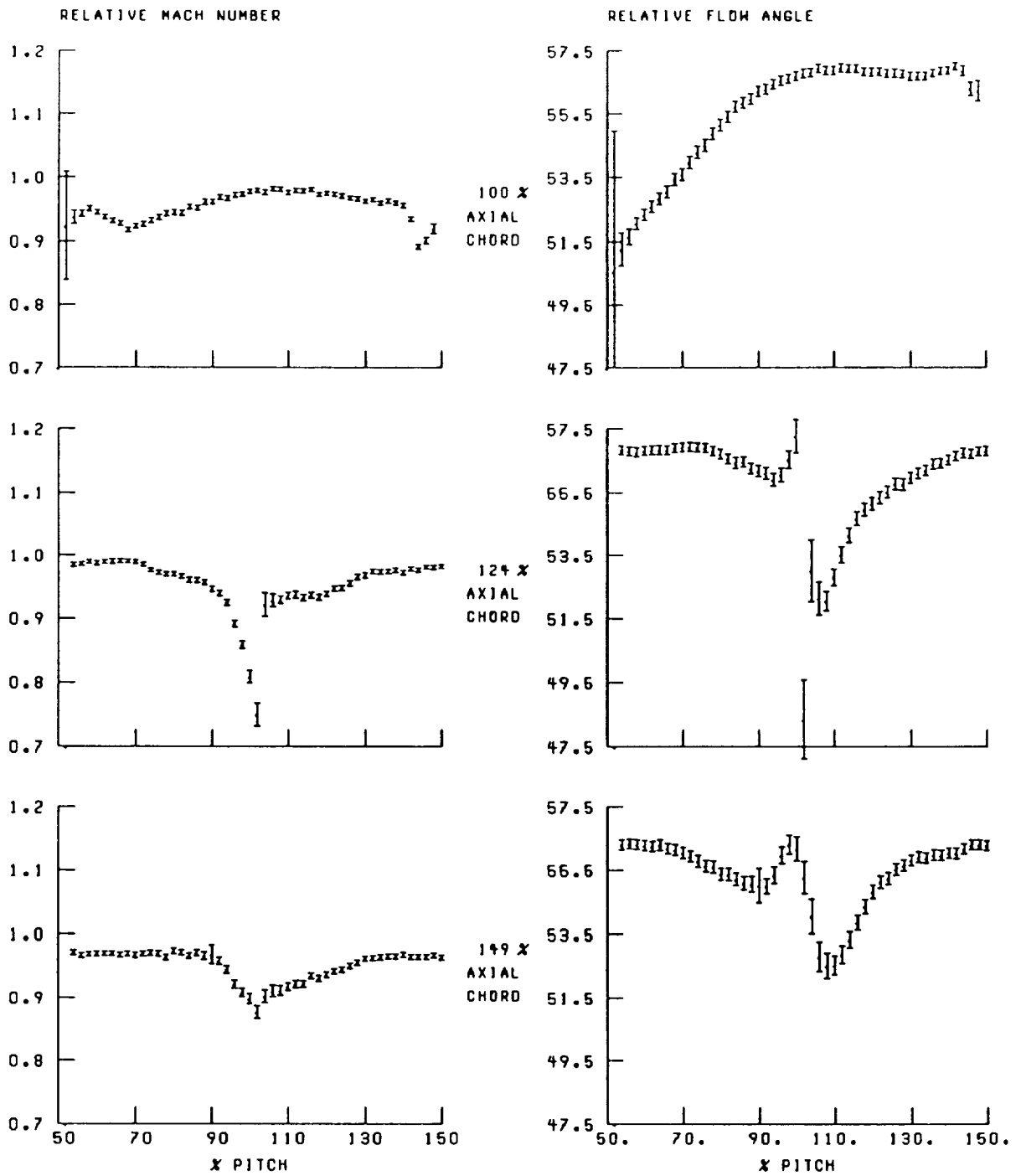


Figure 19.—Continued.

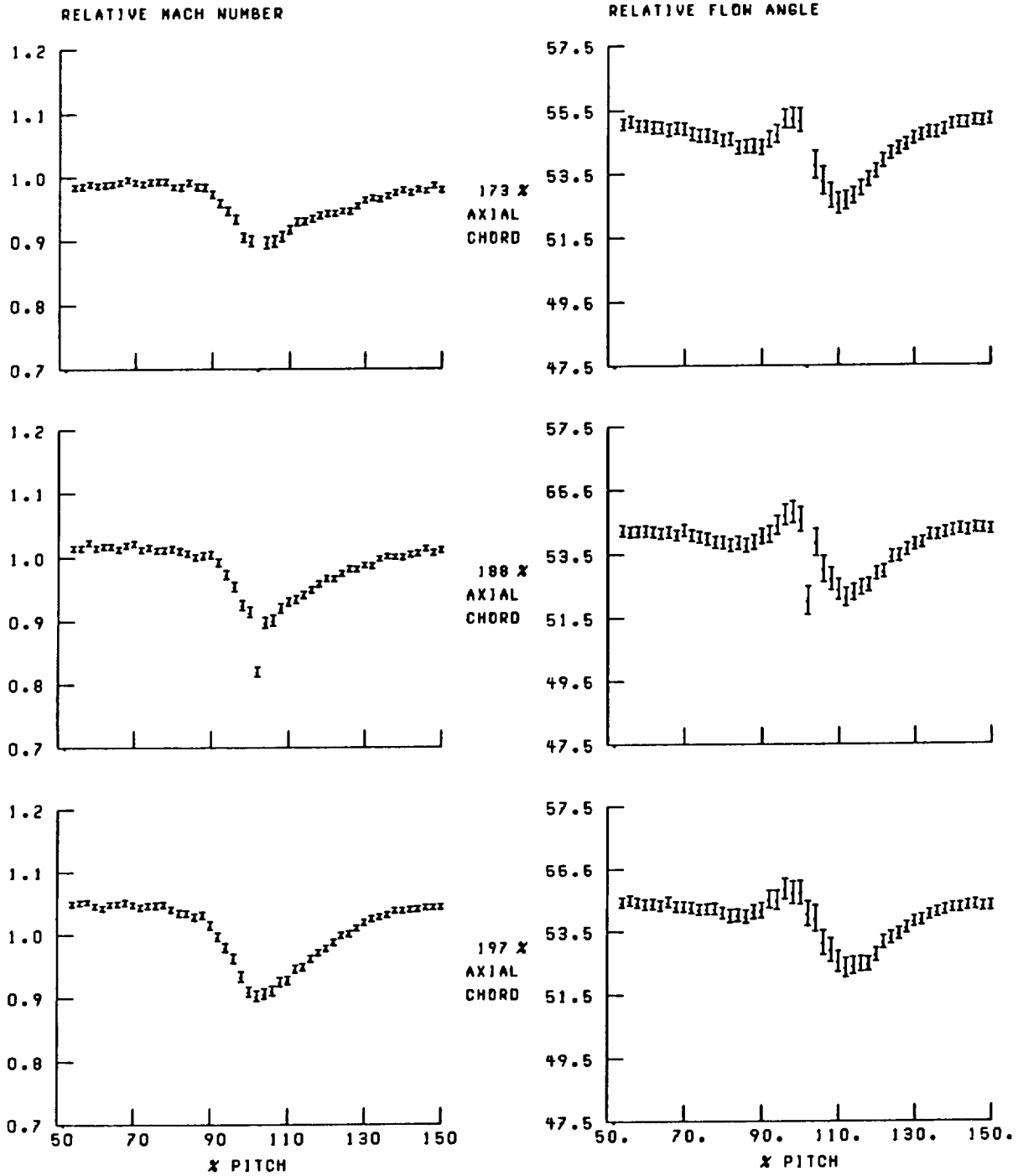


Figure 19.—Continued.

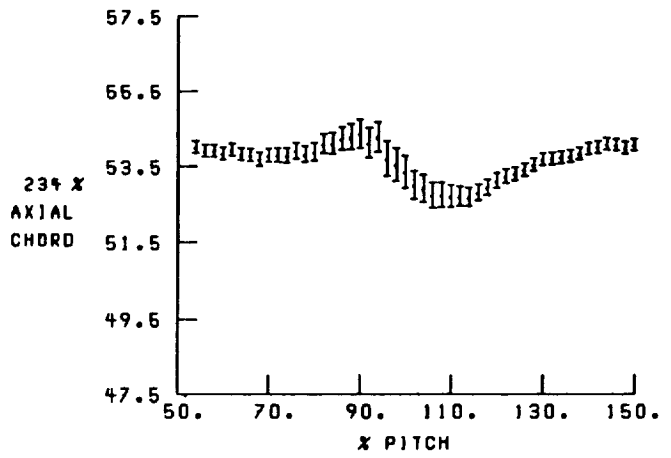
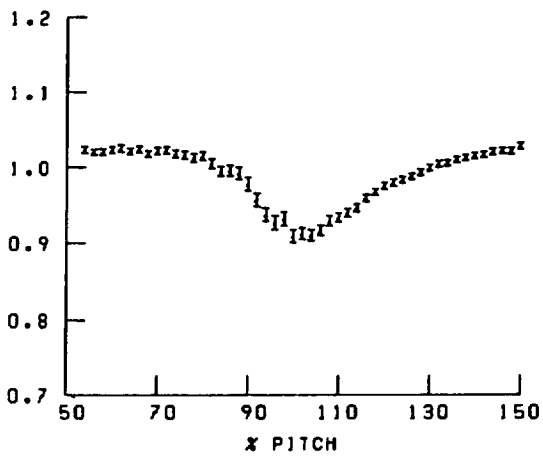
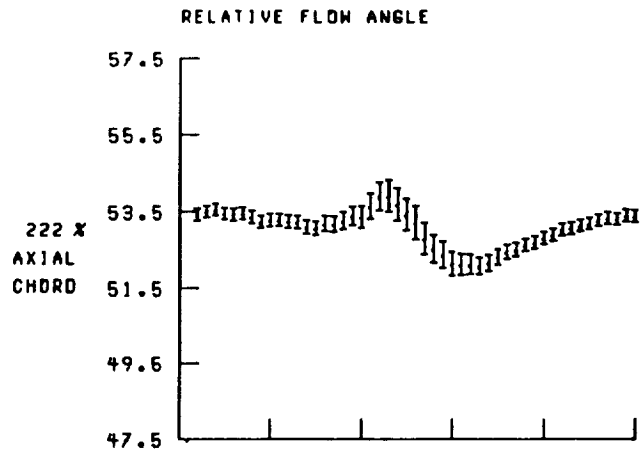
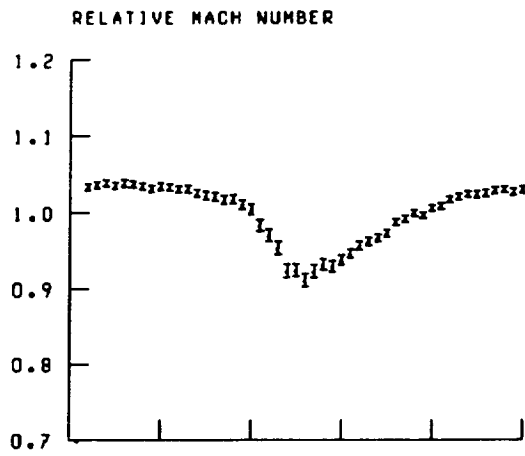


Figure 19.—Concluded.

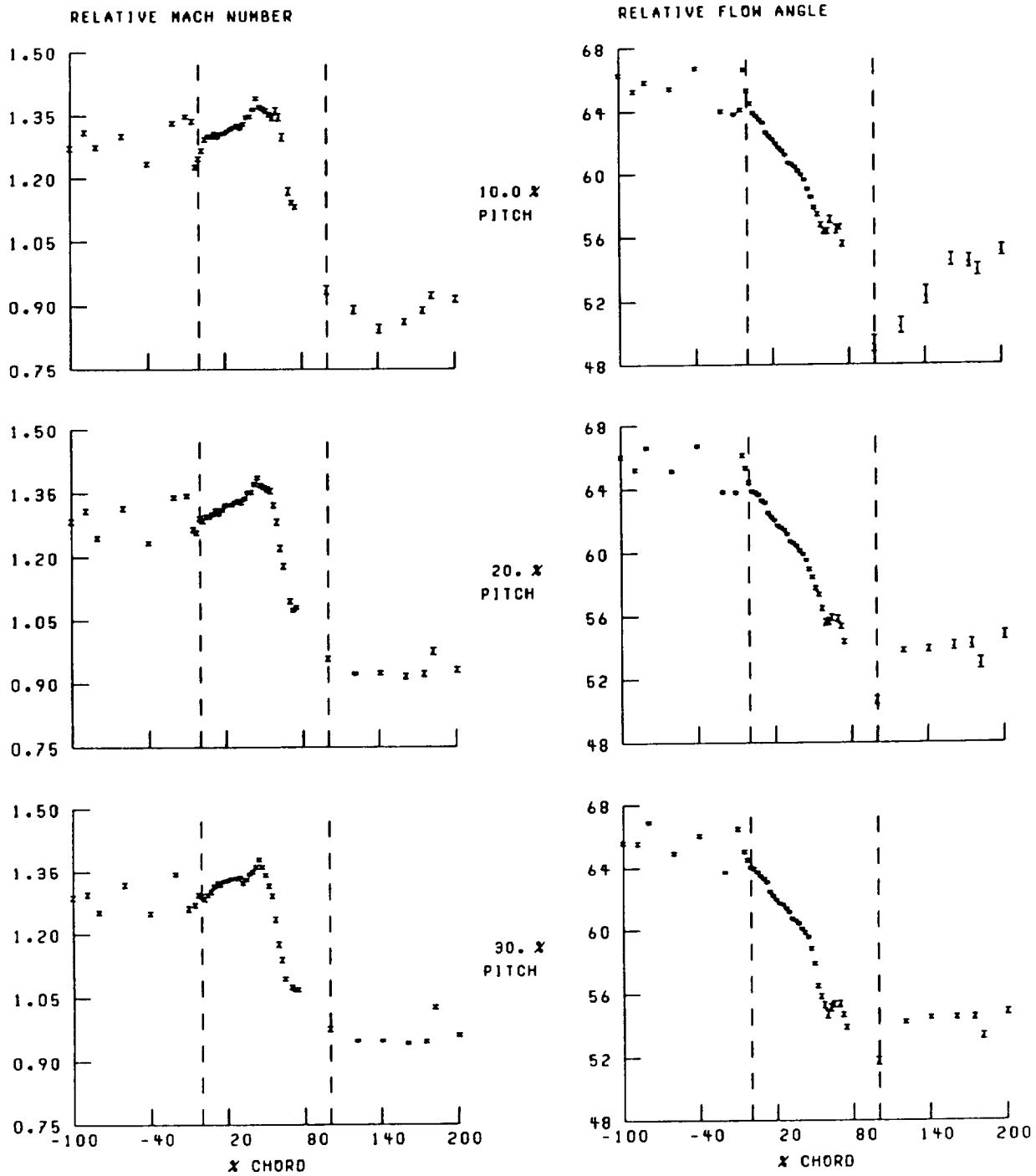


Figure 20.—Streamwise distribution of relative Mach number flow angle at 20-percent span and near peak efficiency. Broken lines denote location of blade leading and trailing edges.

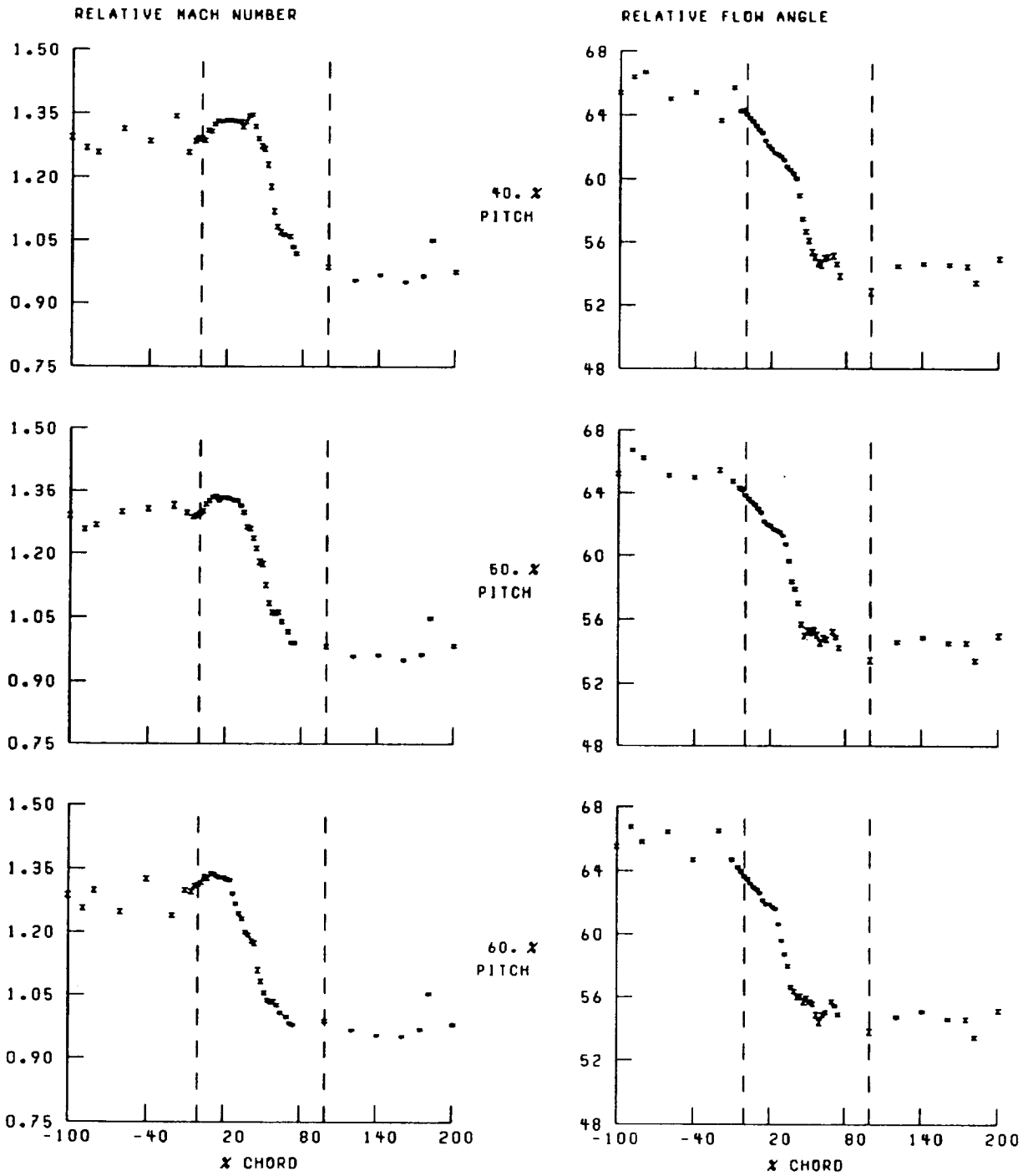


Figure 20.—Continued.

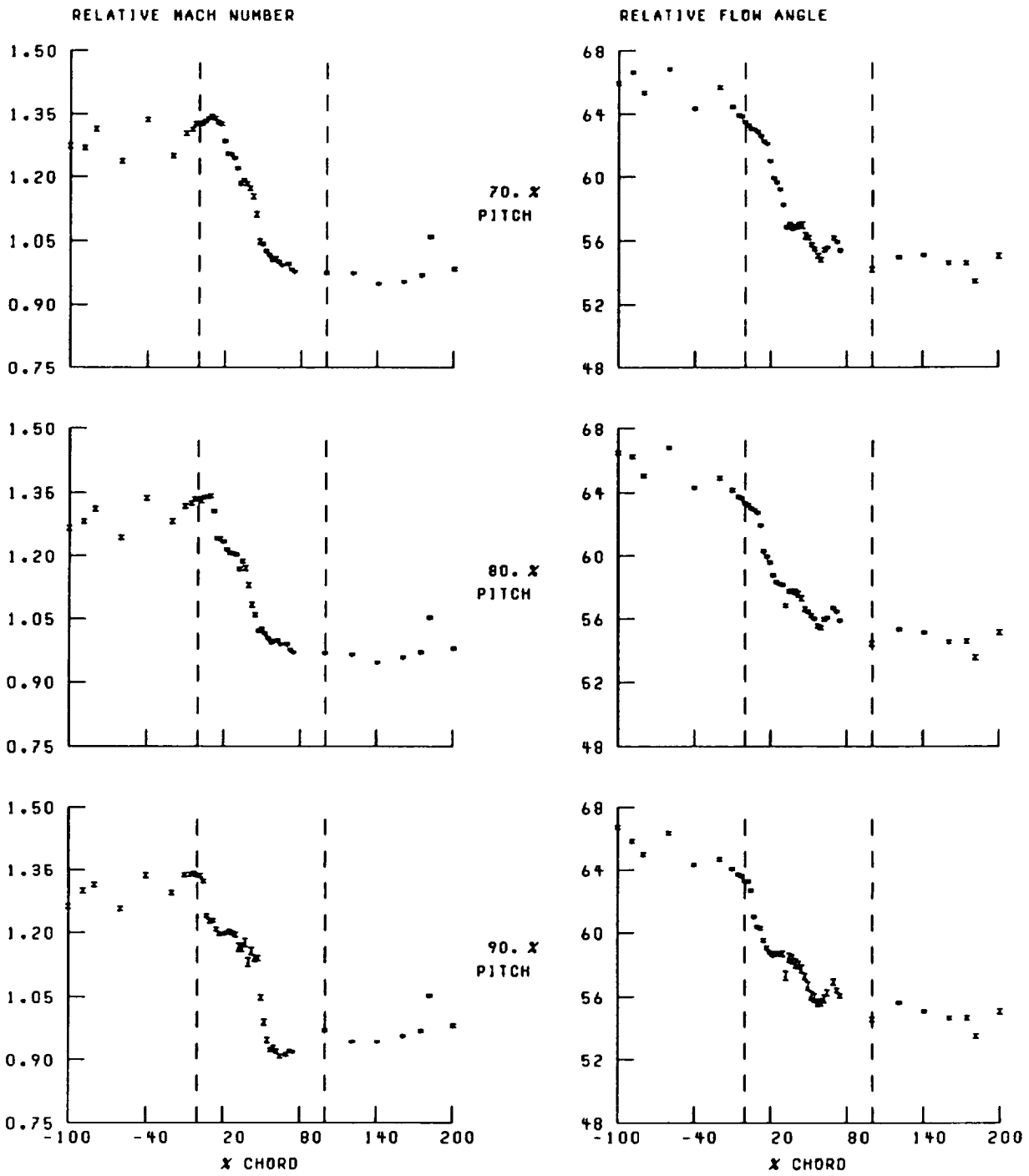


Figure 20.—Concluded.

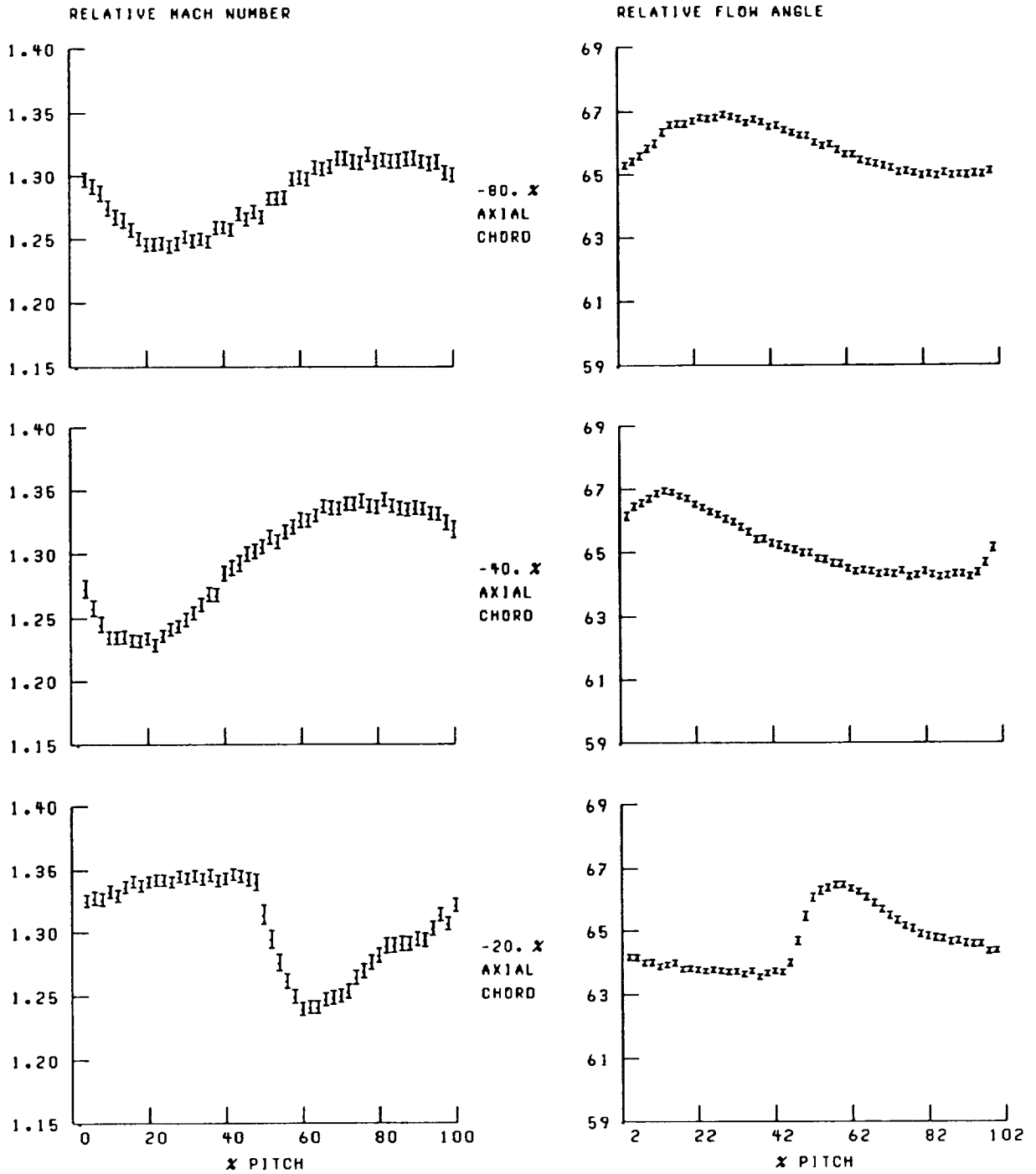


Figure 21.—Blade-to-blade distribution of relative Mach number and flow angle at 20-percent span and near peak efficiency.

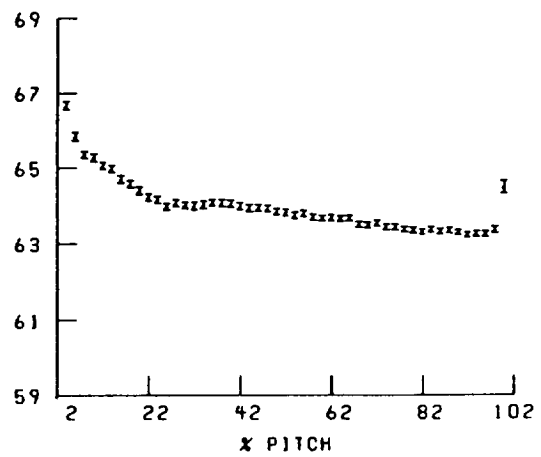
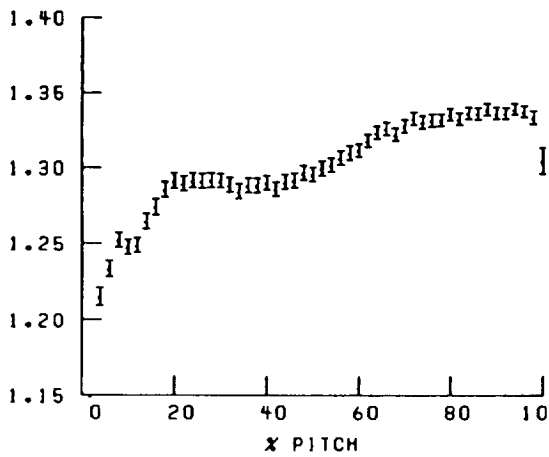
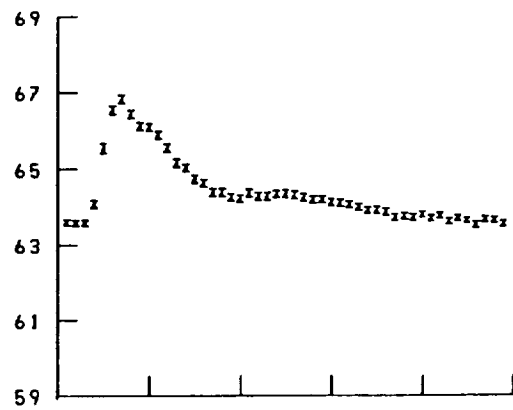
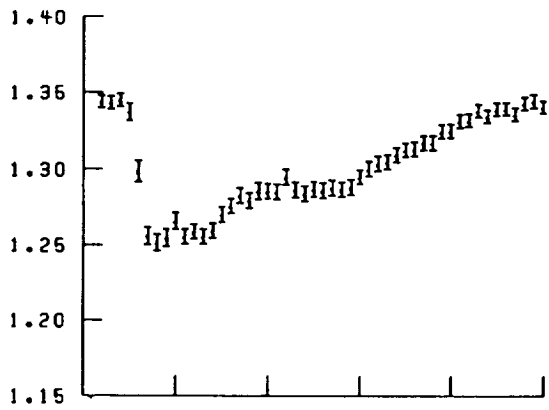
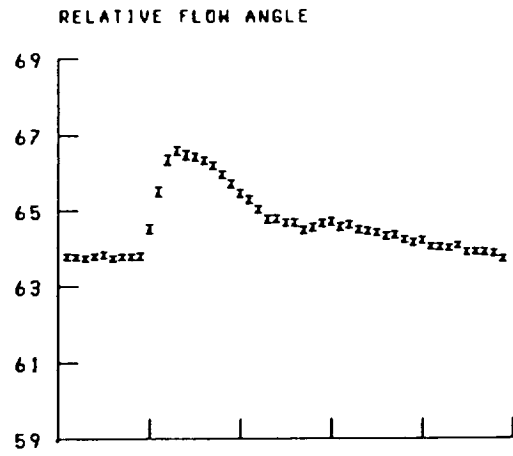
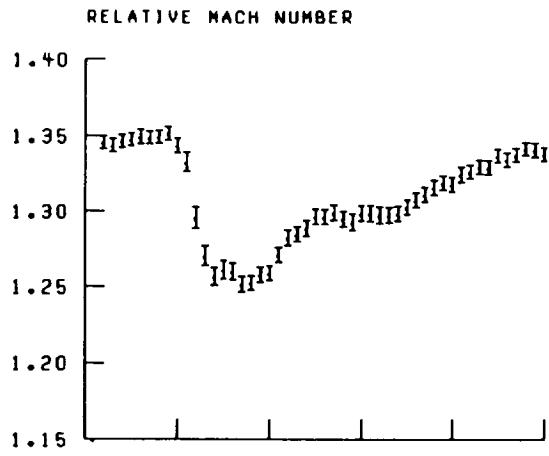


Figure 21.—Continued.

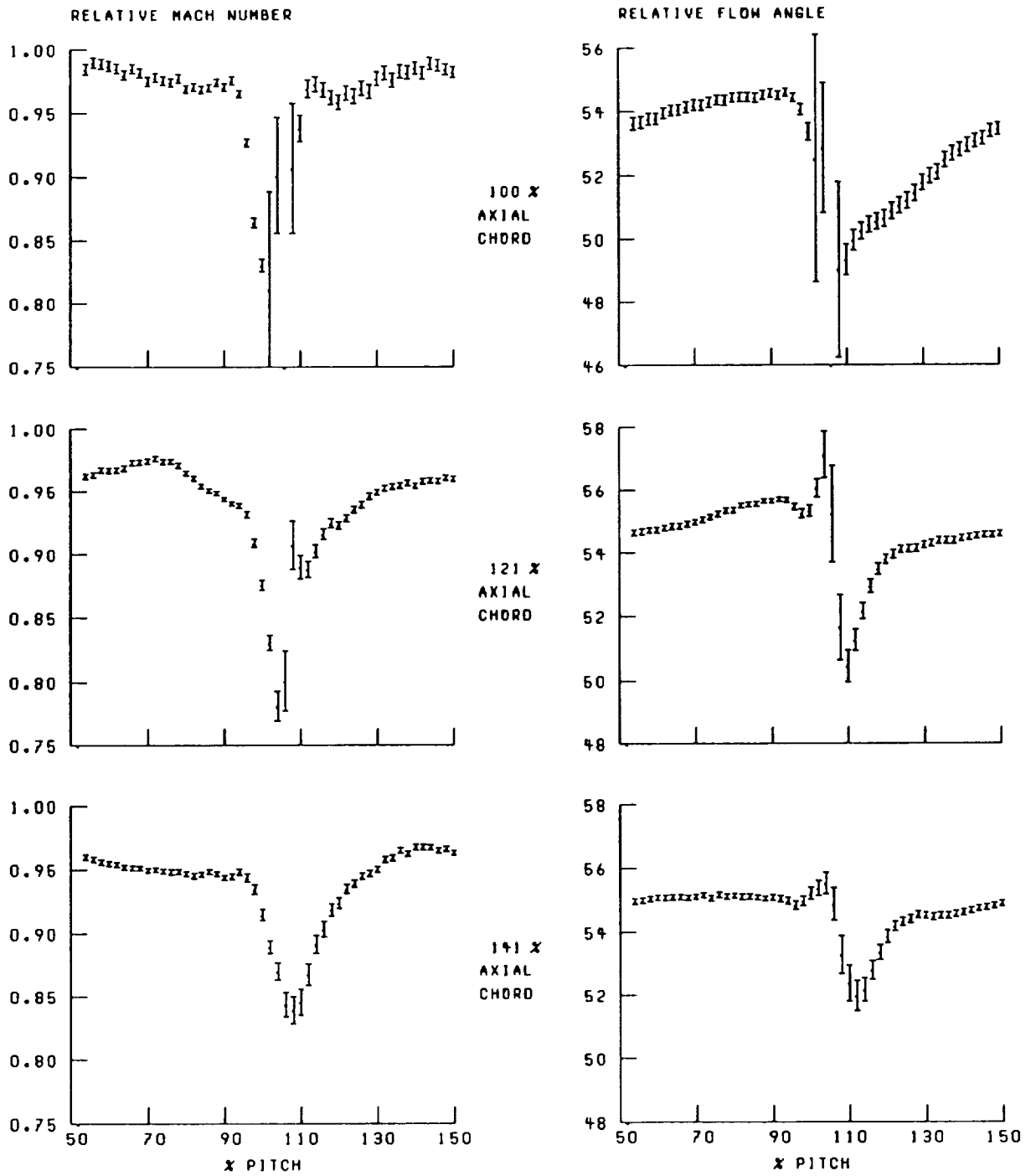


Figure 21.—Continued.

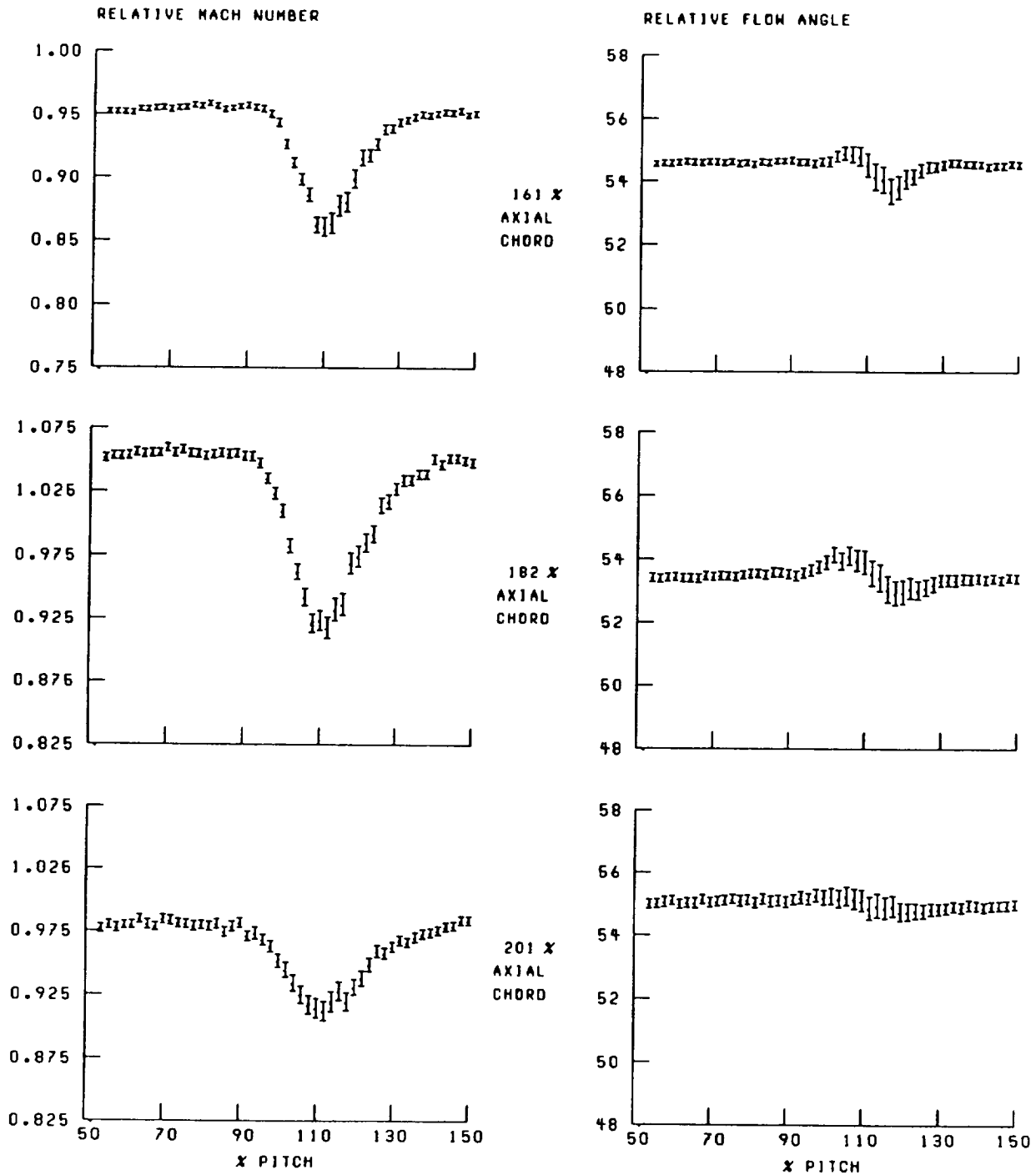


Figure 21.—Concluded.

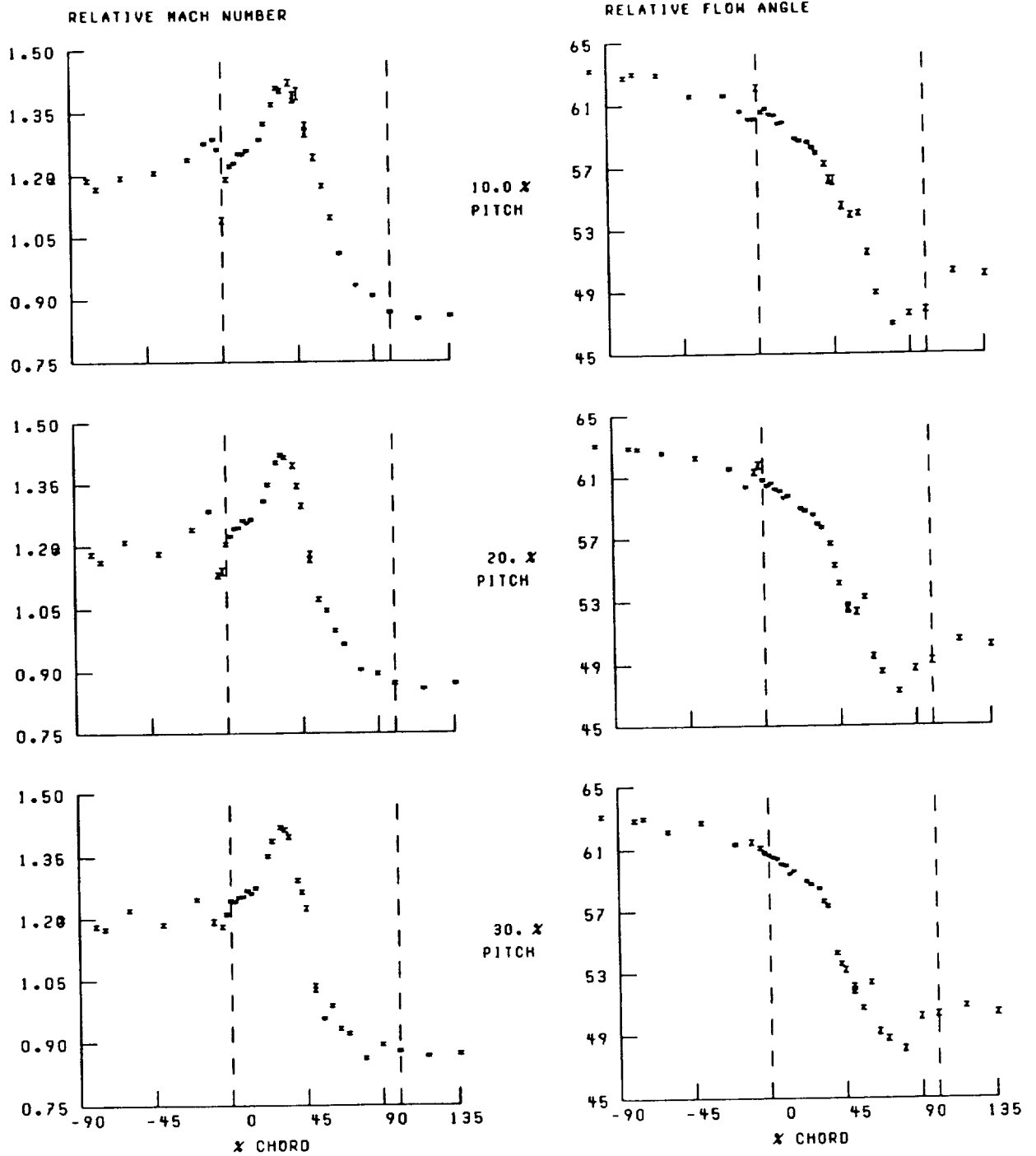


Figure 22.—Streamwise distribution of relative Mach number and flow angle at 30-percent span and near peak efficiency. Broken lines denote location of blade leading and trailing edges.

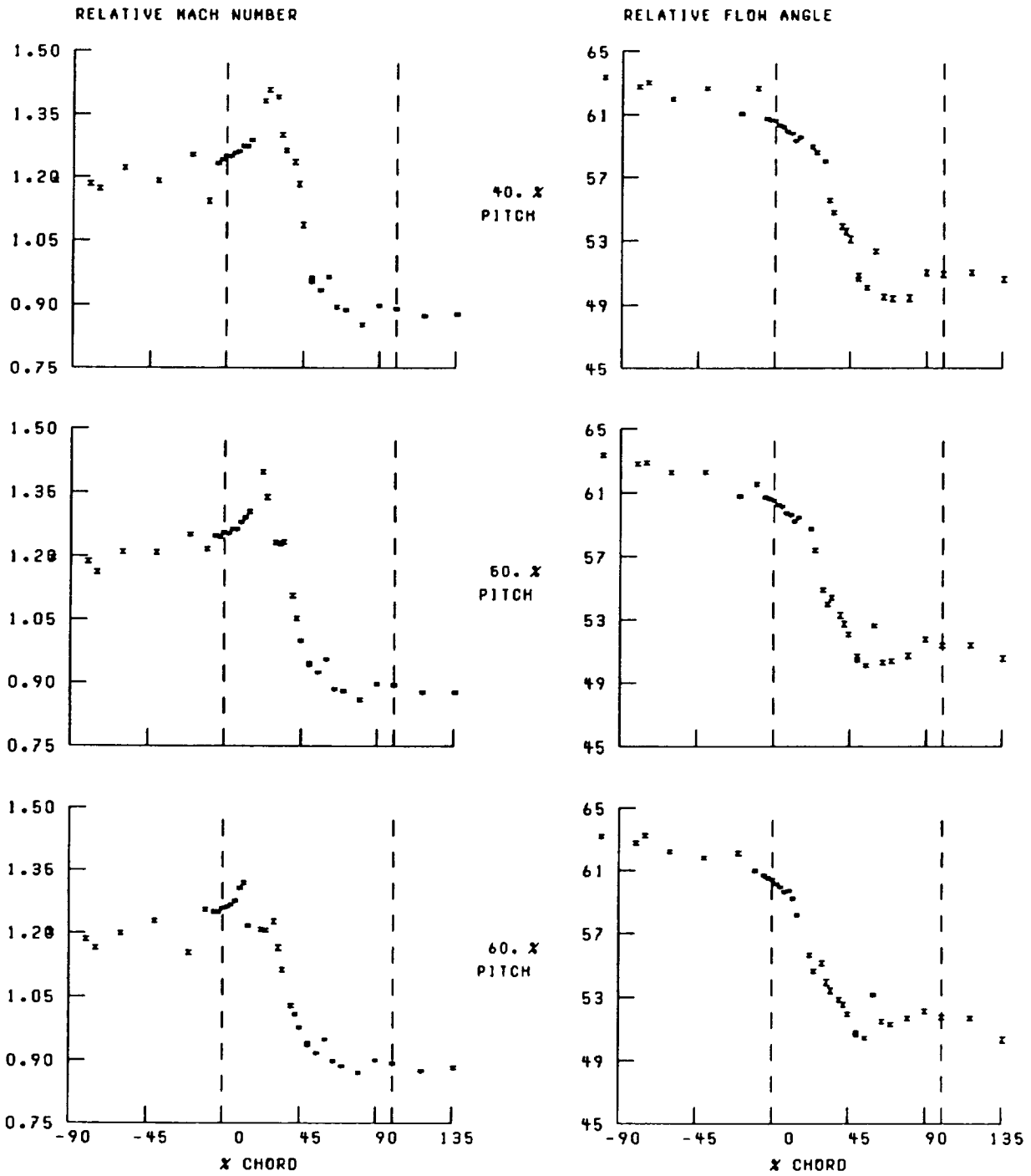


Figure 22.—Continued.

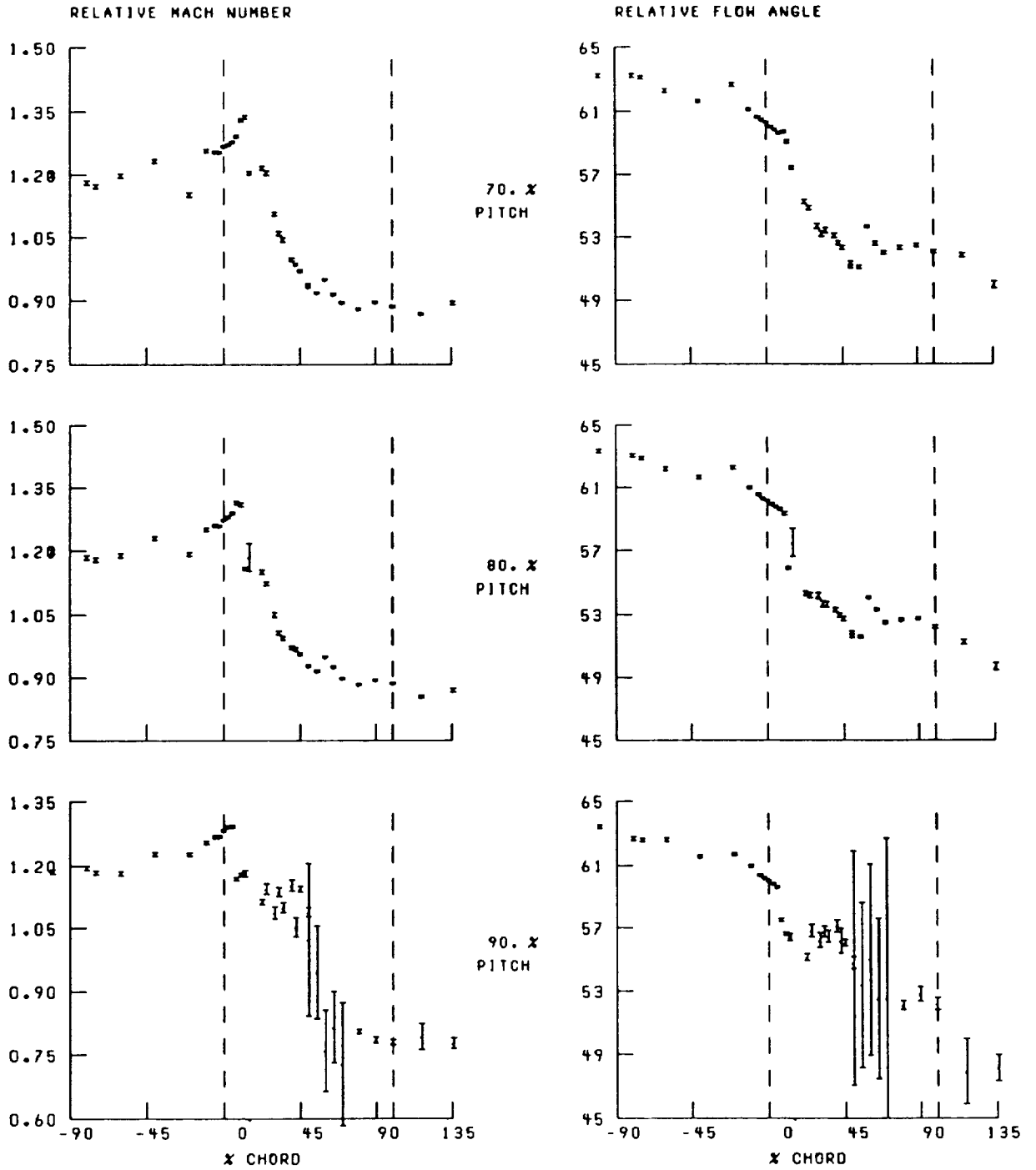


Figure 22.—Concluded.

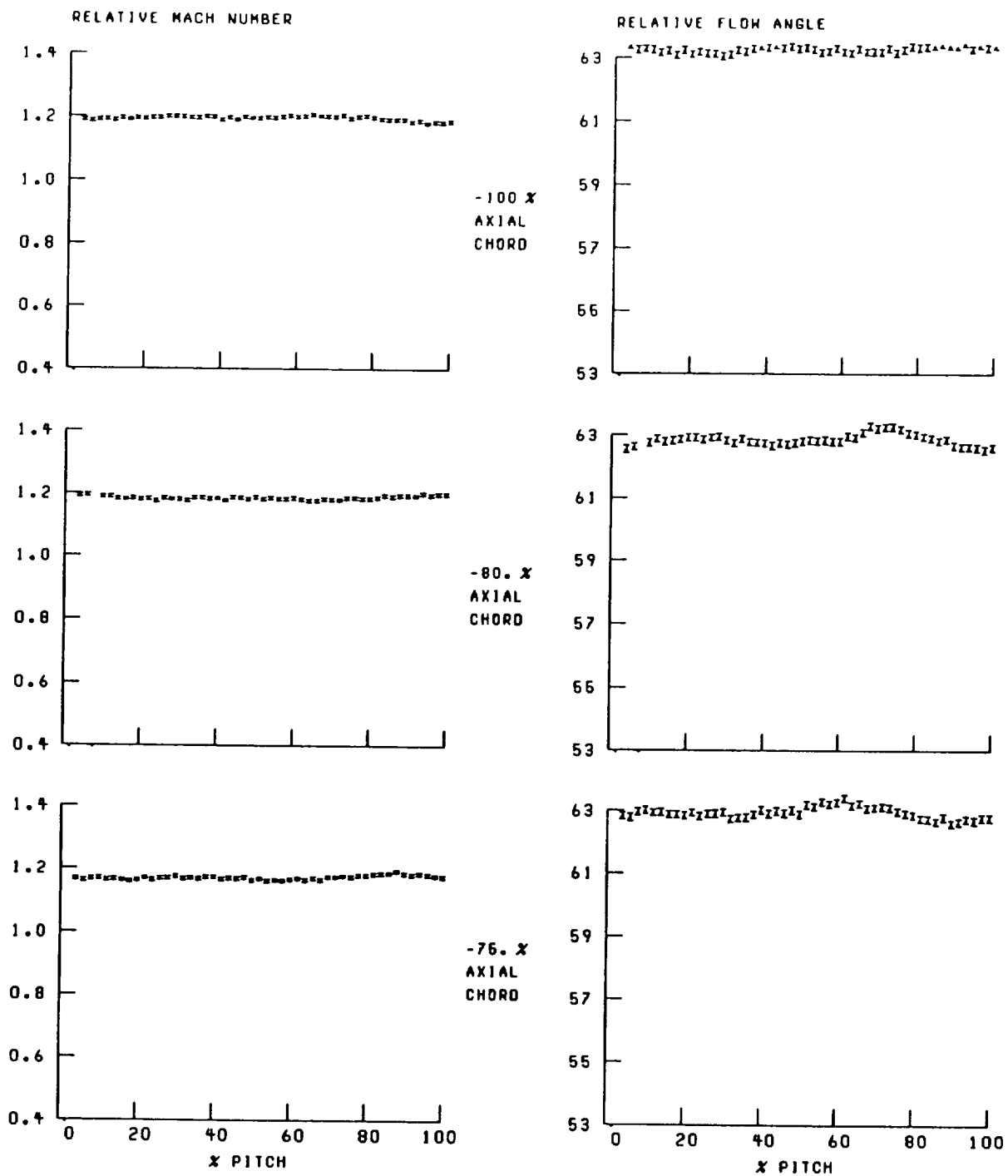


Figure 23.—Blade-to-blade distribution of relative Mach number and flow angle at 30-percent span and near peak efficiency.

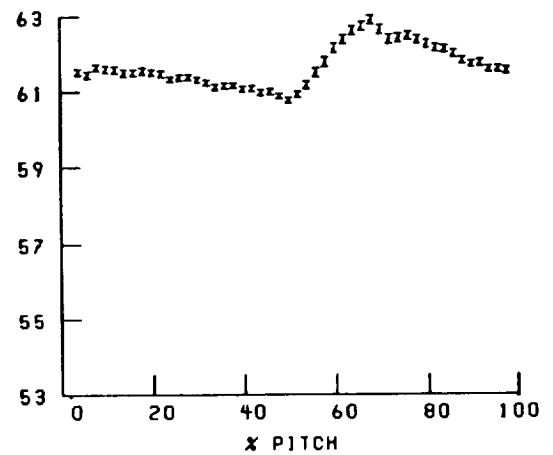
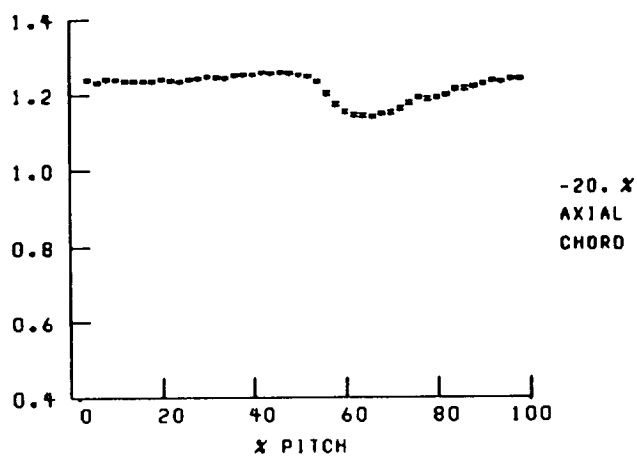
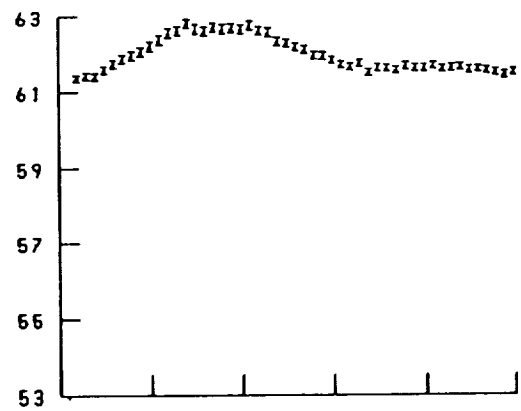
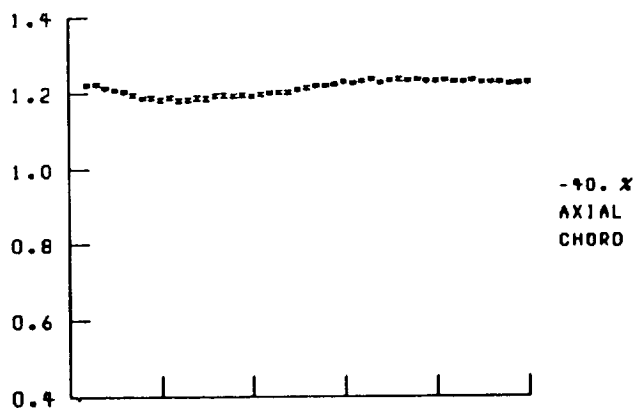
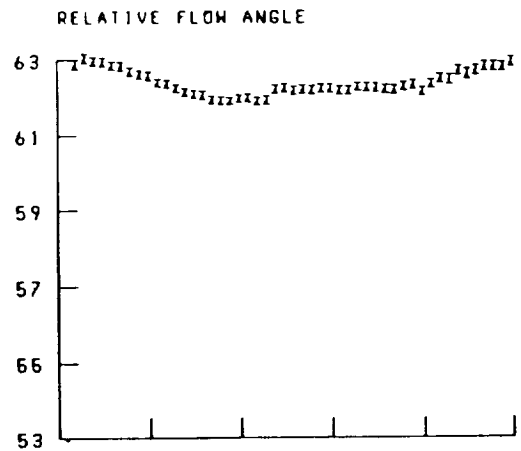
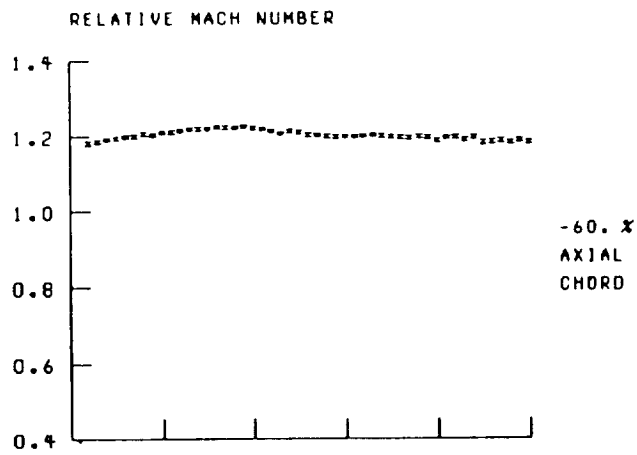


Figure 23.—Continued.

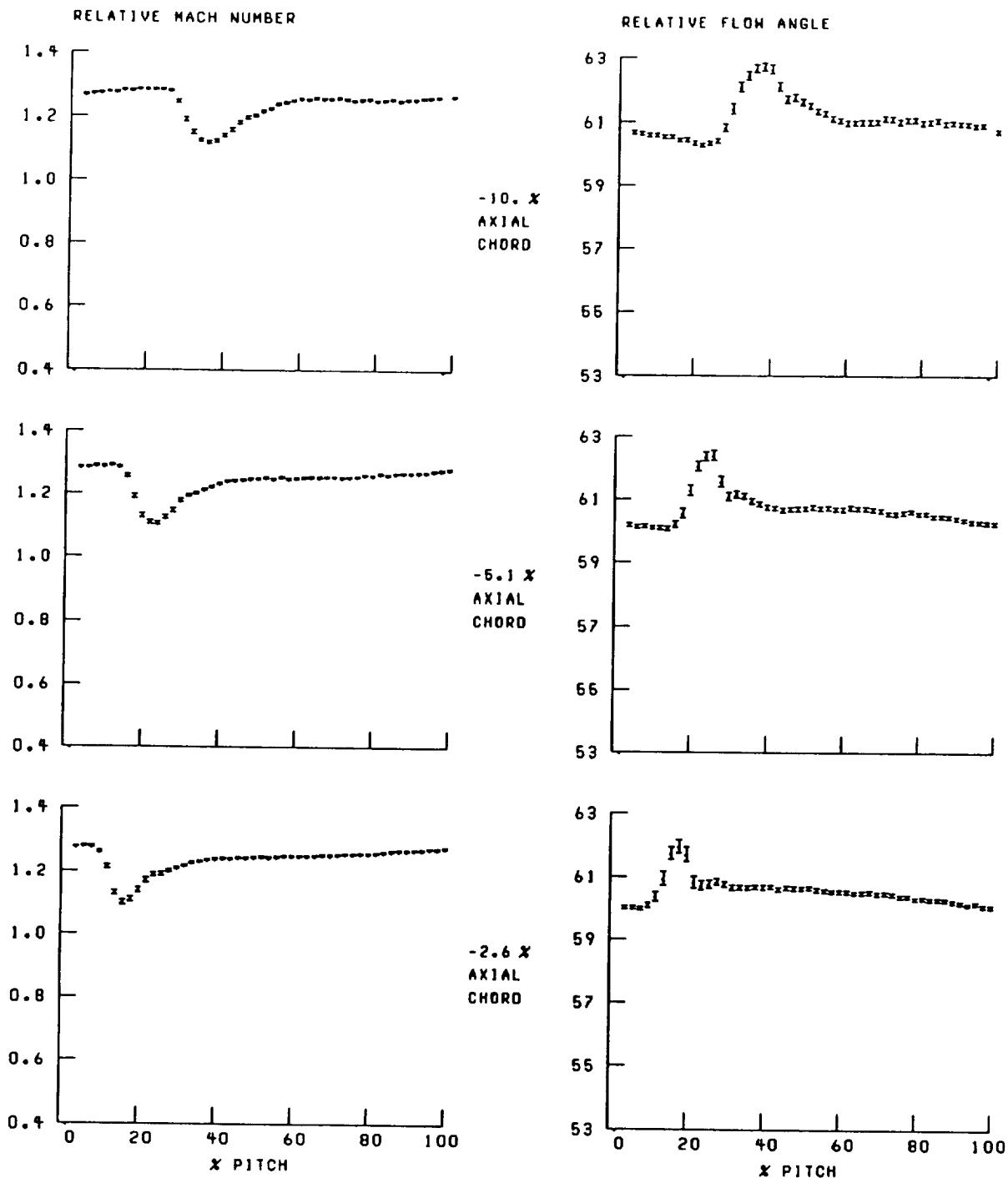


Figure 23.—Continued.

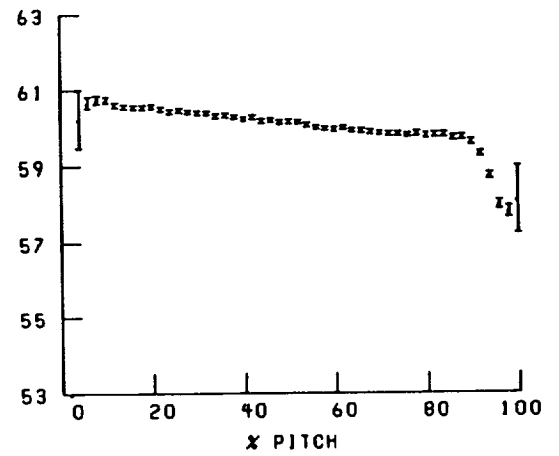
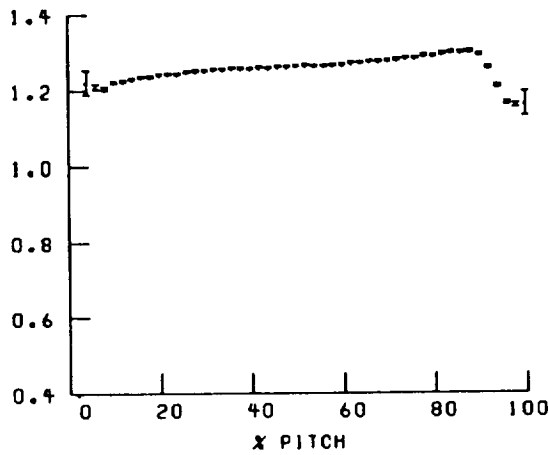
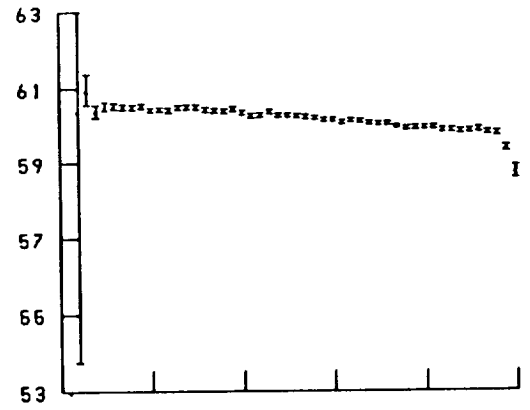
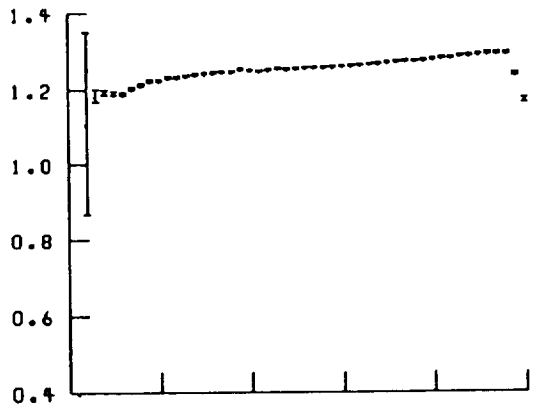
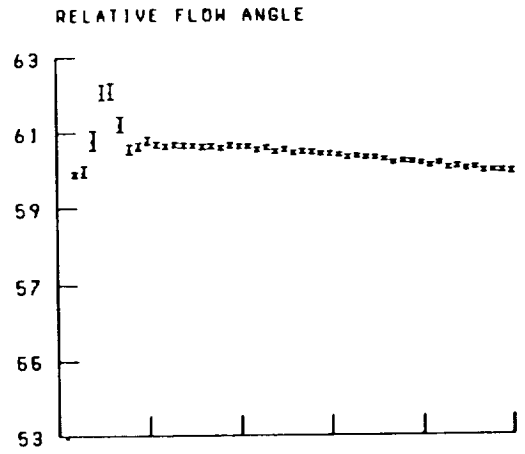
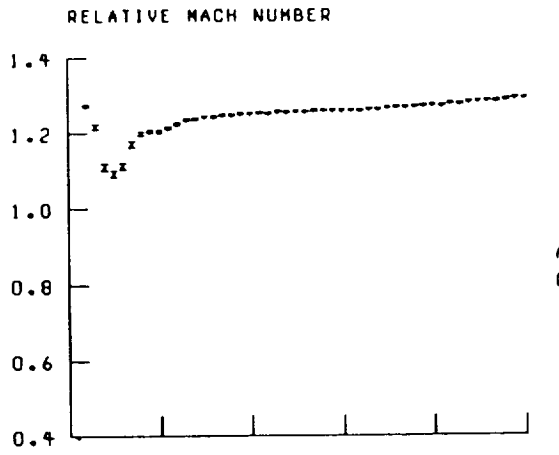


Figure 23.—Continued.

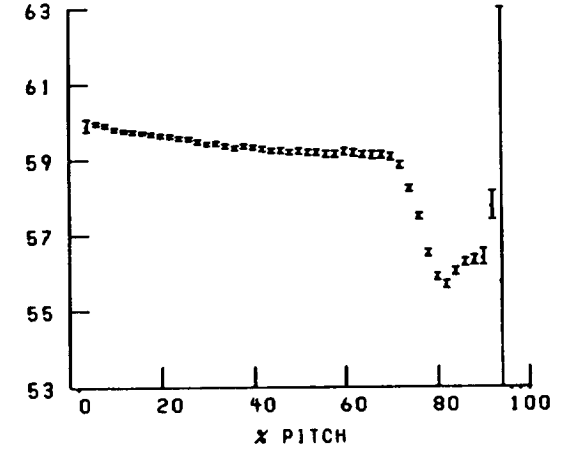
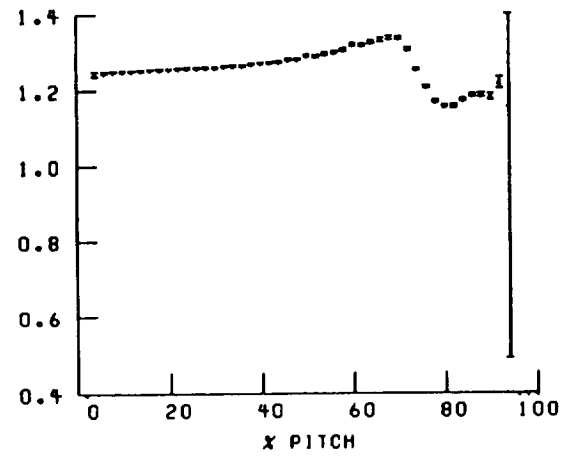
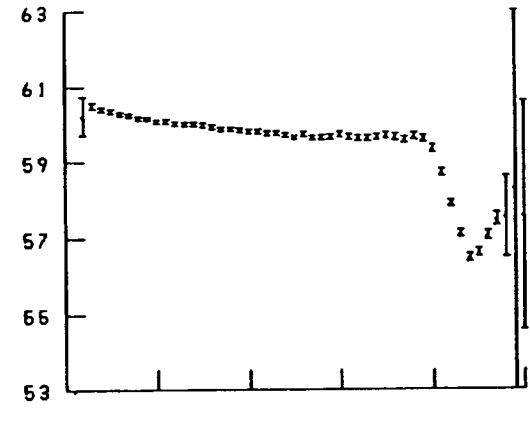
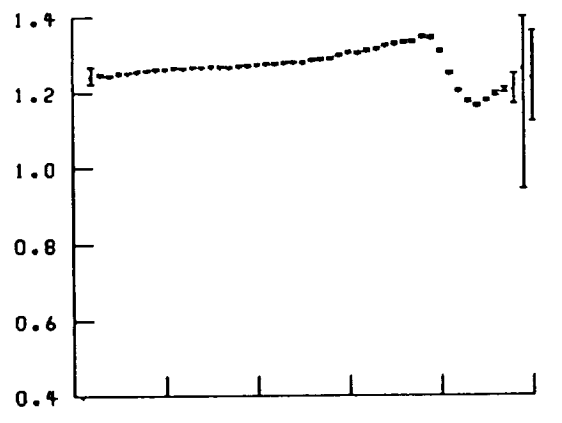
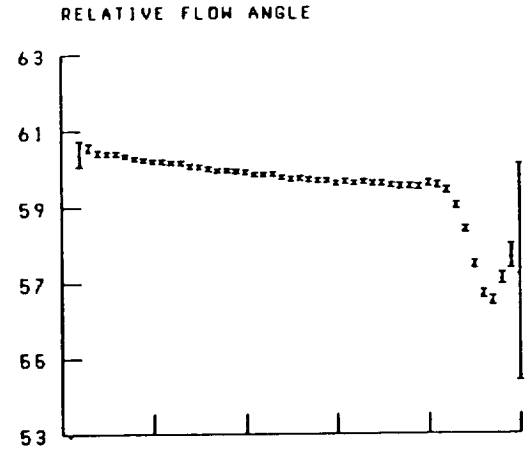
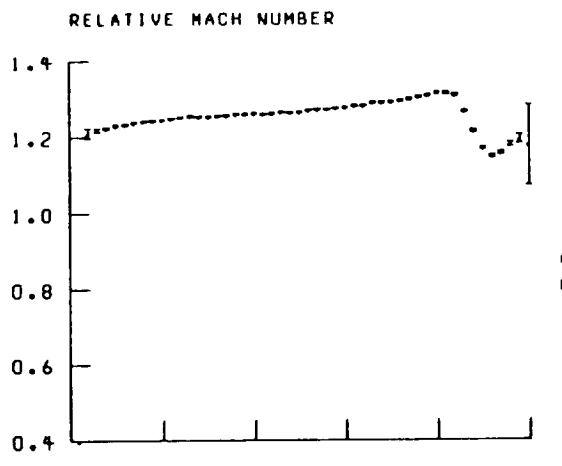


Figure 23.—Continued.

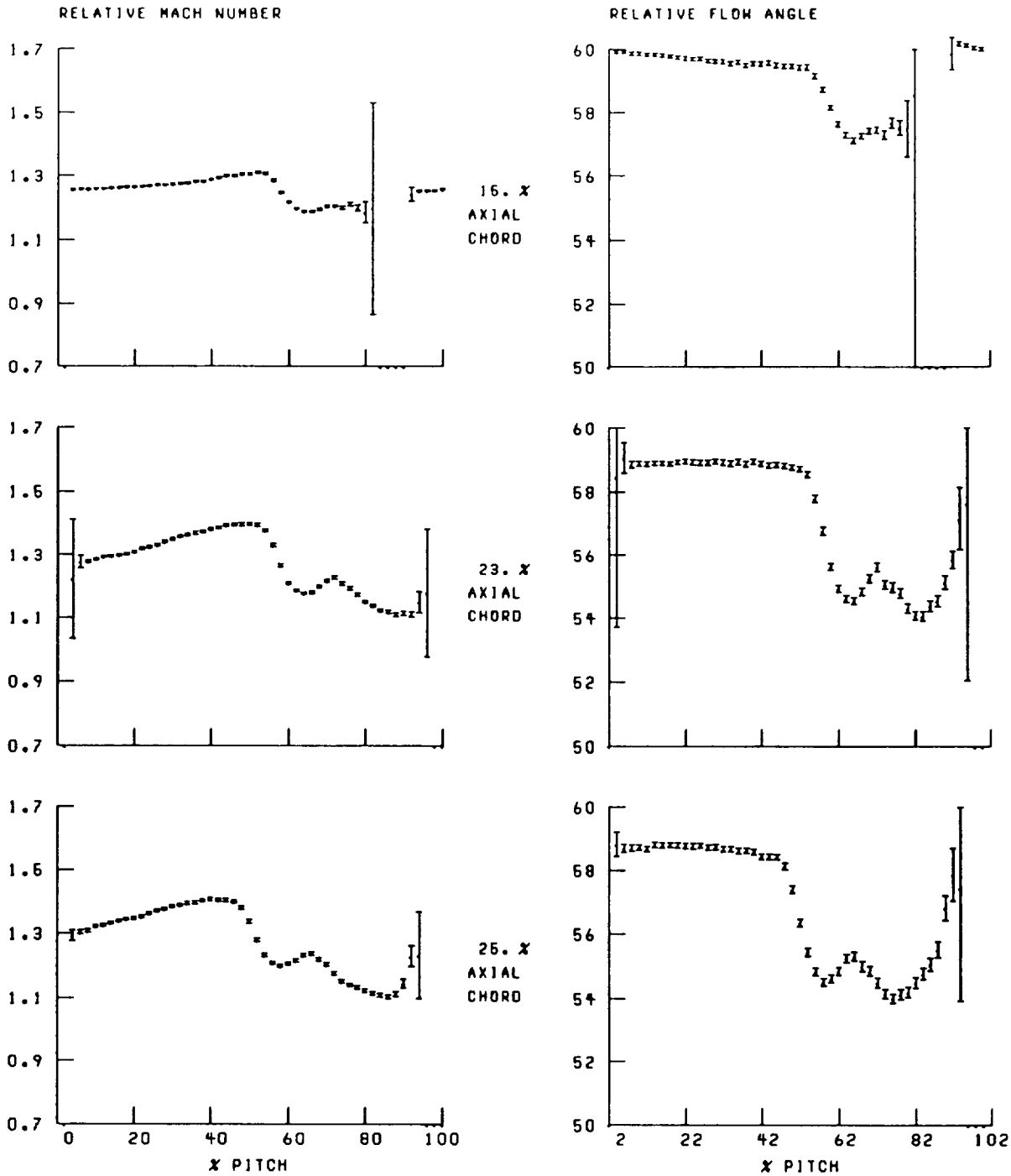


Figure 23.—Continued.

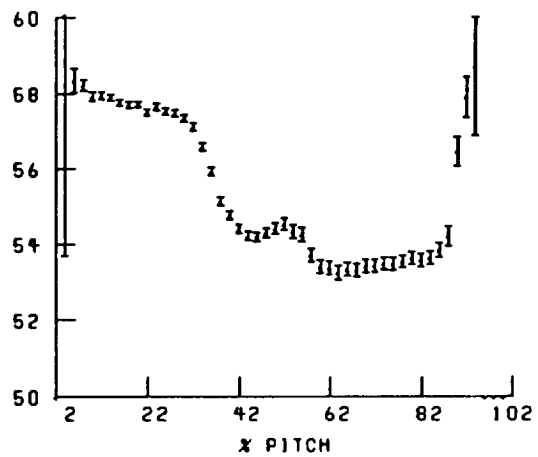
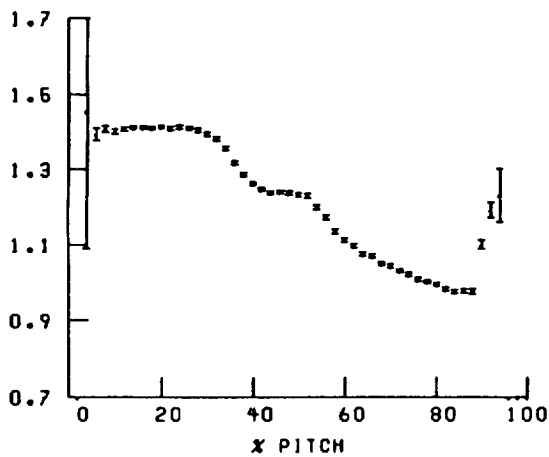
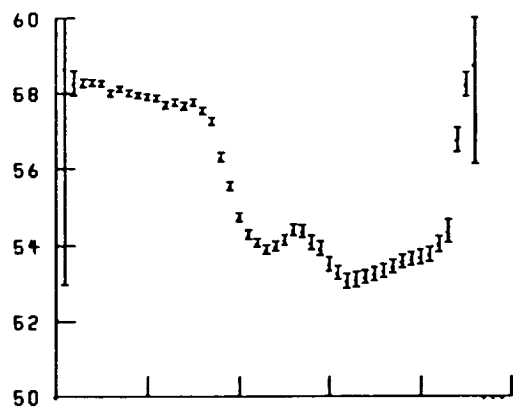
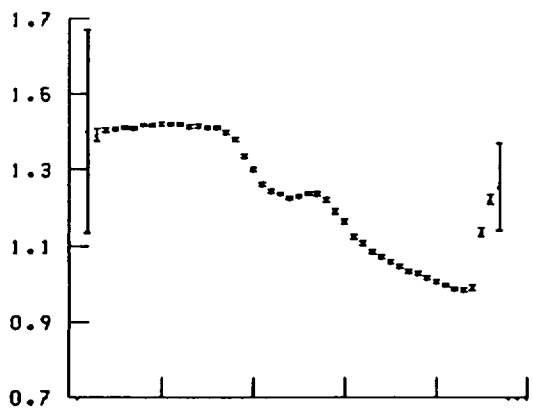
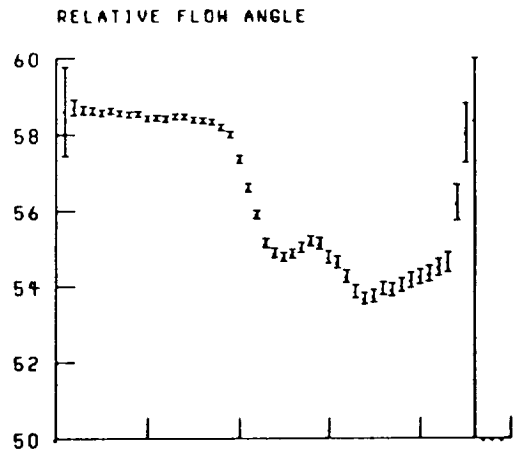
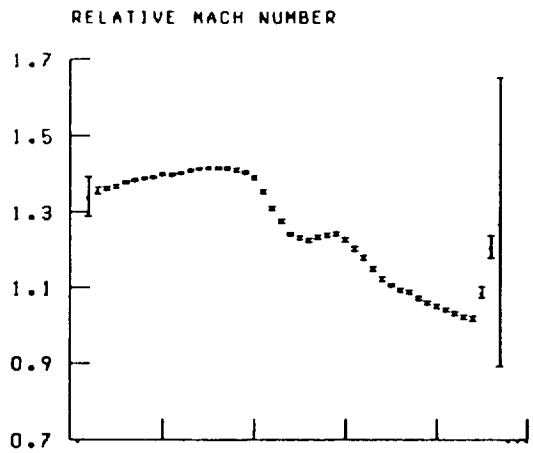


Figure 23.—Continued.

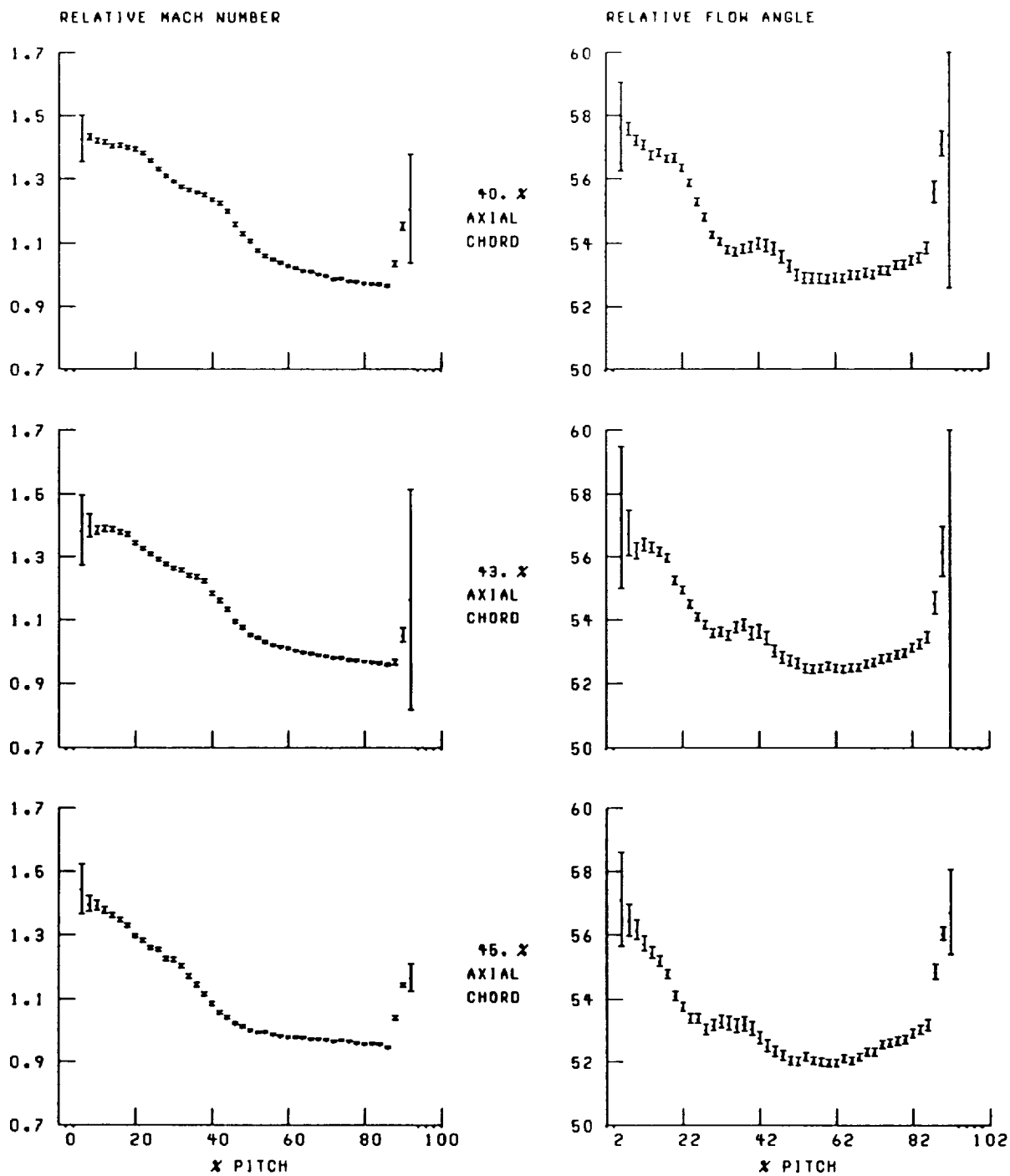


Figure 23.—Continued.

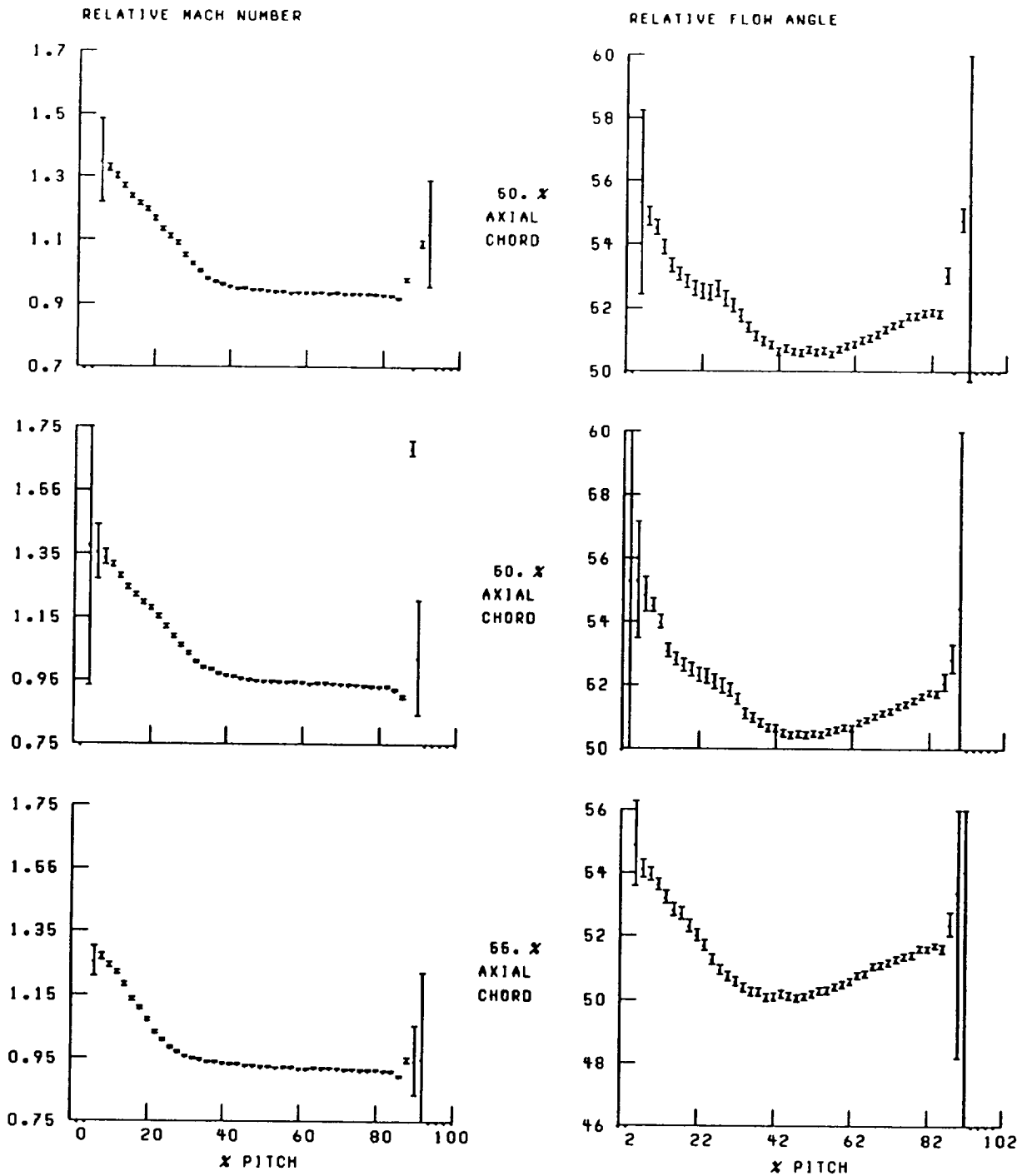
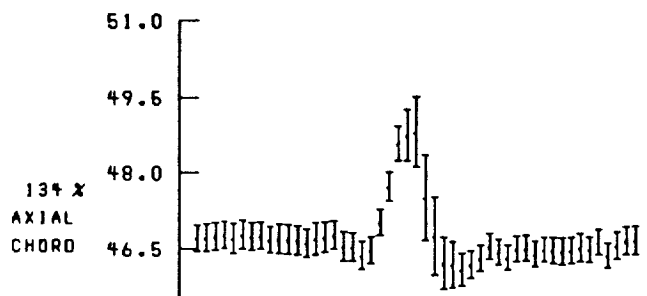
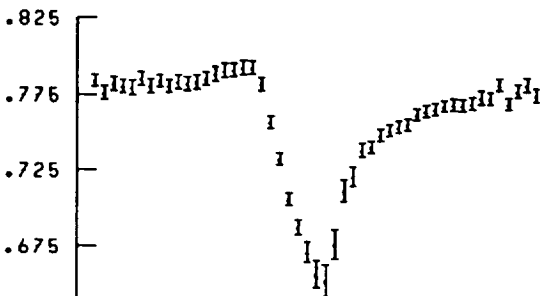
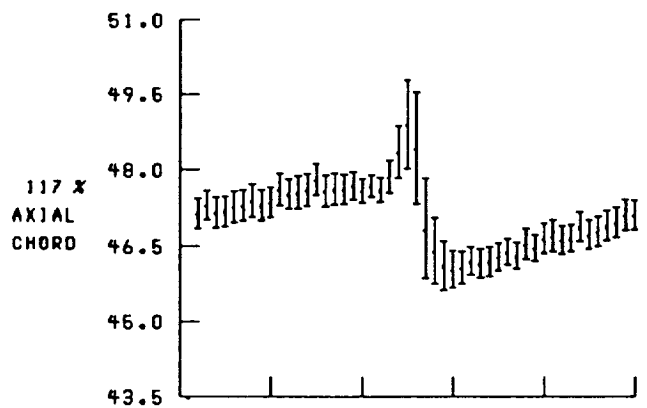
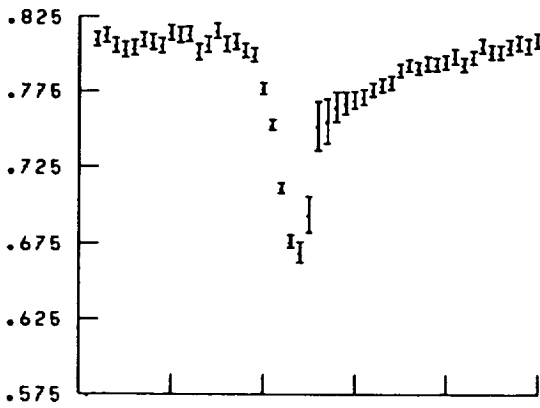
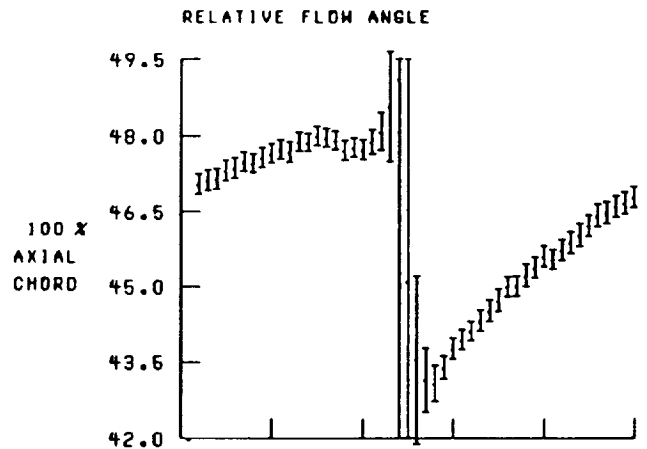
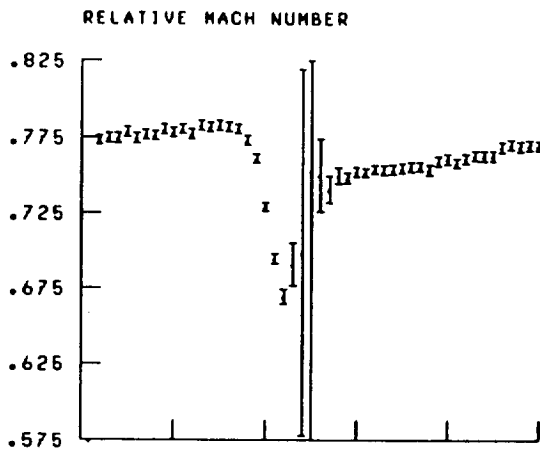
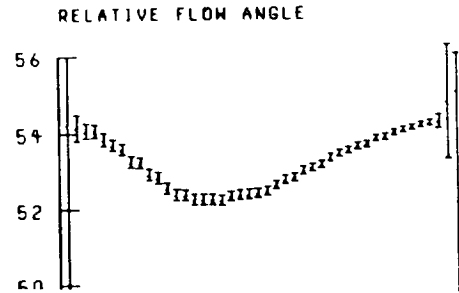
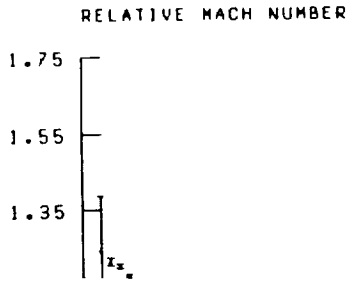


Figure 23.—Continued.



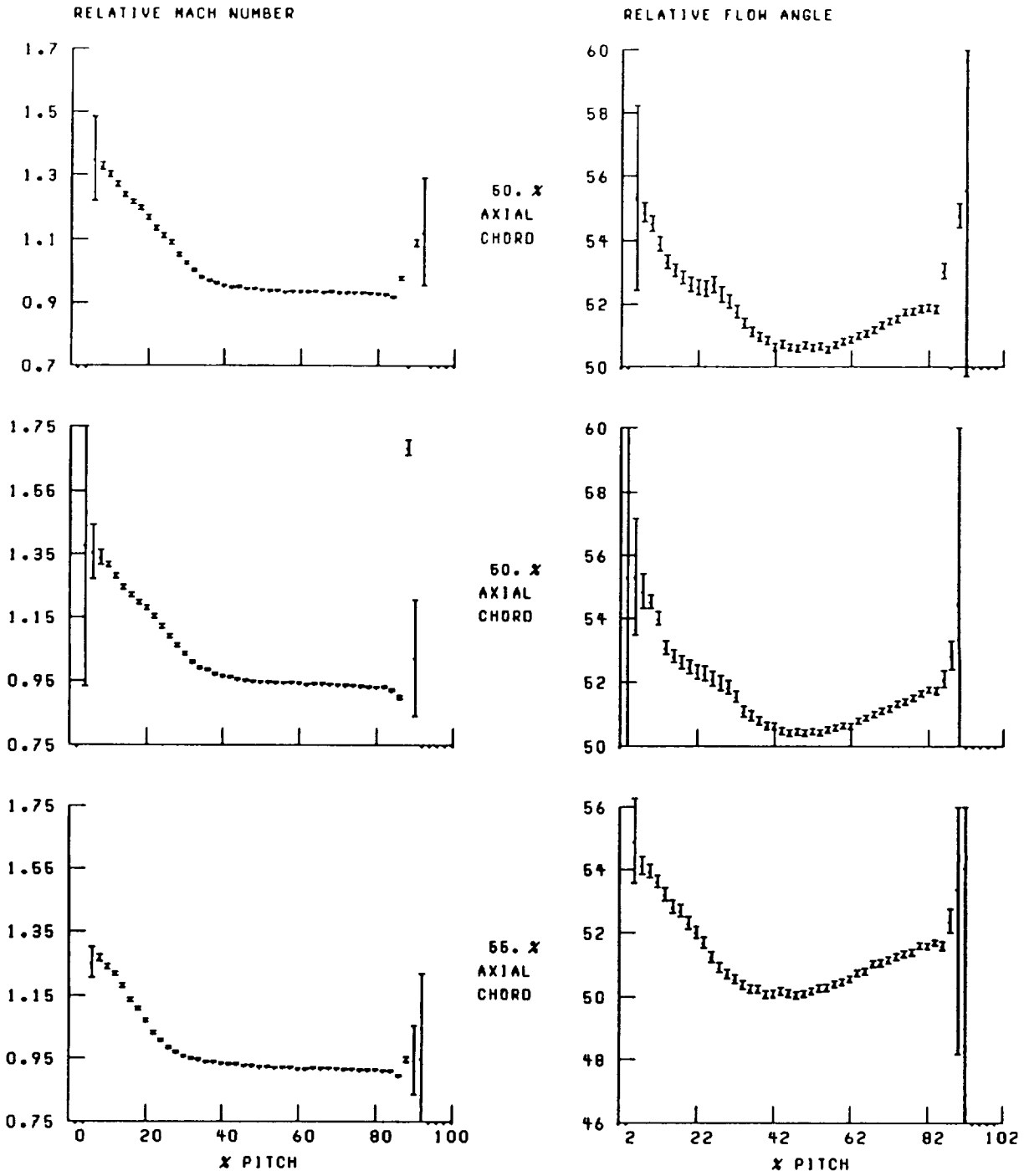


Figure 23.—Continued.

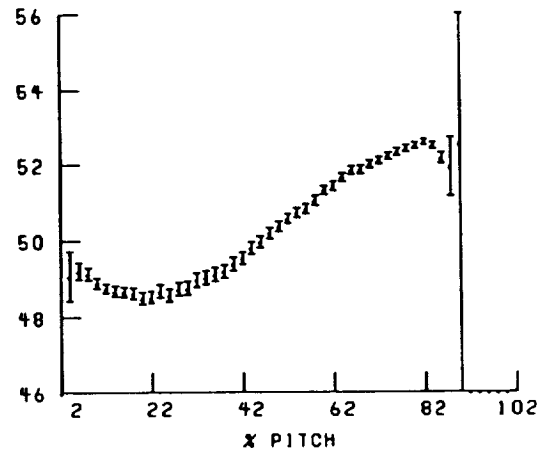
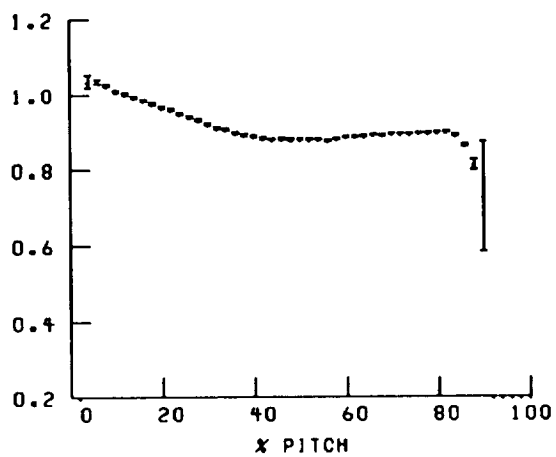
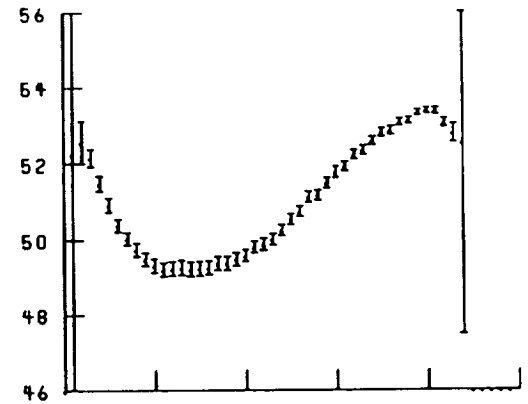
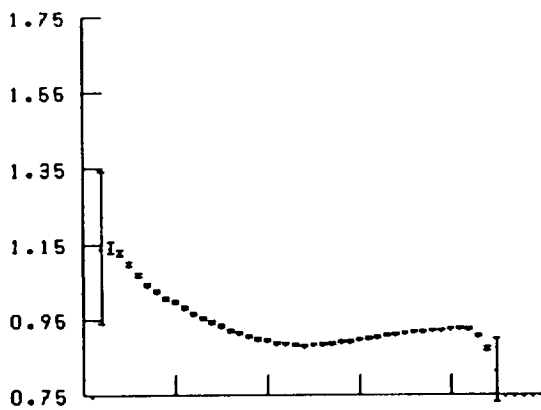
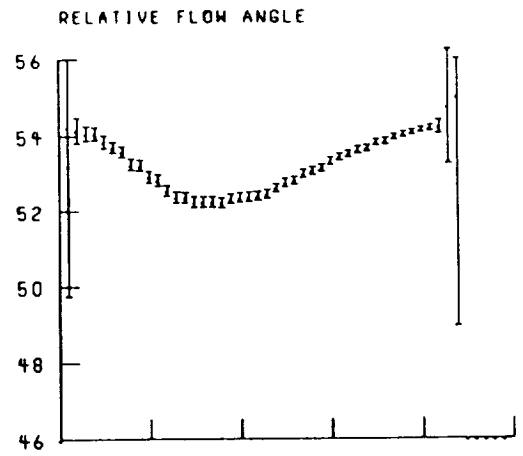
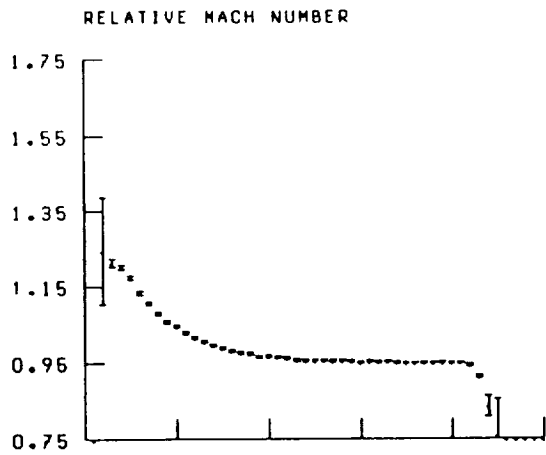


Figure 23.—Continued.

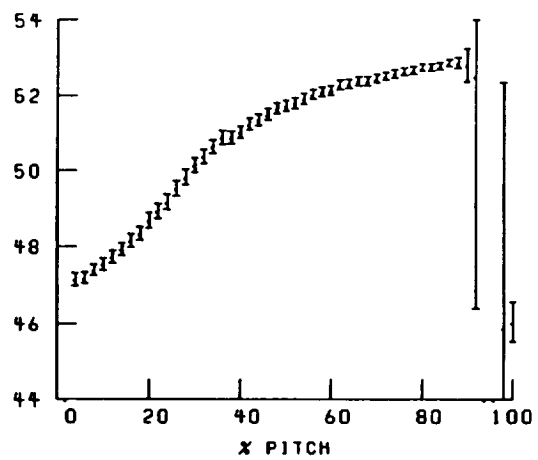
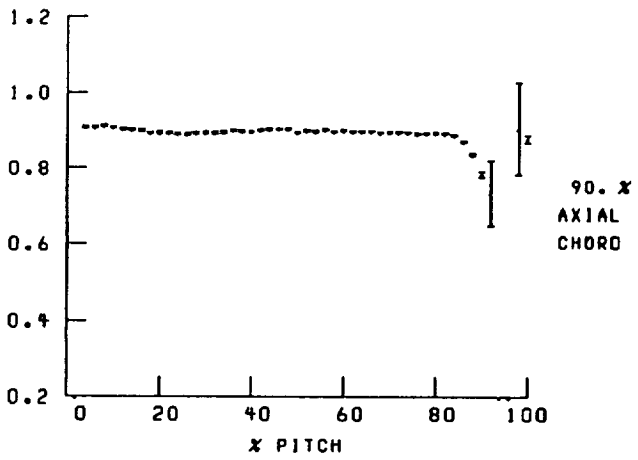
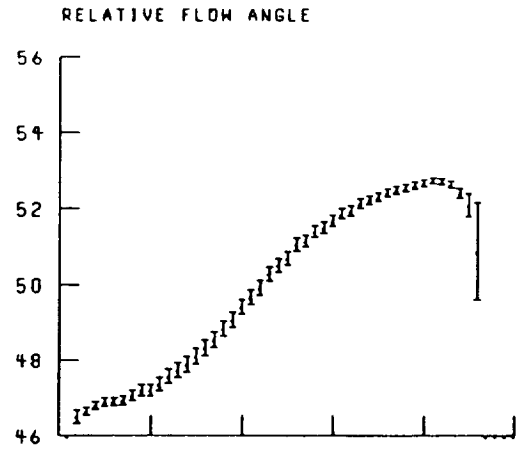
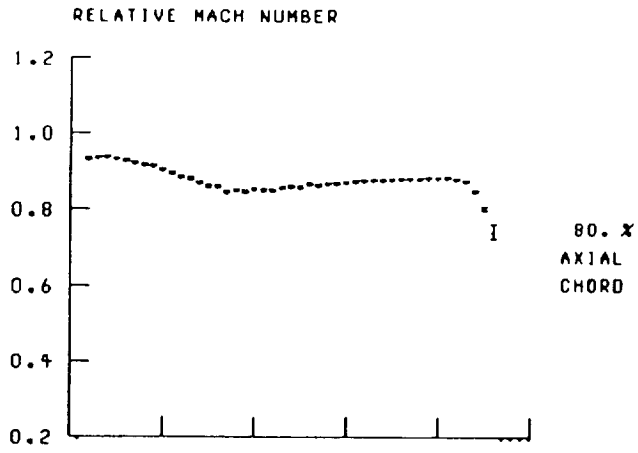


Figure 23.—Continued.

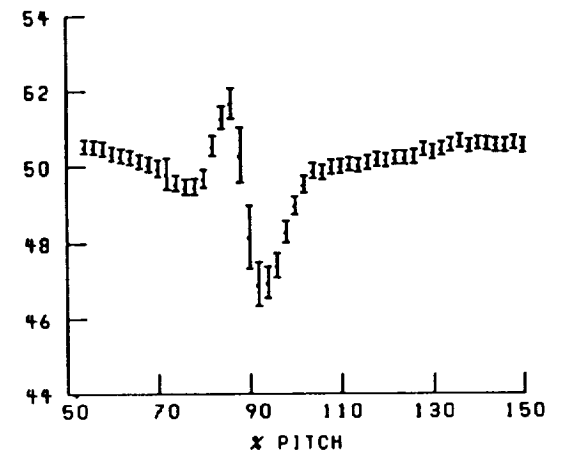
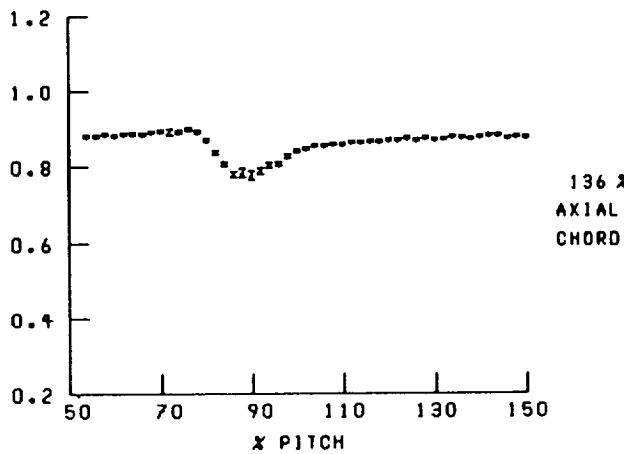
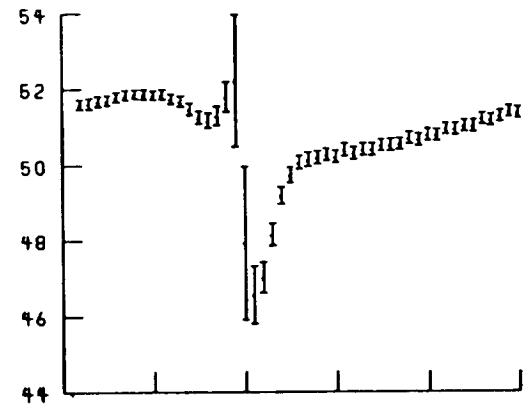
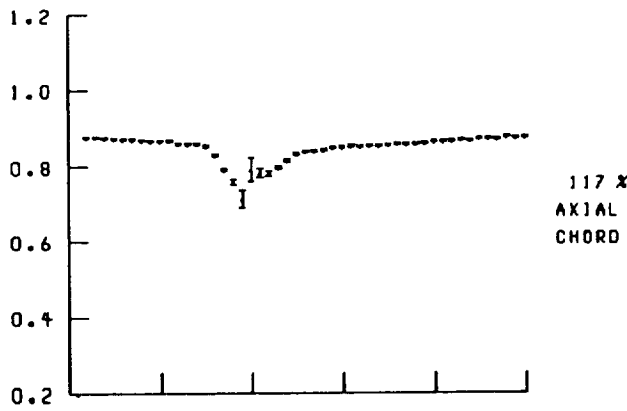
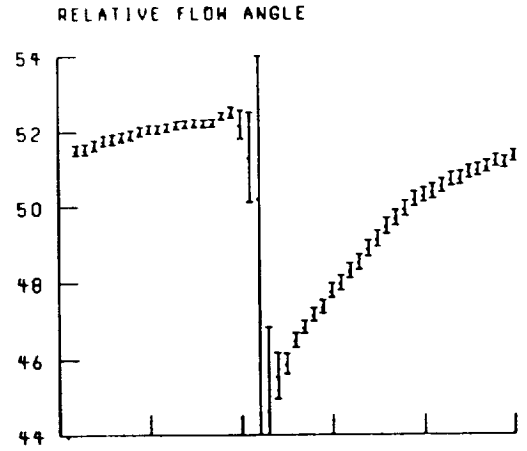
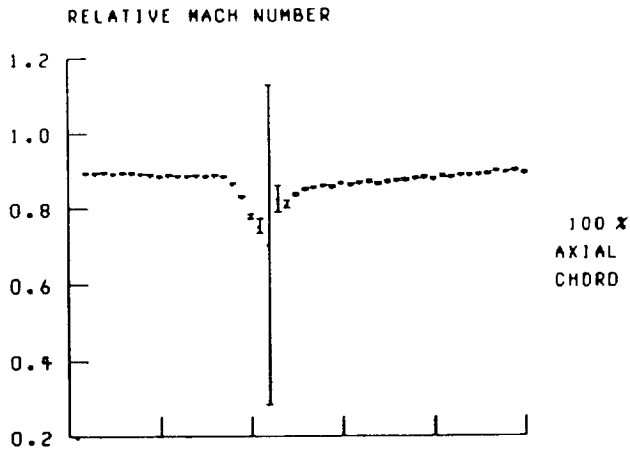


Figure 23.—Concluded.

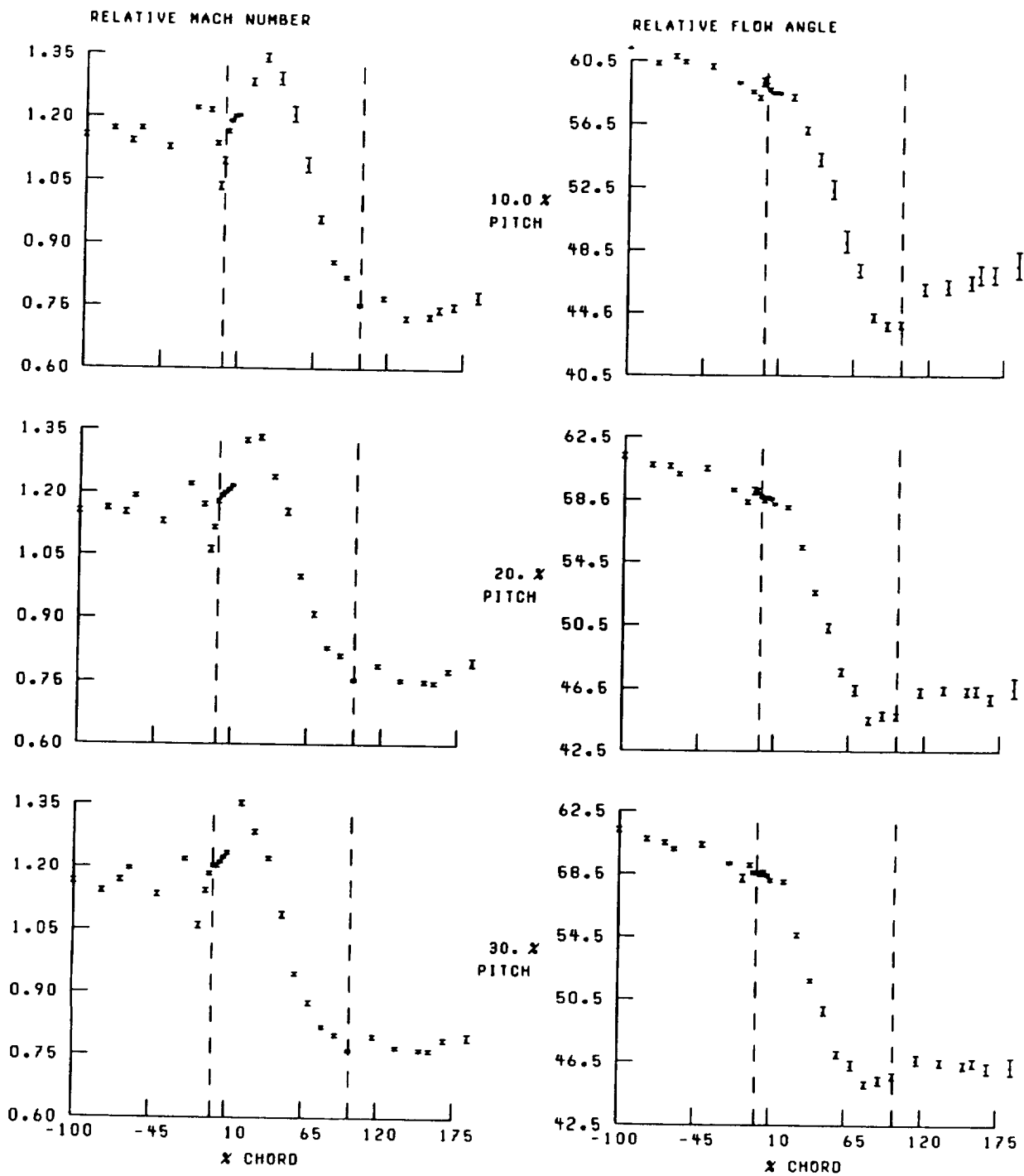


Figure 24.—Streamwise distribution of relative Mach number and flow angle at 40-percent span and near peak efficiency. Broken lines denote location of blade leading and trailing edges.

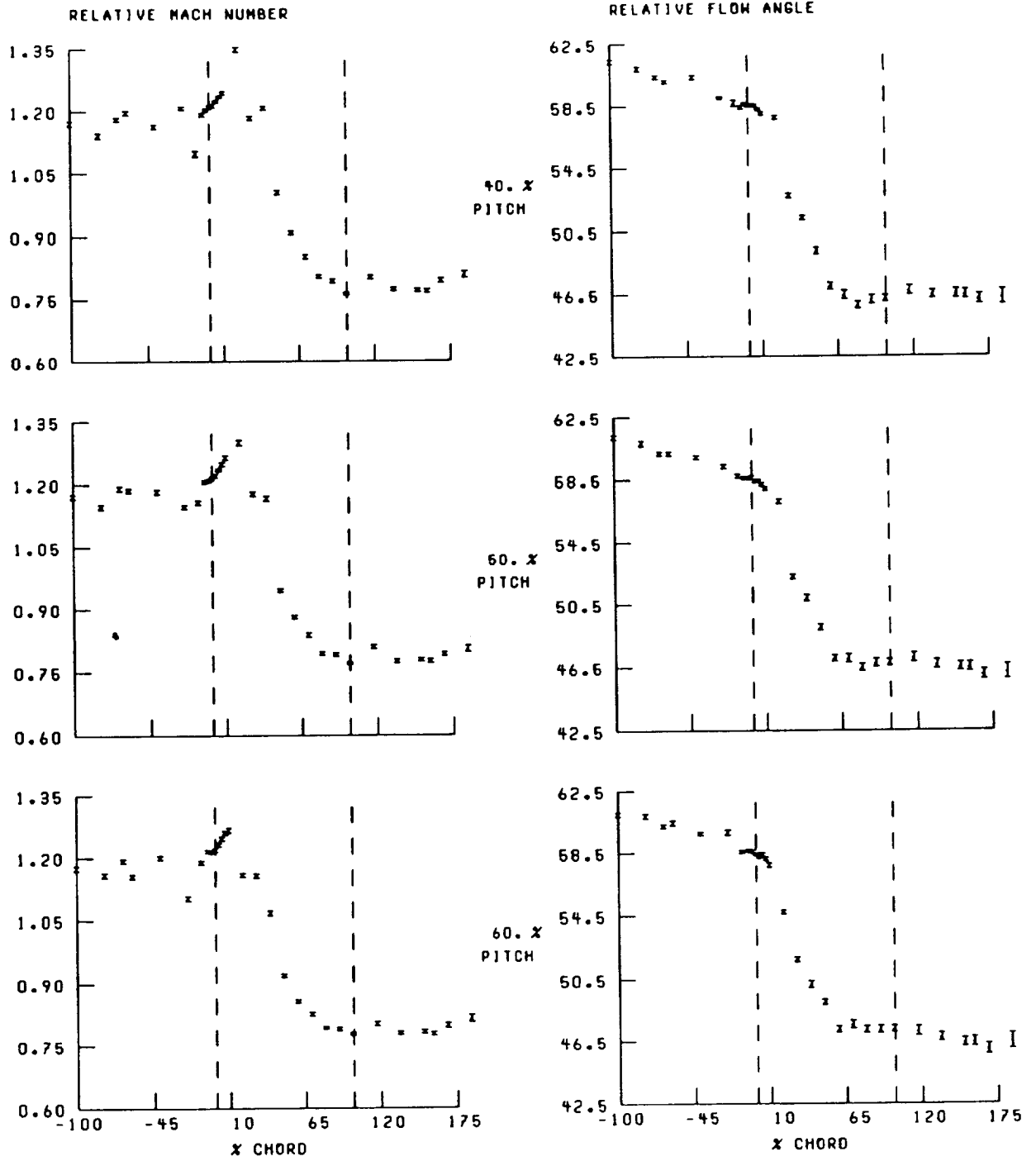


Figure 24.—Continued.

C-2

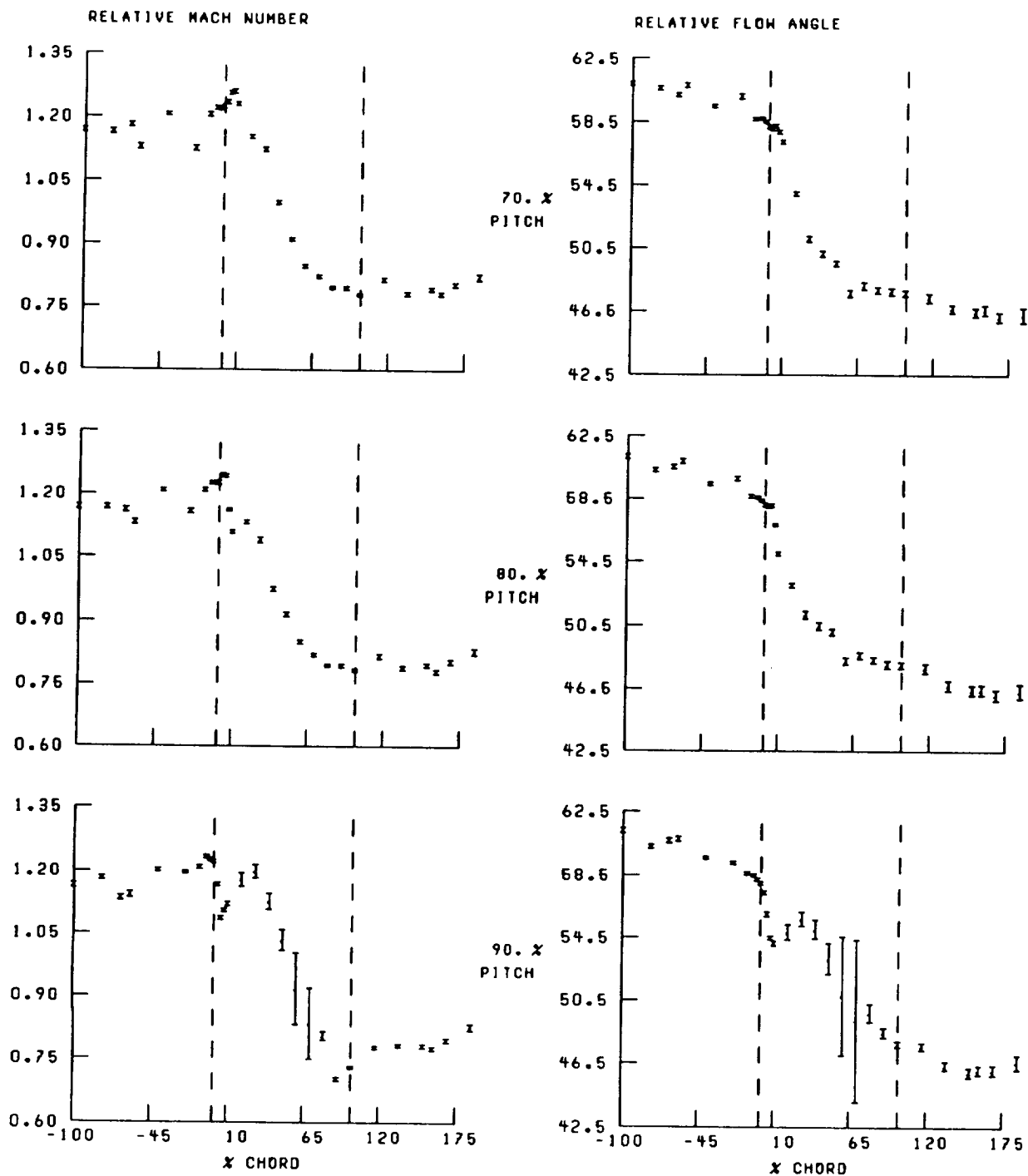


Figure 24.—Concluded.

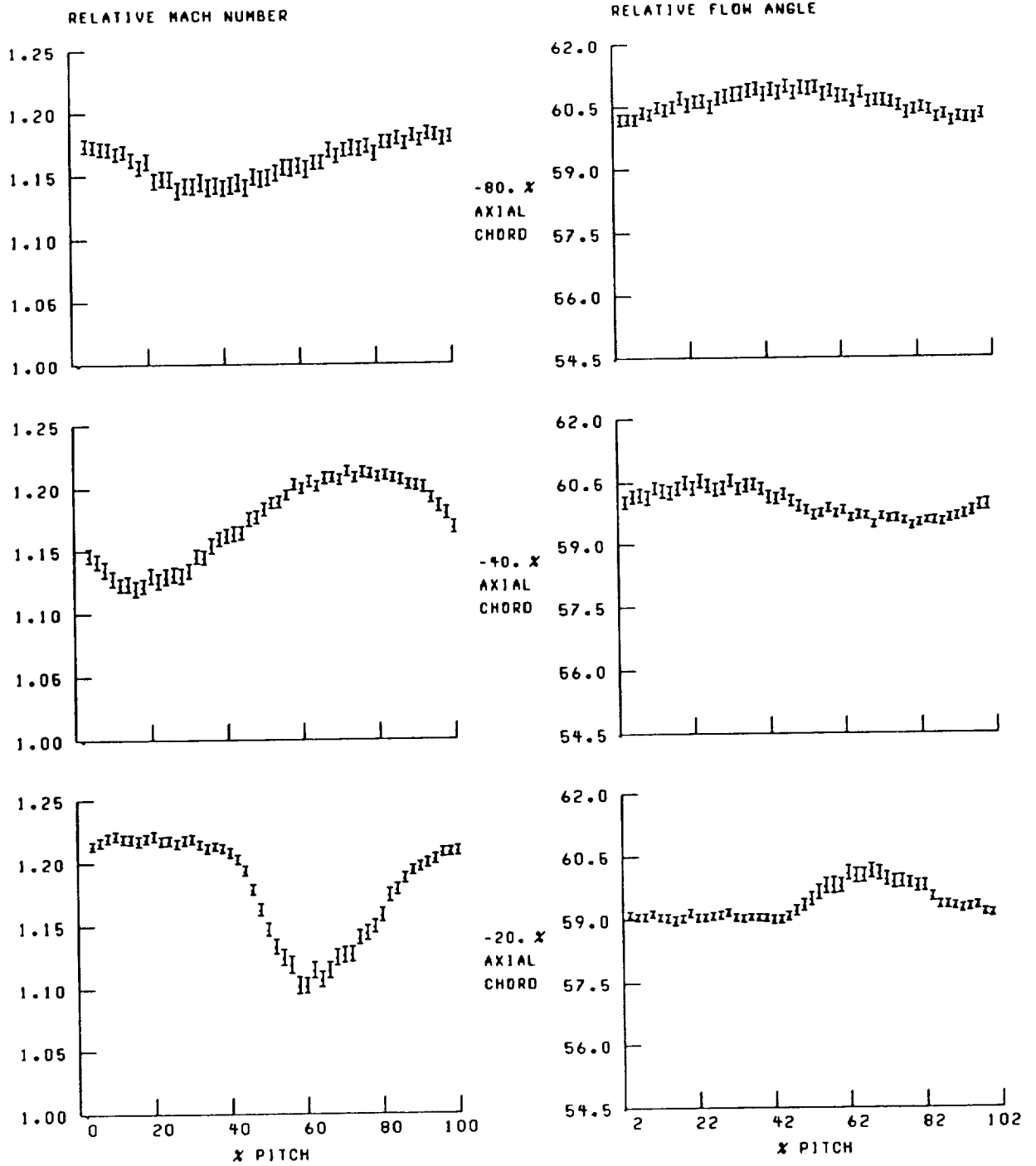


Figure 25.—Blade-to-blade distribution of relative Mach number and flow angle at 40-percent span and near peak efficiency.

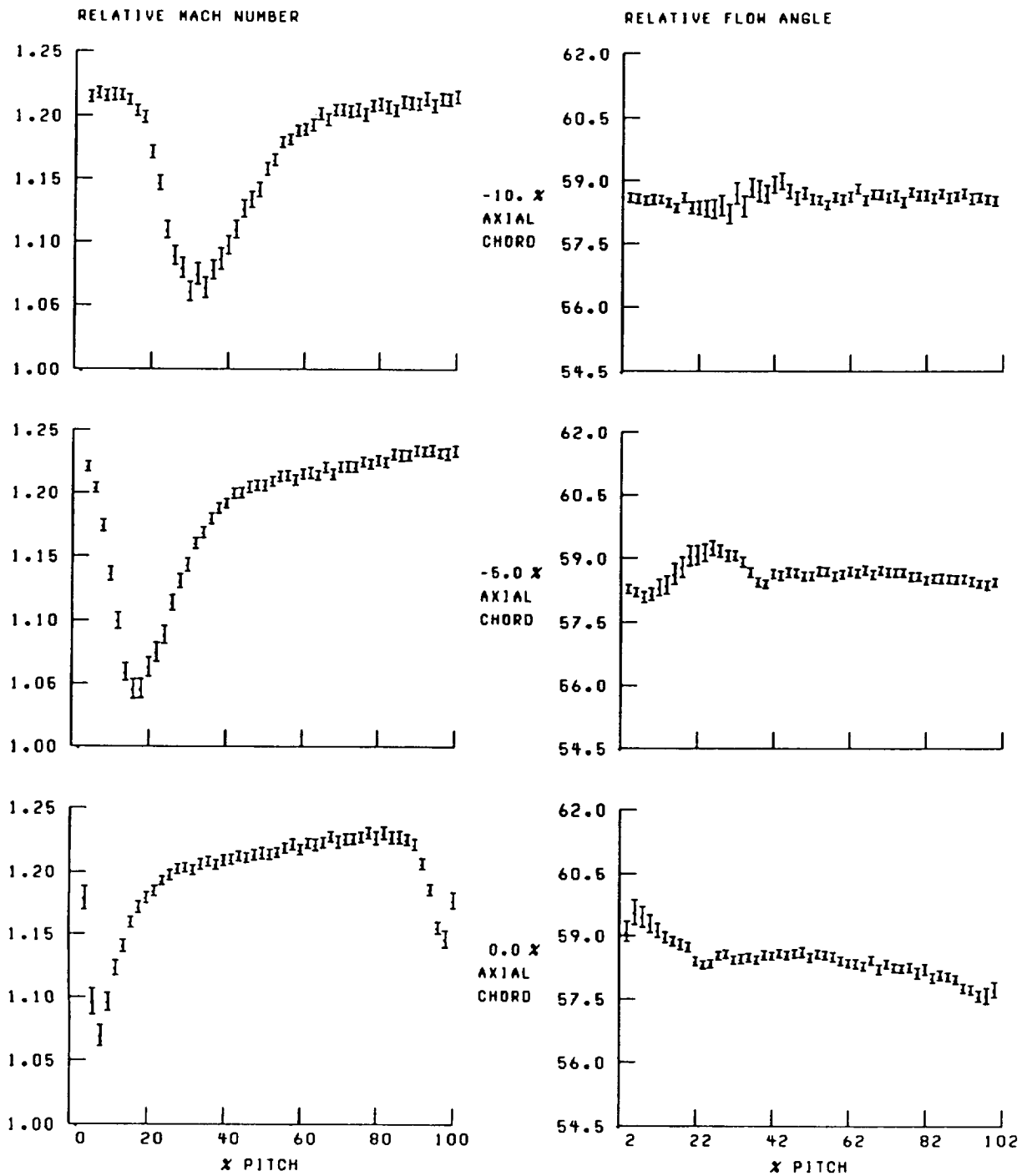


Figure 25.—Continued.

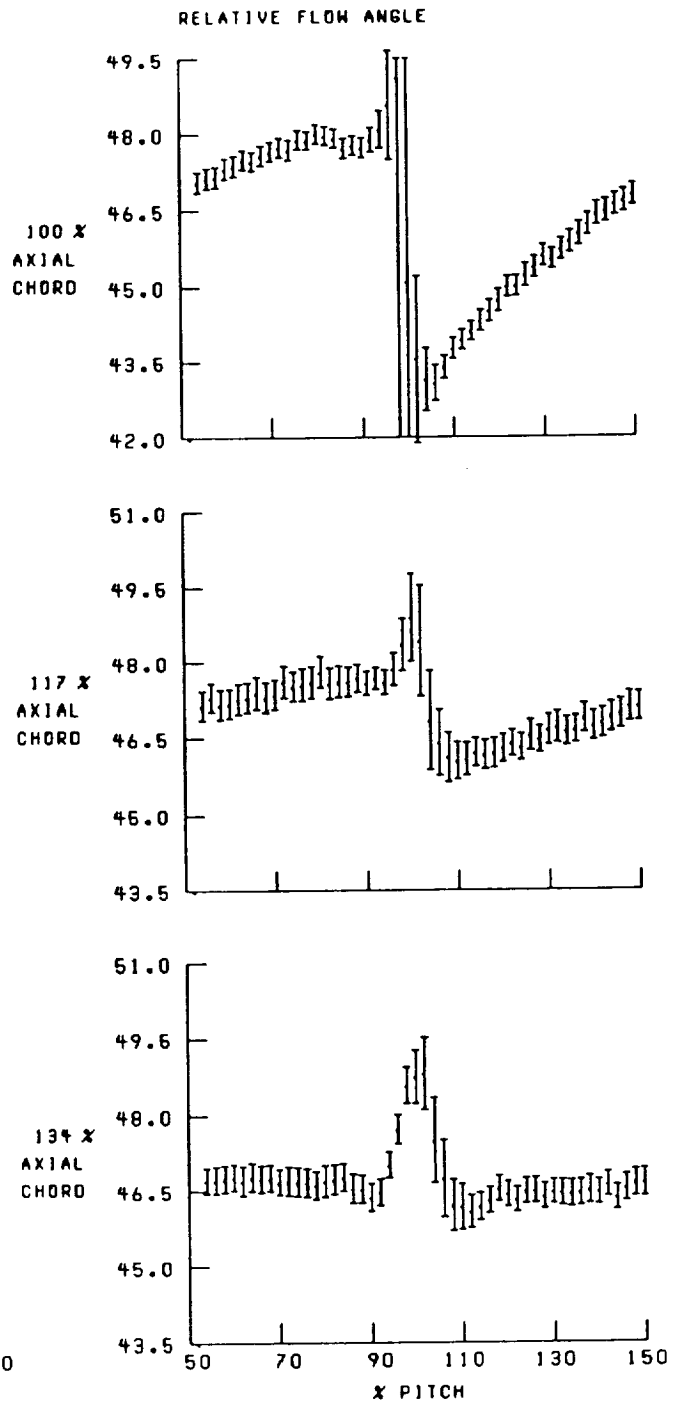
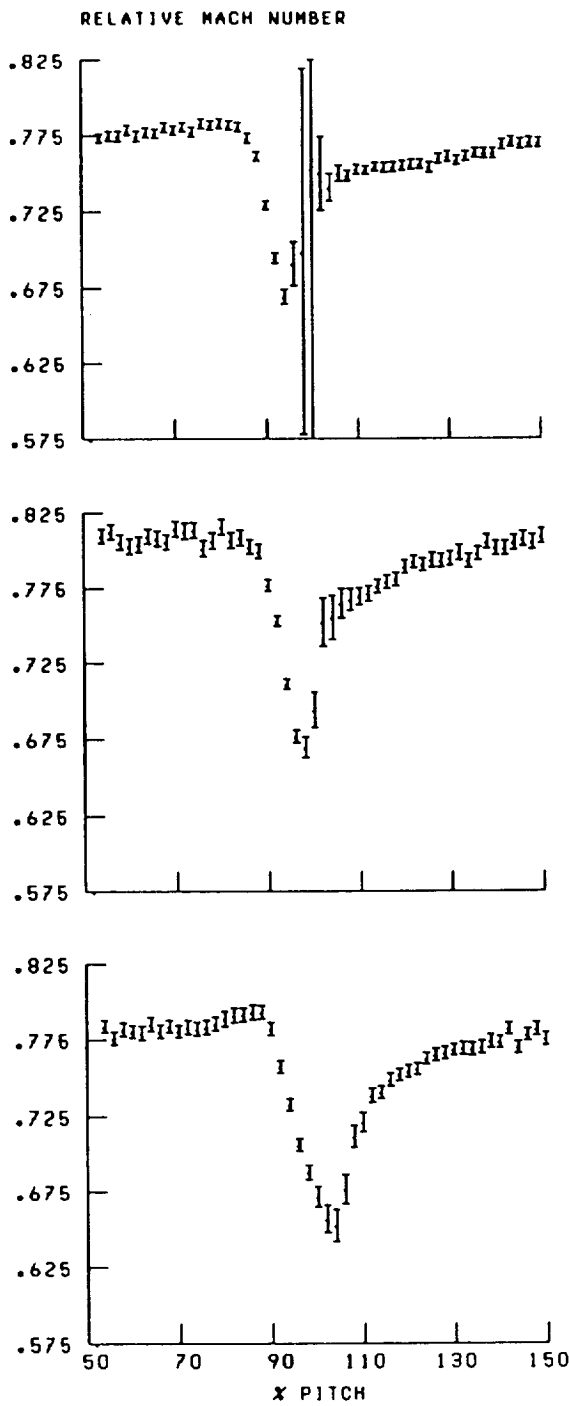


Figure 25.—Continued.

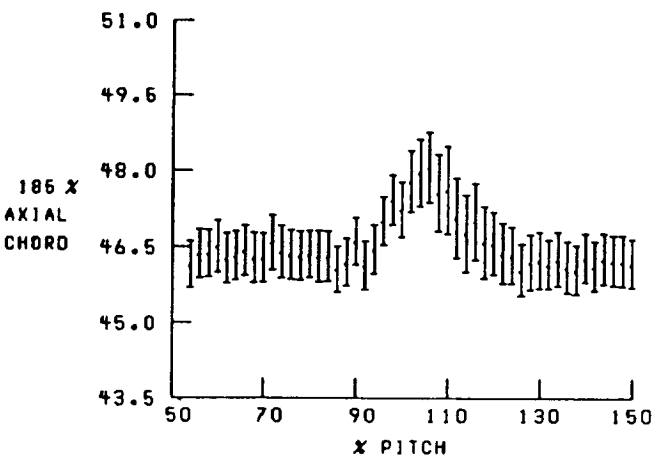
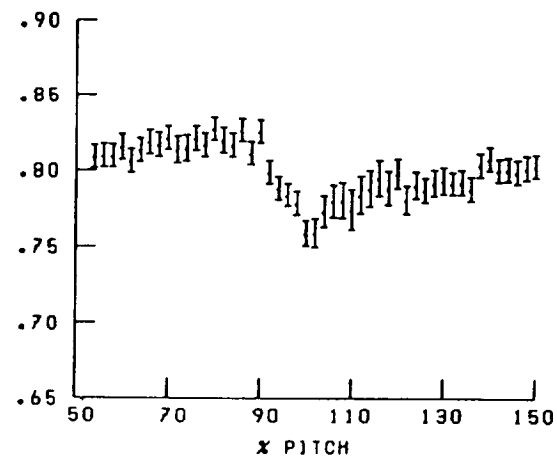
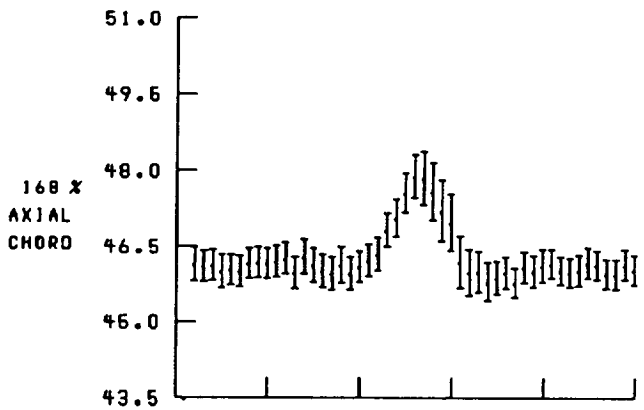
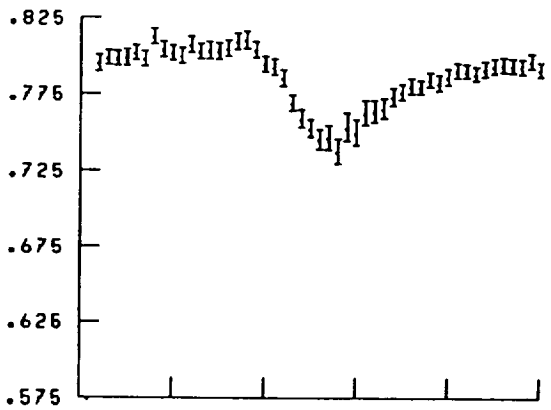
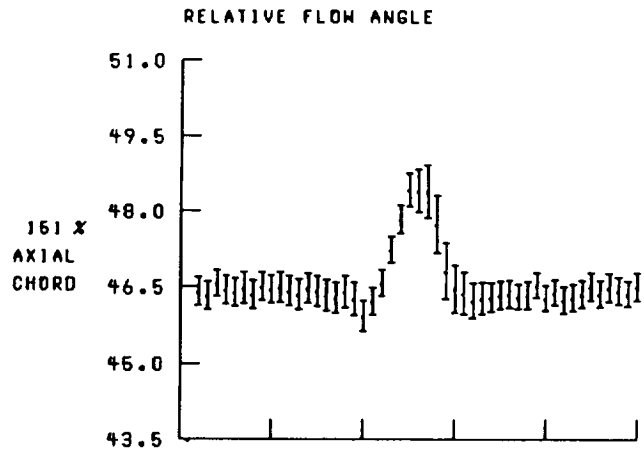
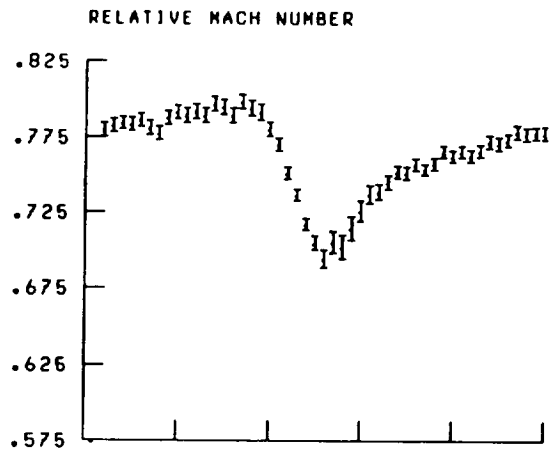


Figure 25.—Concluded.

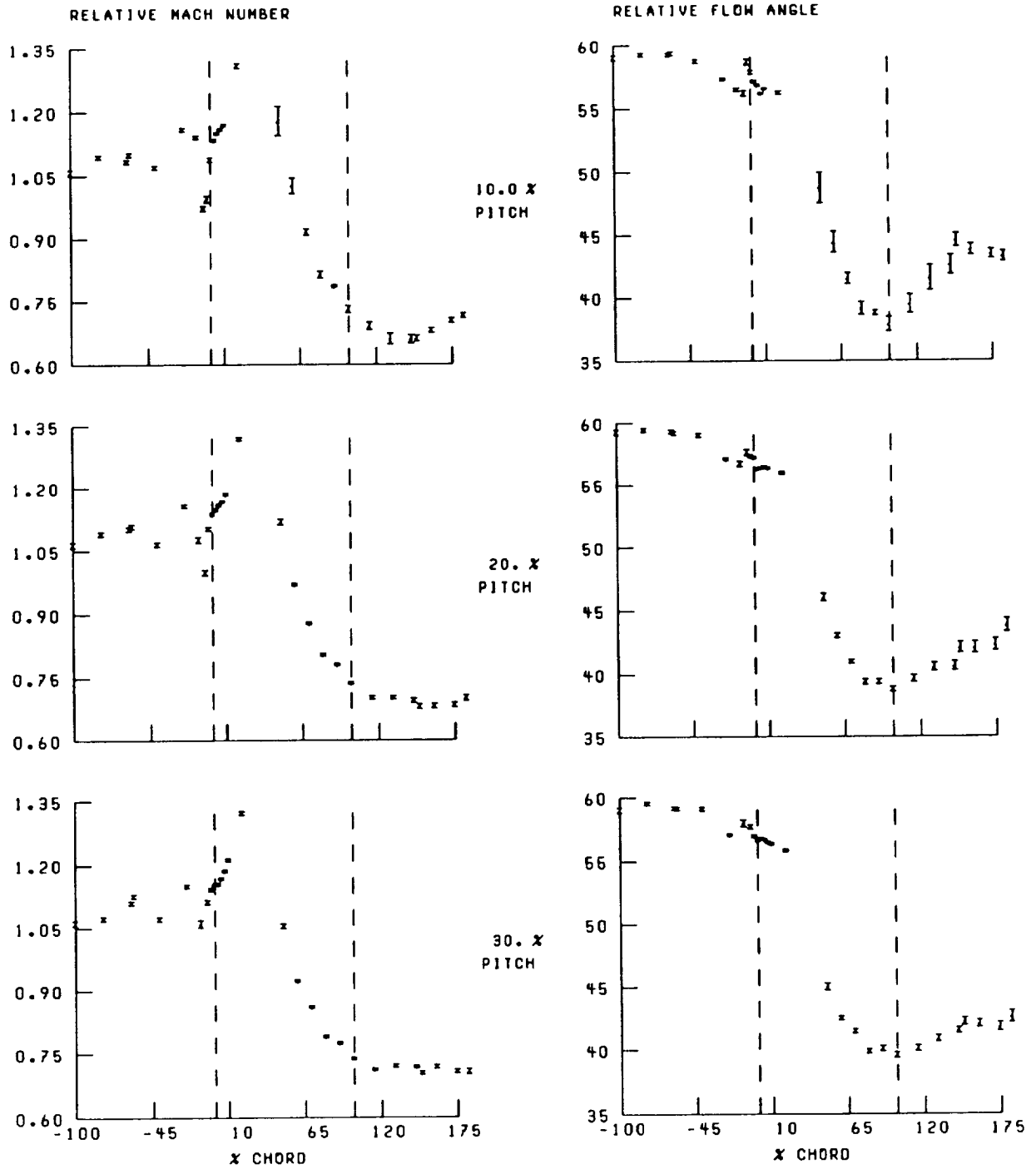


Figure 26.—Streamwise distribution of relative Mach number and flow angle at 50-percent span and near peak efficiency. Broken lines denote location of blade leading and trailing edges.

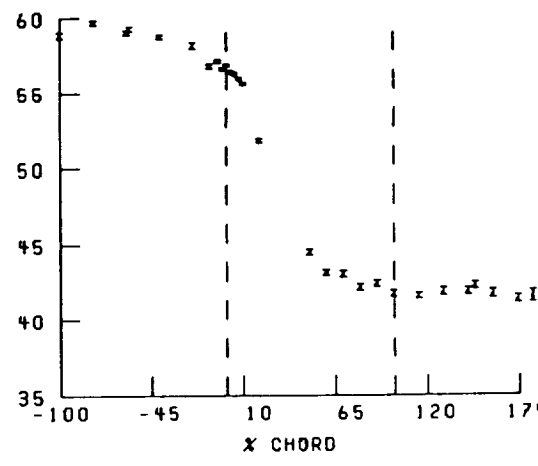
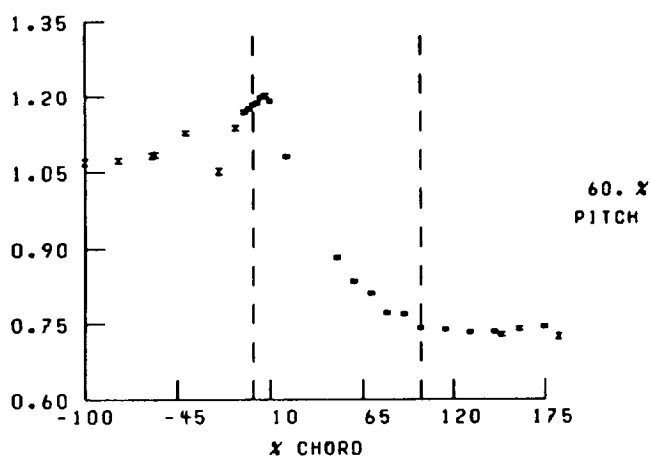
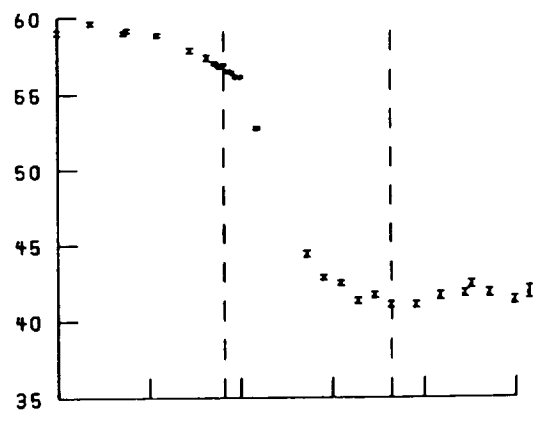
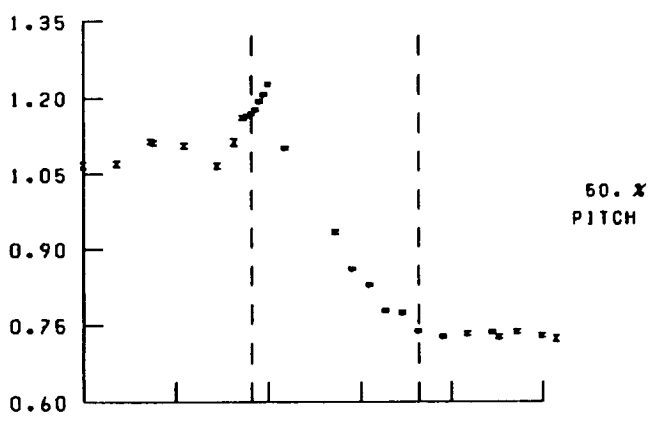
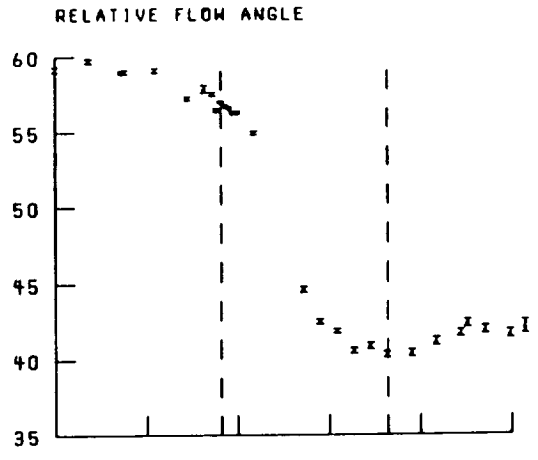
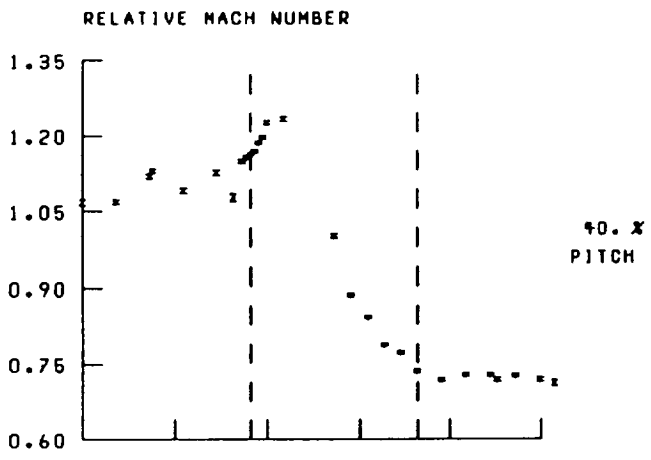


Figure 26.—Continued.

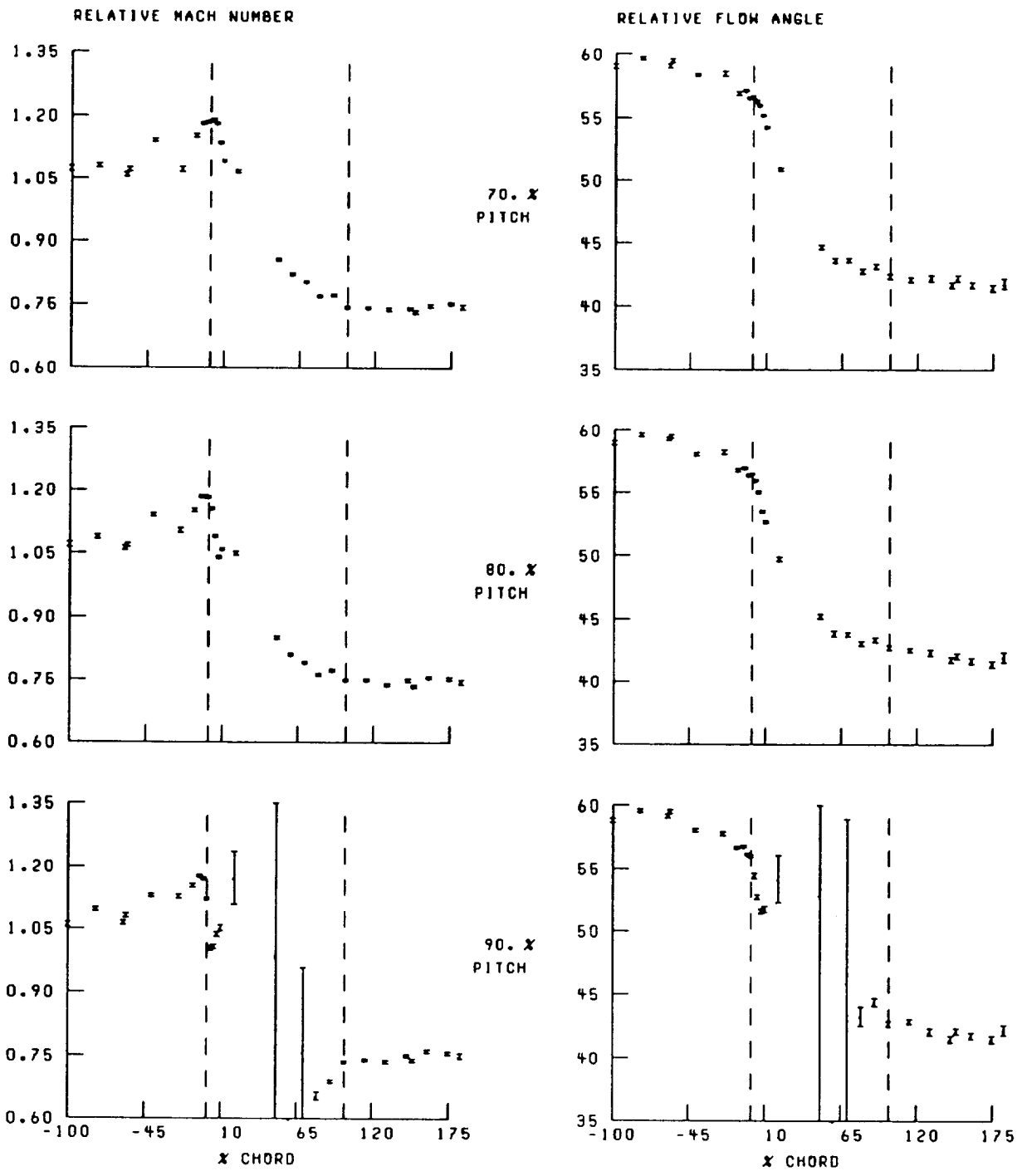


Figure 26.—Concluded.

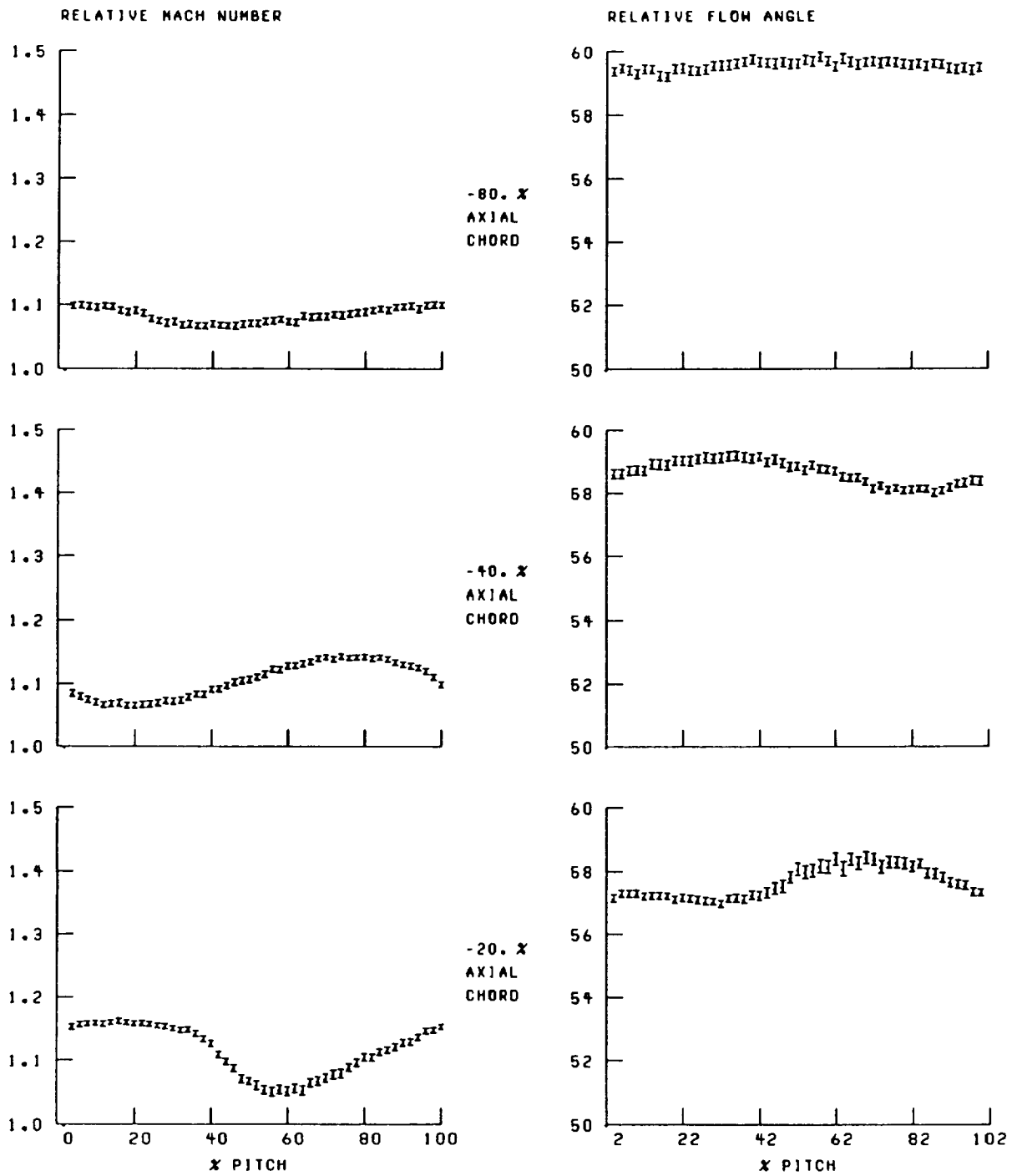


Figure 27.—Blade-to-blade distribution of relative Mach number and flow angle at 50-percent span and near peak efficiency.

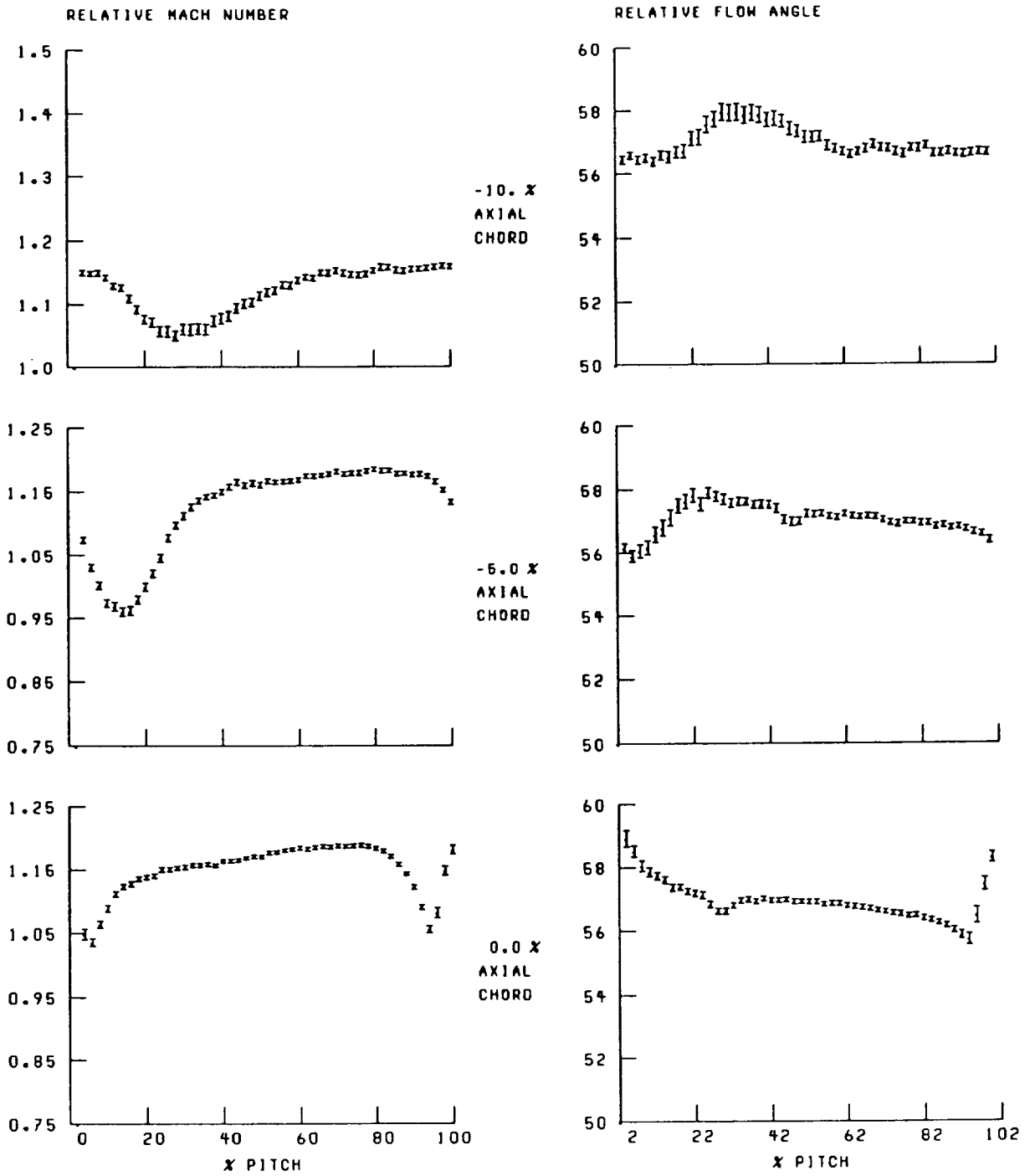


Figure 27.—Continued.

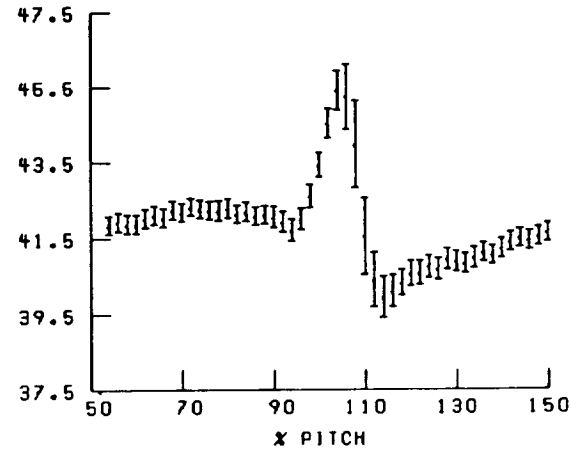
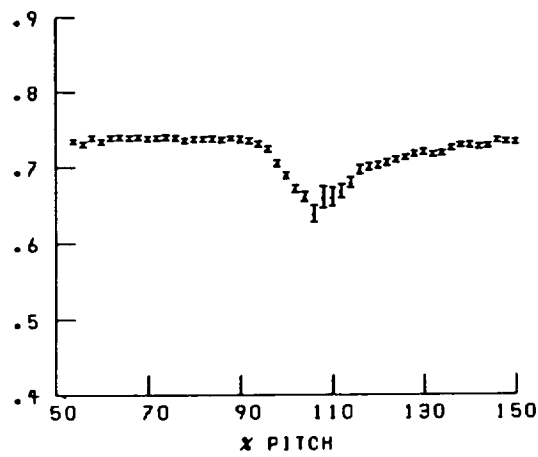
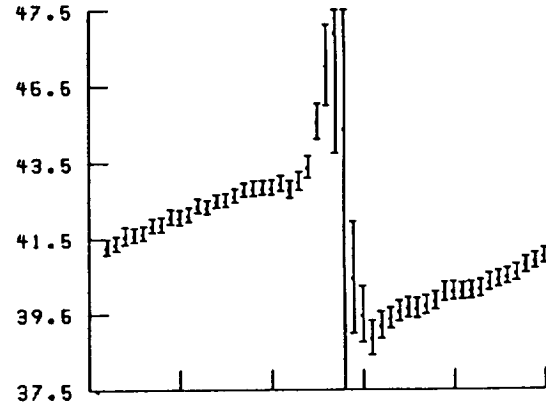
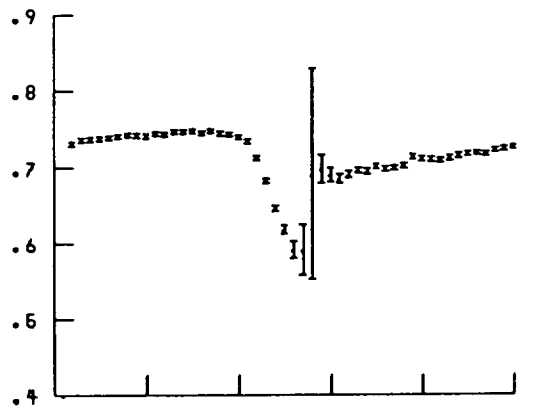
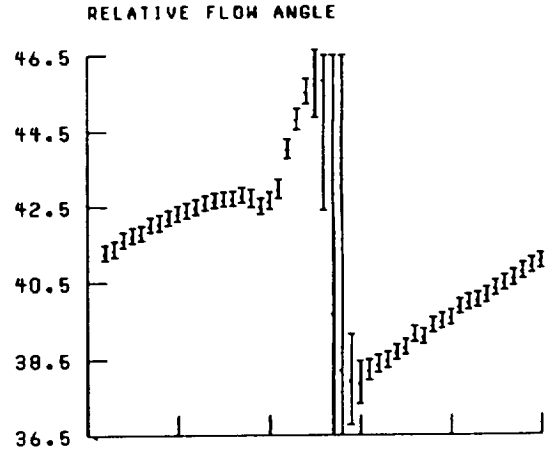
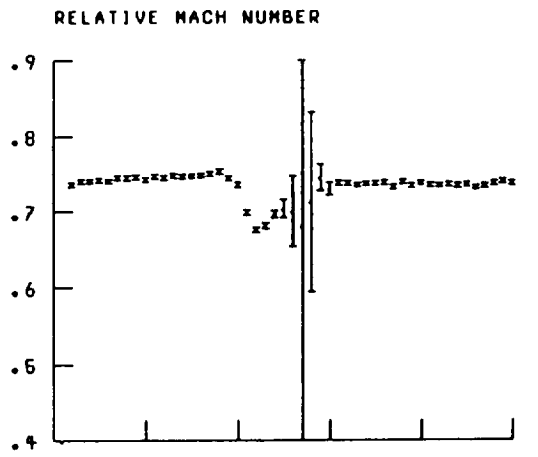


Figure 27.—Continued.

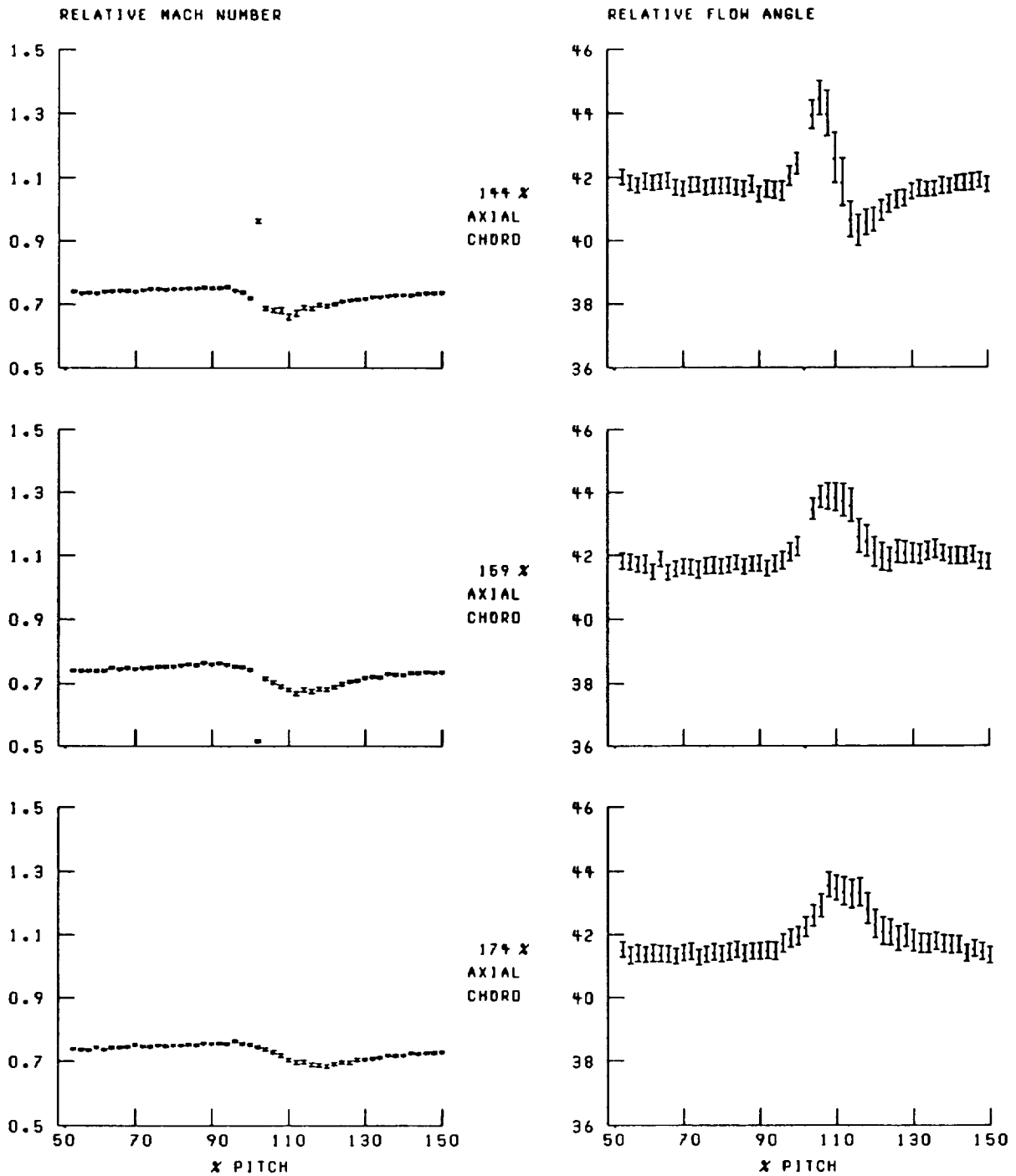


Figure 27.—Concluded.

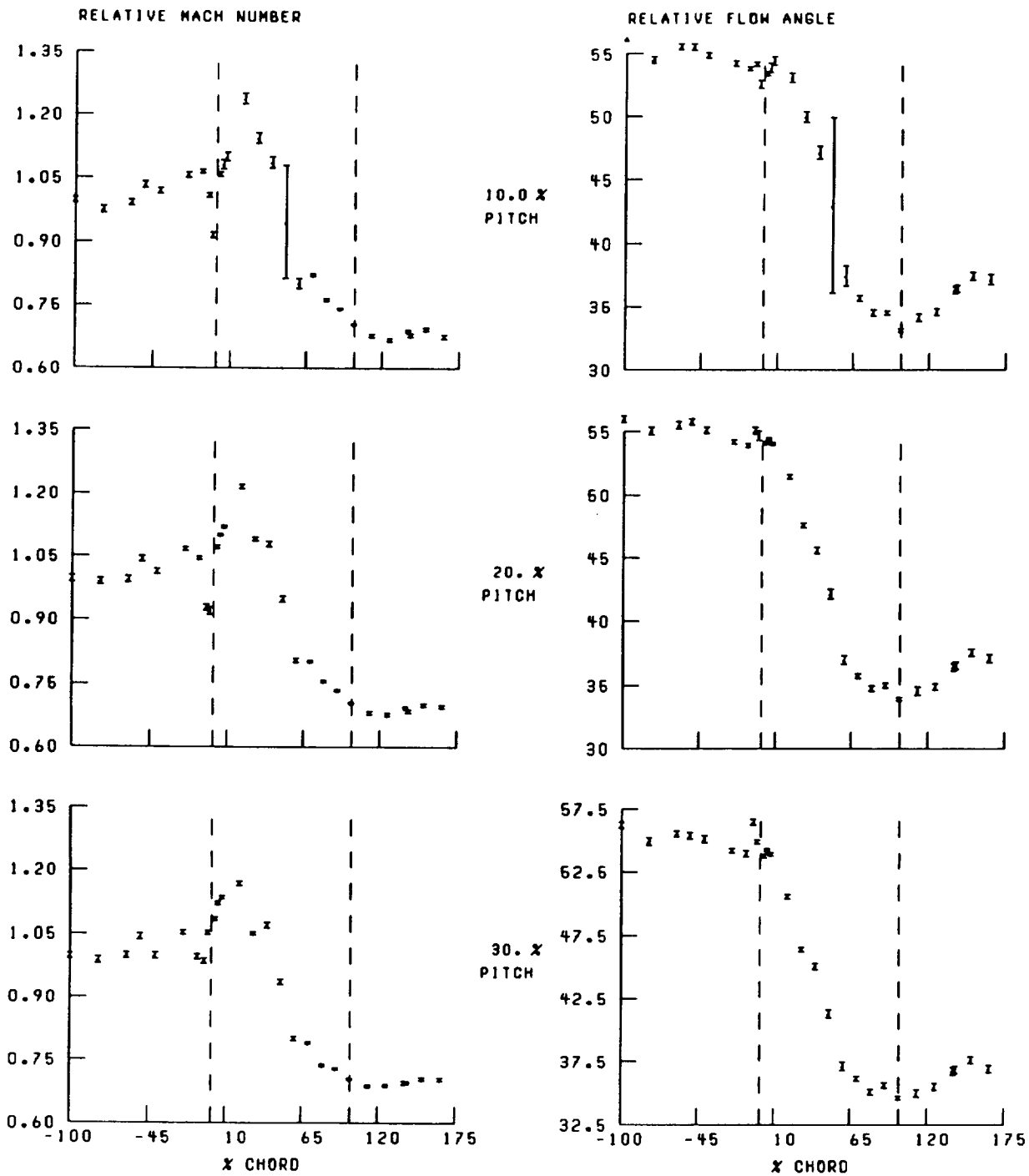


Figure 28.—Streamwise distribution of relative Mach number and flow angle at 60-percent span and near peak efficiency. Broken lines denote location of blade leading and trailing edges.

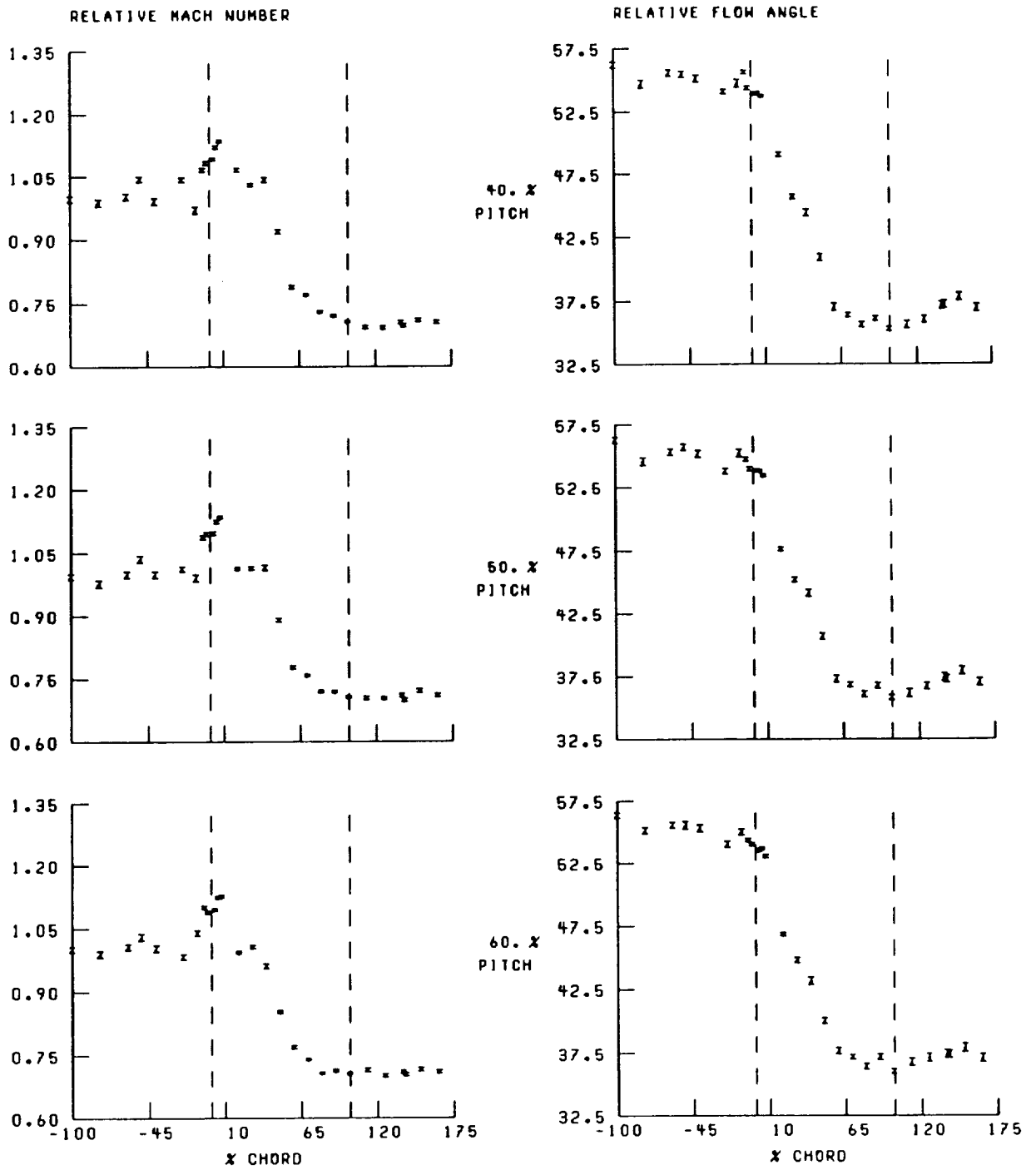


Figure 28.—Continued.

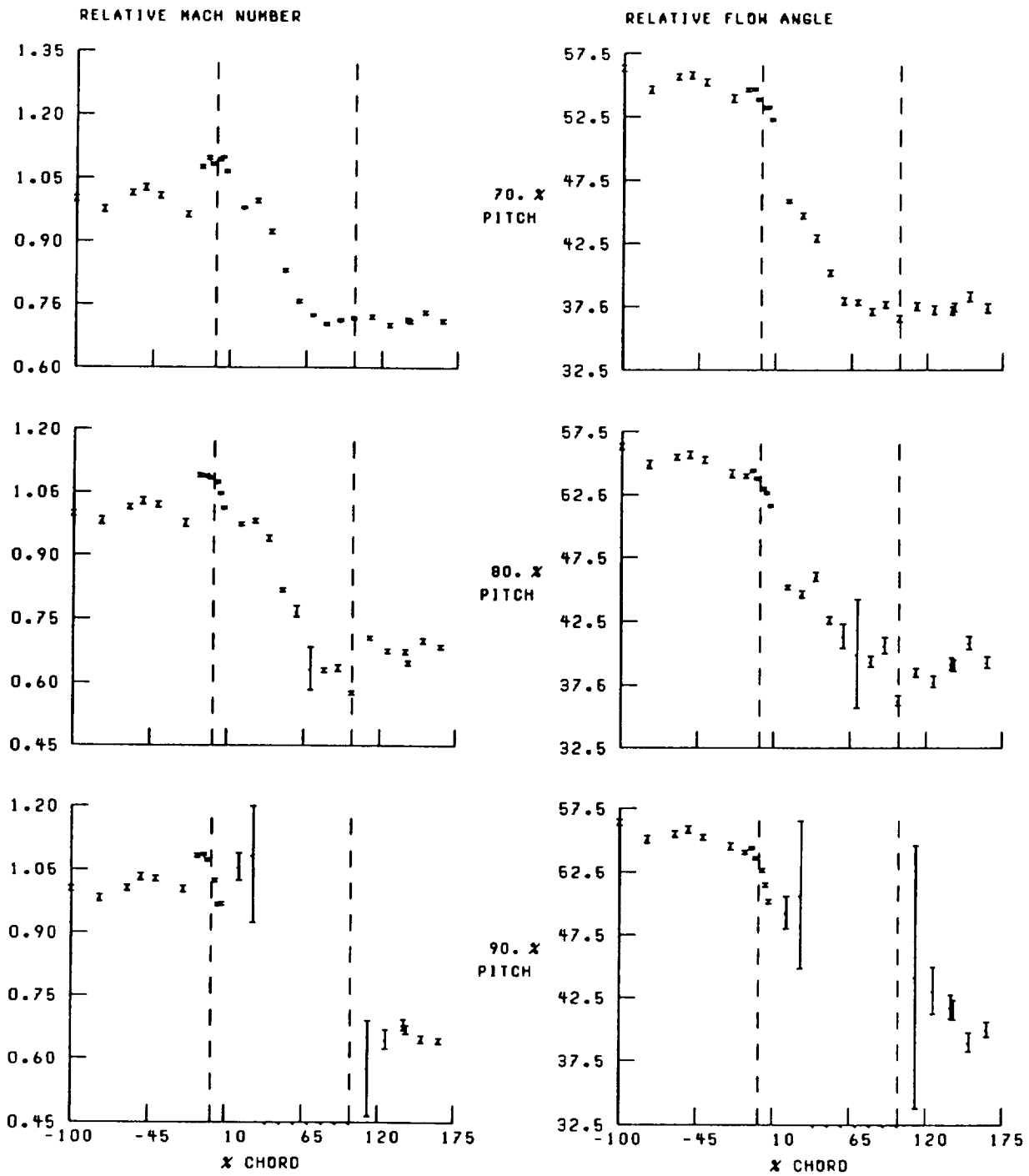


Figure 28.—Concluded.

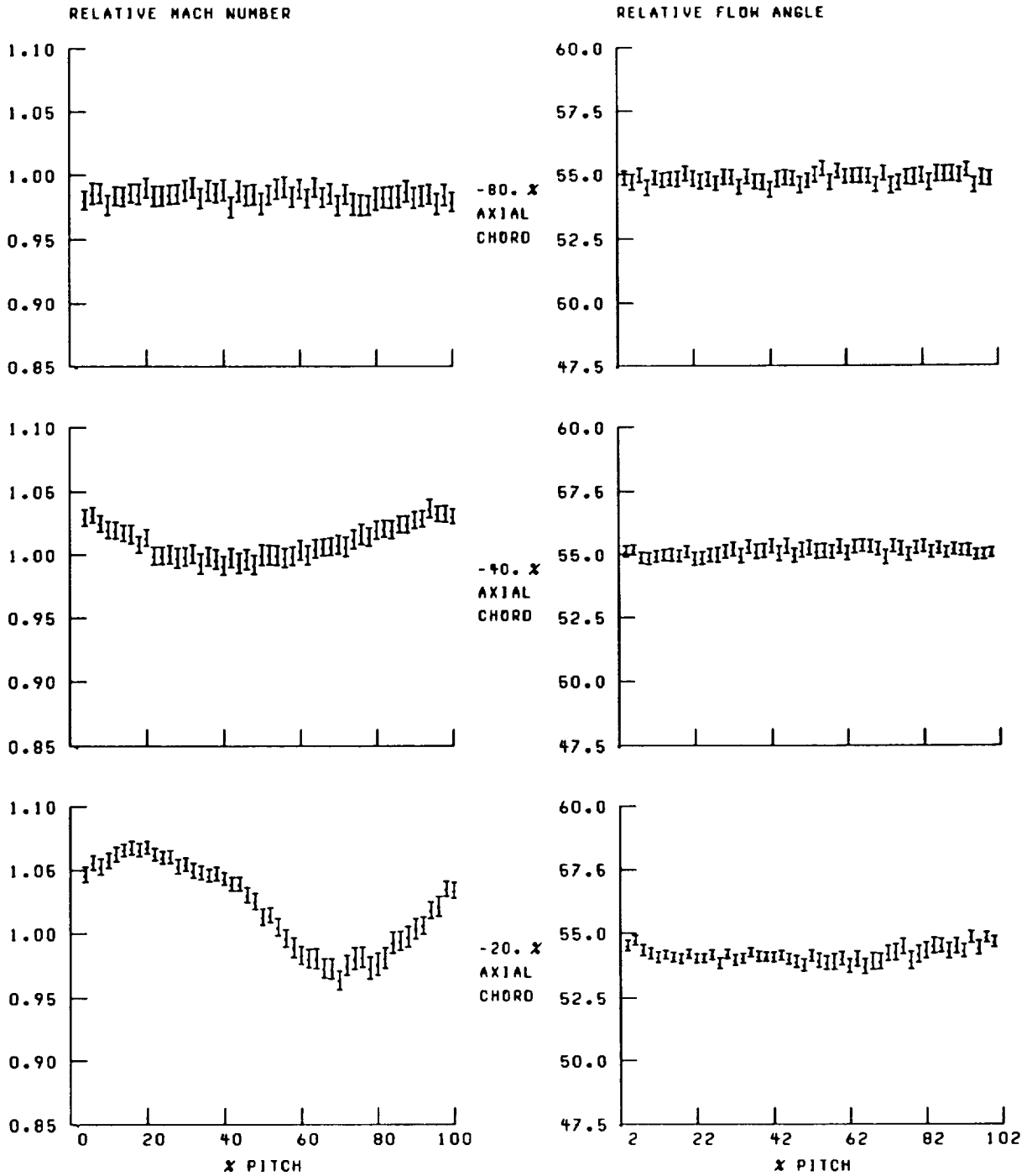


Figure 29.—Blade-to-blade distribution of relative Mach number and flow angle at 60-percent span and near peak efficiency.

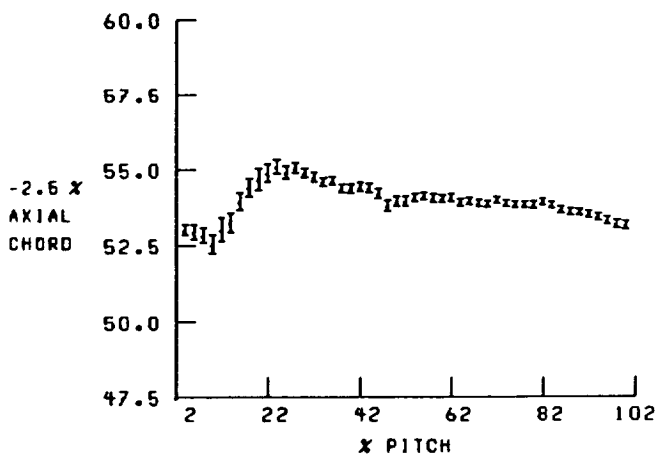
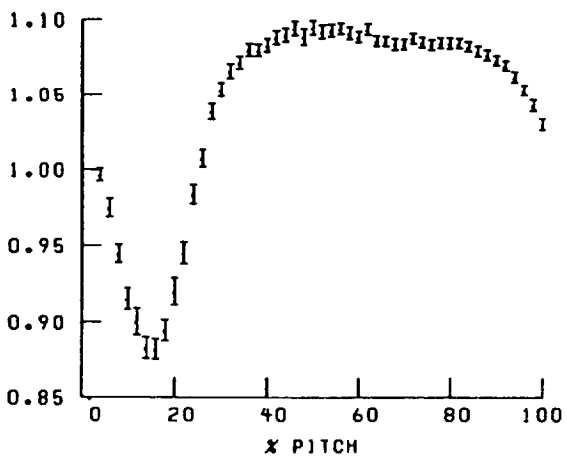
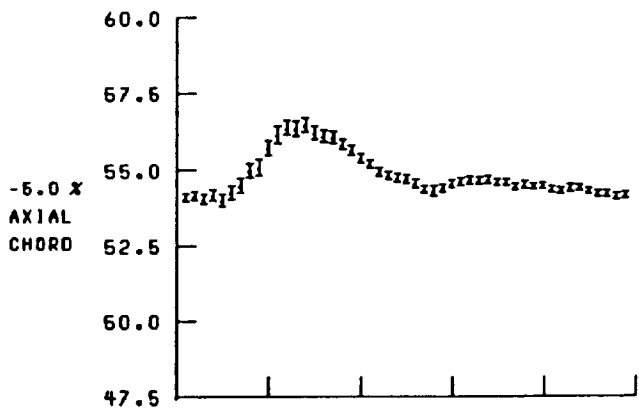
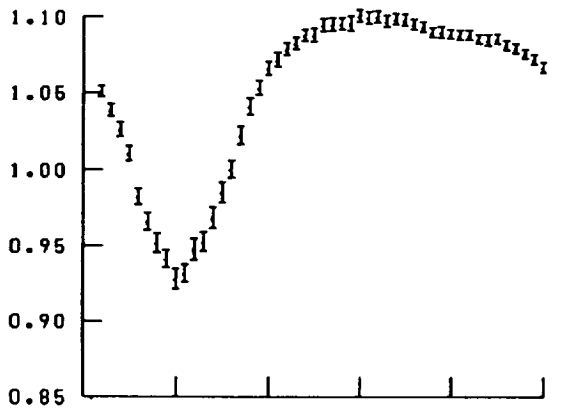
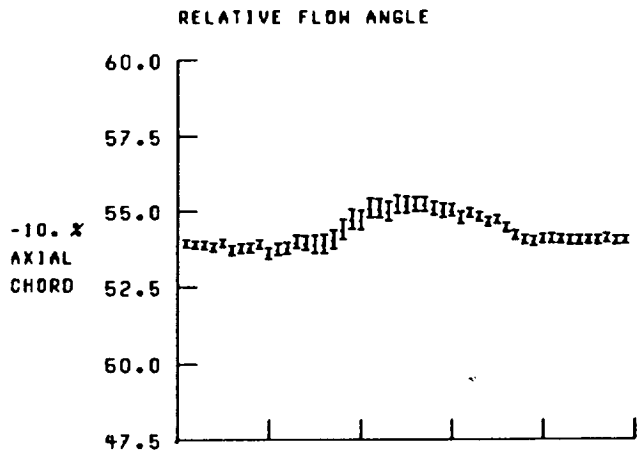
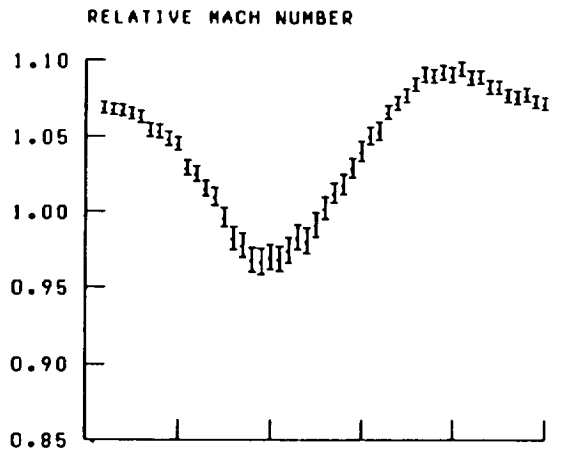


Figure 29.—Continued.

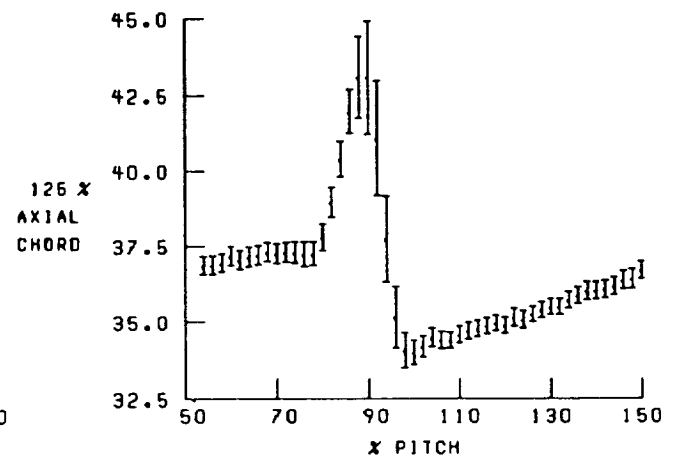
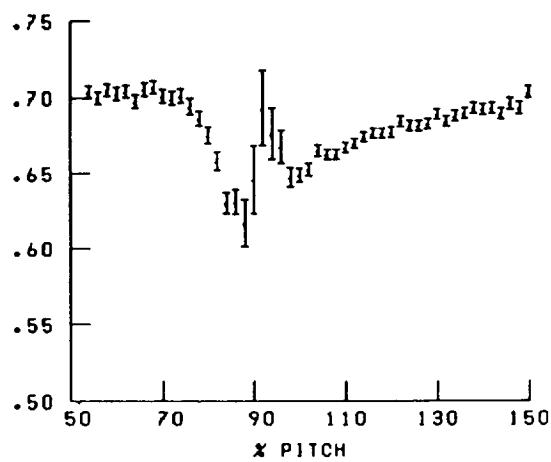
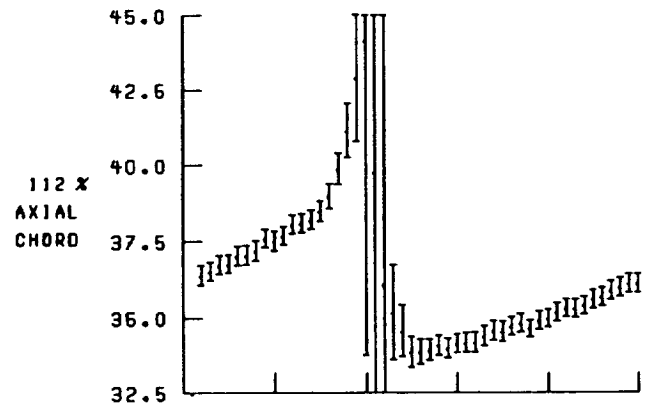
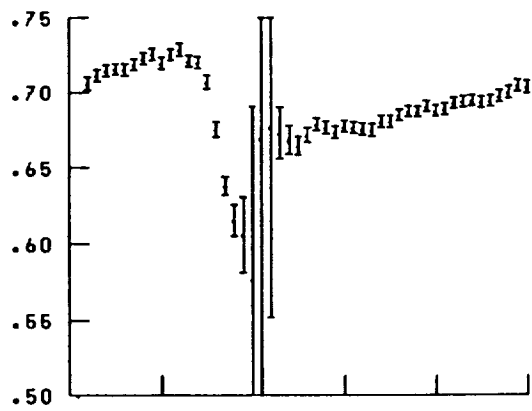
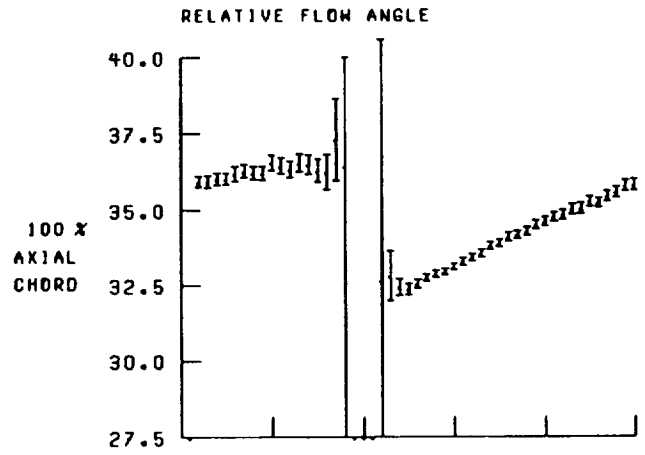
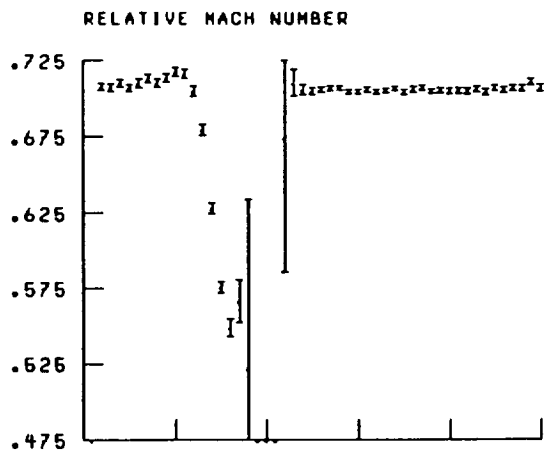


Figure 29.—Continued.

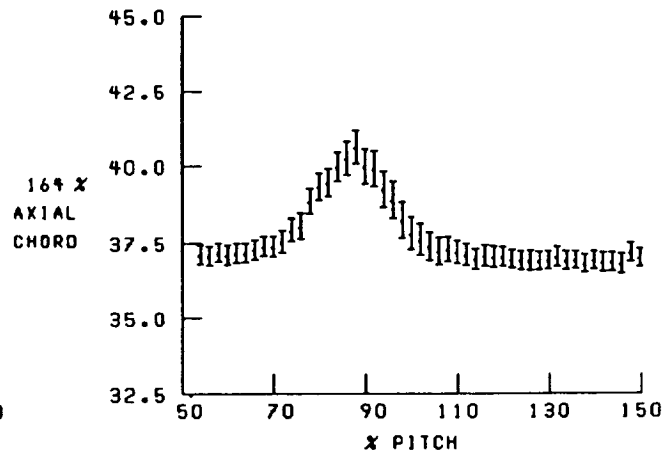
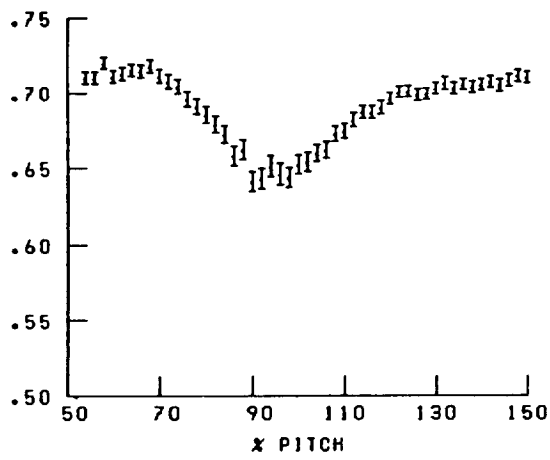
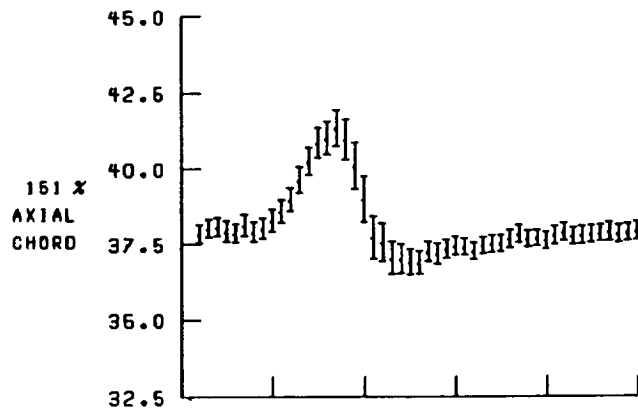
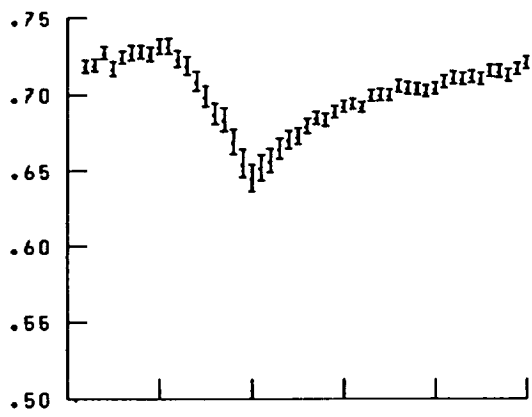
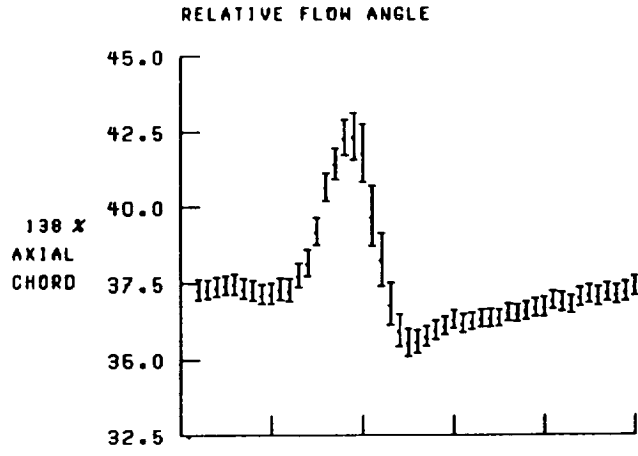
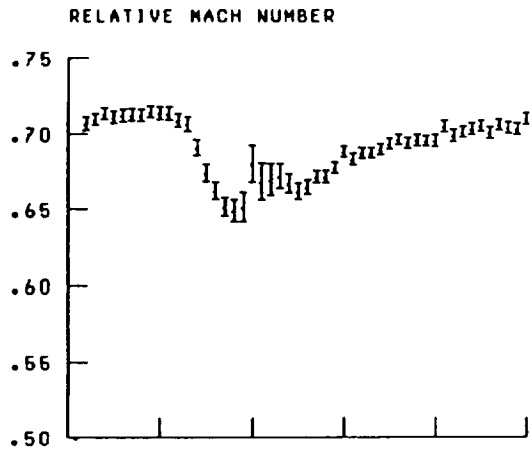


Figure 29.—Concluded.

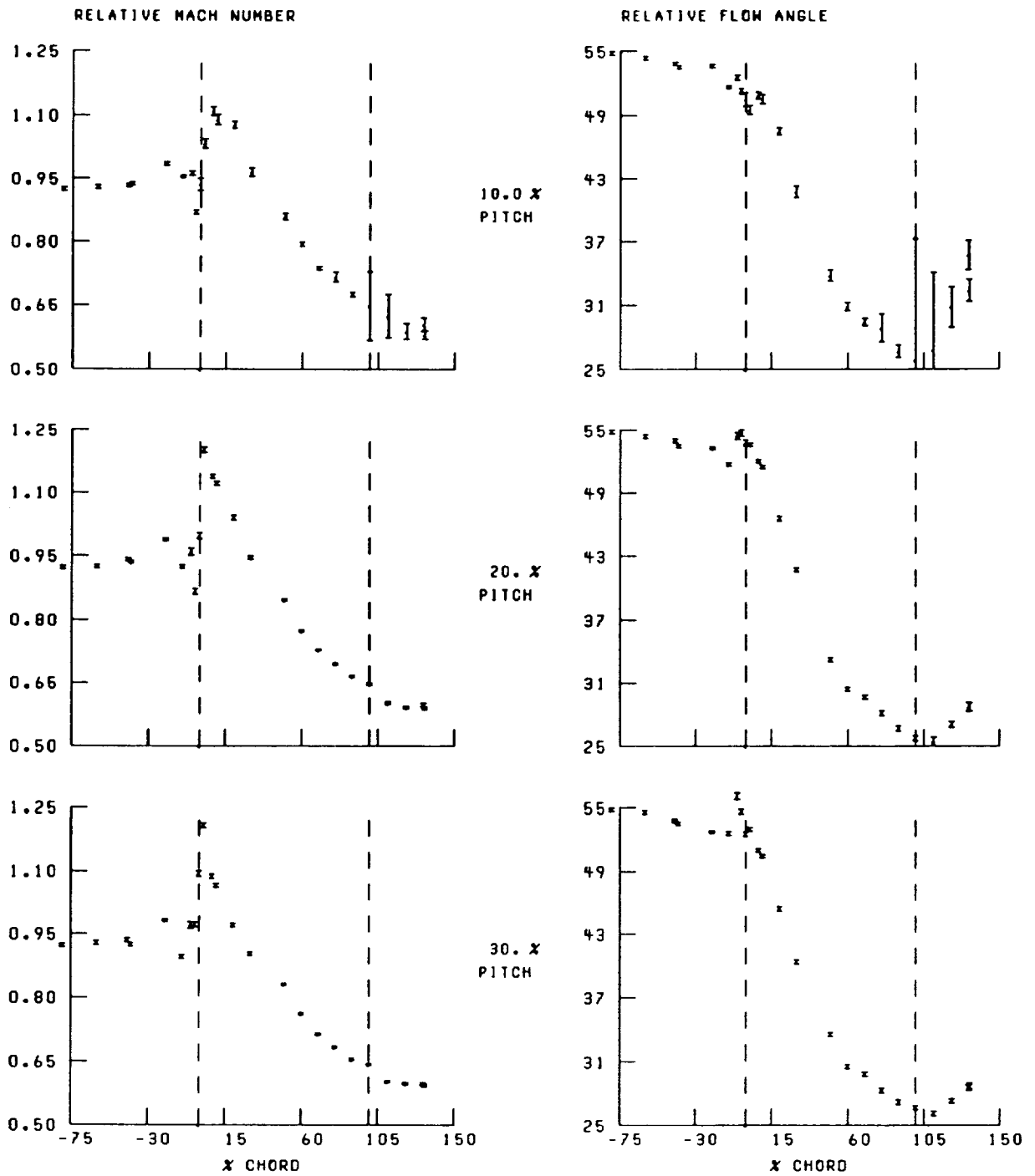


Figure 30.—Streamwise distribution of relative Mach number and flow angle at 70-percent span and near peak efficiency. Broken lines denote location of blade leading and trailing edges.

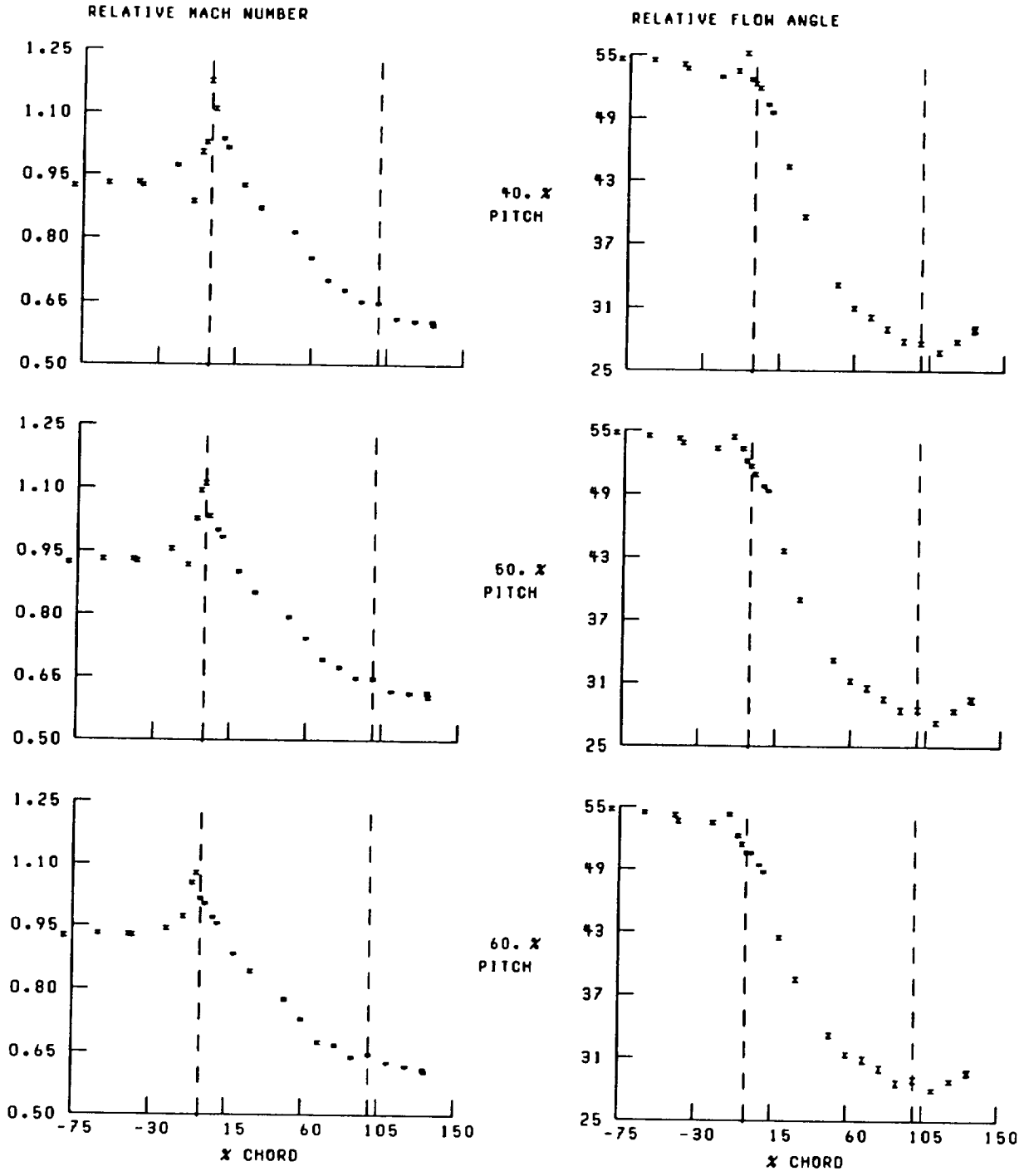


Figure 30.—Continued.

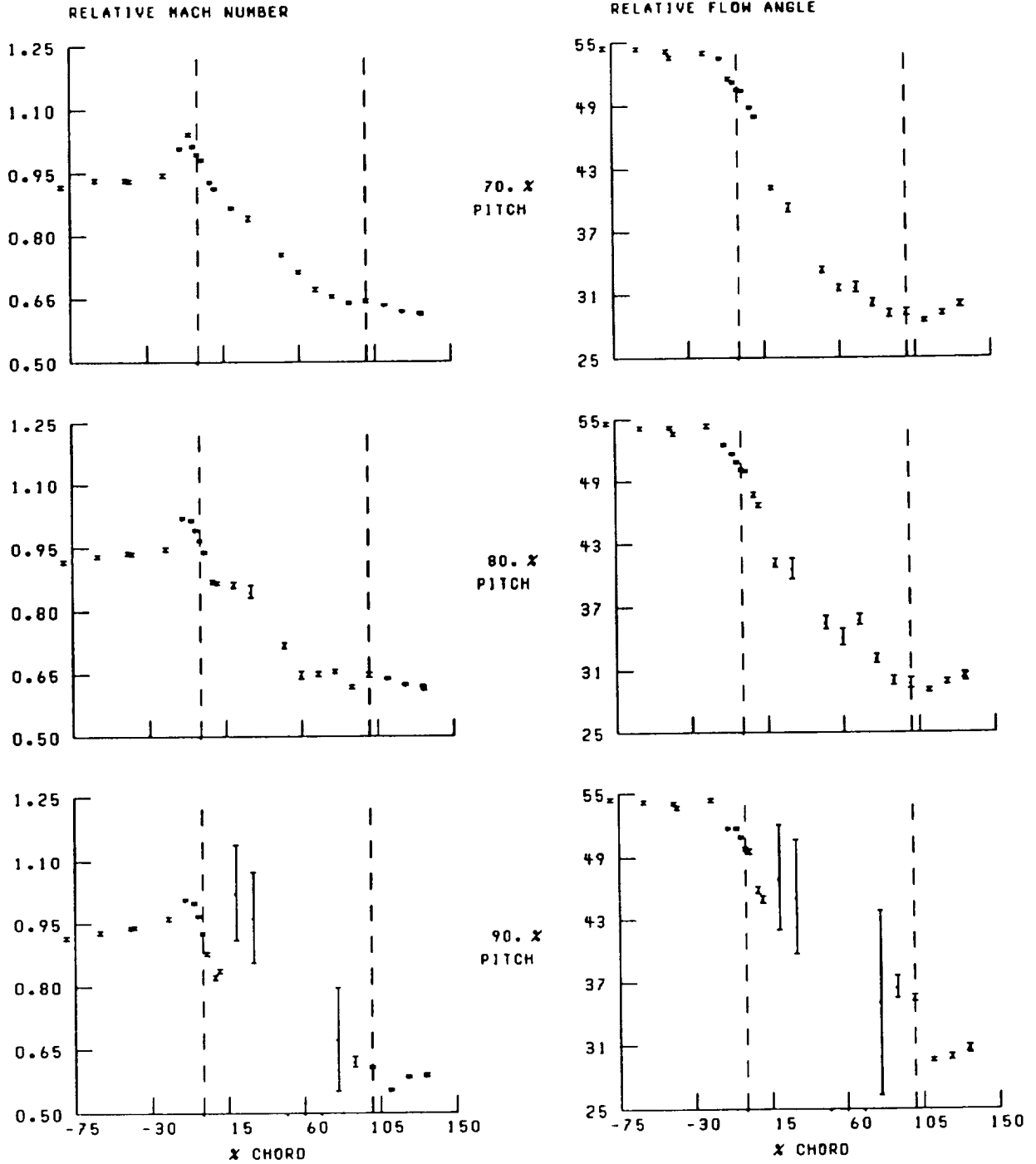


Figure 30.—Concluded.

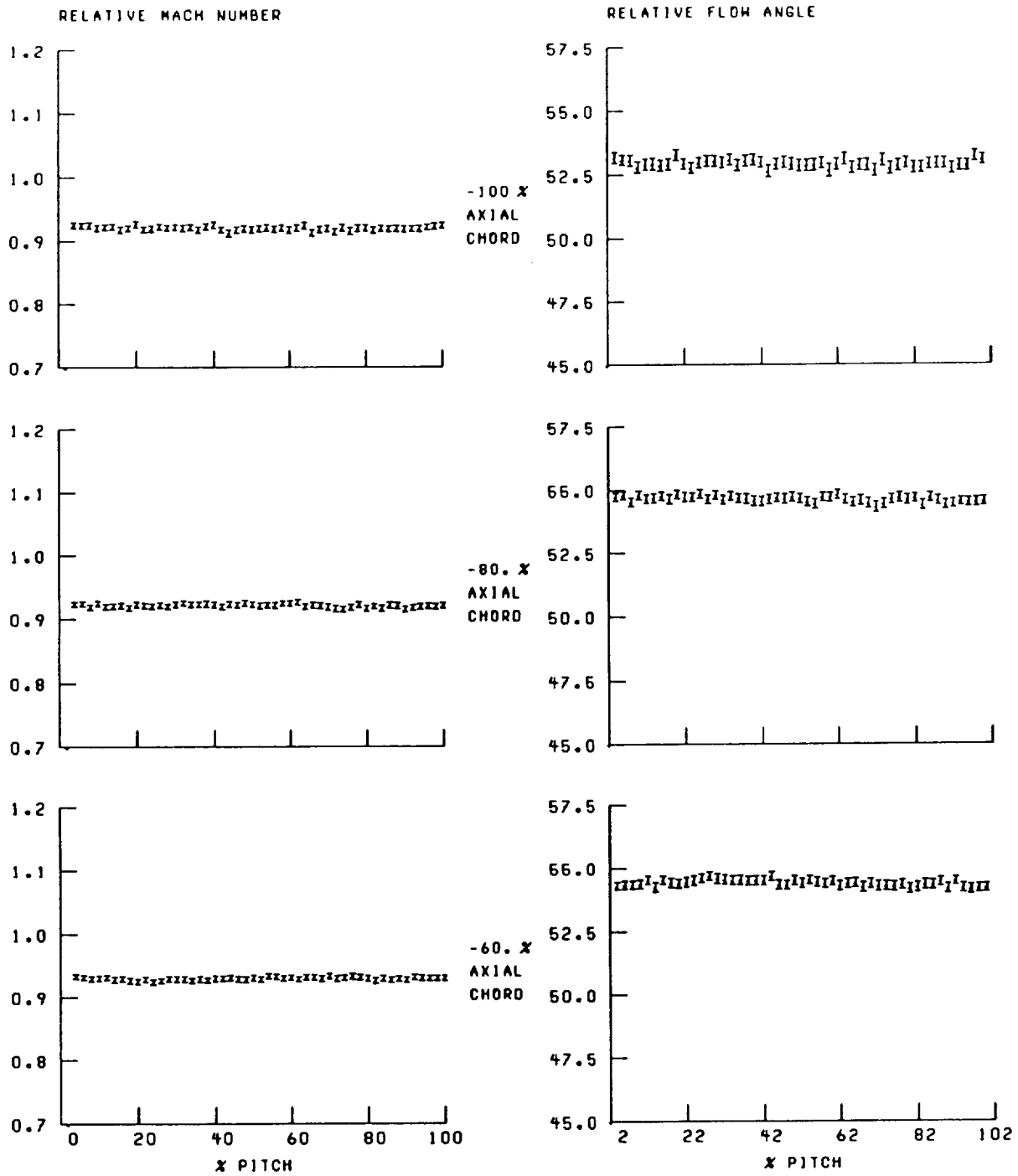


Figure 31.—Blade-to-blade distribution of relative Mach number and flow angle at 70-percent span and near peak efficiency.

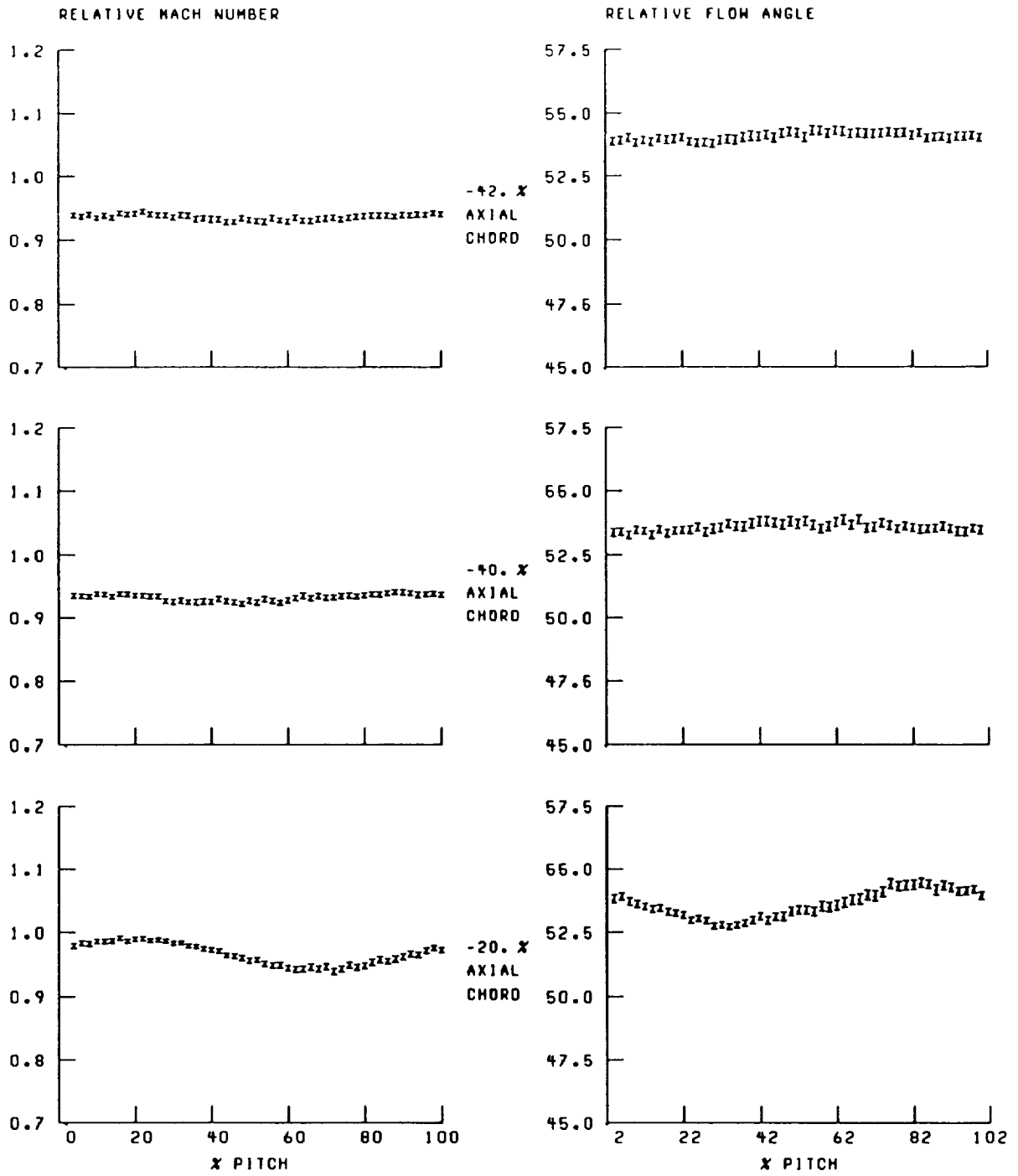


Figure 31.—Continued.

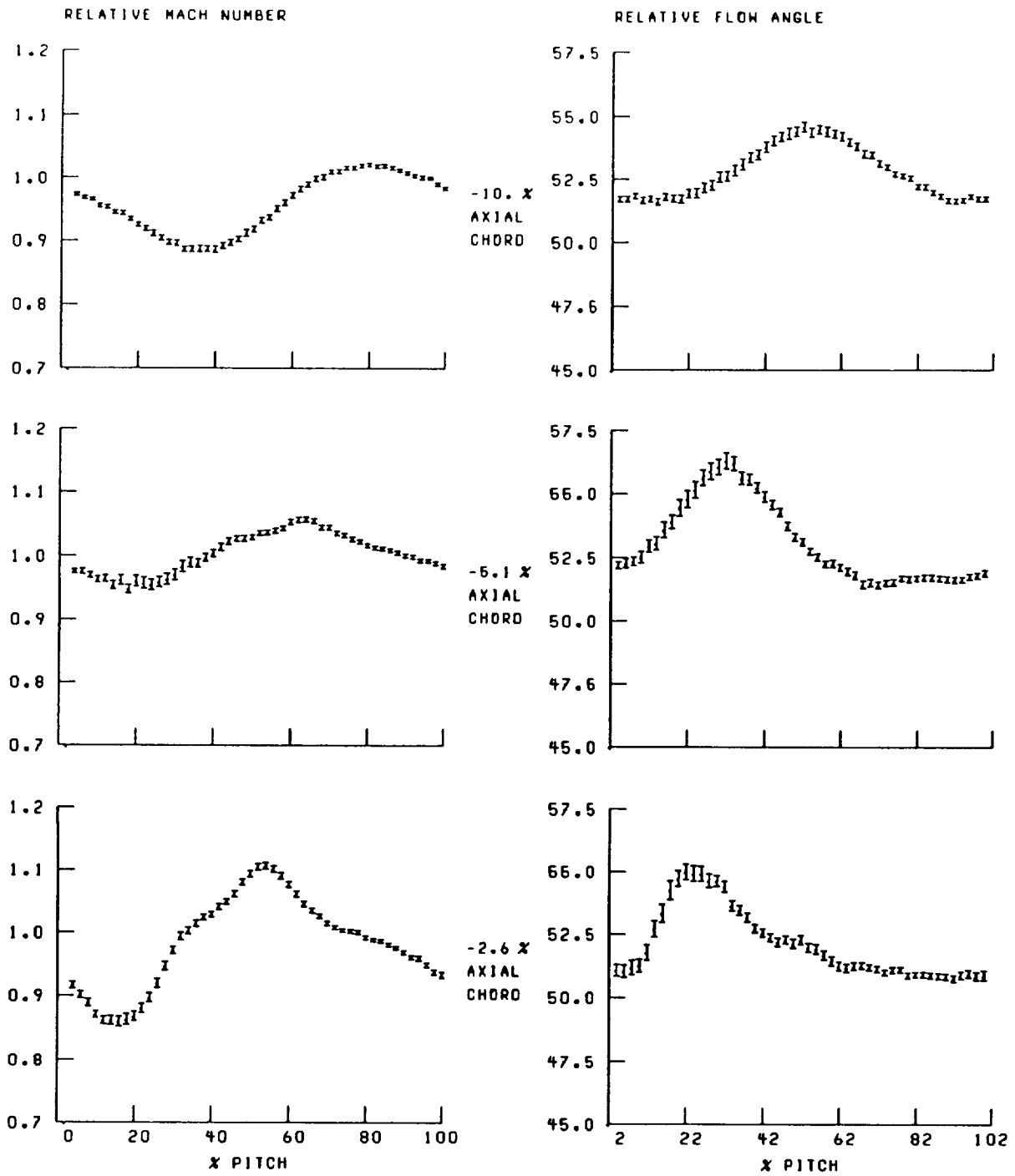


Figure 31.—Continued.

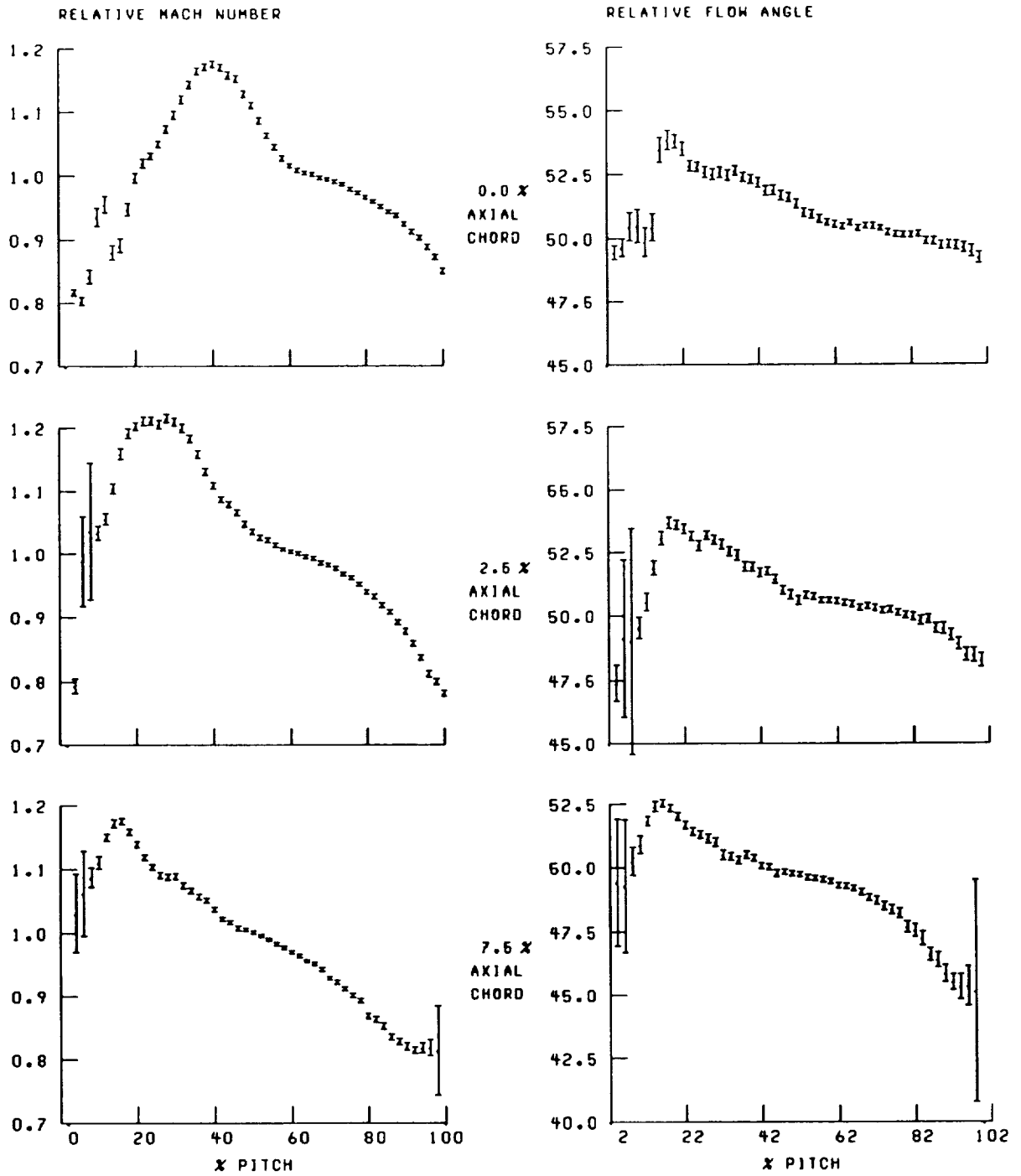


Figure 31.—Continued.

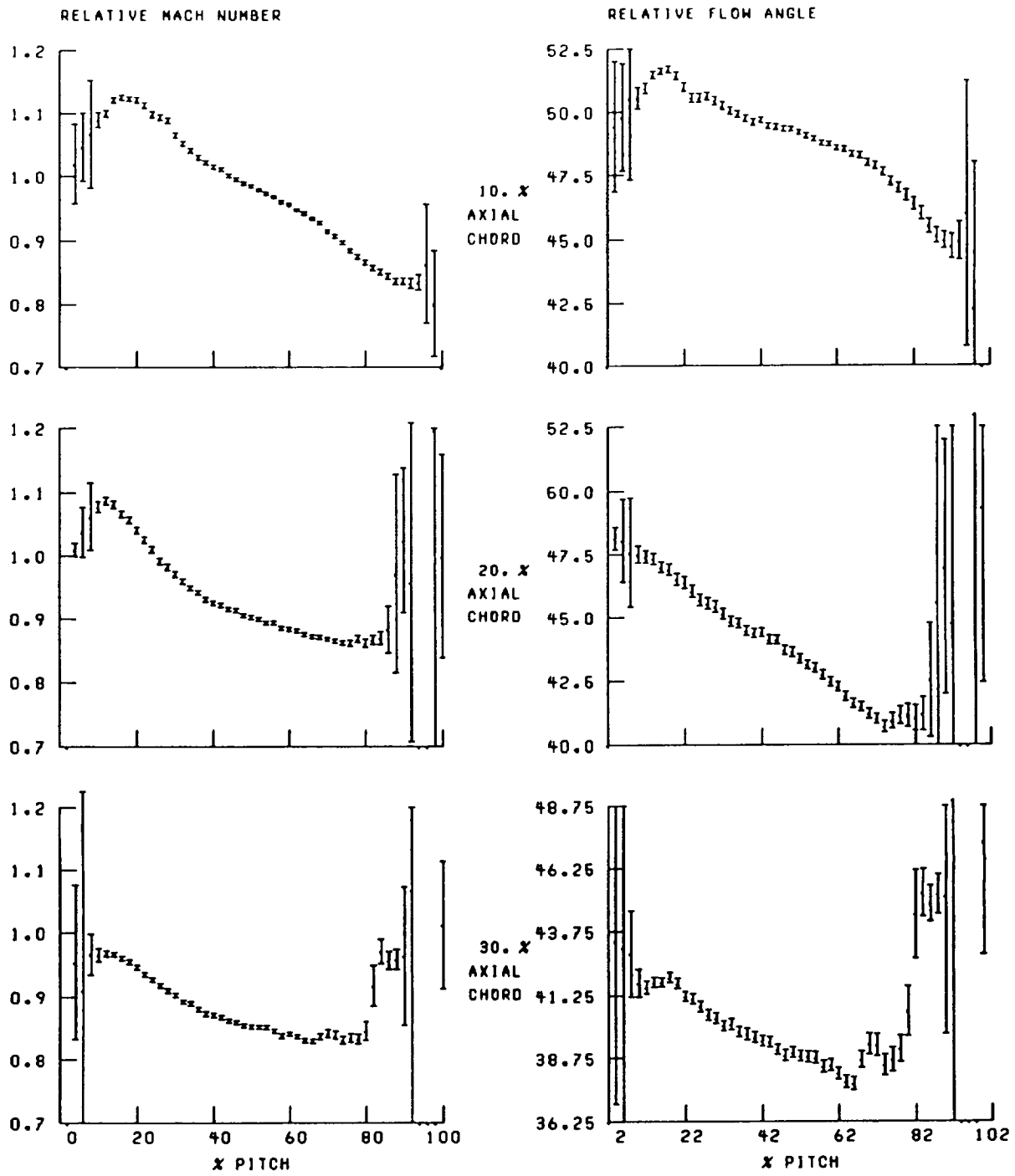


Figure 31.—Continued.

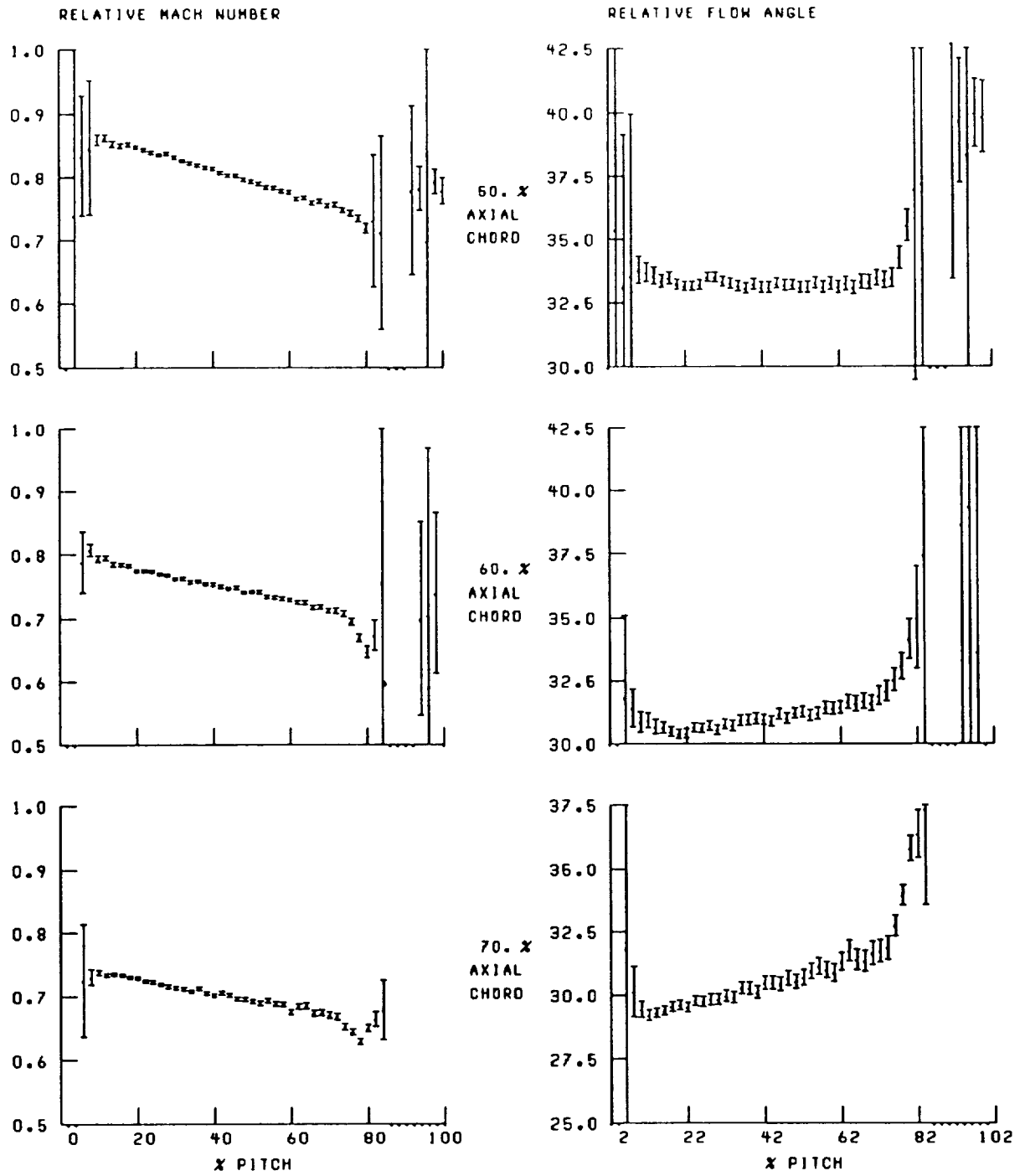


Figure 31.—Continued.

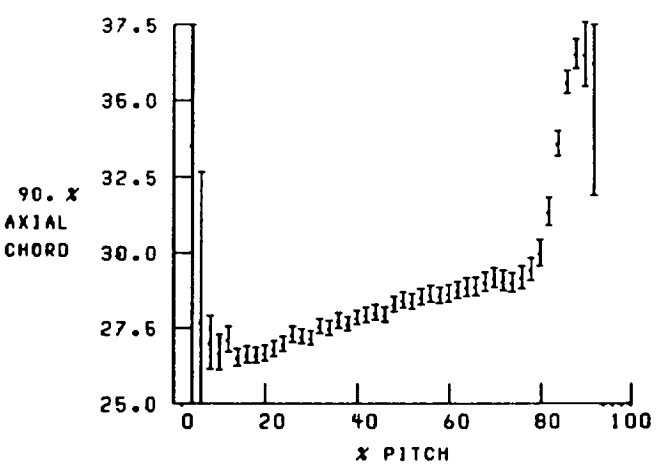
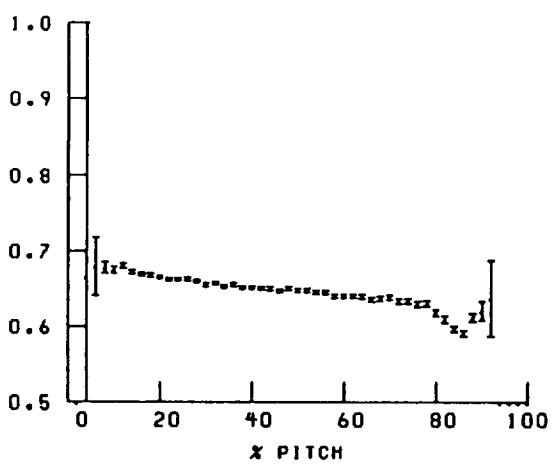
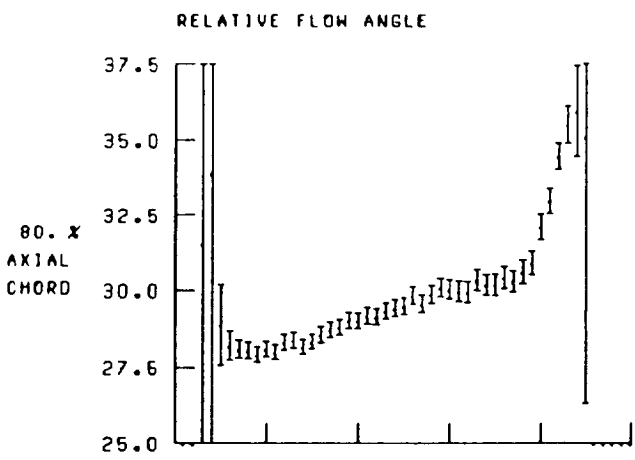
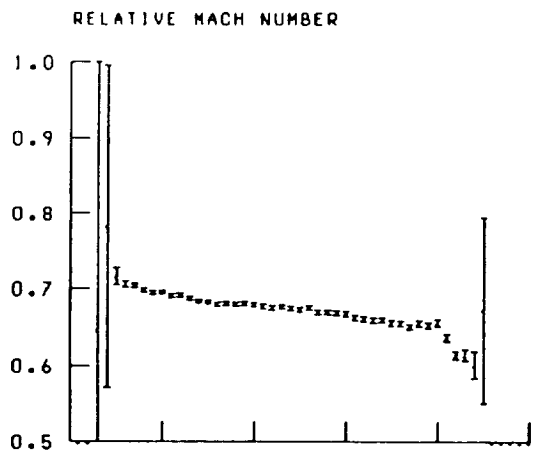


Figure 31.—Continued.

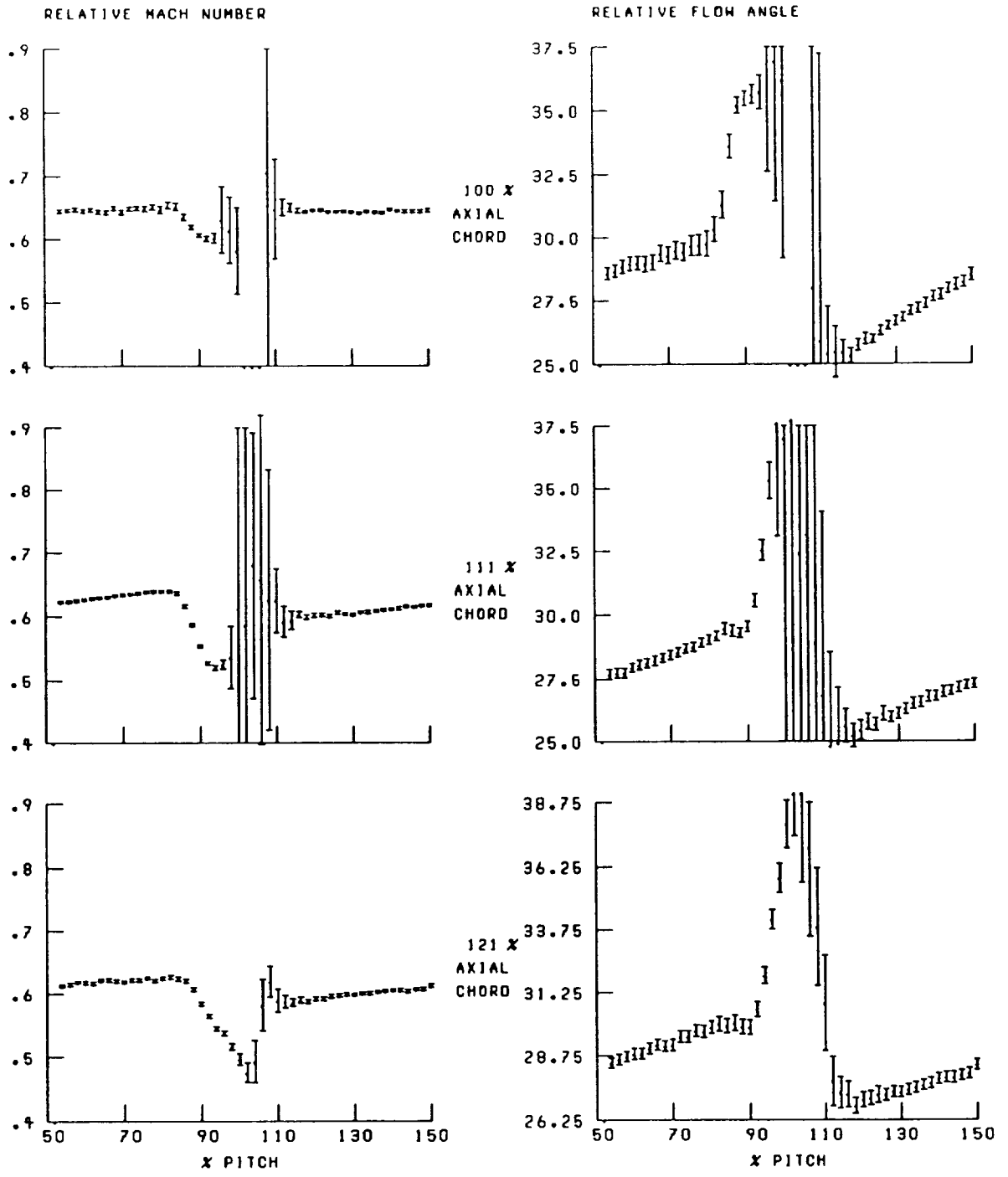


Figure 31.—Continued.

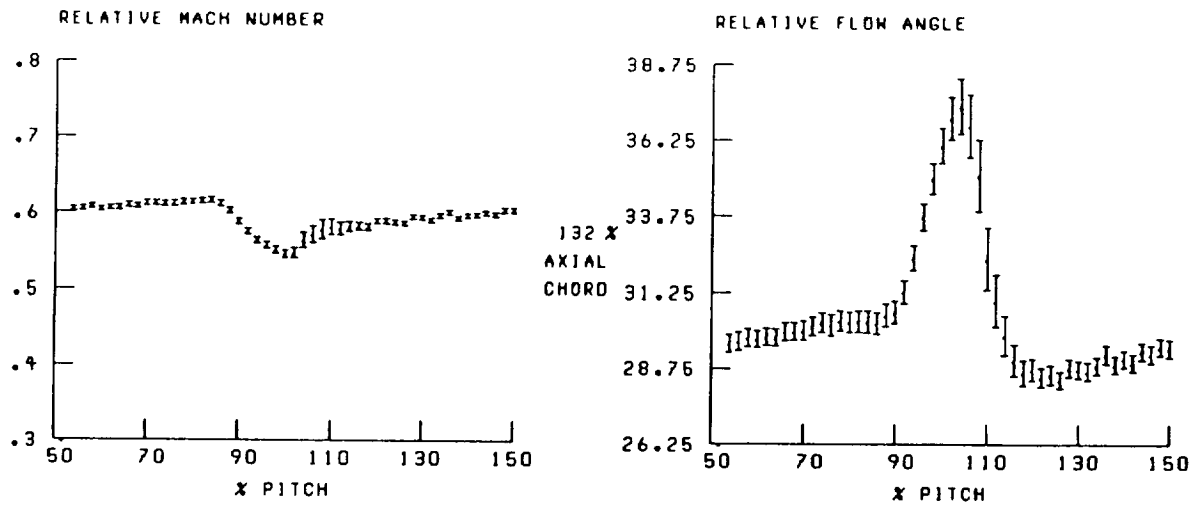


Figure 31.—Concluded.

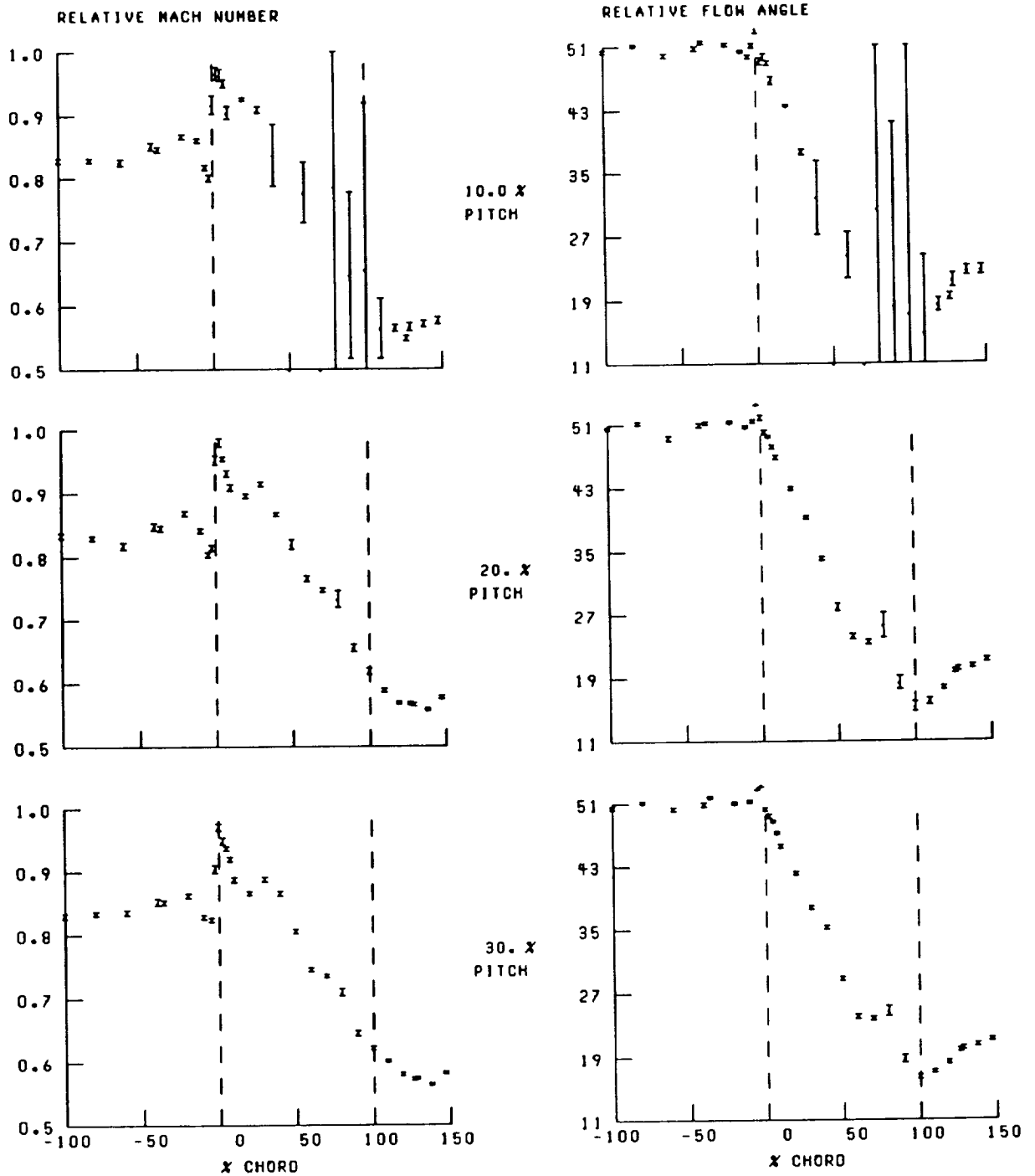


Figure 32.—Streamwise distribution of relative Mach number and flow angle at 80-percent span and near peak efficiency. Broken lines denote location of blade leading and trailing edges.

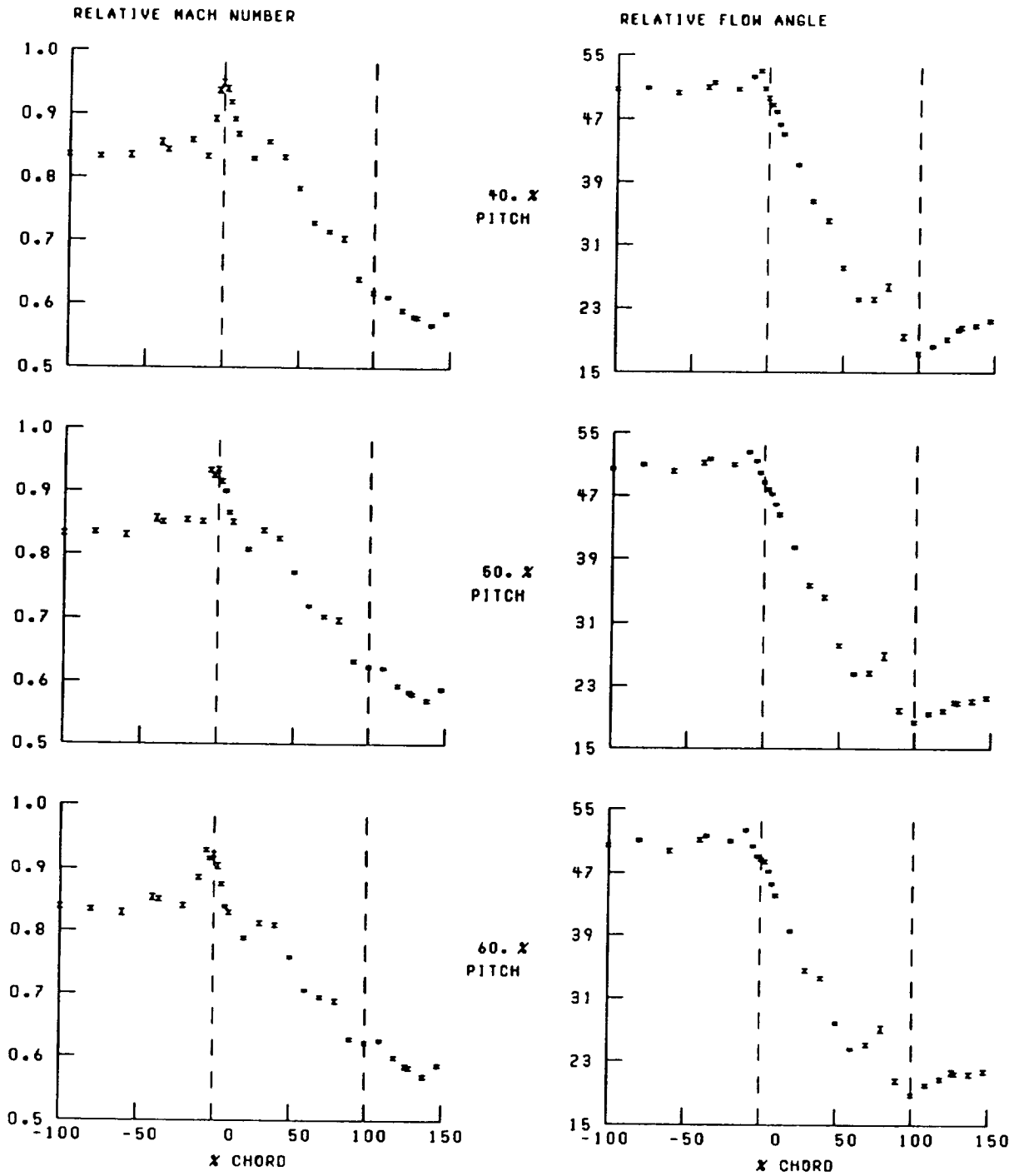


Figure 32.—Continued.

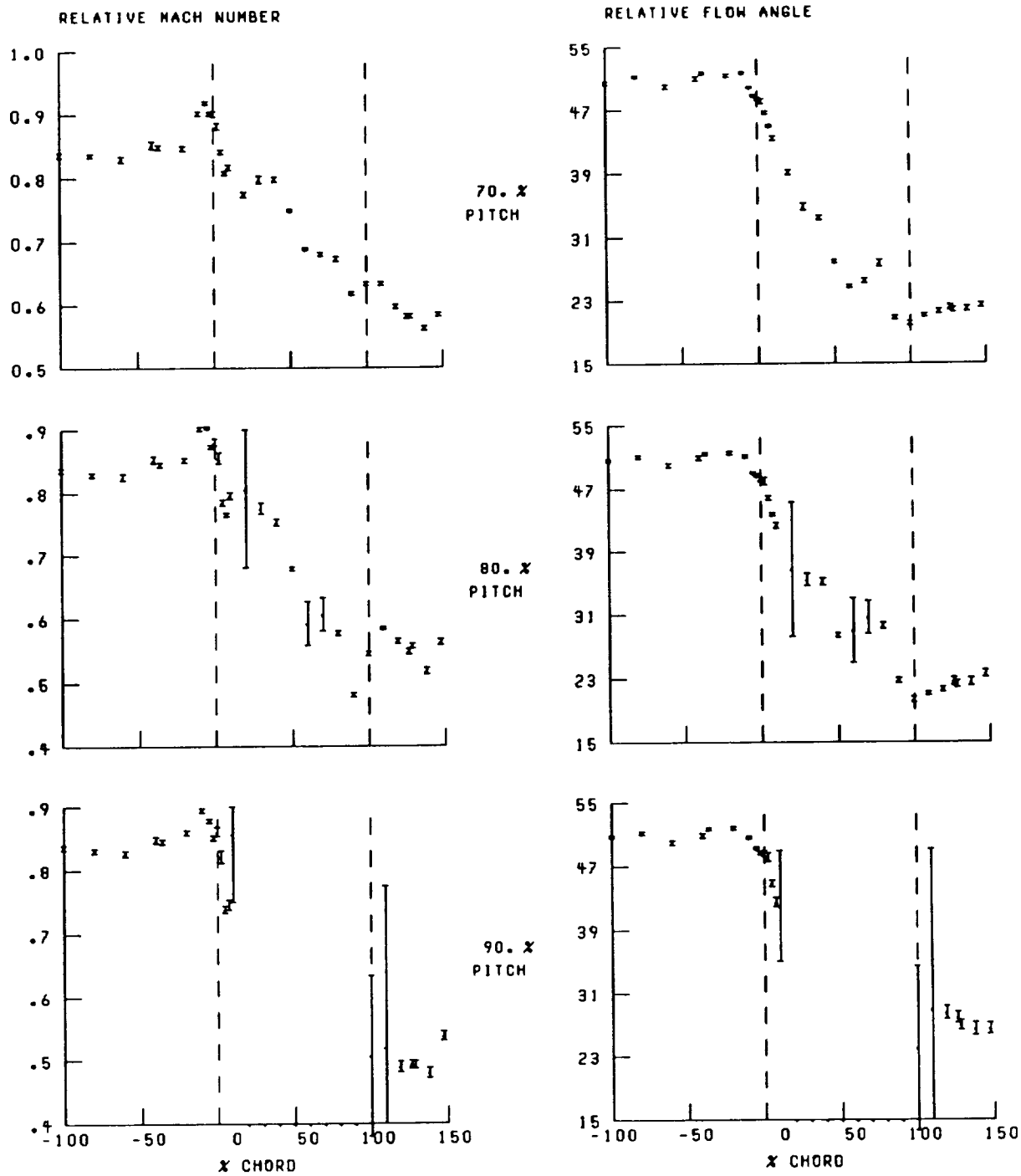


Figure 32.—Concluded.

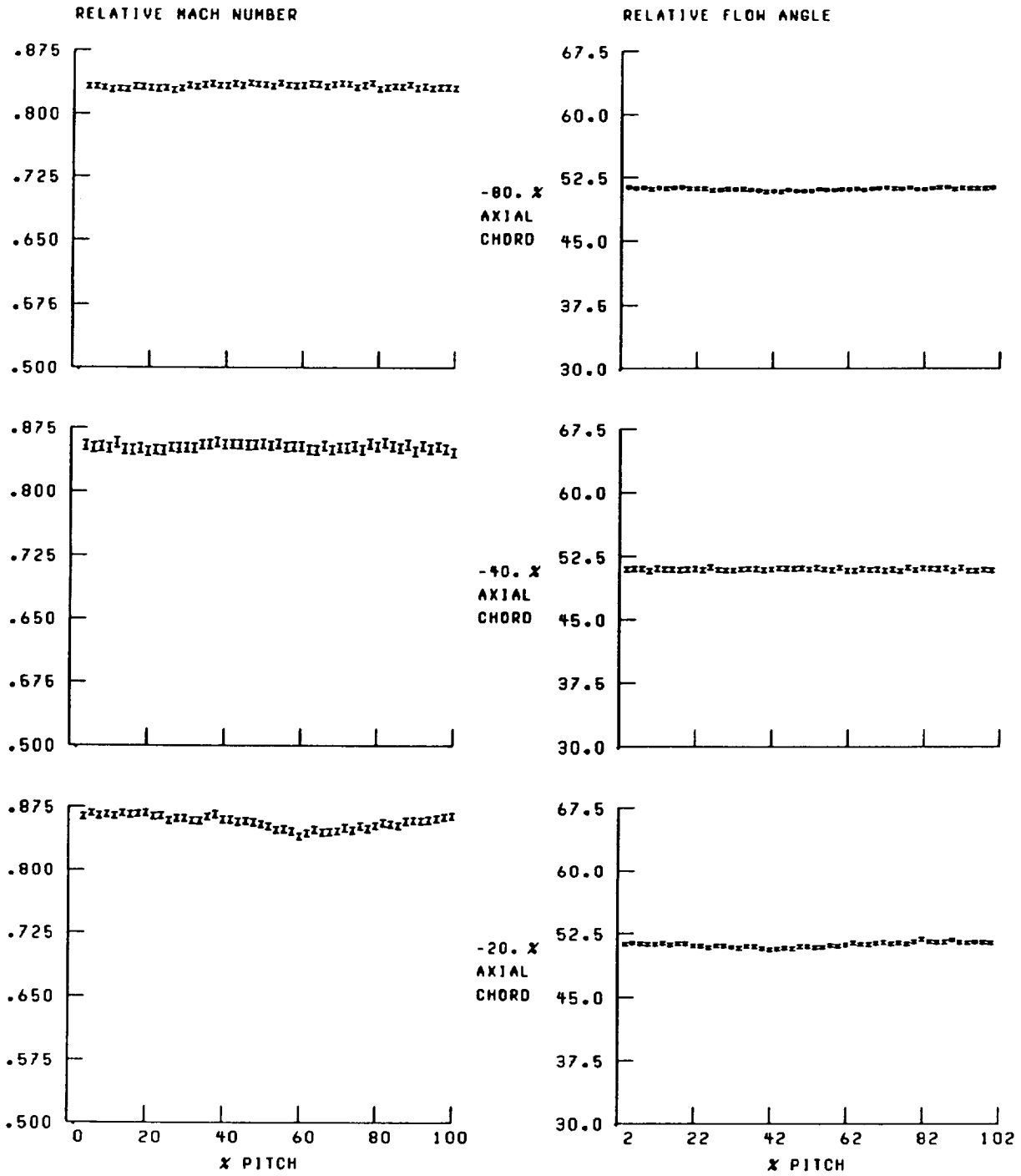


Figure 33.—Blade-to-blade distribution of relative Mach number and flow angle at 80-percent span and near peak efficiency.

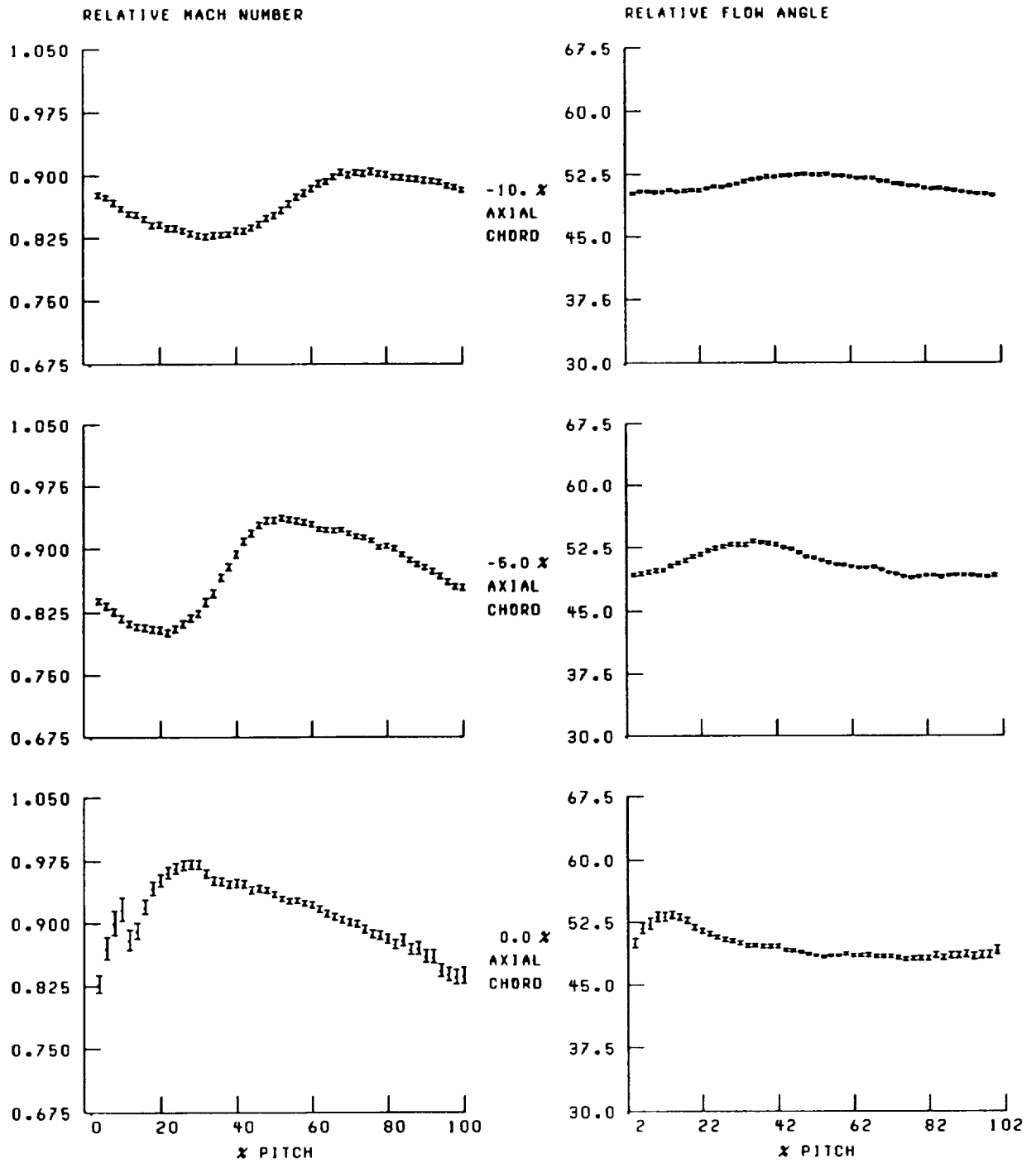


Figure 33.—Continued.

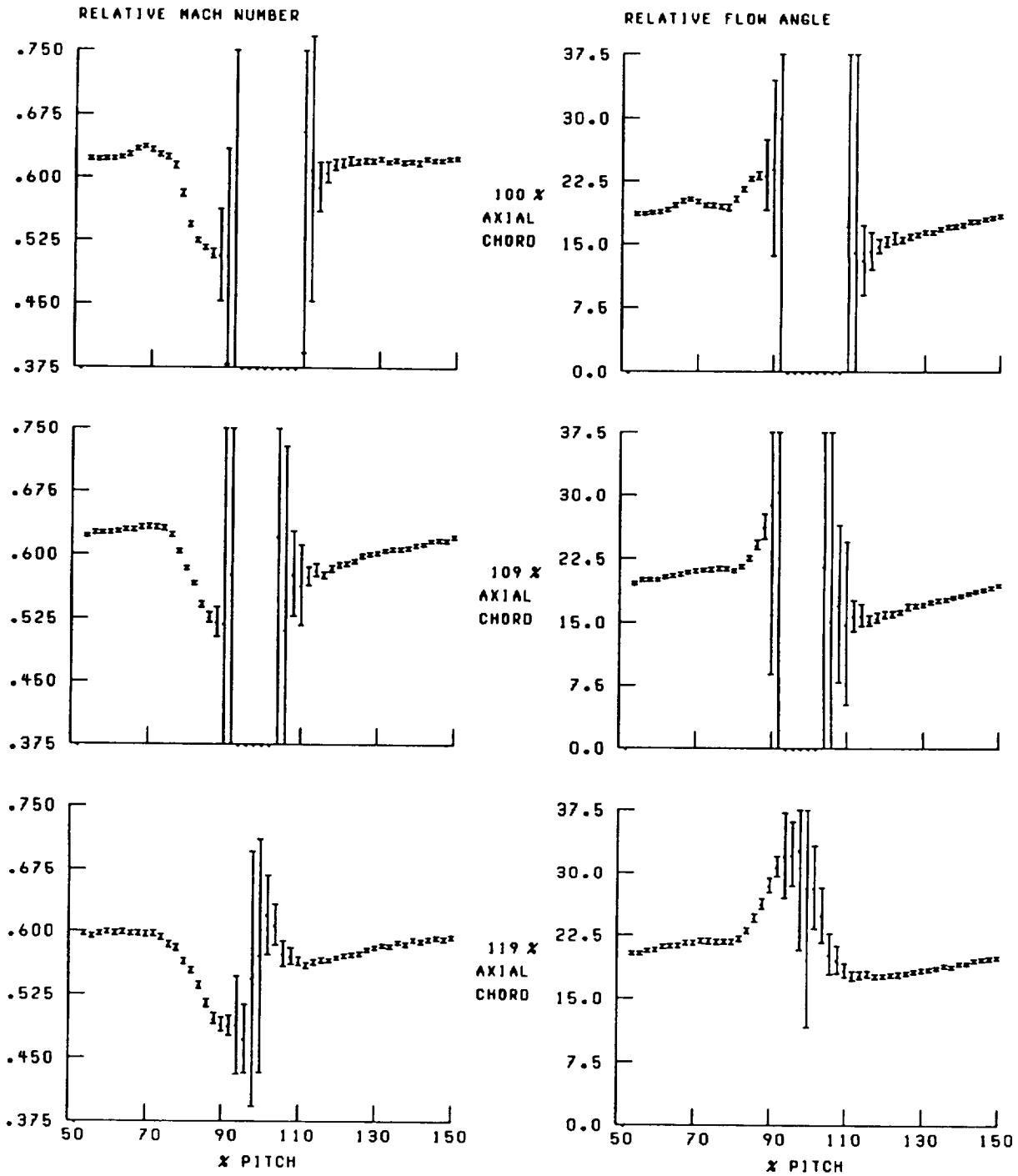


Figure 33.—Continued.

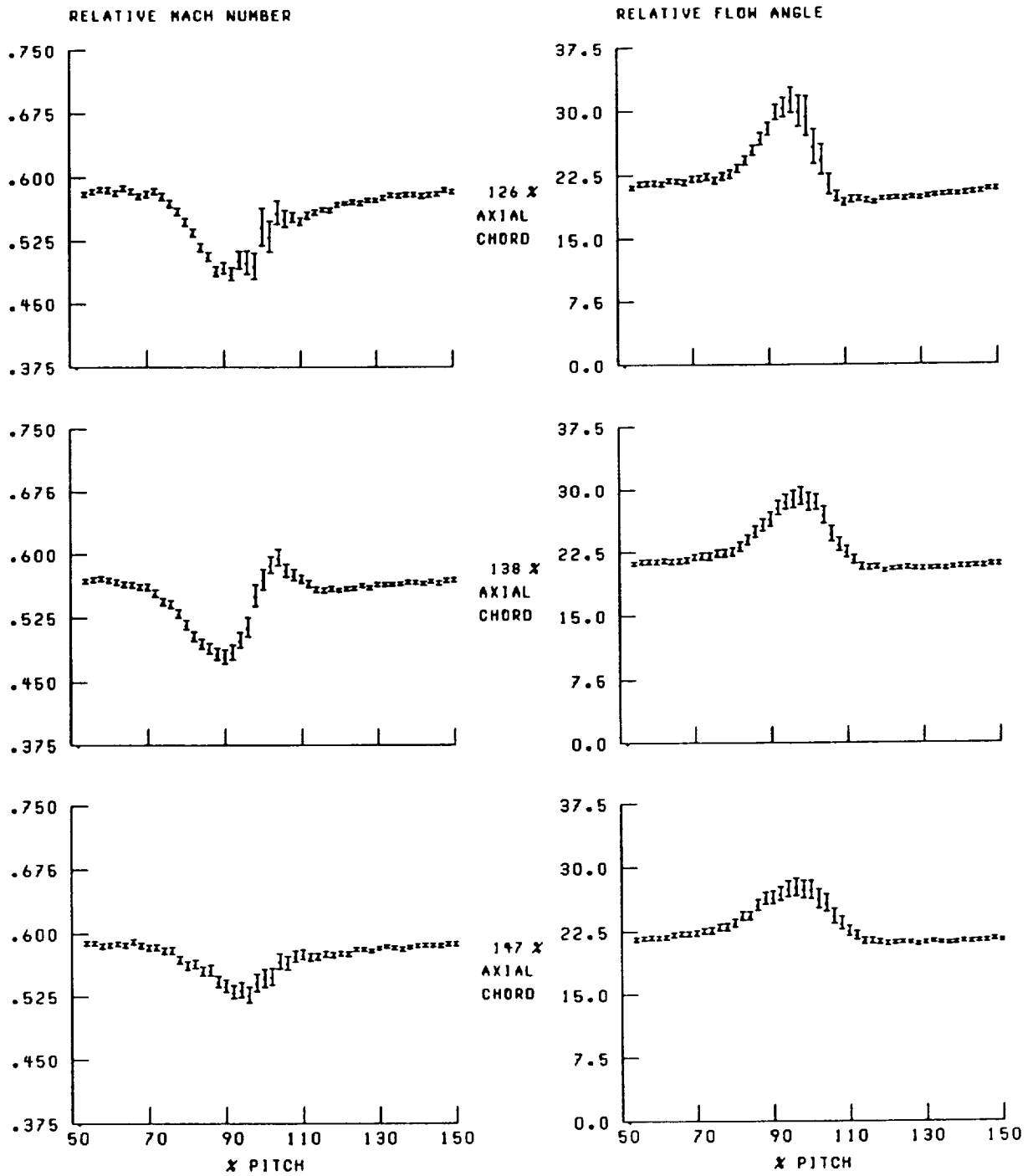


Figure 33.—Concluded.

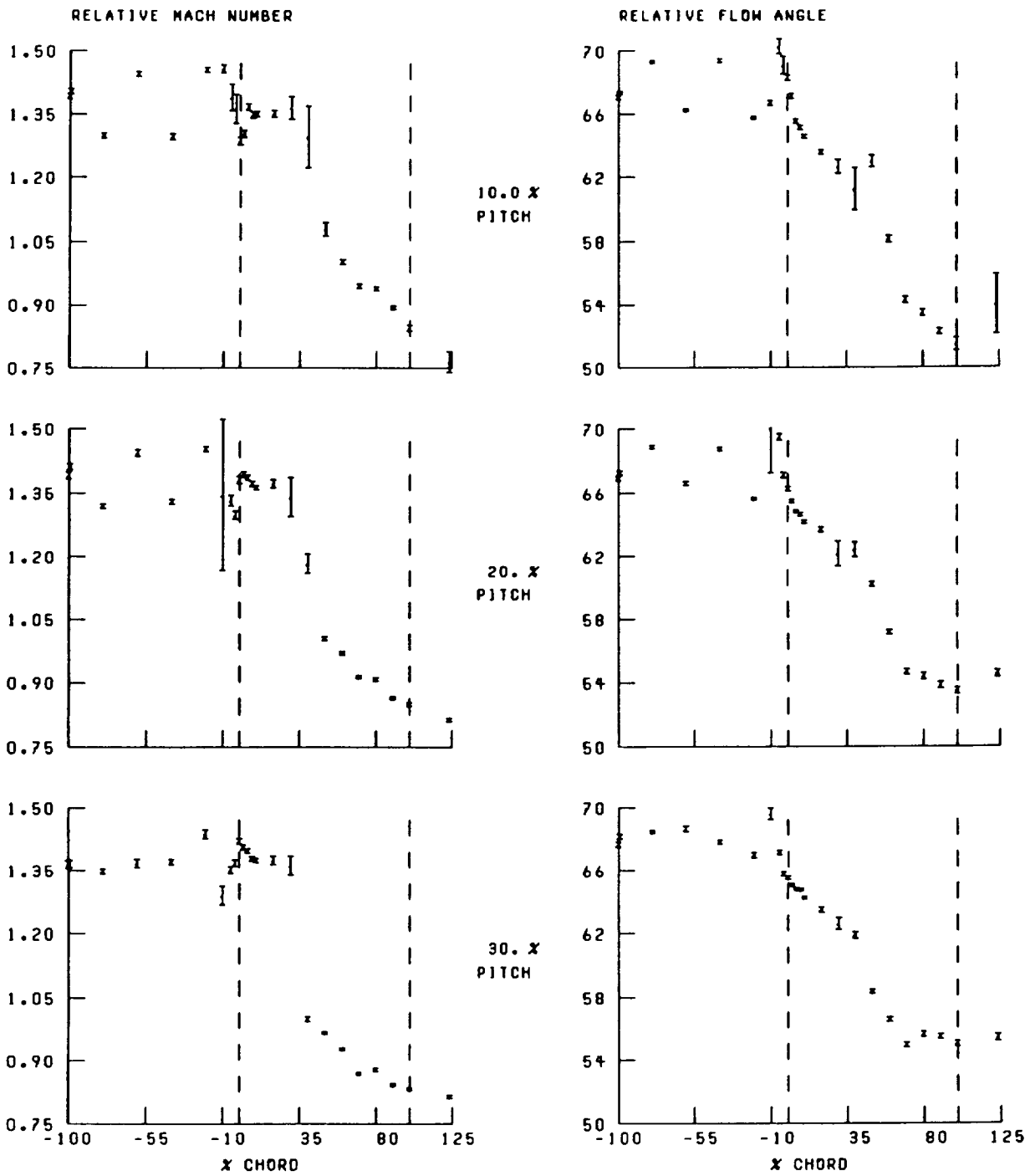


Figure 34.—Streamwise distribution of relative Mach number and flow angle at 10-percent span and near stall. Broken lines denote location of blade leading and trailing edges.

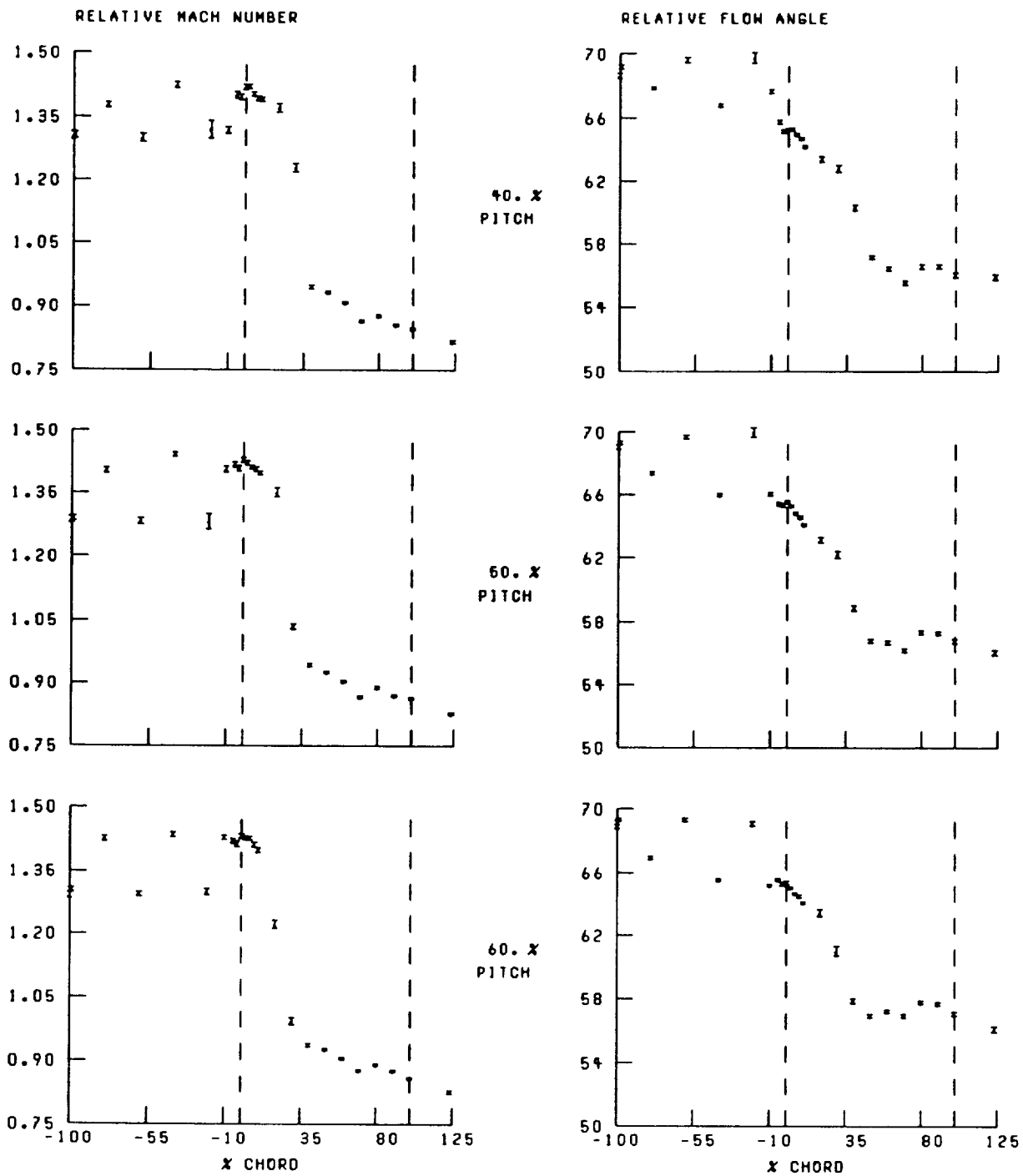


Figure 34.—Continued.

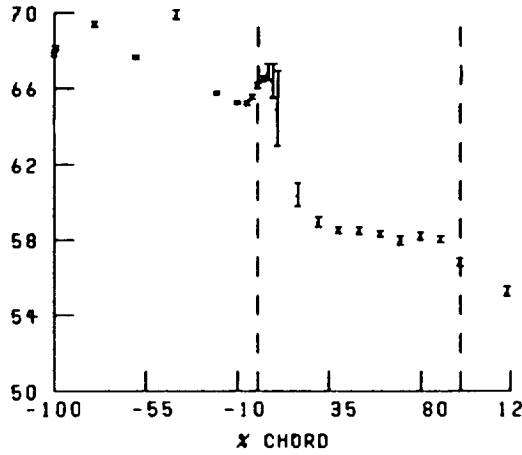
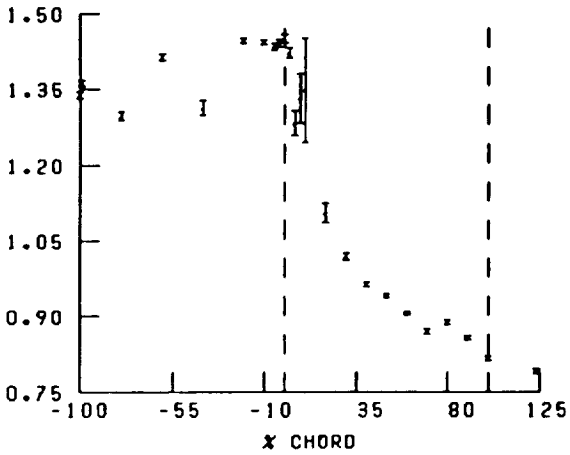
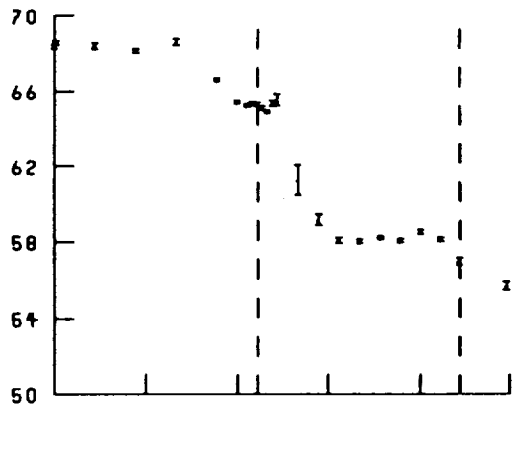
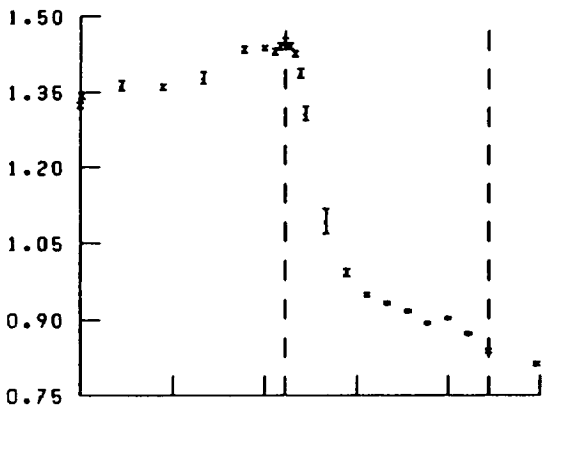
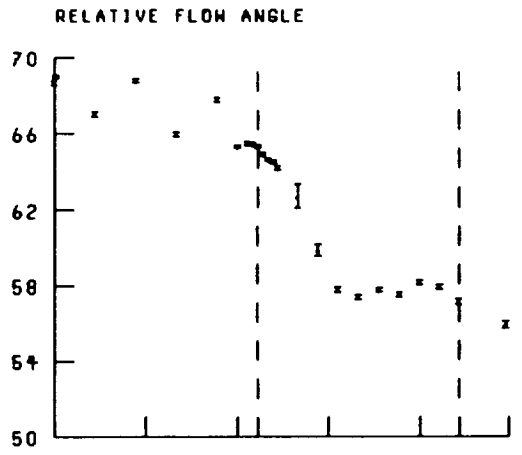
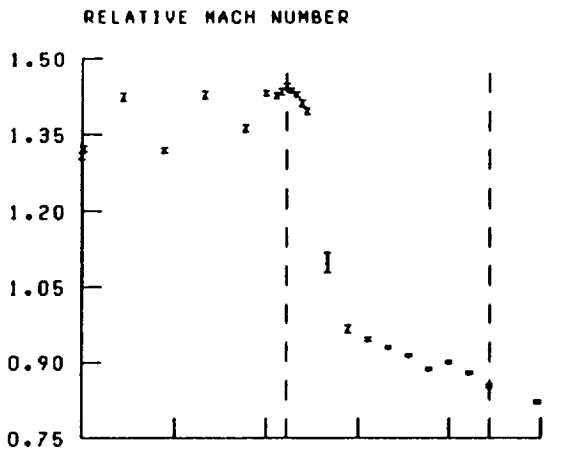


Figure 34.—Concluded.

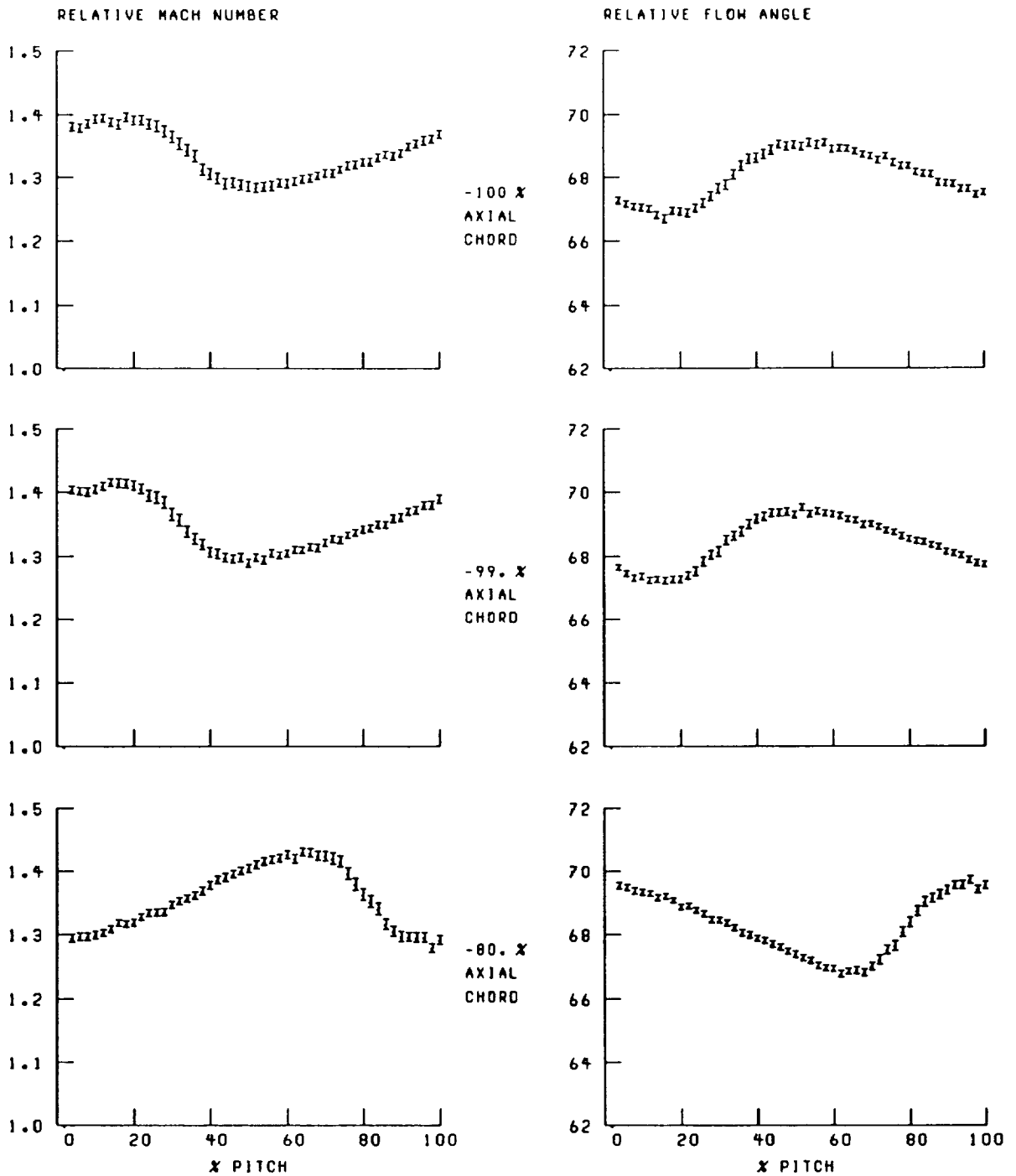


Figure 35.—Blade-to-blade distribution of relative Mach number and flow angle at 10-percent span and near stall.

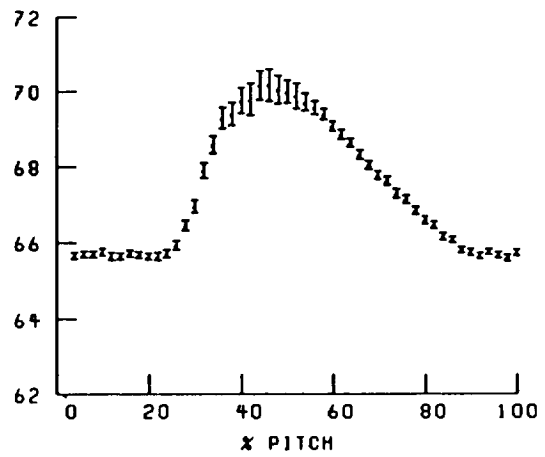
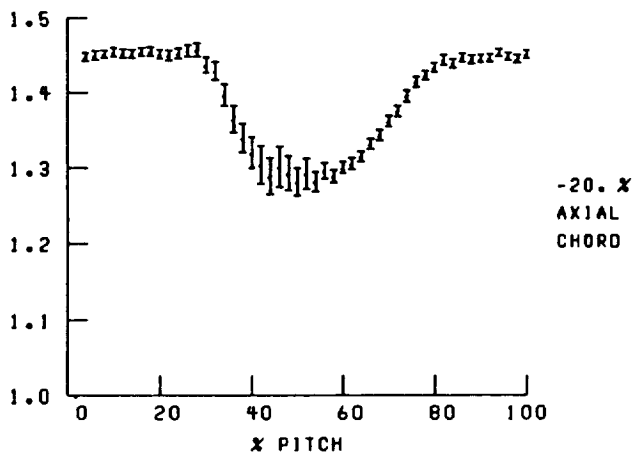
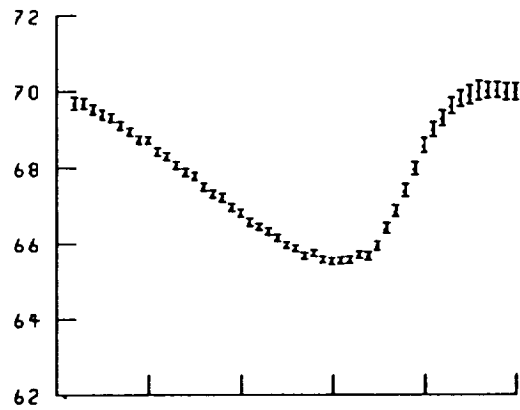
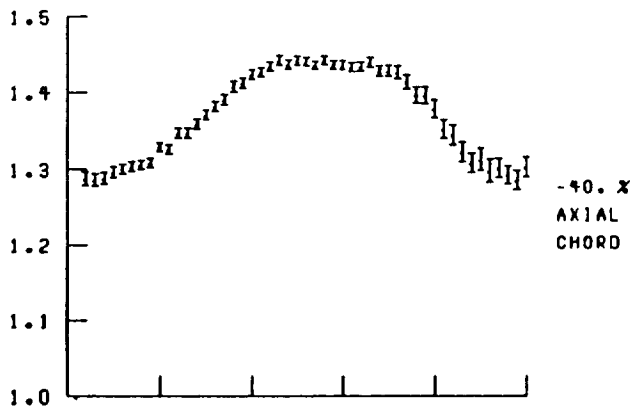
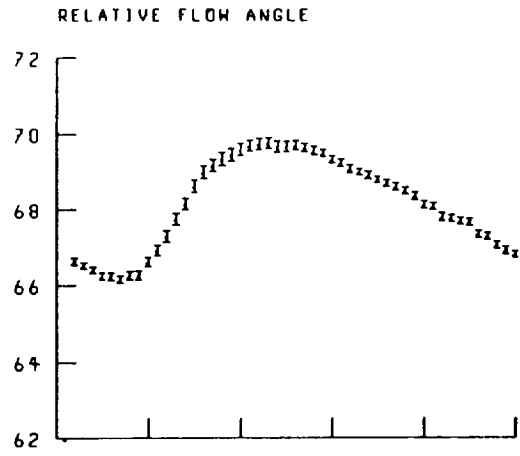
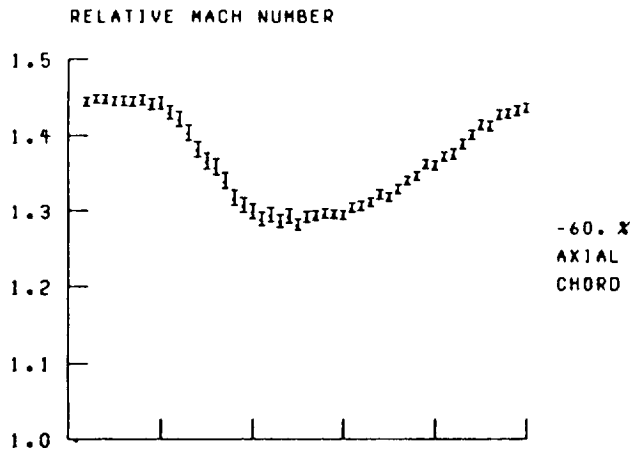


Figure 35.—Continued.

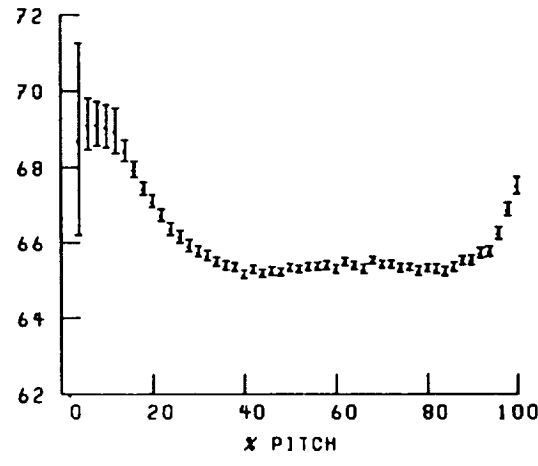
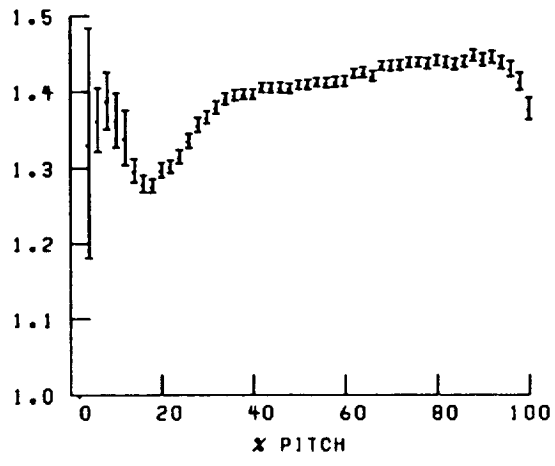
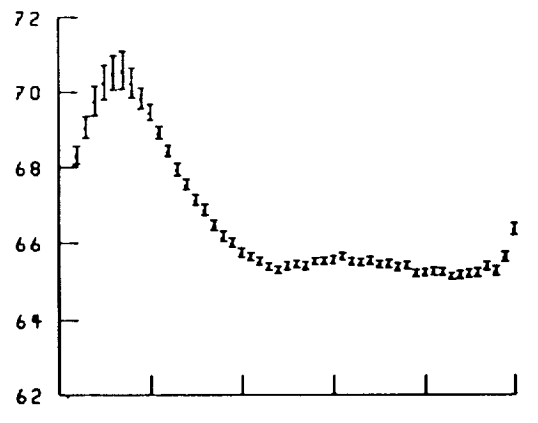
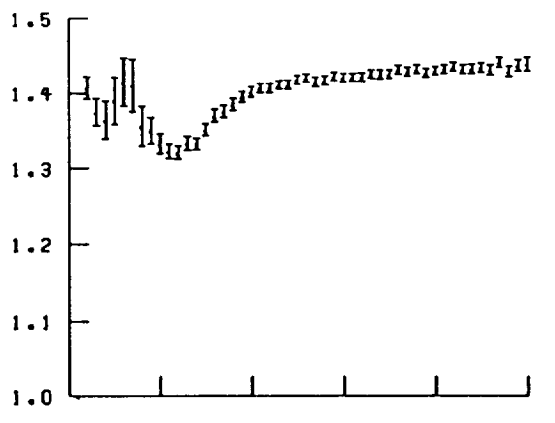
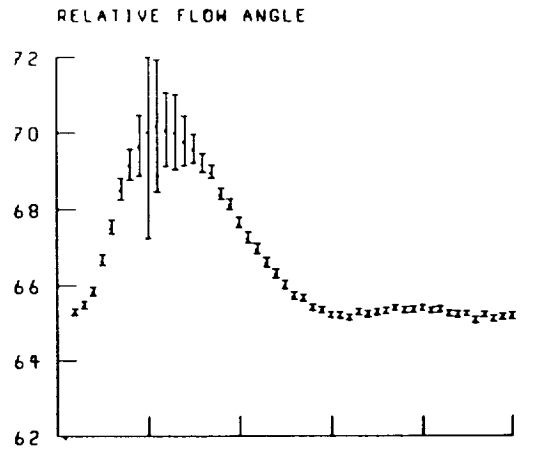
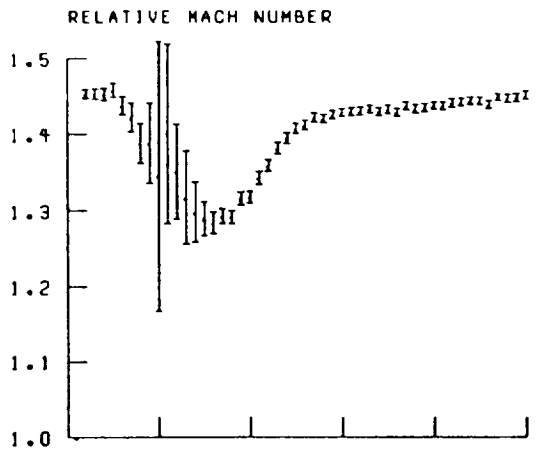


Figure 35.—Continued.

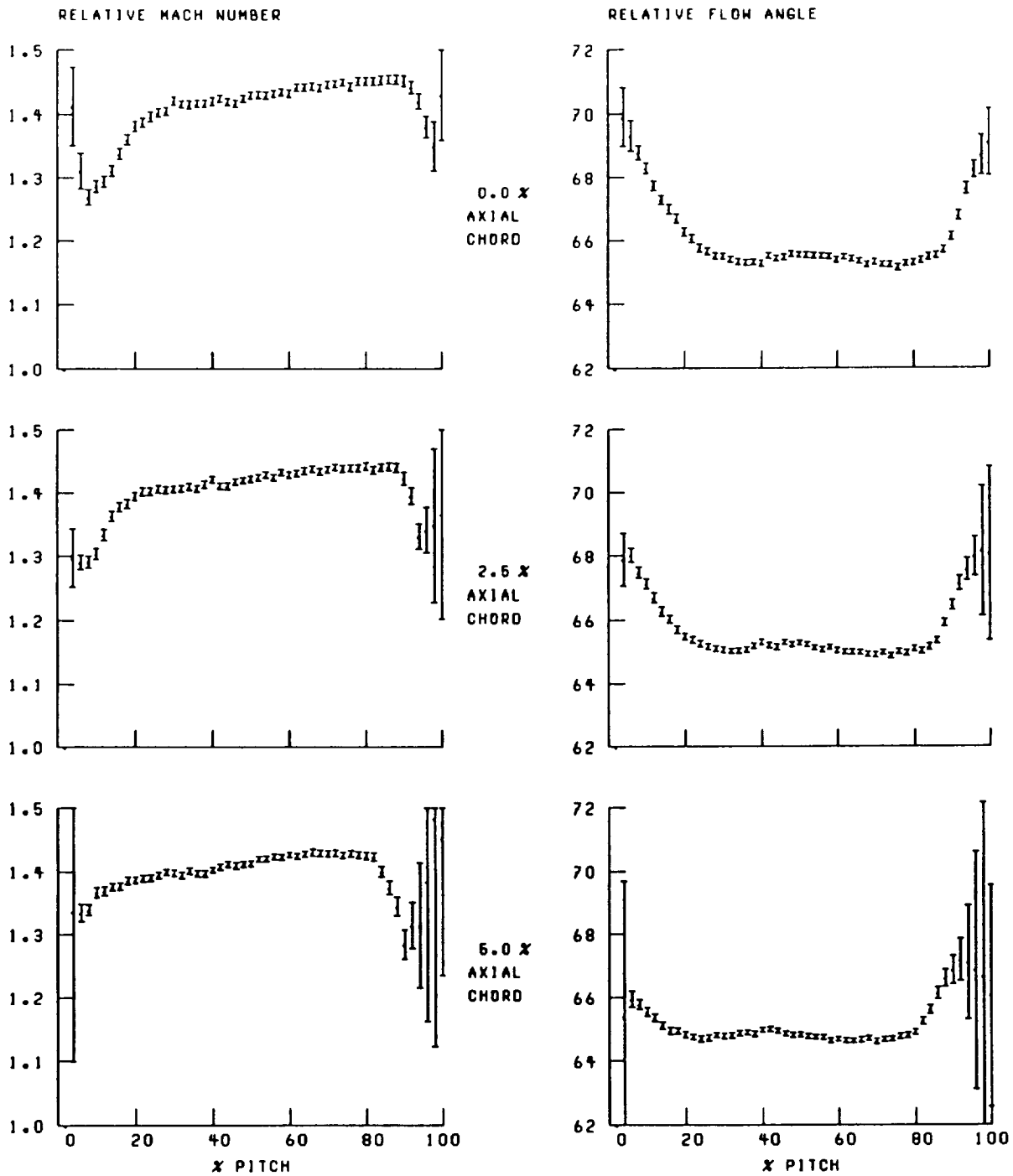


Figure 35.—Continued.

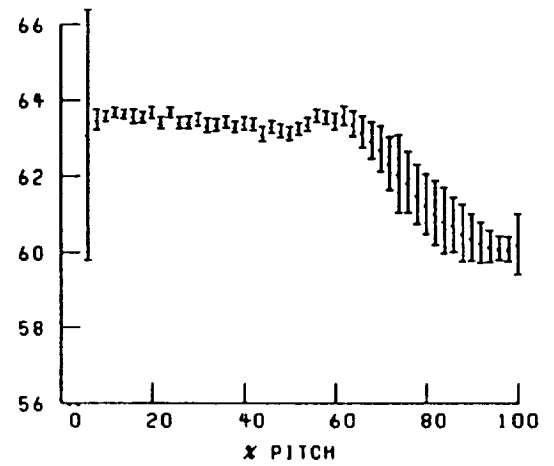
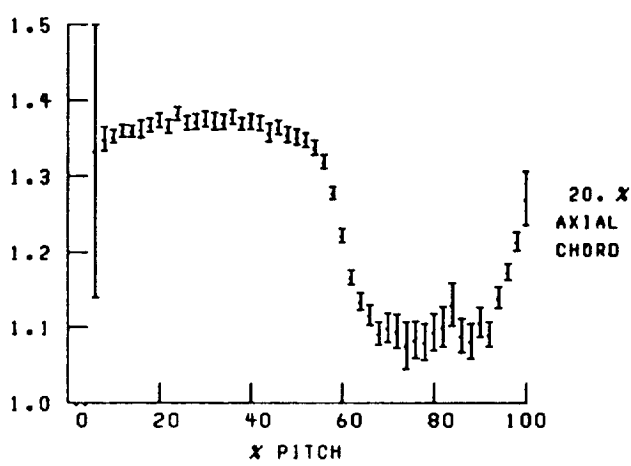
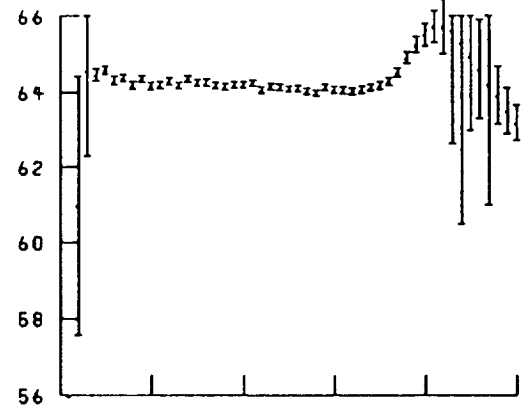
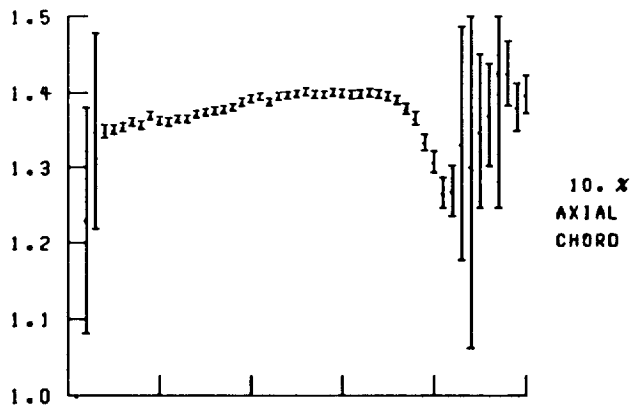
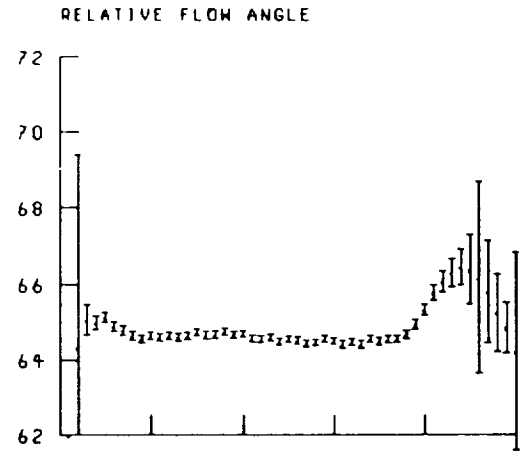
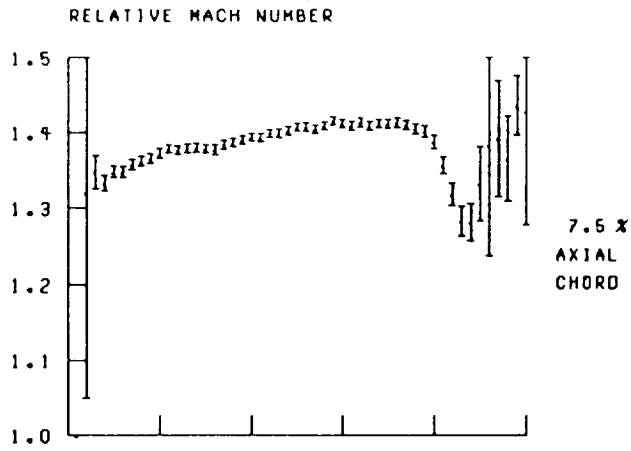


Figure 35.—Continued.

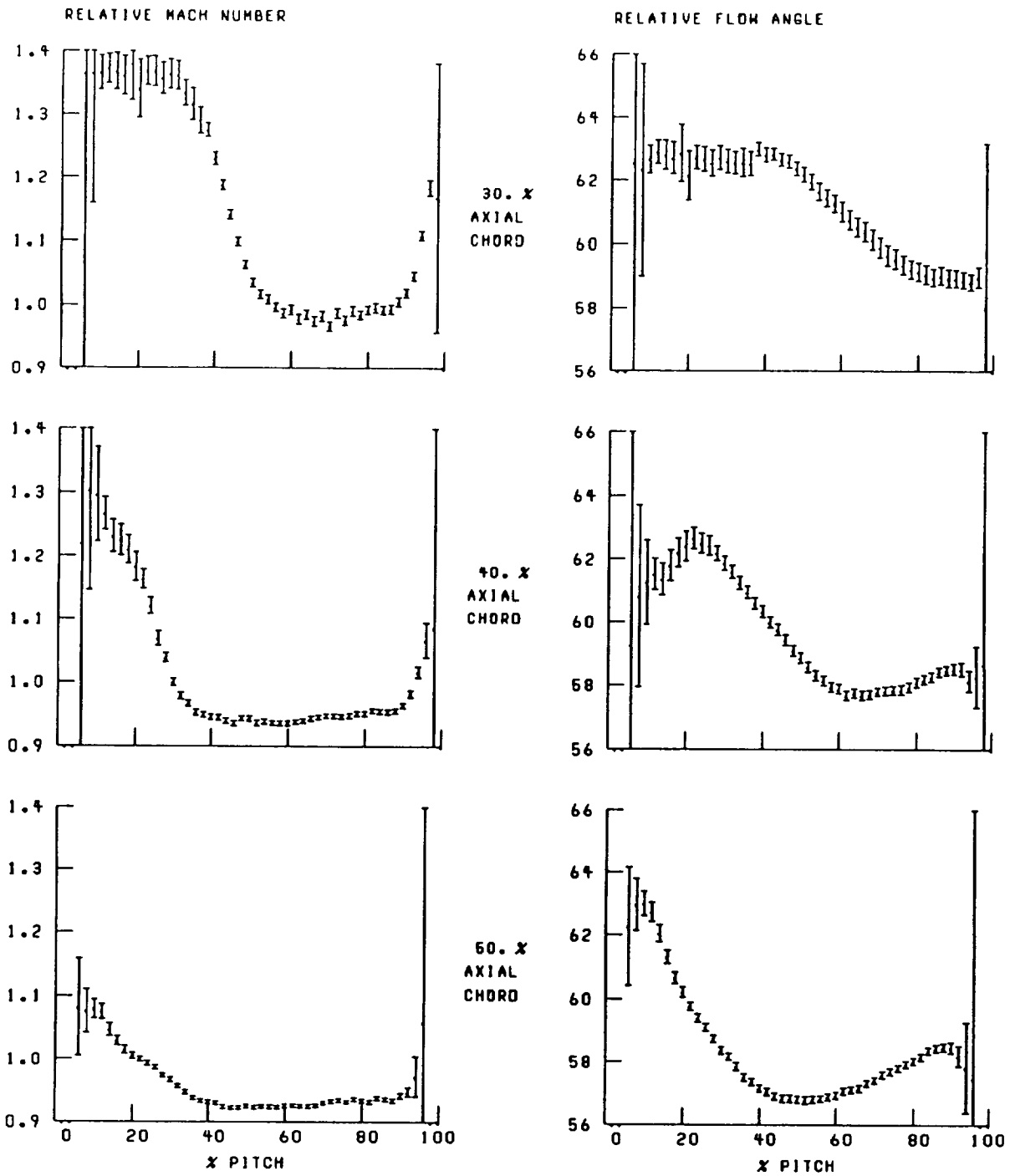


Figure 35.—Continued.

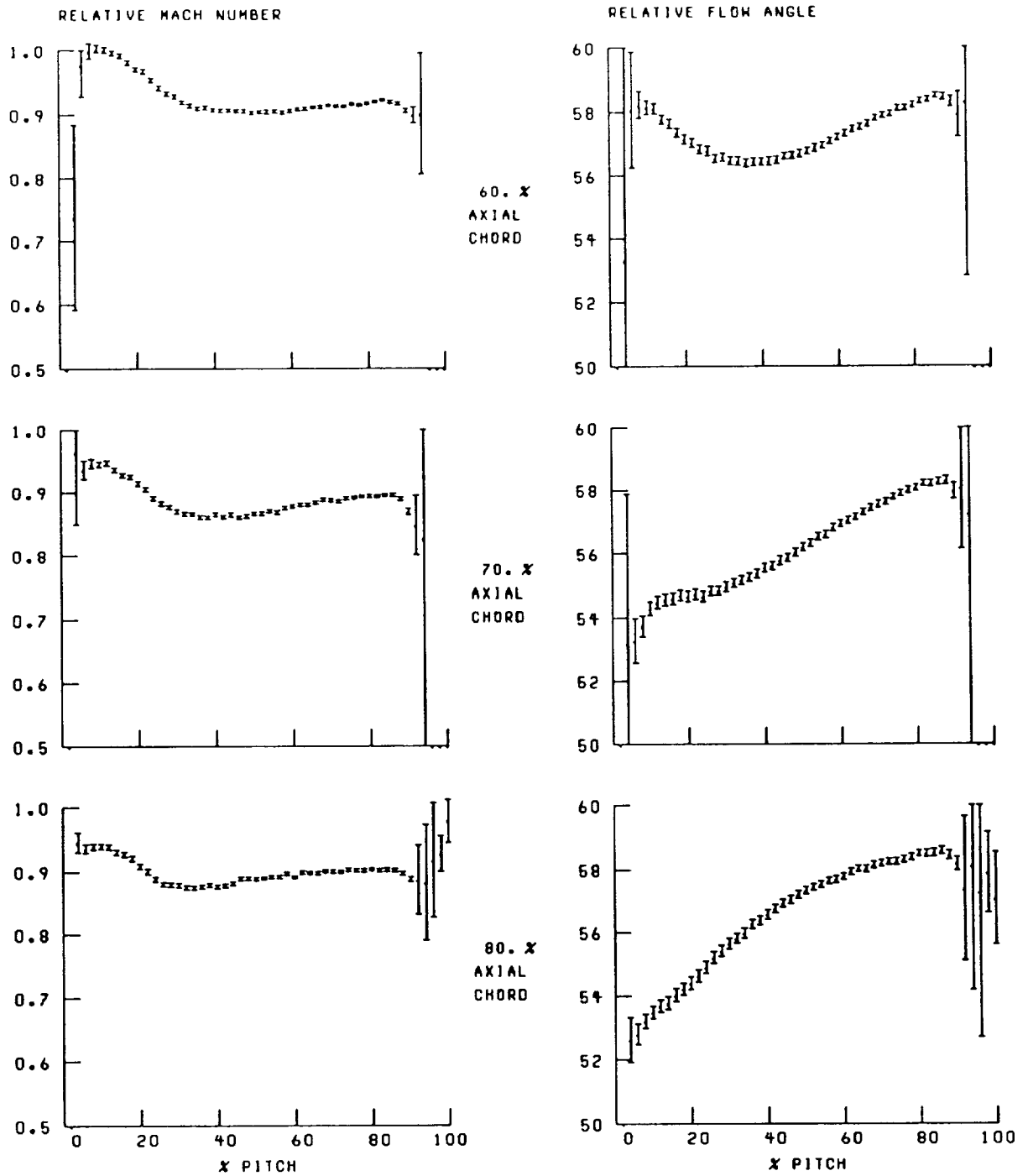


Figure 35.—Continued.

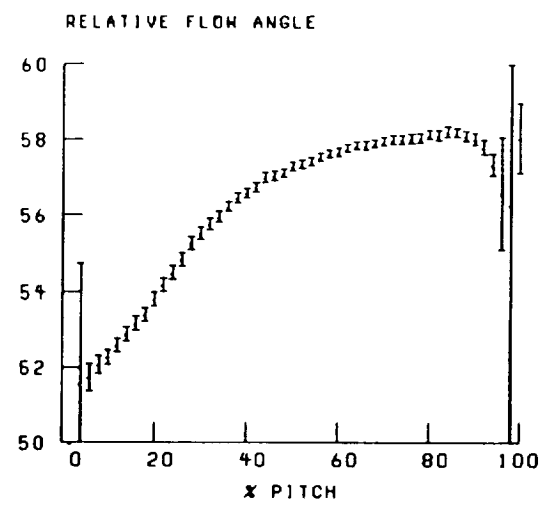
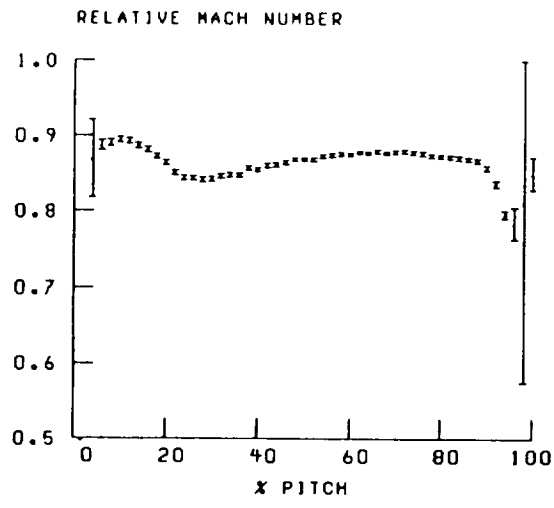


Figure 35.—Continued.

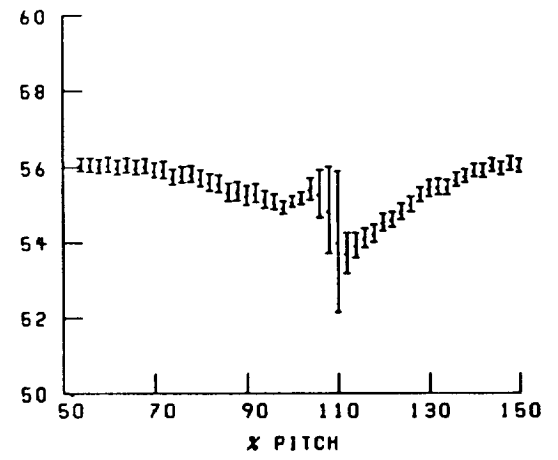
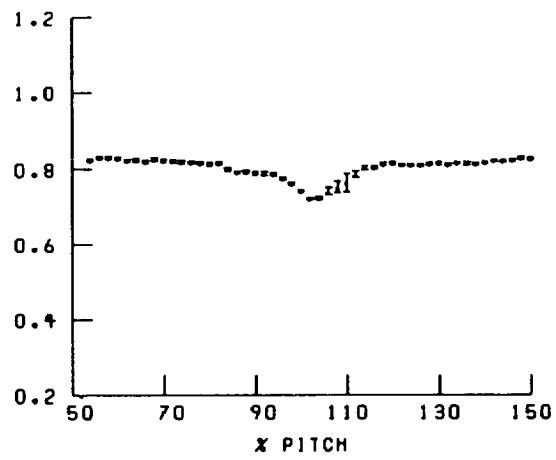
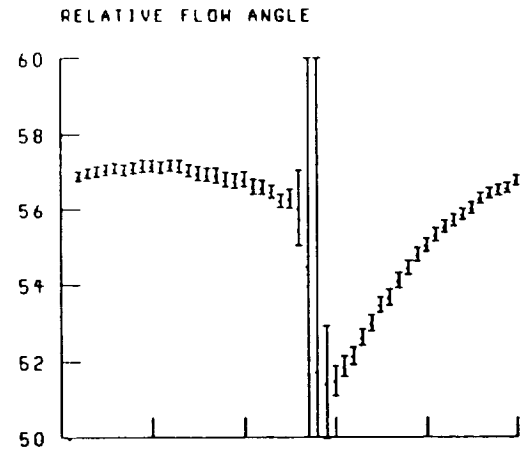
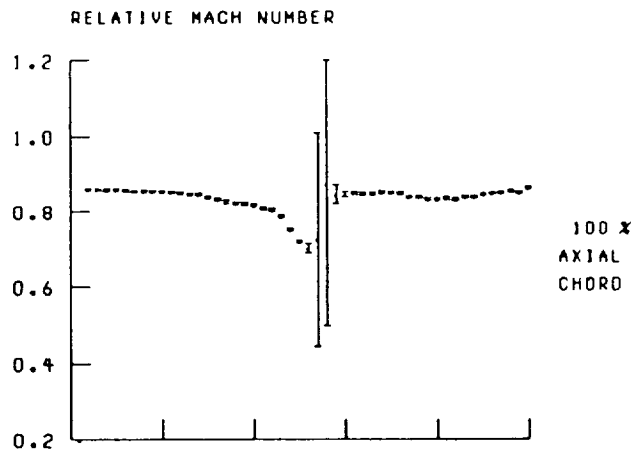


Figure 35.—Concluded.

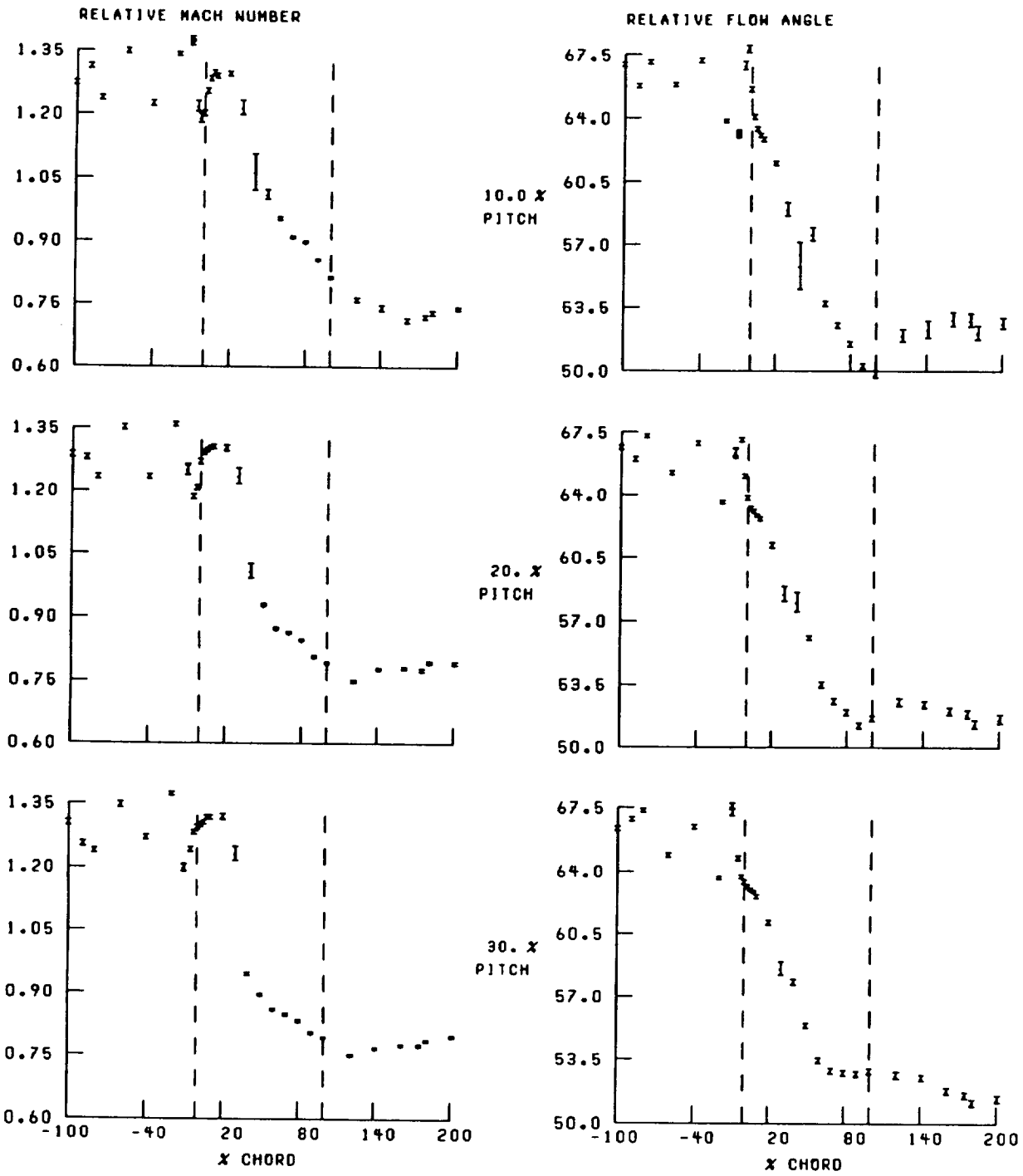


Figure 36.—Streamwise distribution of relative Mach number and flow angle at 20-percent span and near stall. Broken lines denote location of blade leading and trailing edges.

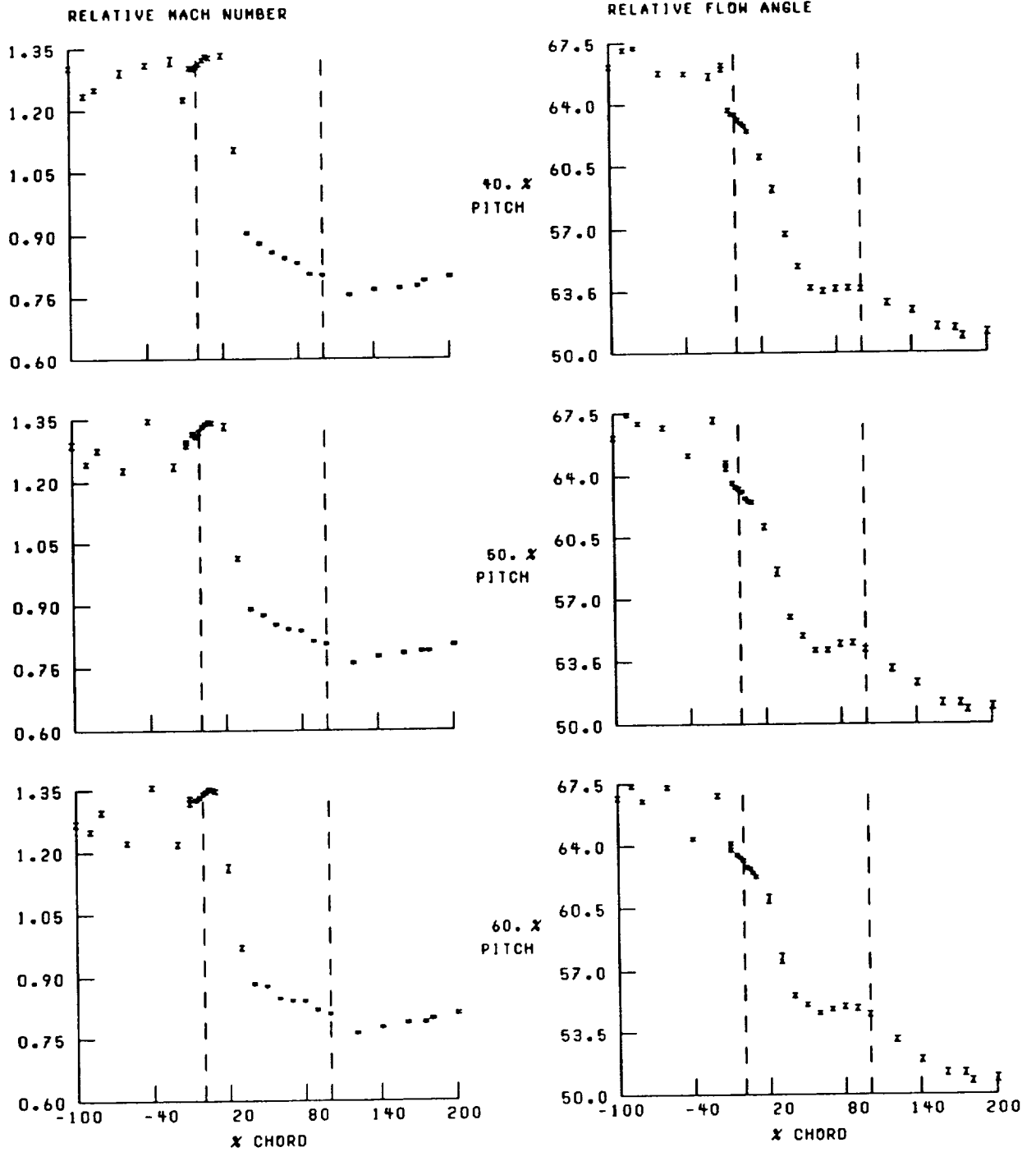


Figure 36.—Continued.

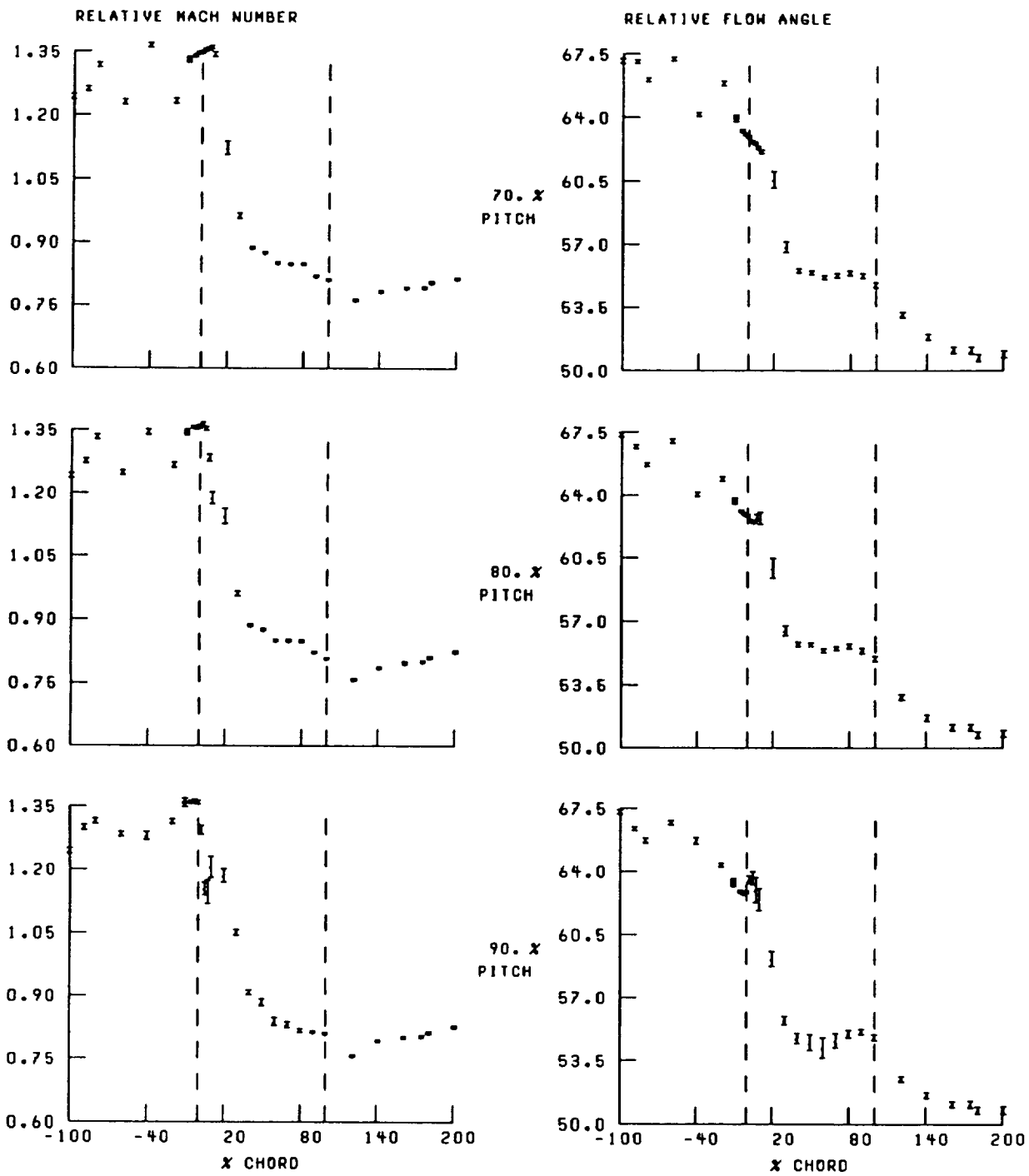


Figure 36.—Concluded.

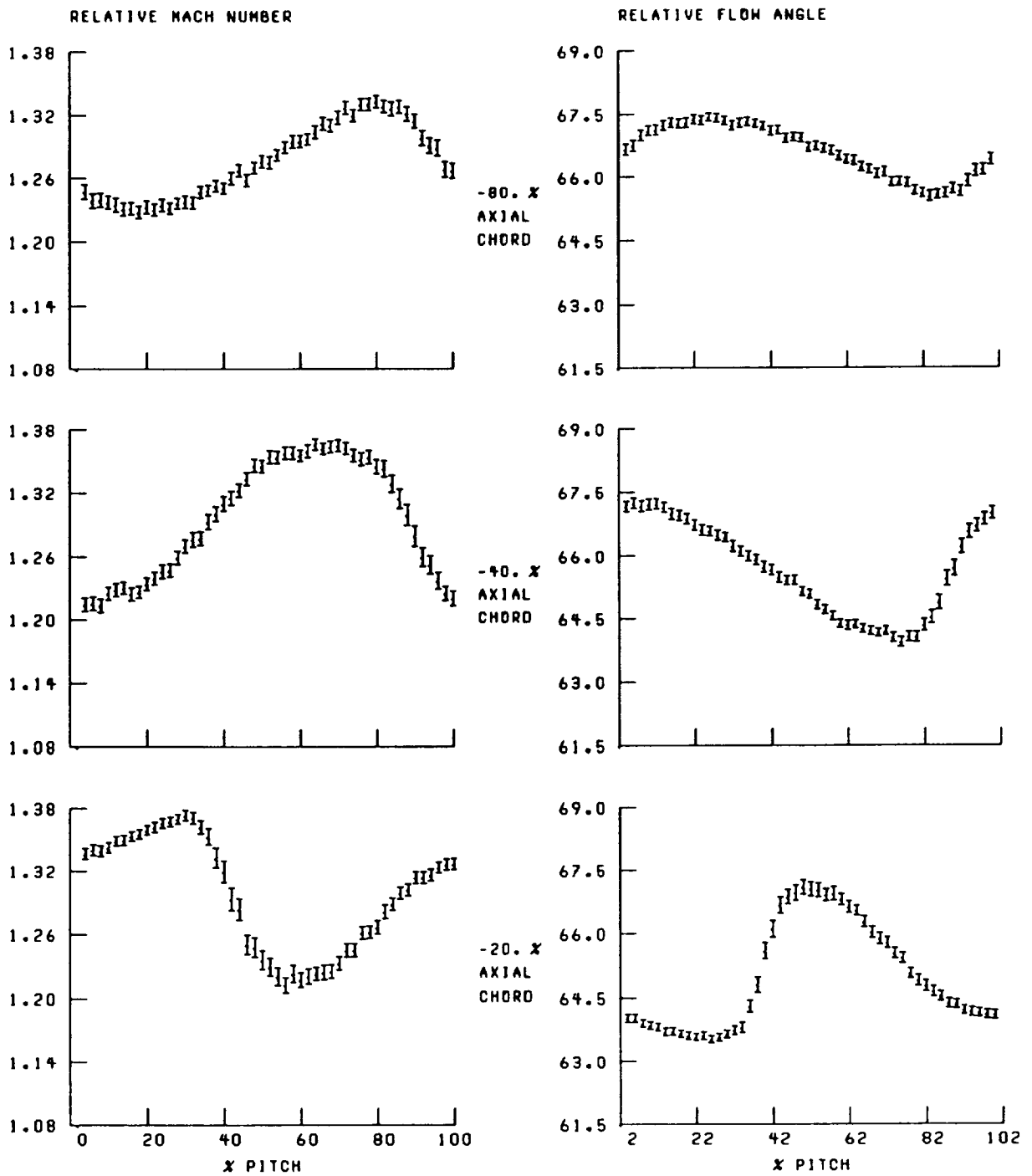


Figure 37.—Blade-to-blade distribution of relative Mach number and flow angle at 20-percent span and near stall.

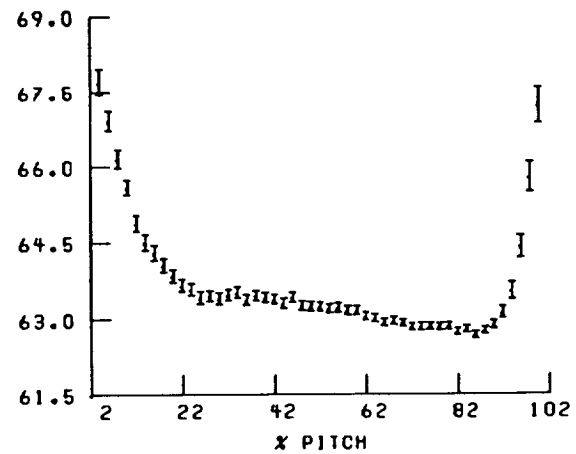
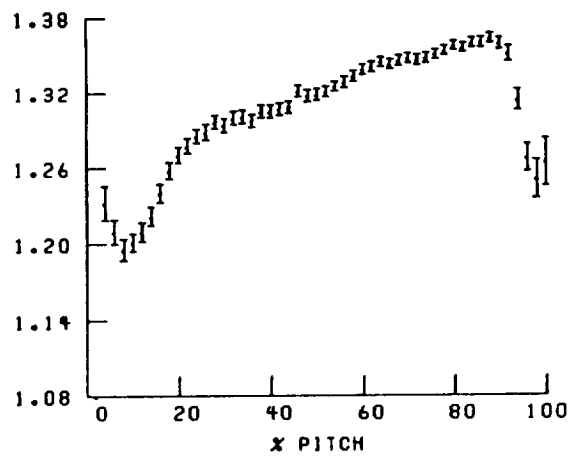
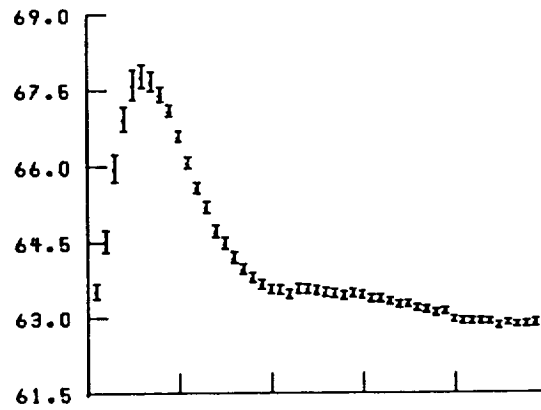
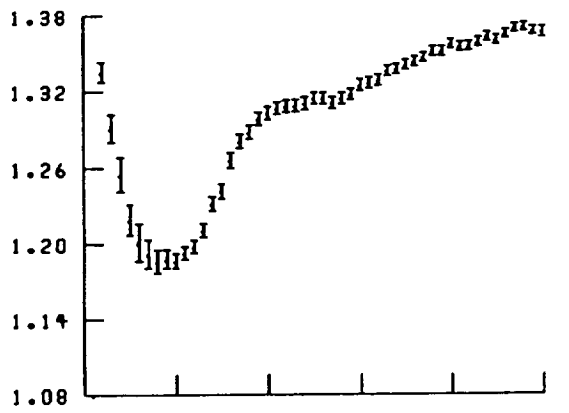
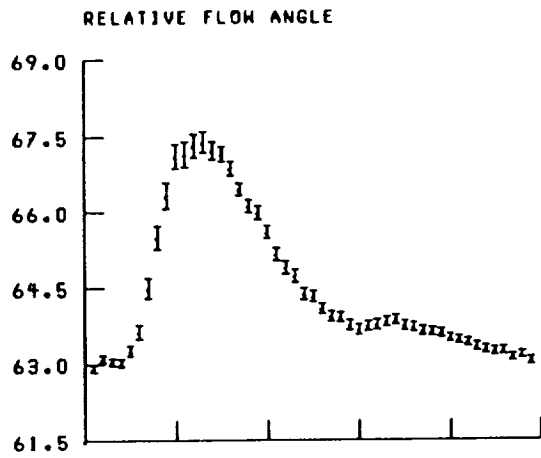
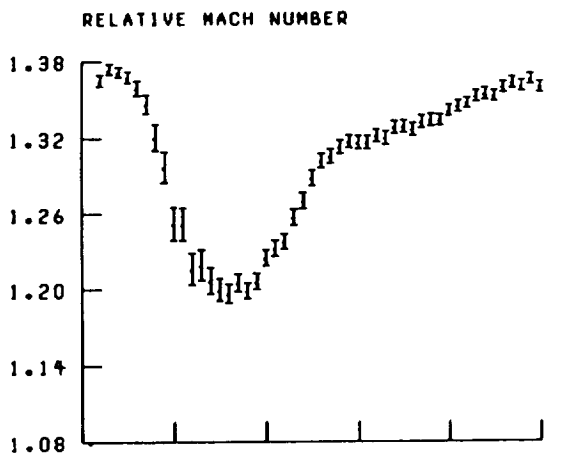


Figure 37.—Continued.

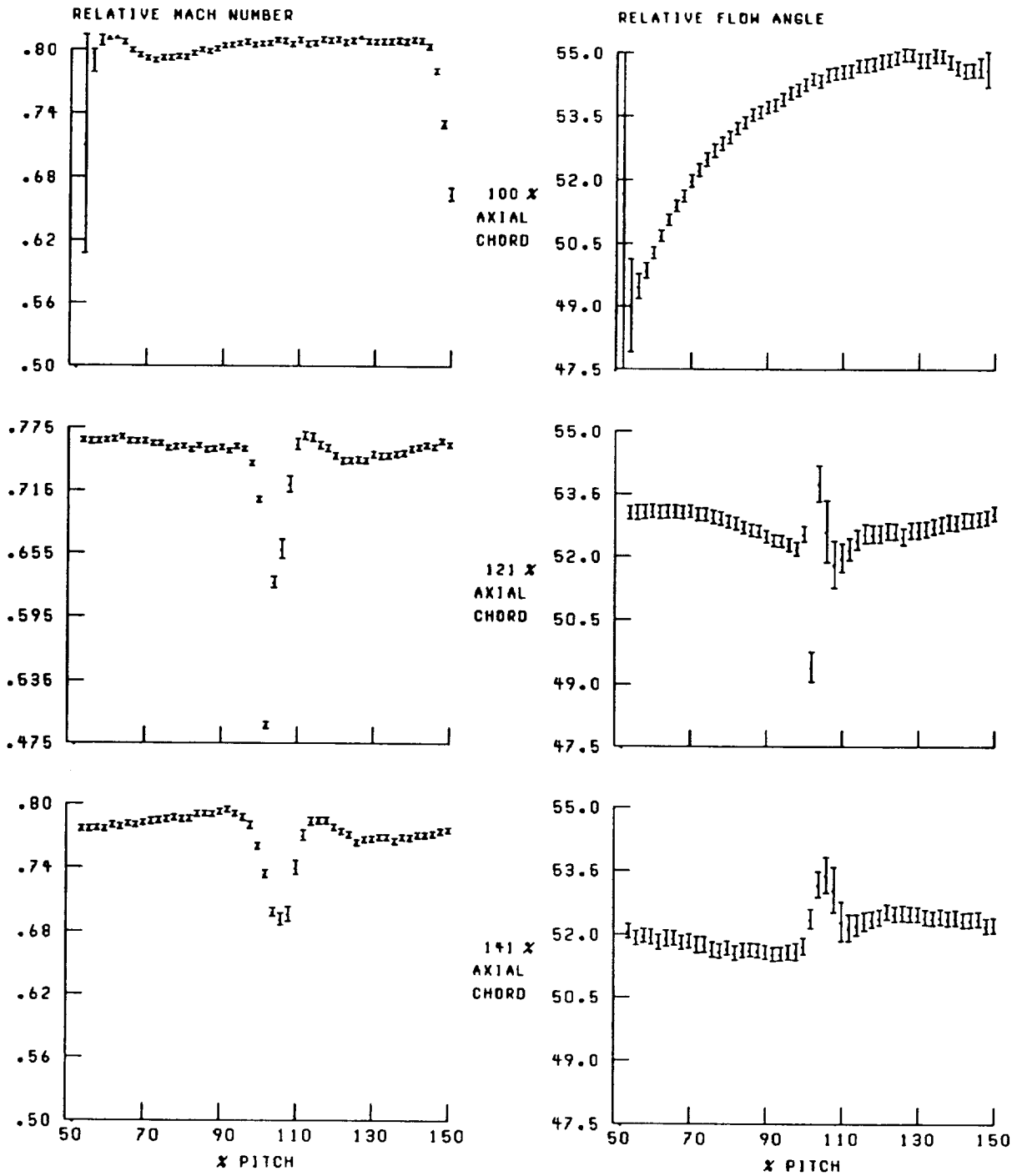


Figure 37.—Continued.

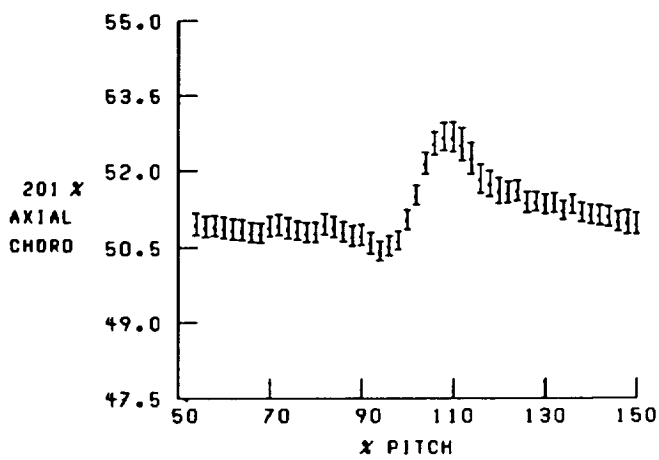
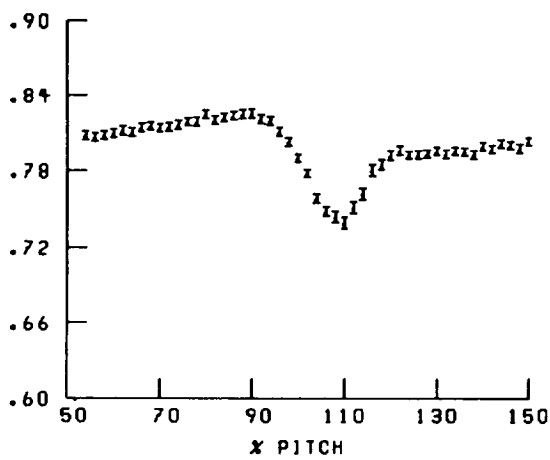
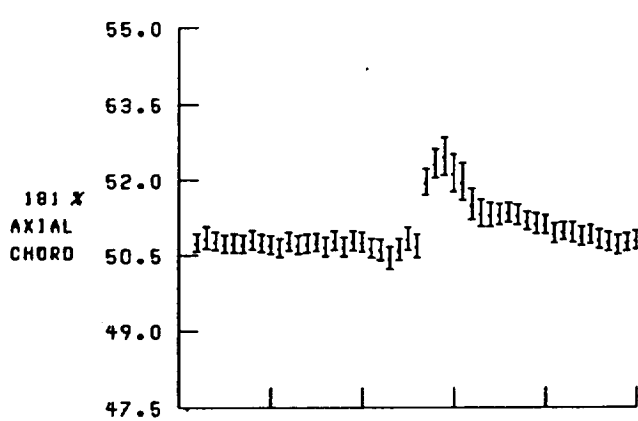
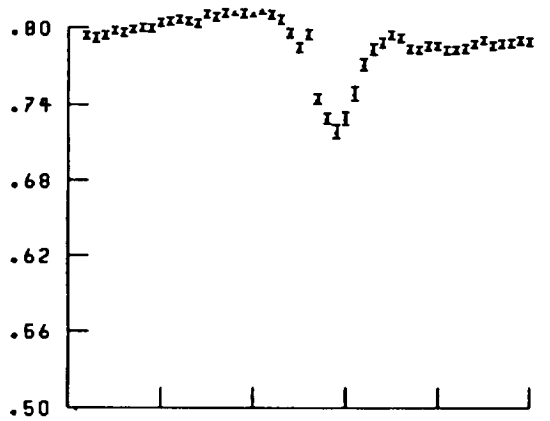
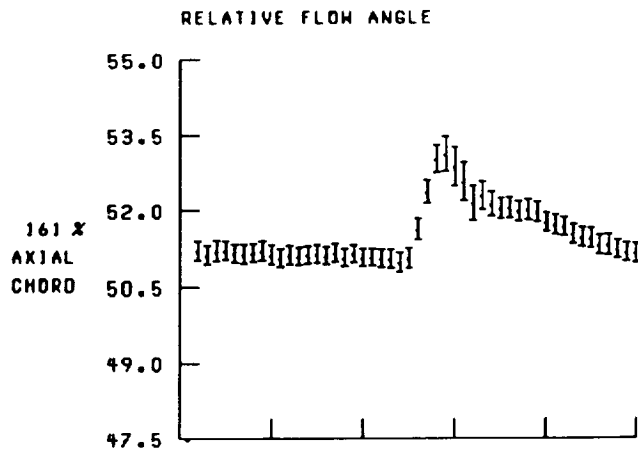
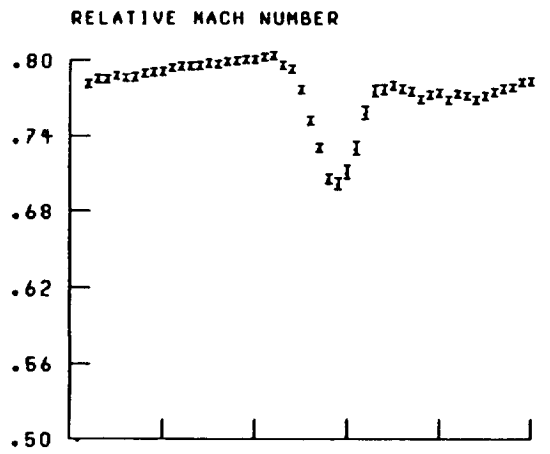


Figure 37.—Concluded.

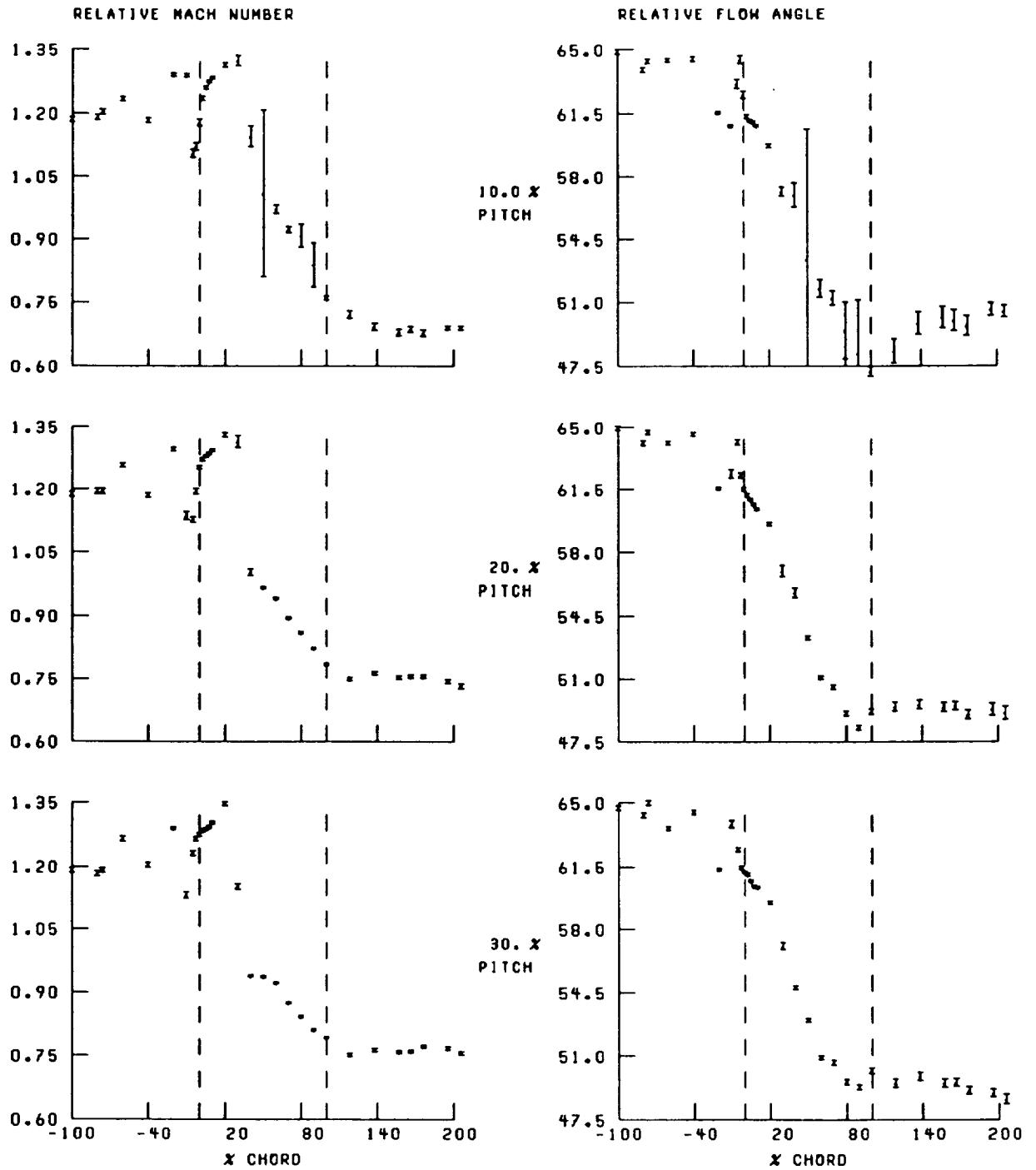


Figure 38.—Streamwise distribution of relative Mach number and flow angle at 30-percent span and near stall. Broken lines denote location of blade leading and trailing edges.

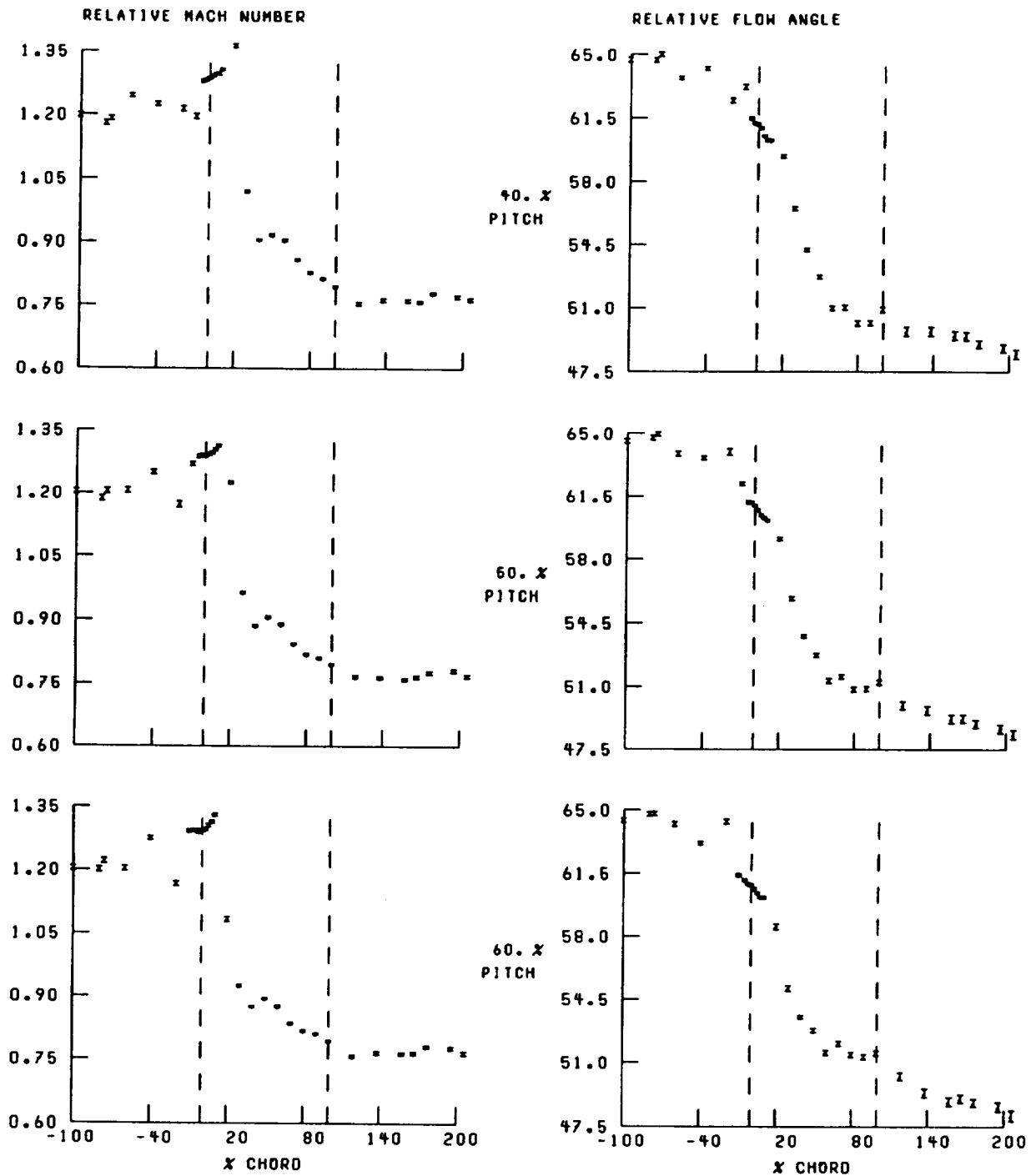


Figure 38.—Continued.

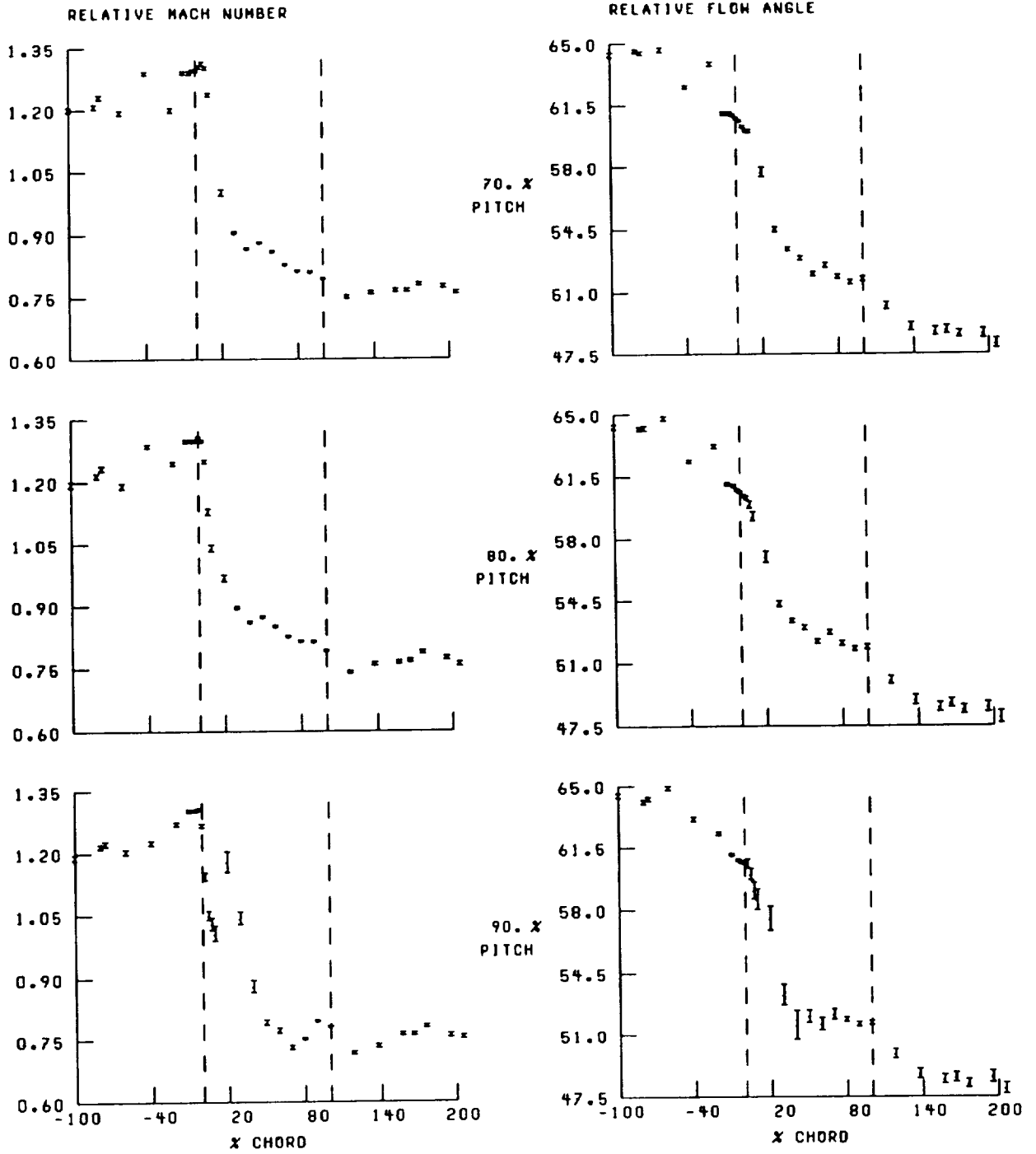


Figure 38.—Concluded.

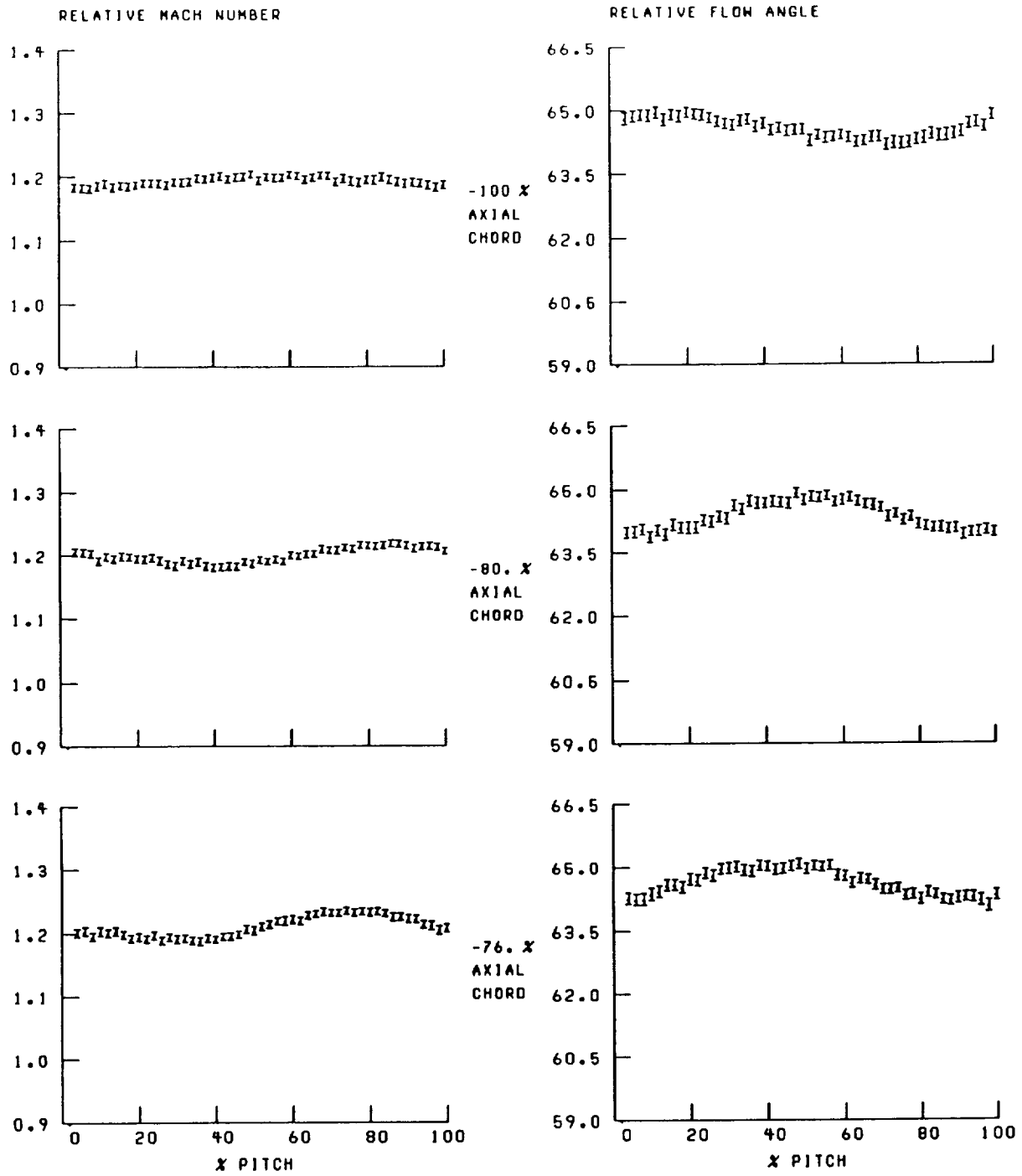


Figure 39.—Blade-to-blade distribution of relative Mach number and flow angle at 30-percent span and near stall.

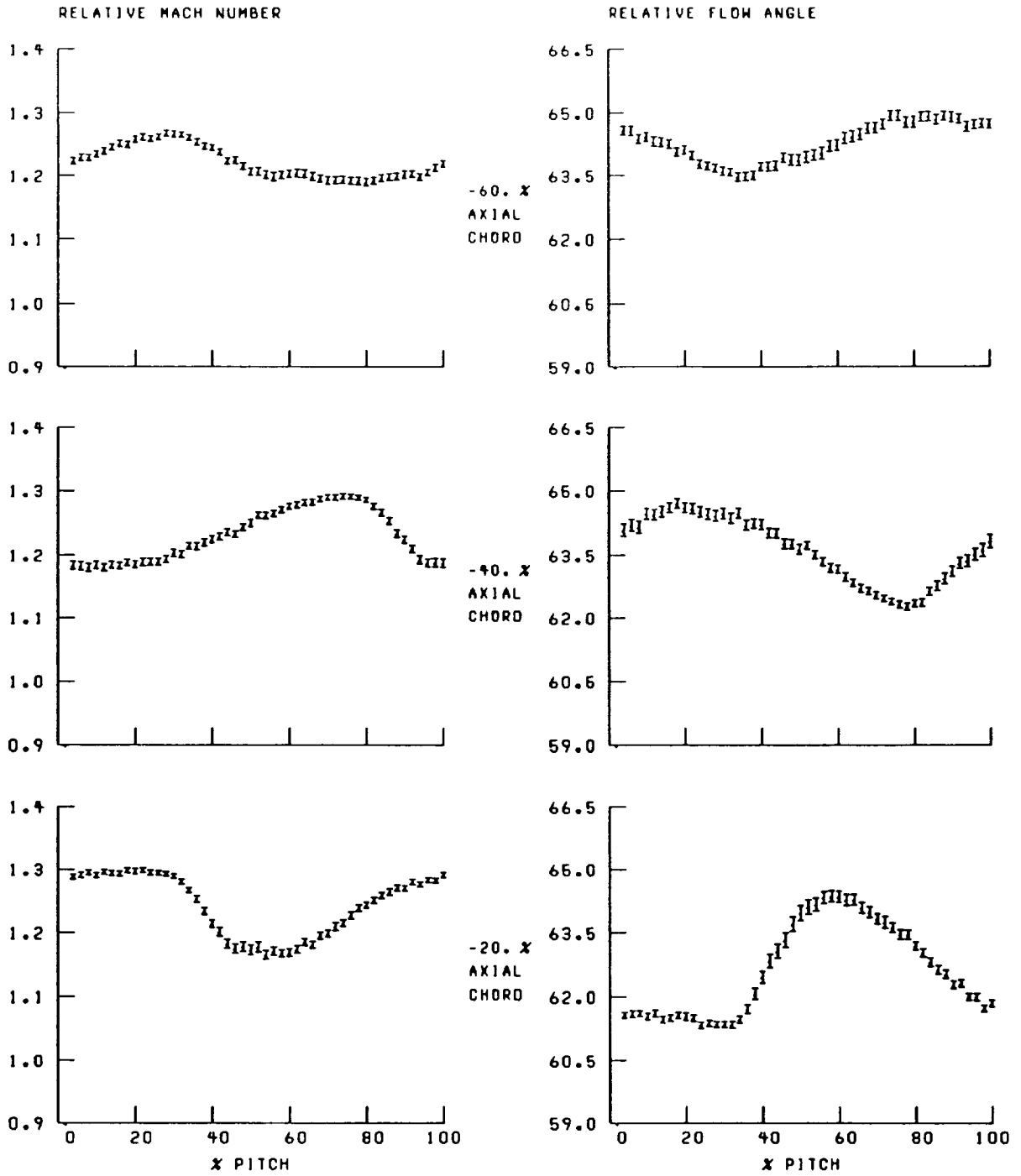


Figure 39.—Continued.

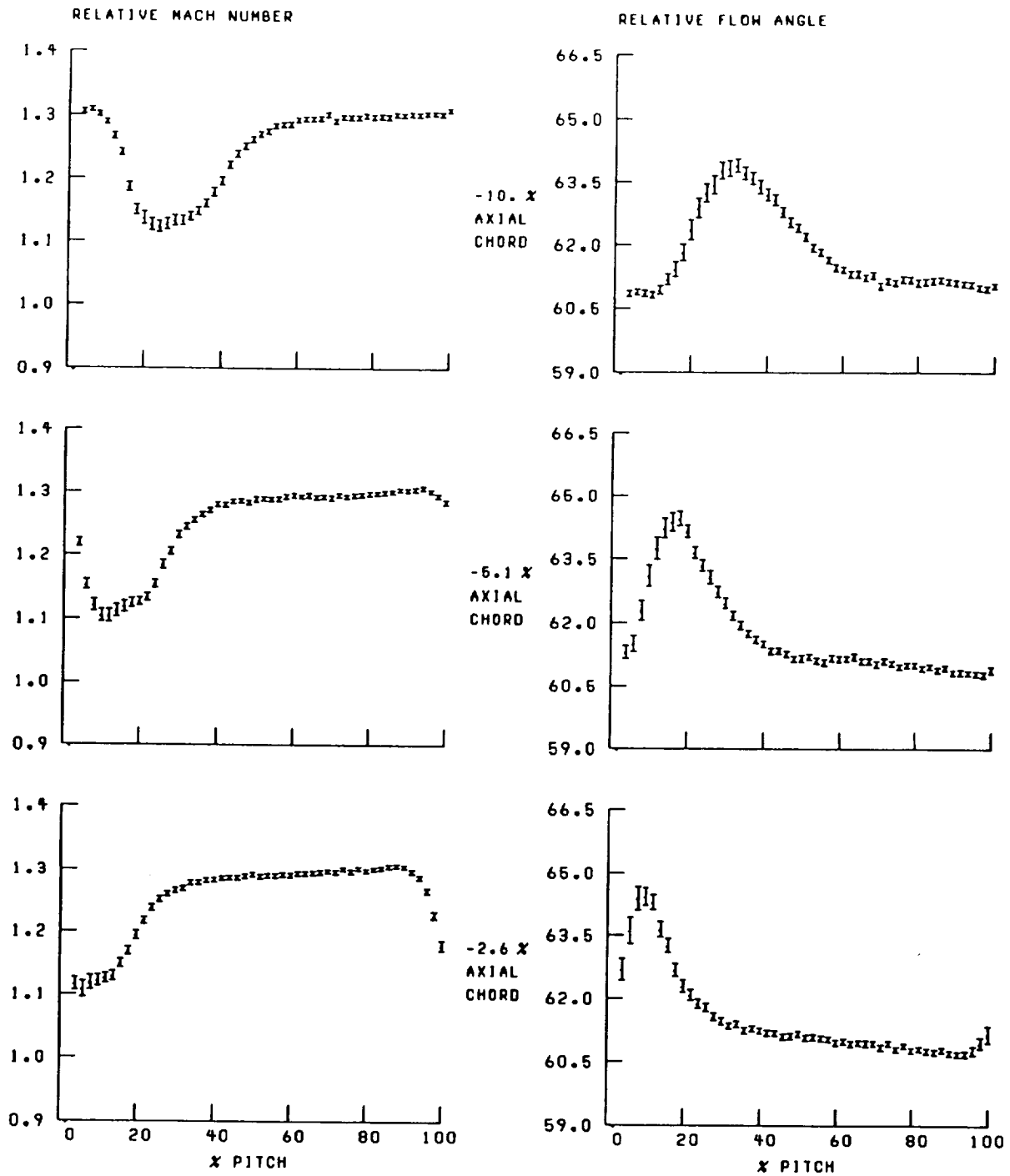


Figure 39.—Continued.

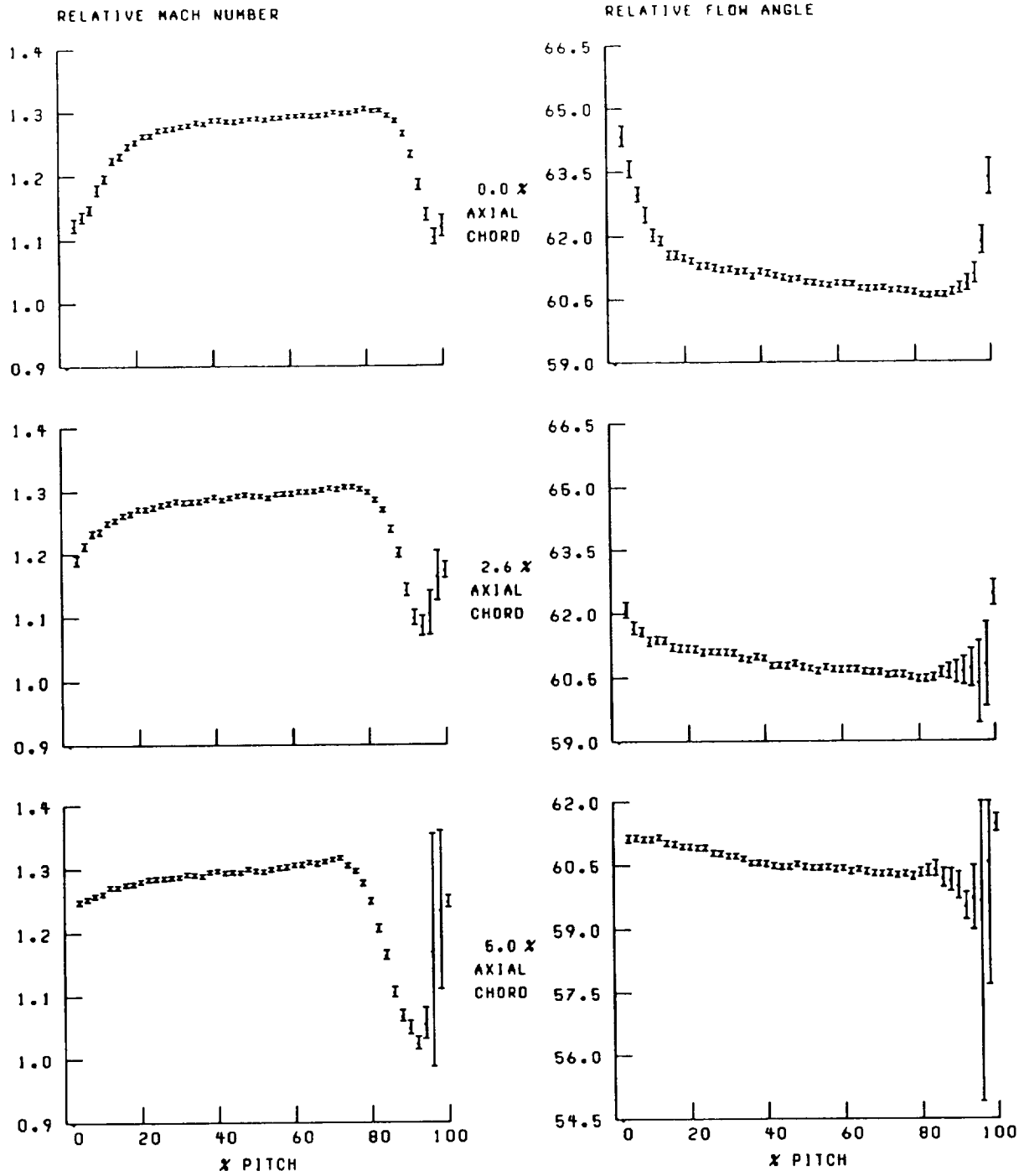


Figure 39.—Continued.

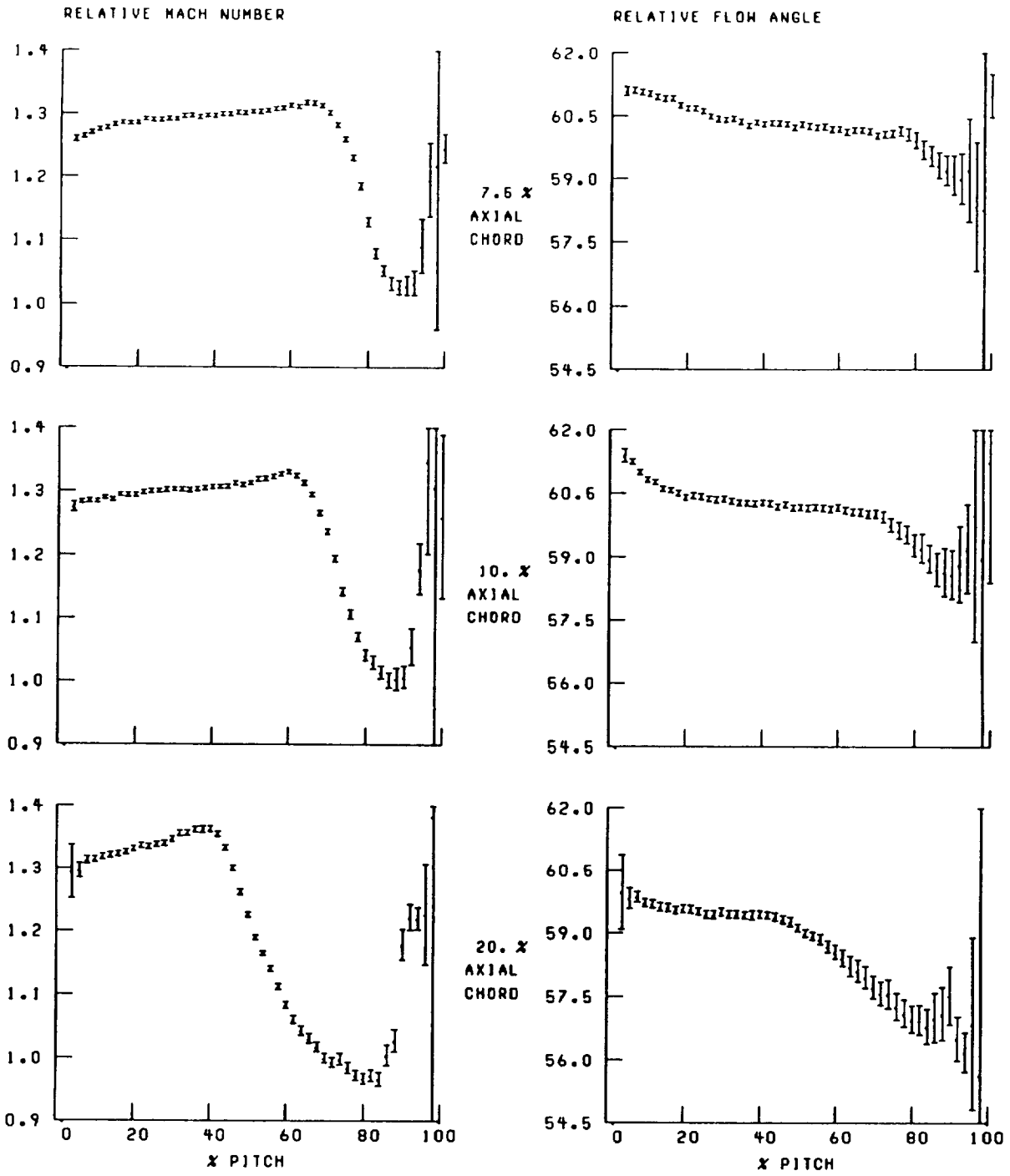


Figure 39.—Continued.

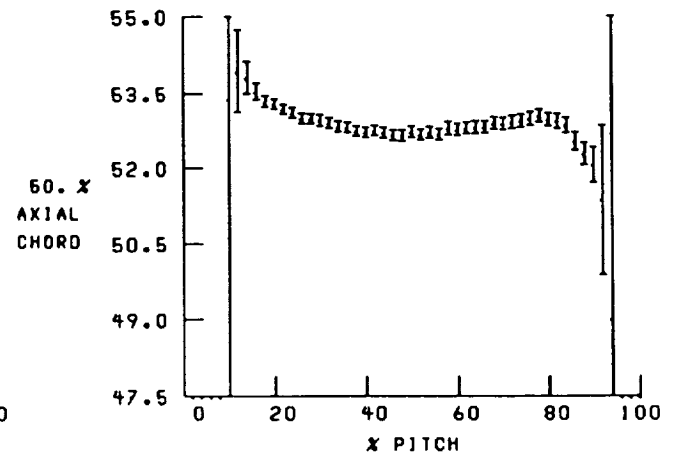
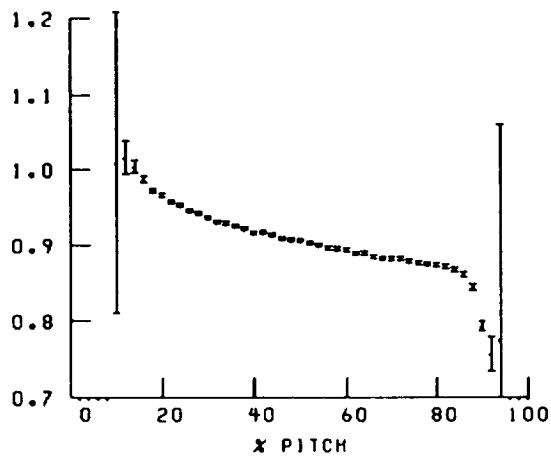
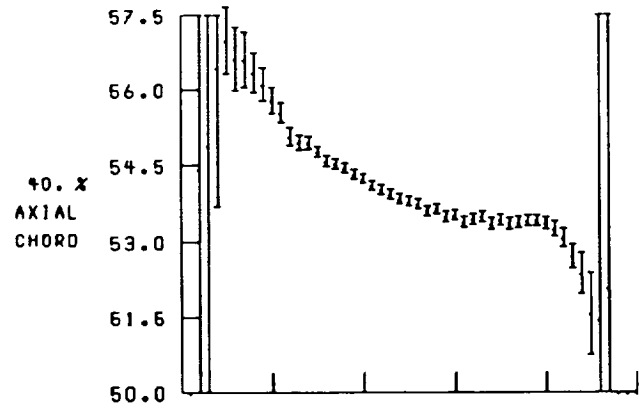
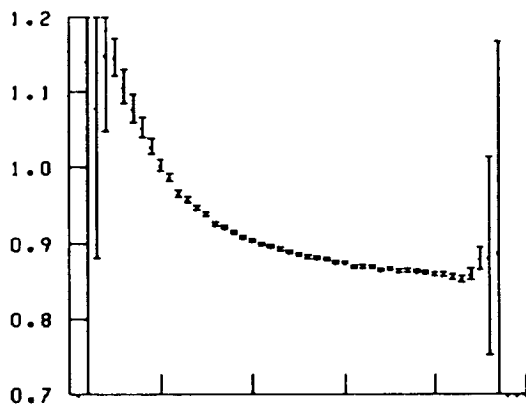
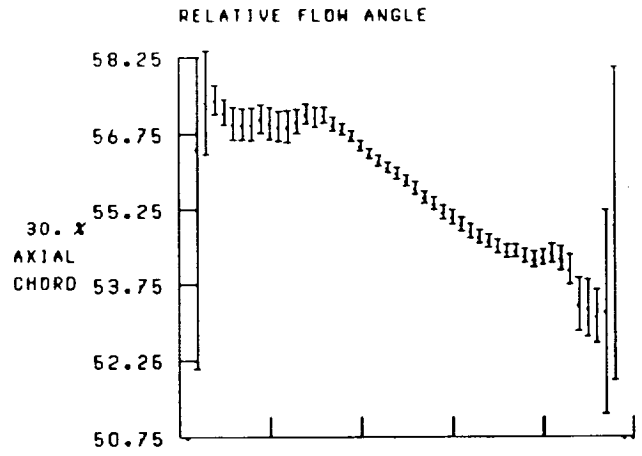
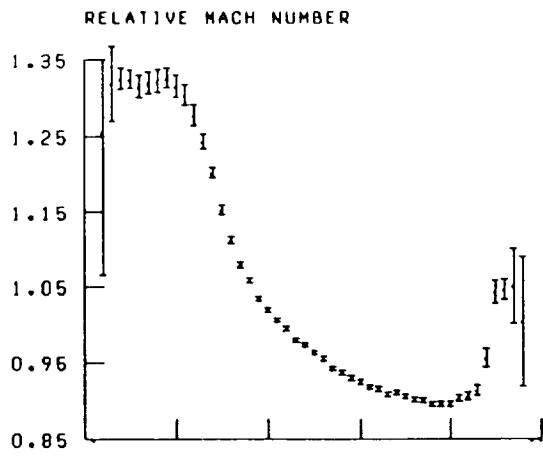


Figure 39.—Continued.

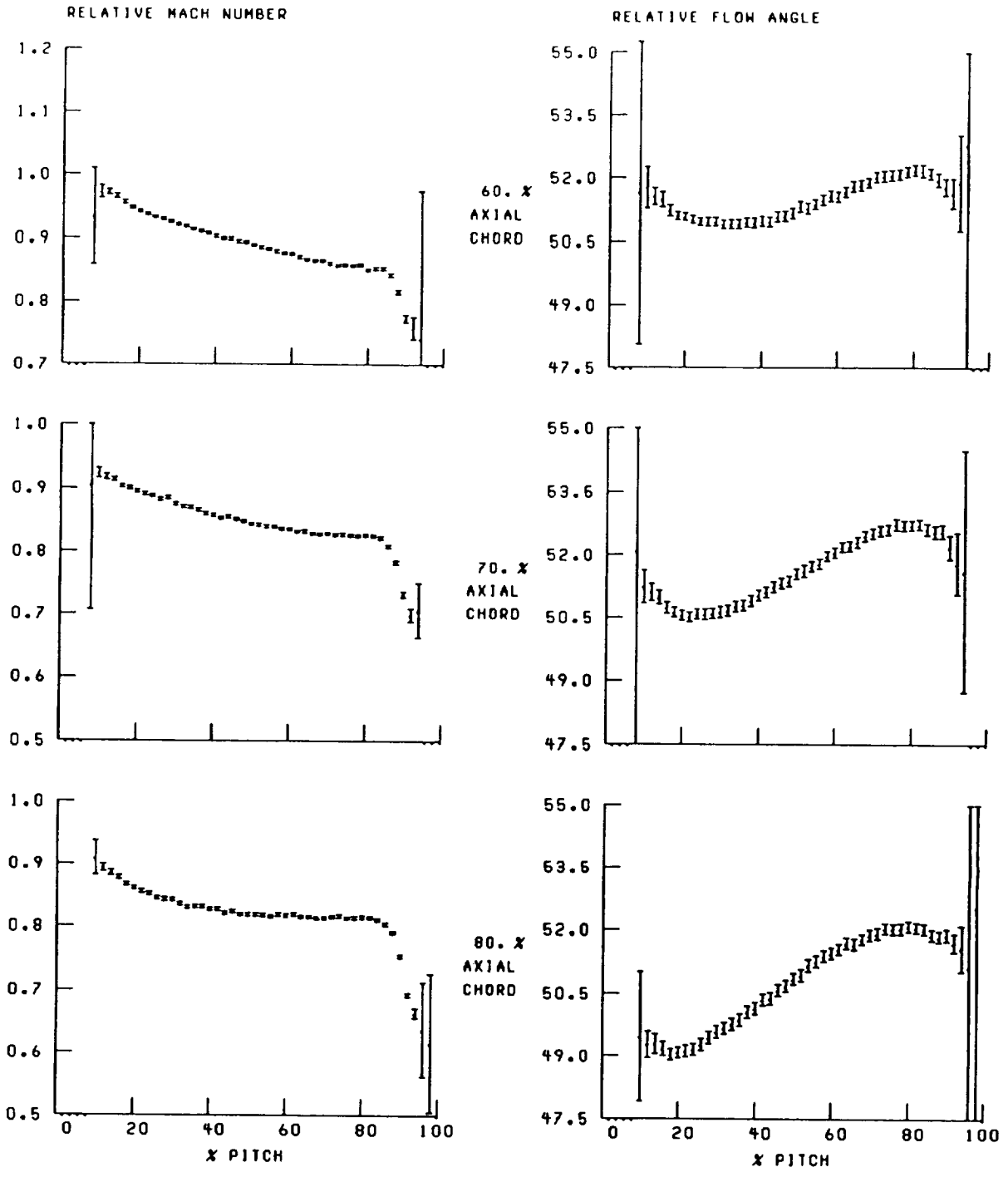


Figure 39.—Continued.

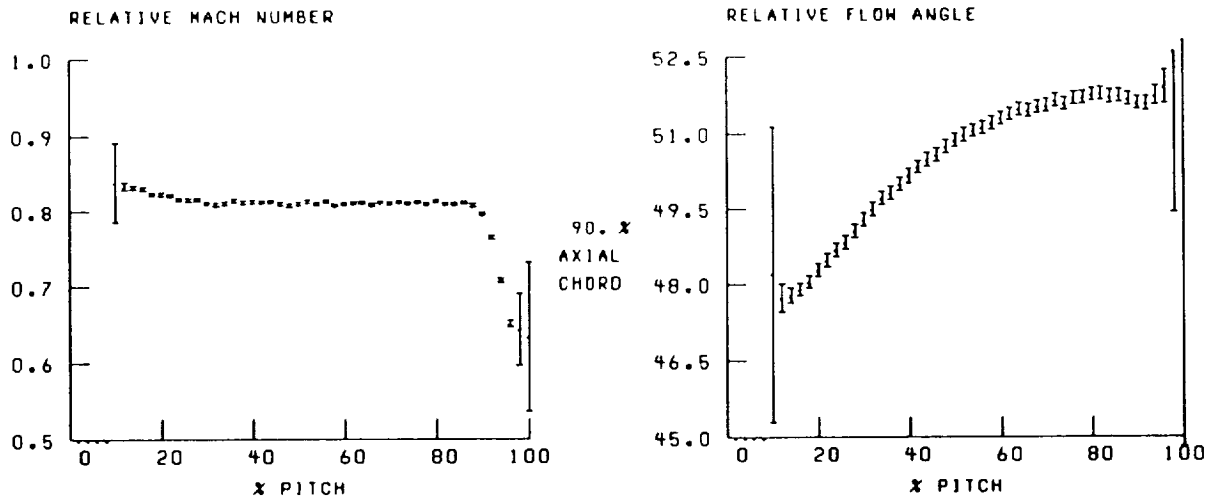


Figure 39.—Continued.

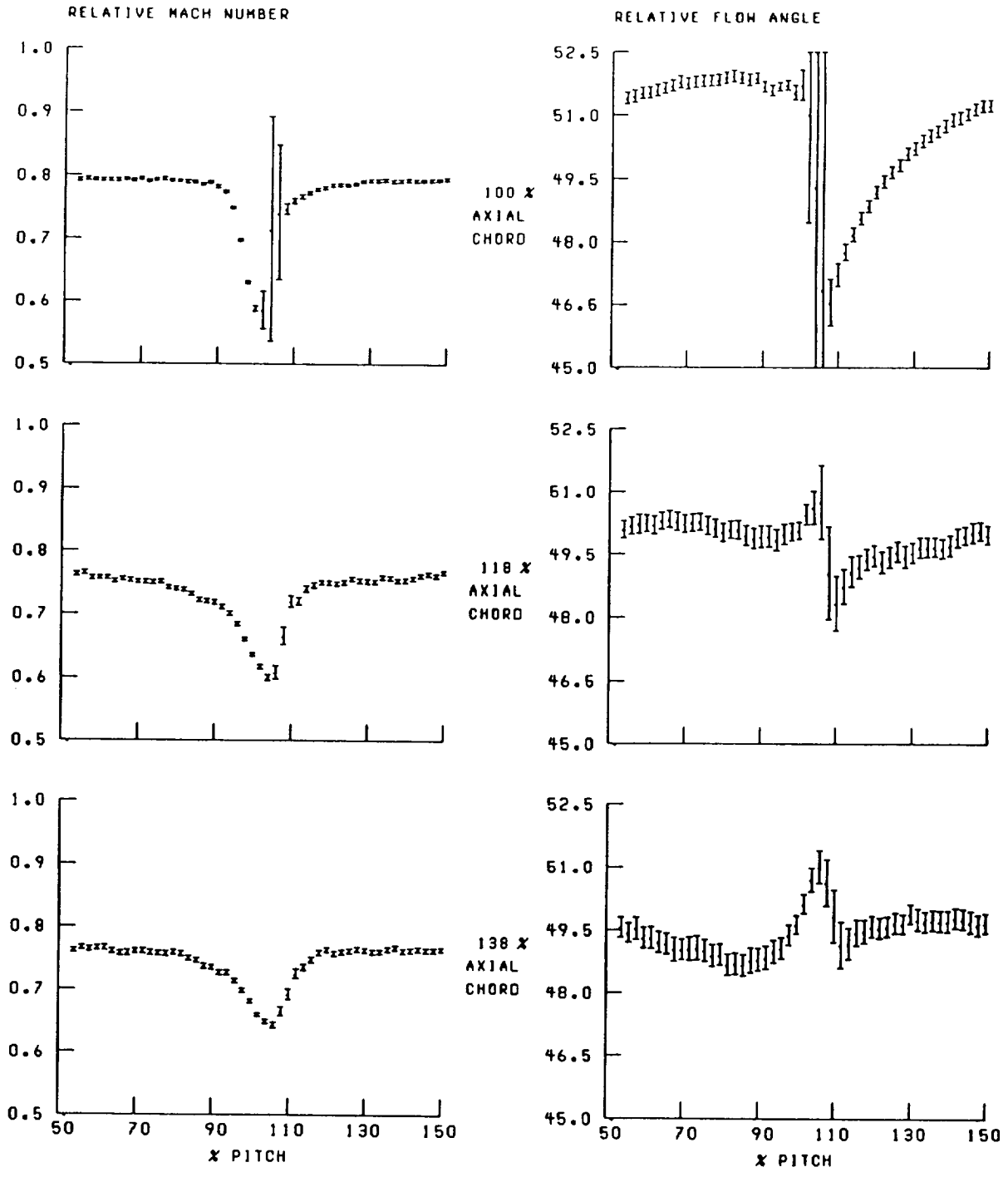


Figure 39.—Continued.

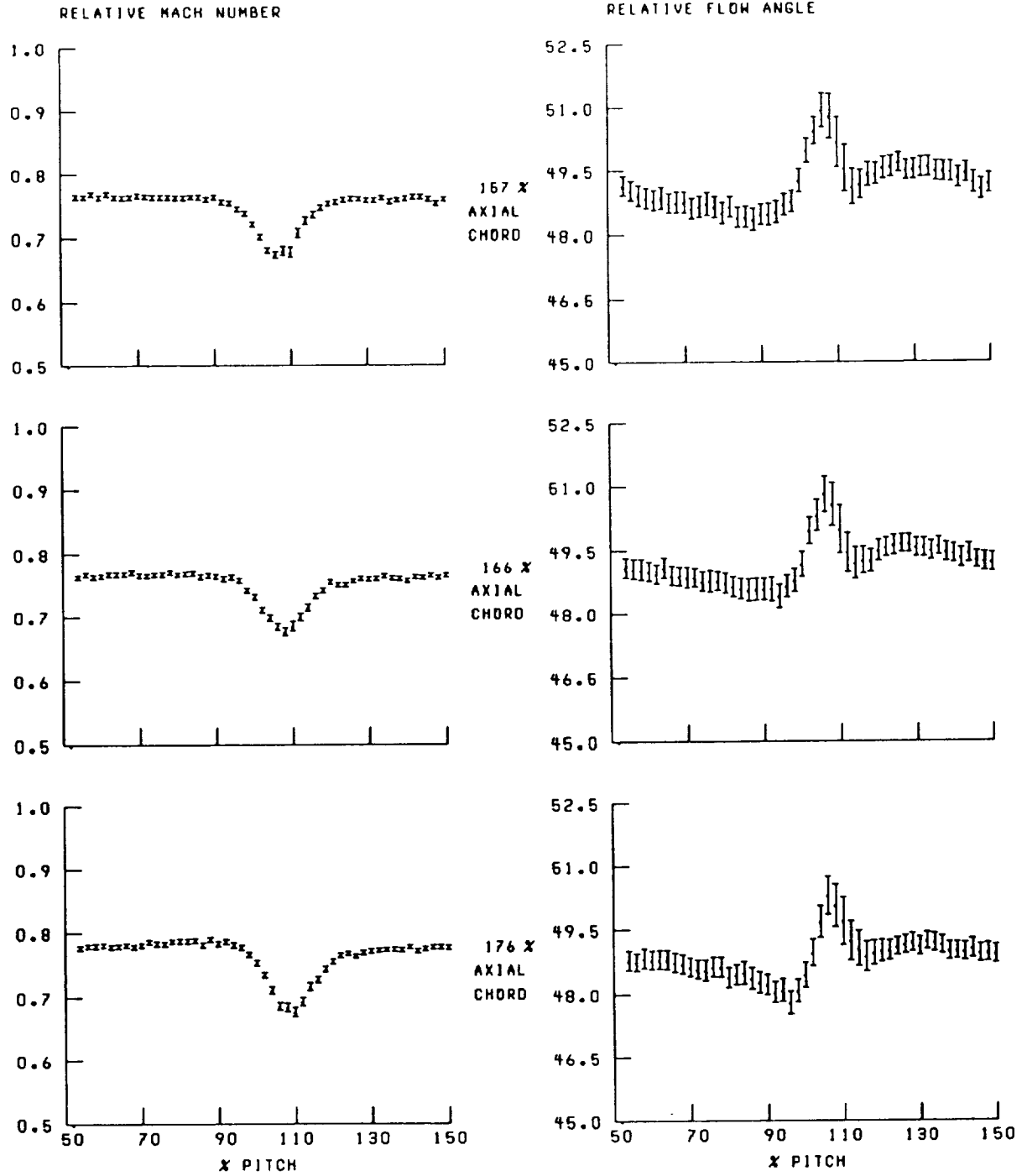


Figure 39.—Continued.

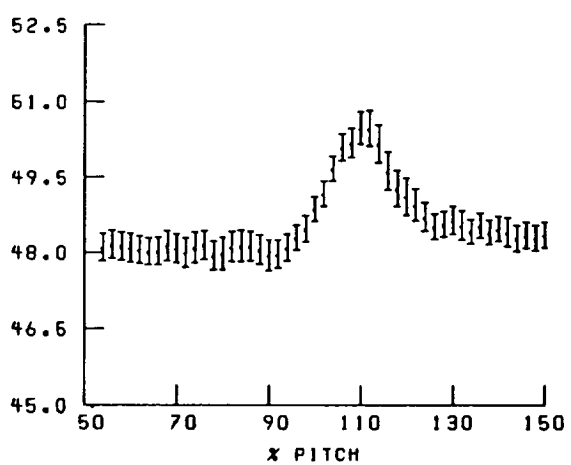
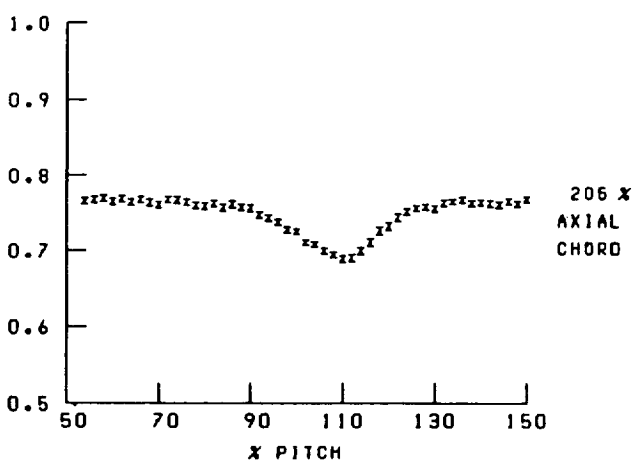
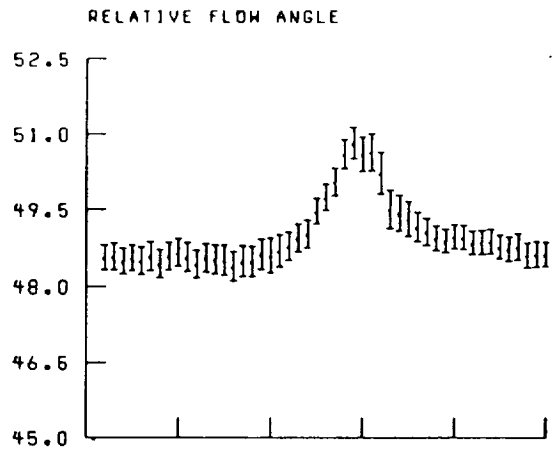
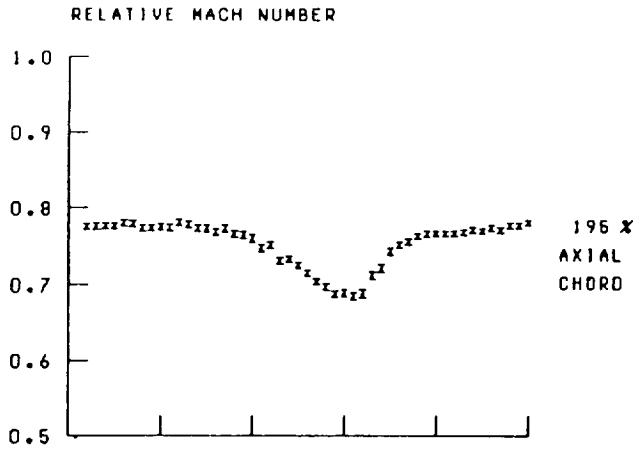


Figure 39.—Concluded.

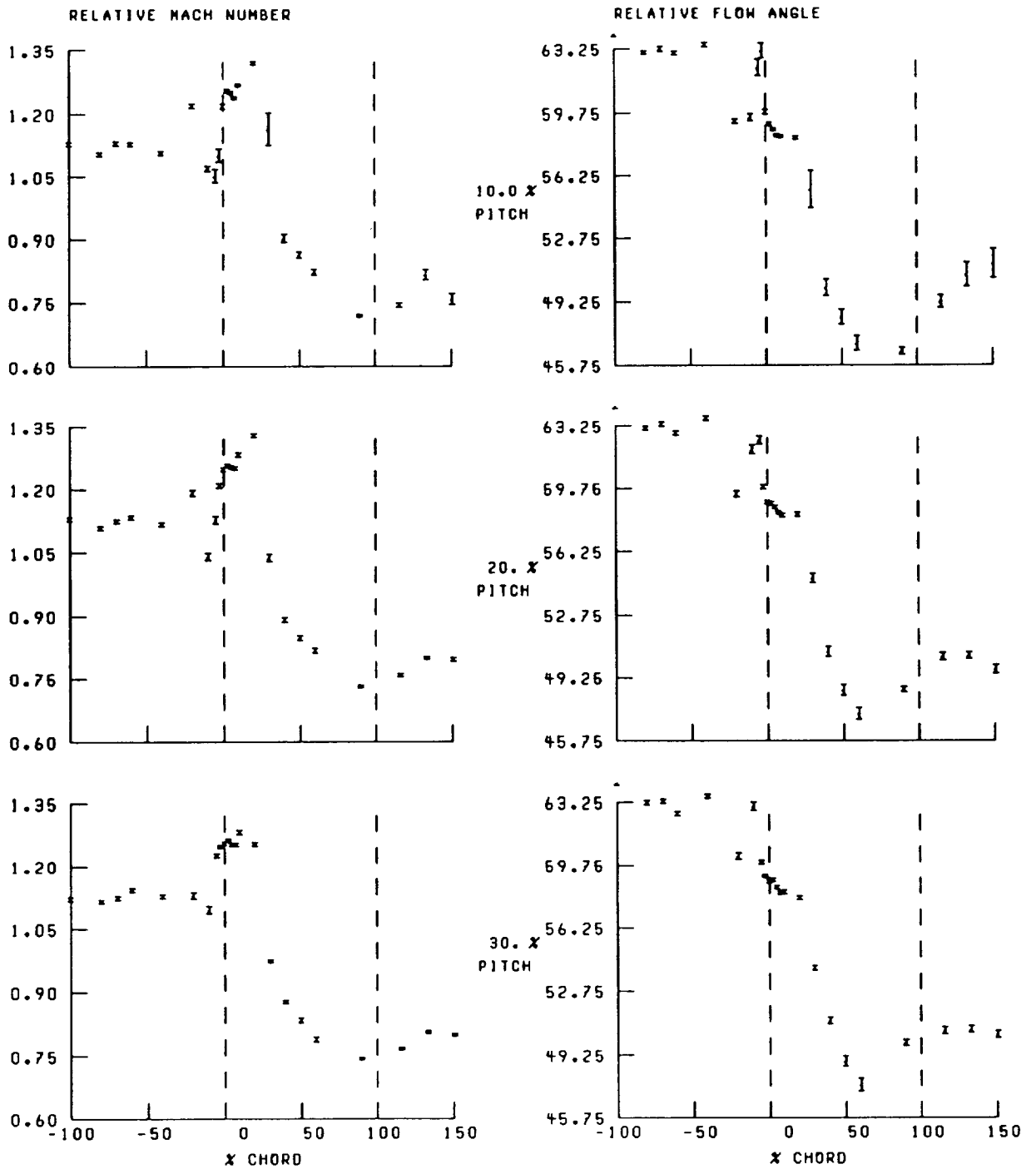


Figure 40.—Streamwise distribution of relative Mach number and flow angle at 40-percent span and near stall. Broken lines denote location of blade lead and trailing edges.

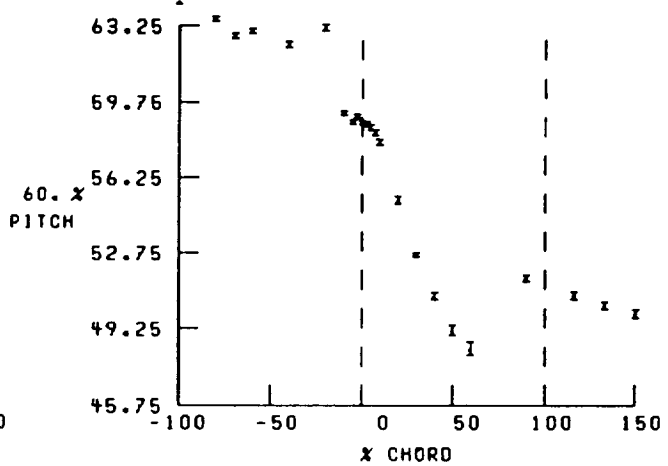
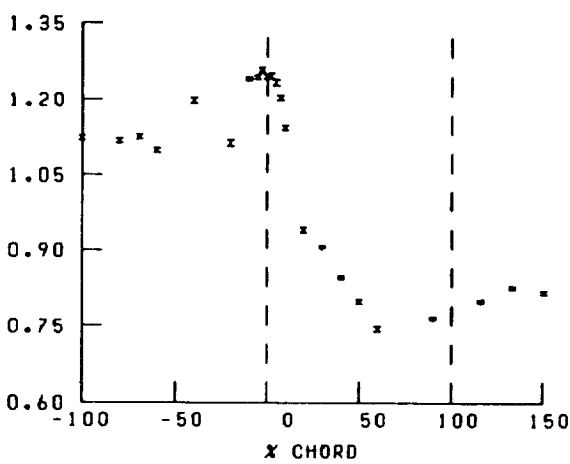
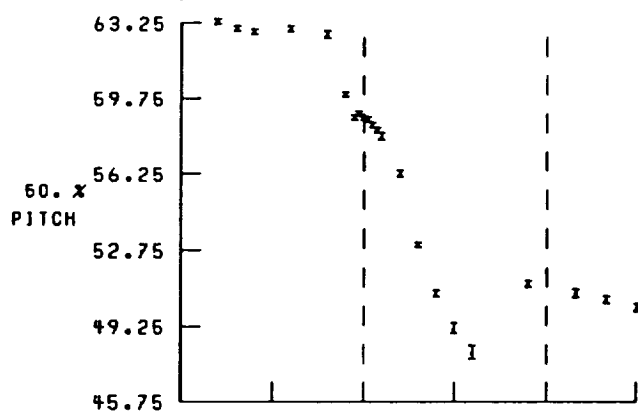
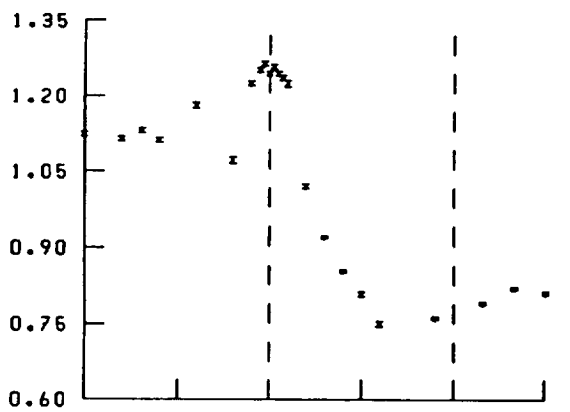
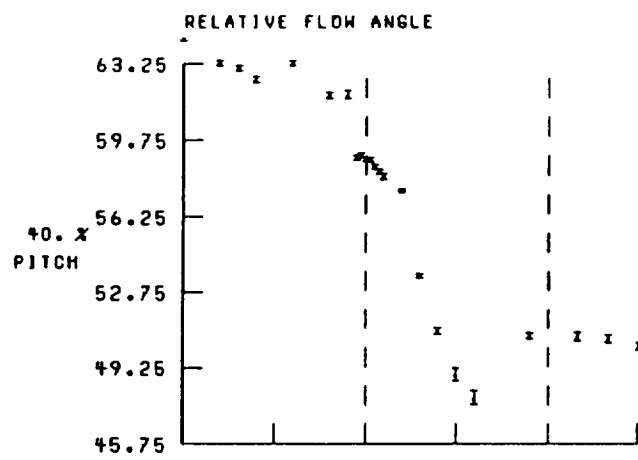
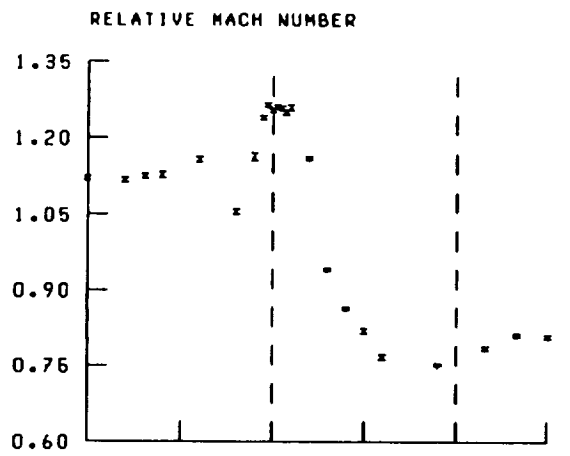


Figure 40.—Continued.

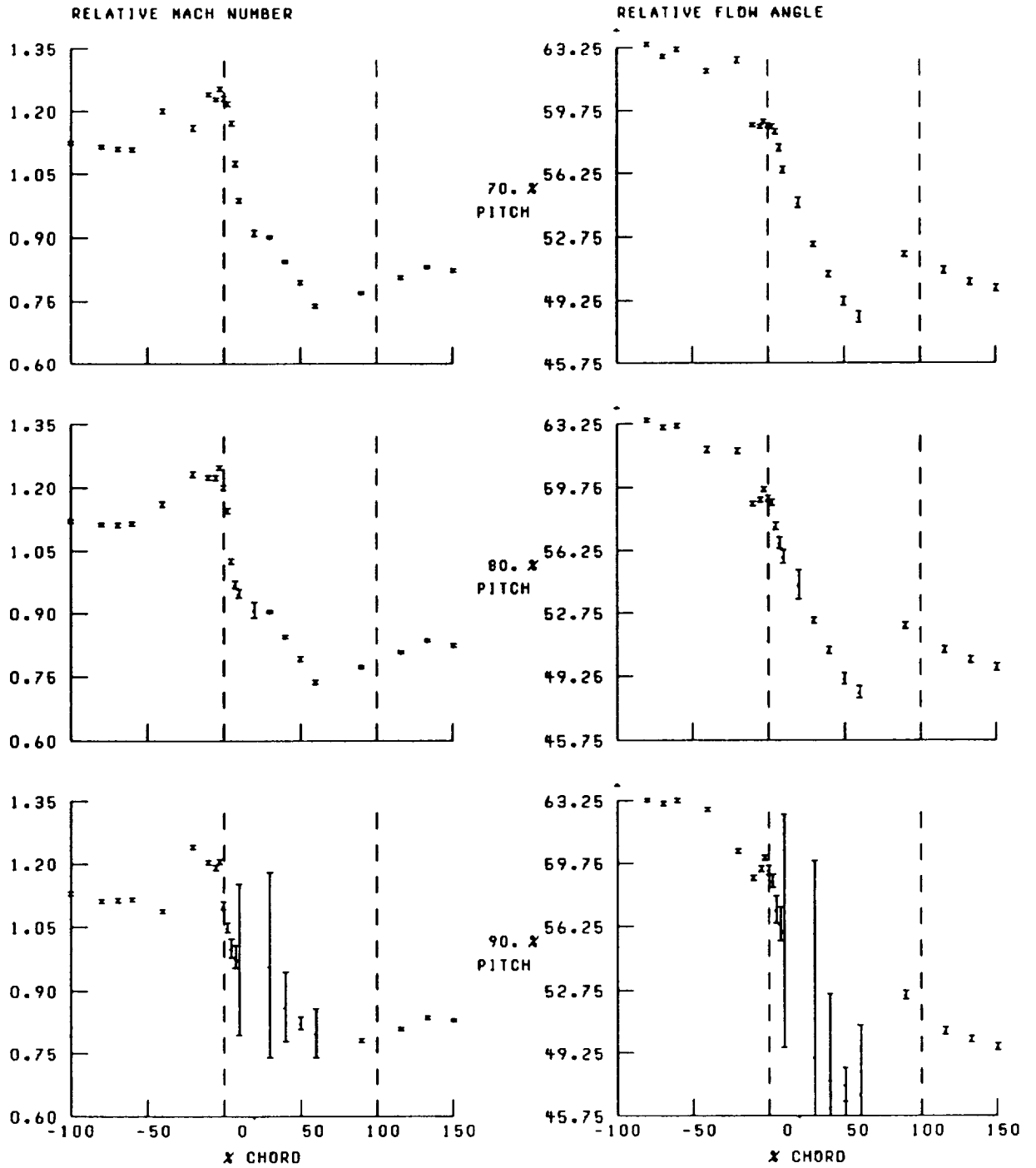


Figure 40.—Concluded.

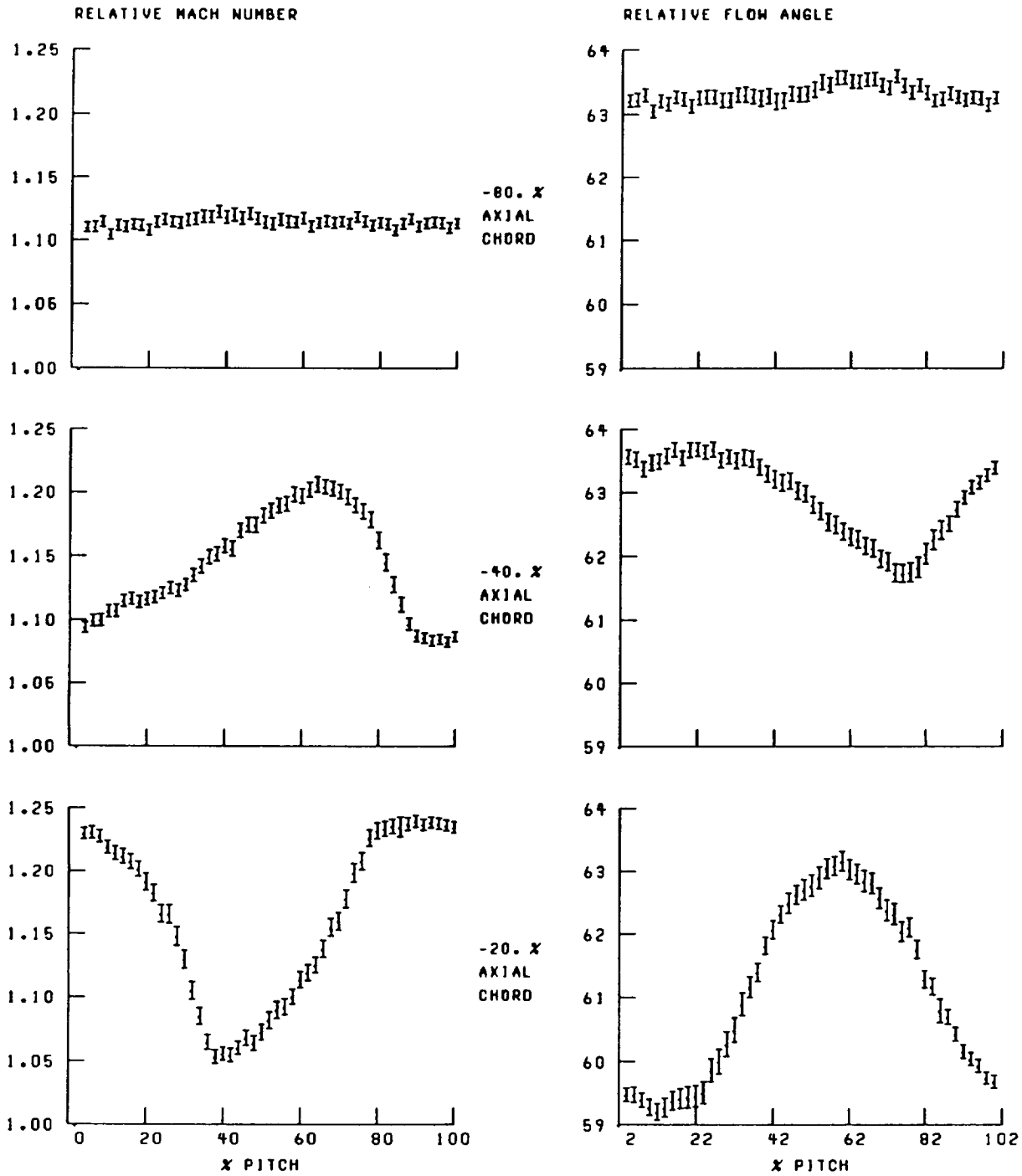


Figure 41.—Blade-to-blade distribution of relative Mach number and flow angle at 40-percent span and near stall.

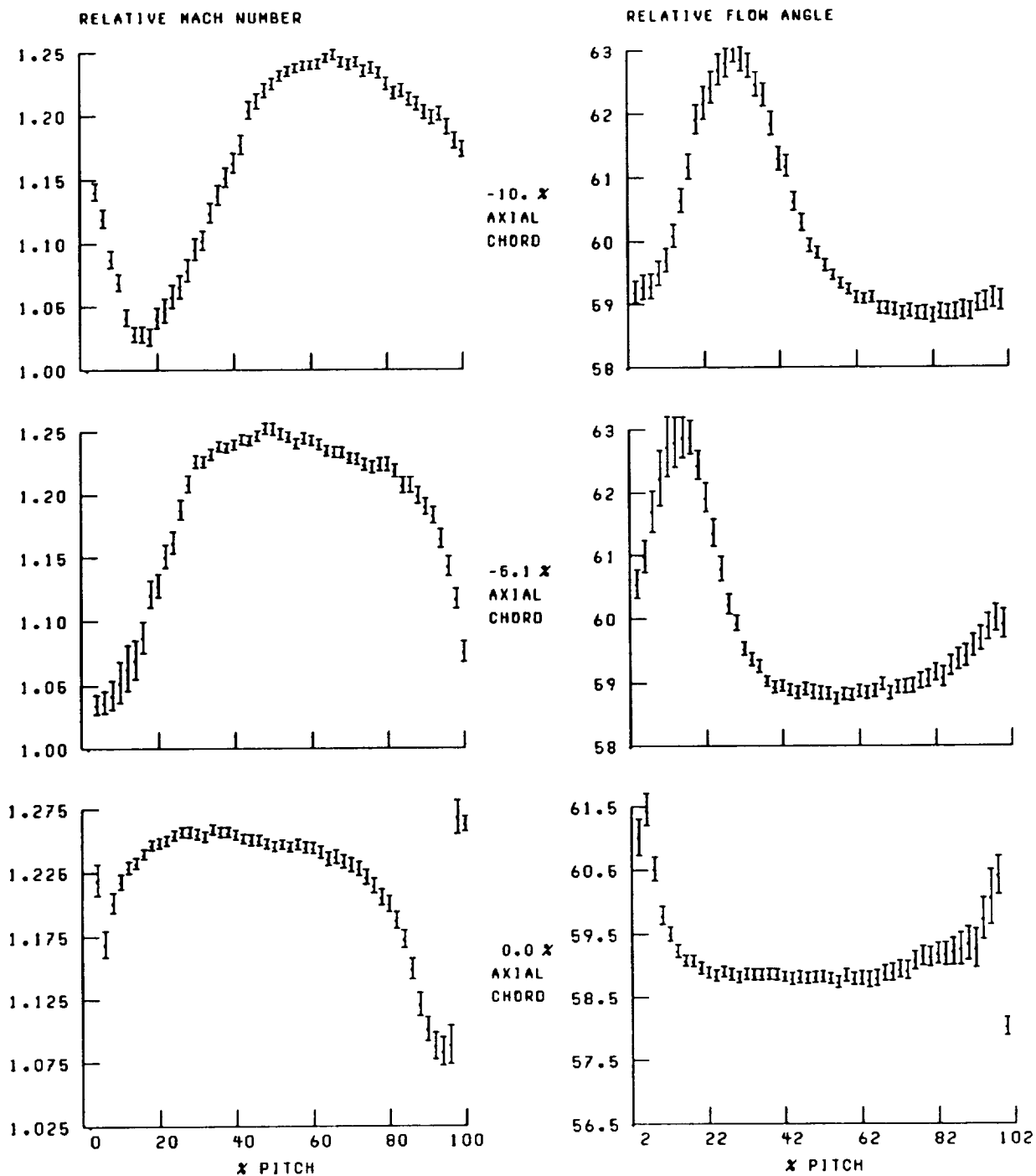


Figure 41.—Continued.

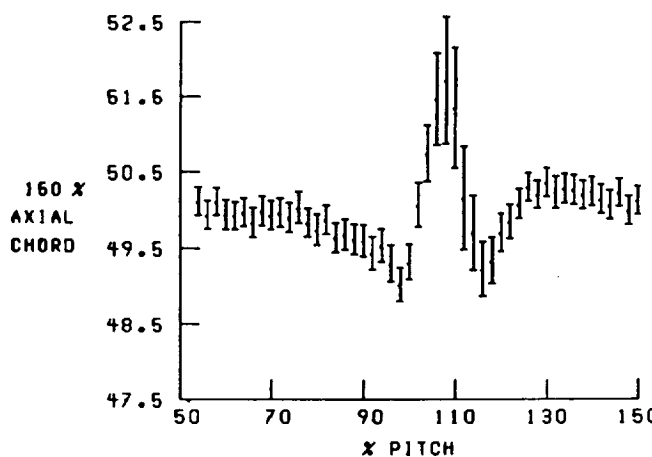
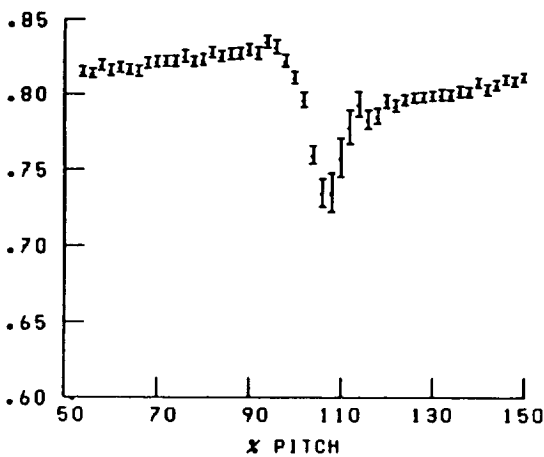
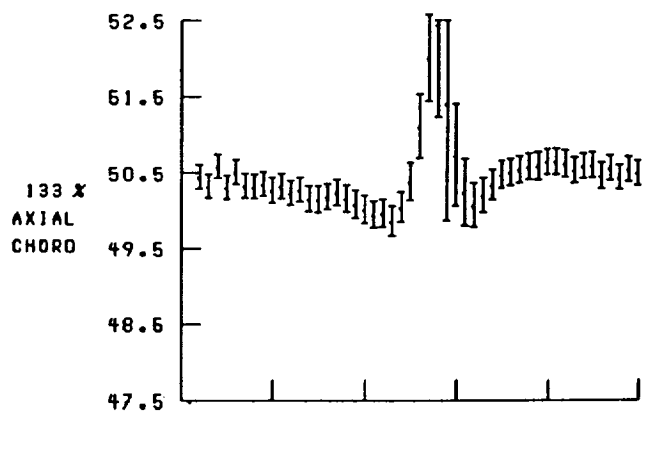
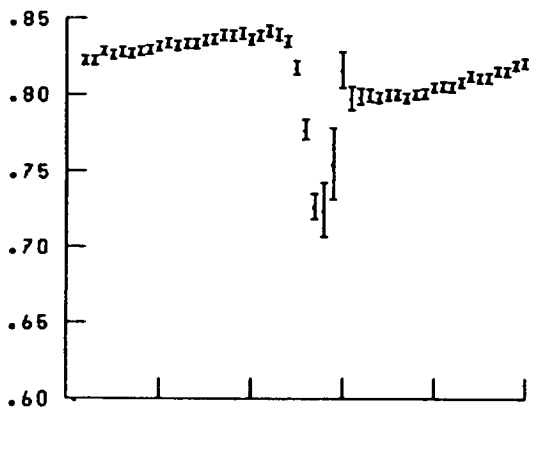
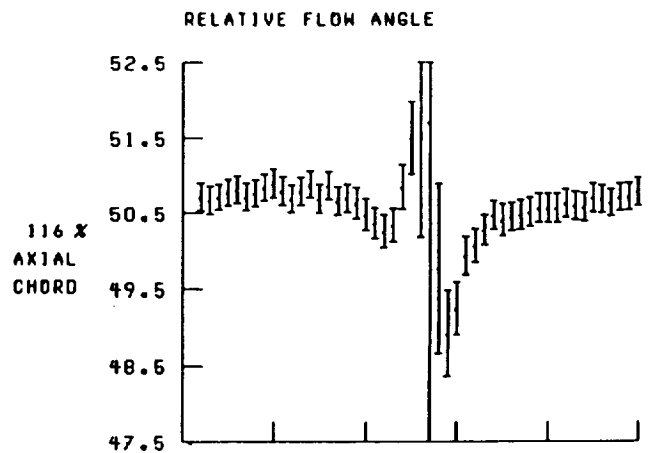
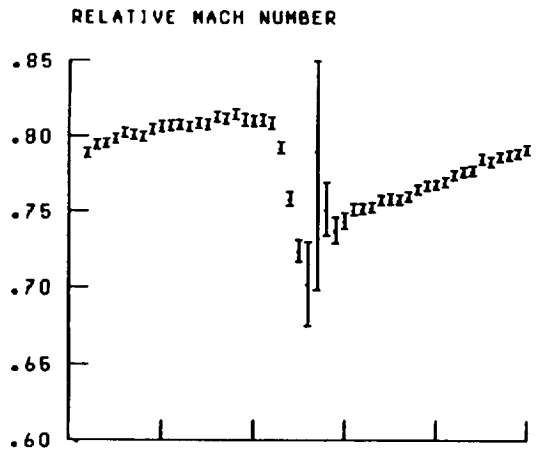


Figure 41.—Concluded.

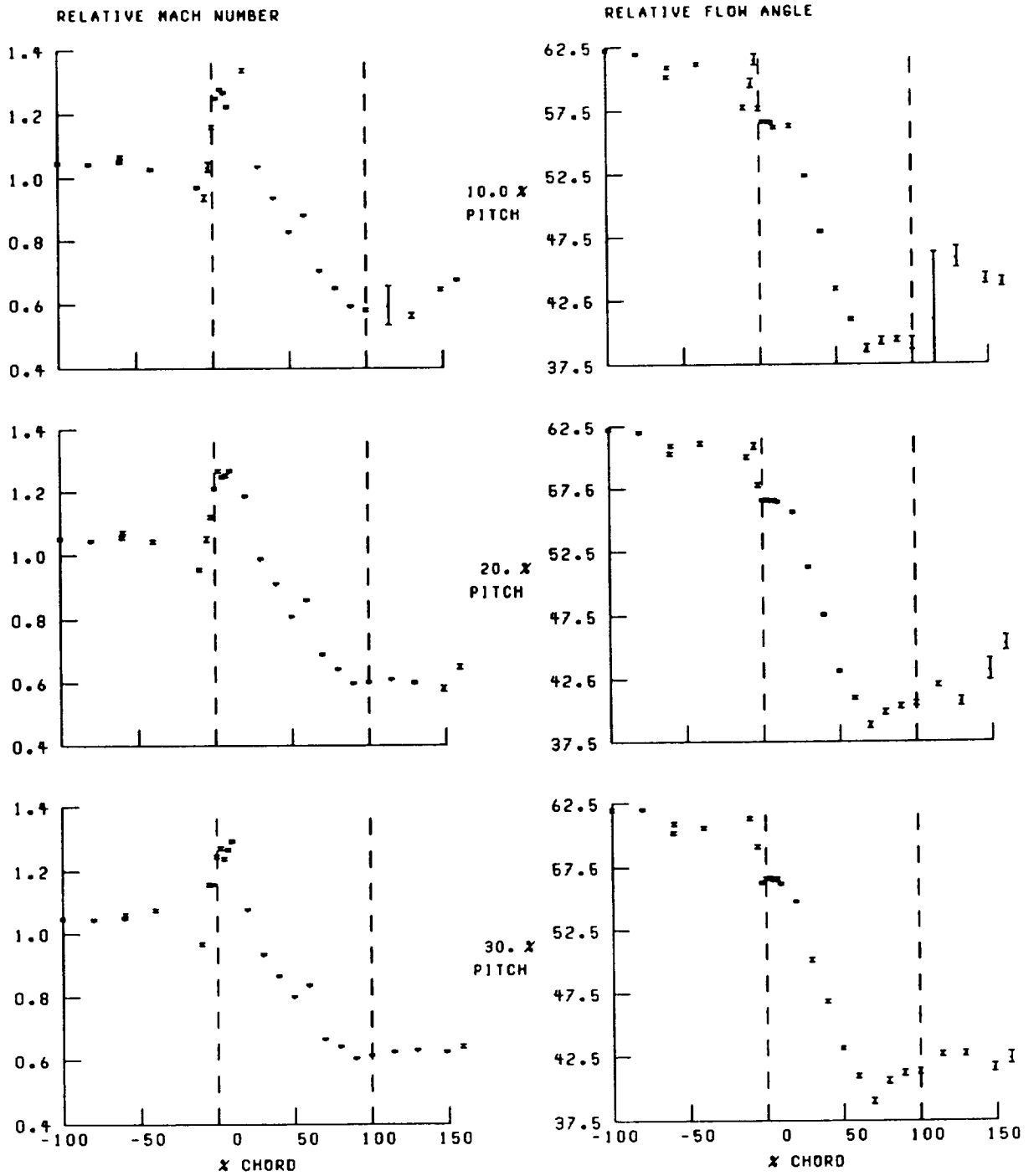


Figure 42.—Streamwise distribution of relative Mach number and flow angle at 50-percent span and near stall. Broken lines denote location of blade leading and trailing edges.

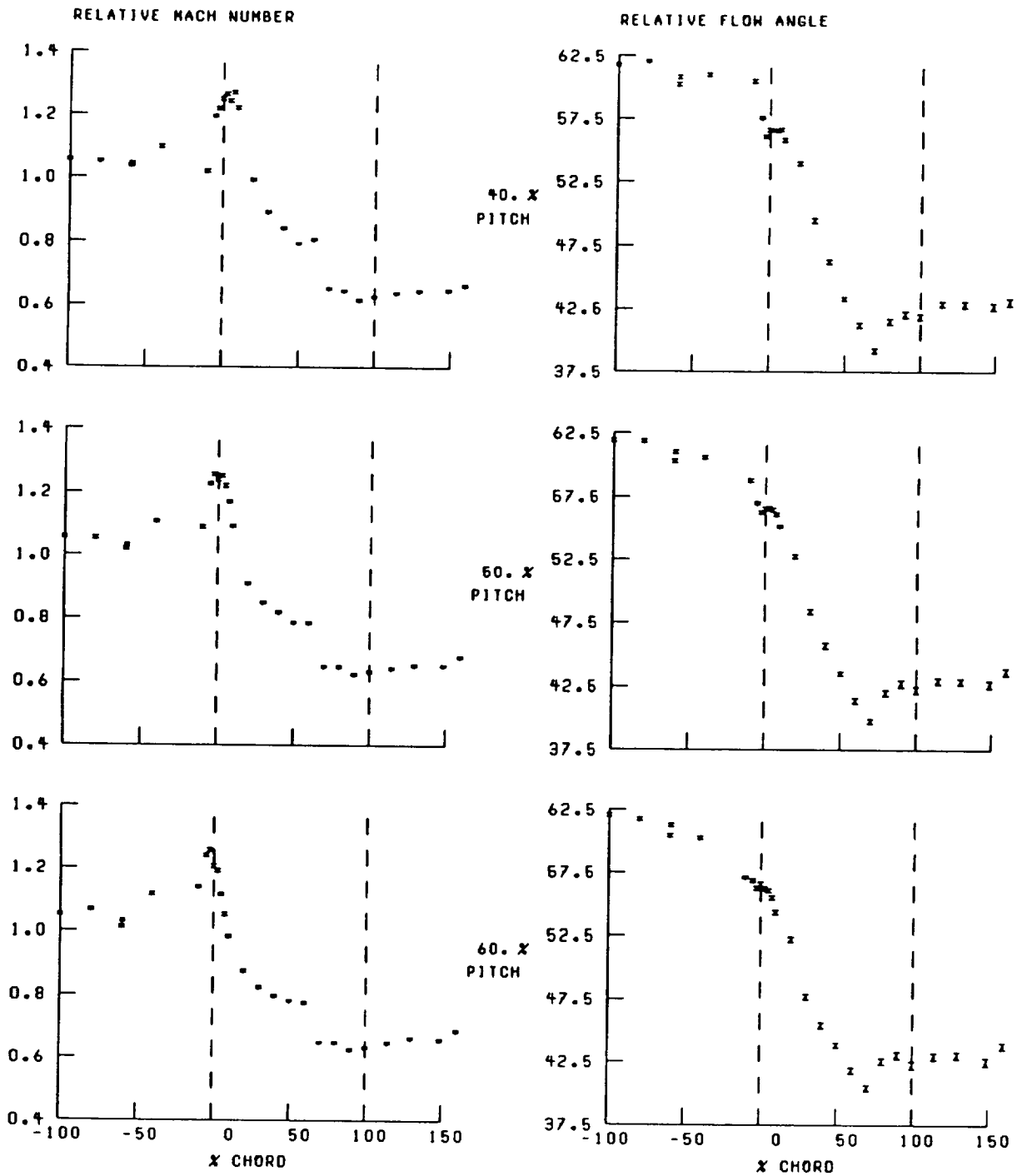


Figure 42.—Continued.

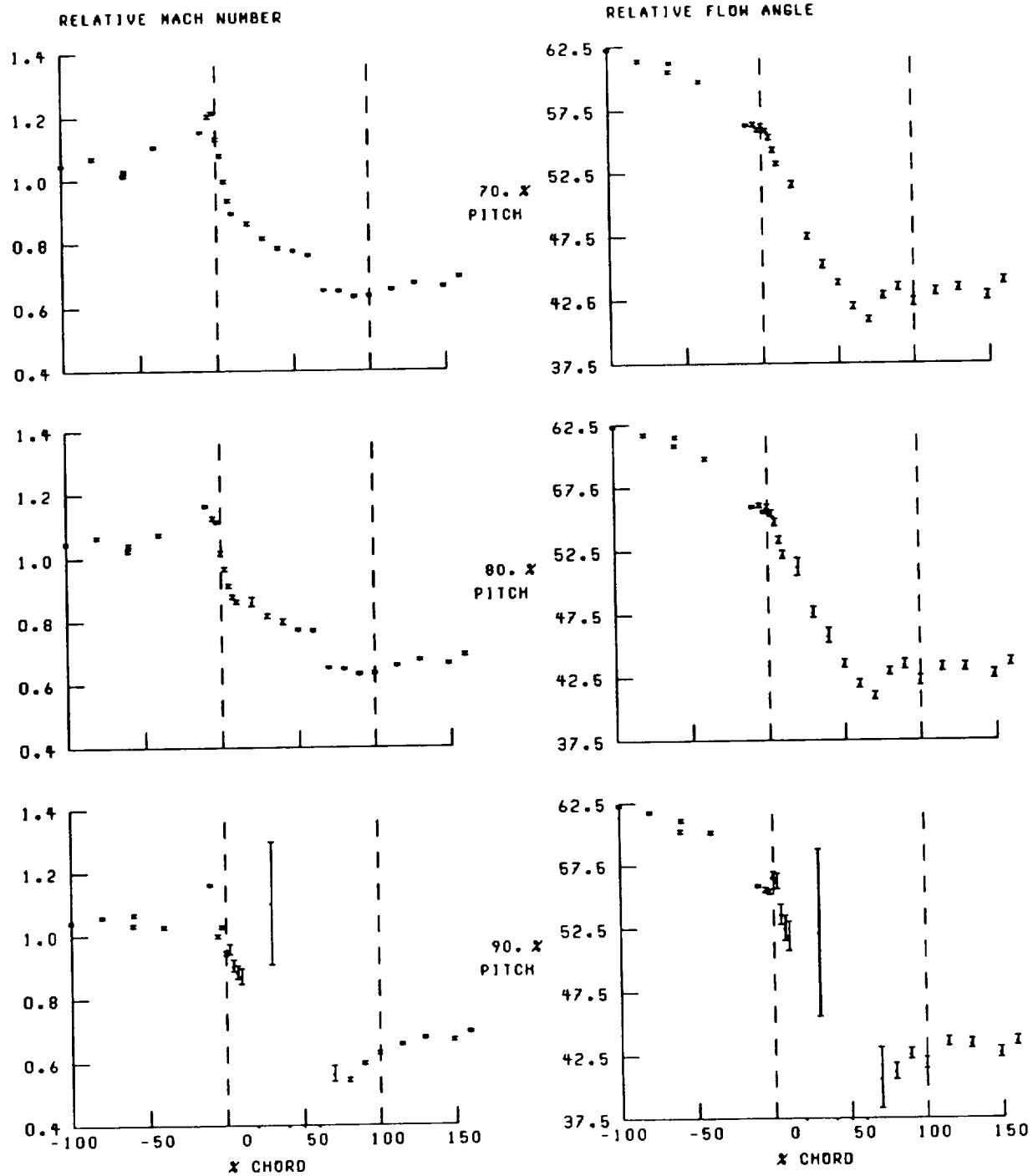


Figure 42.—Concluded.

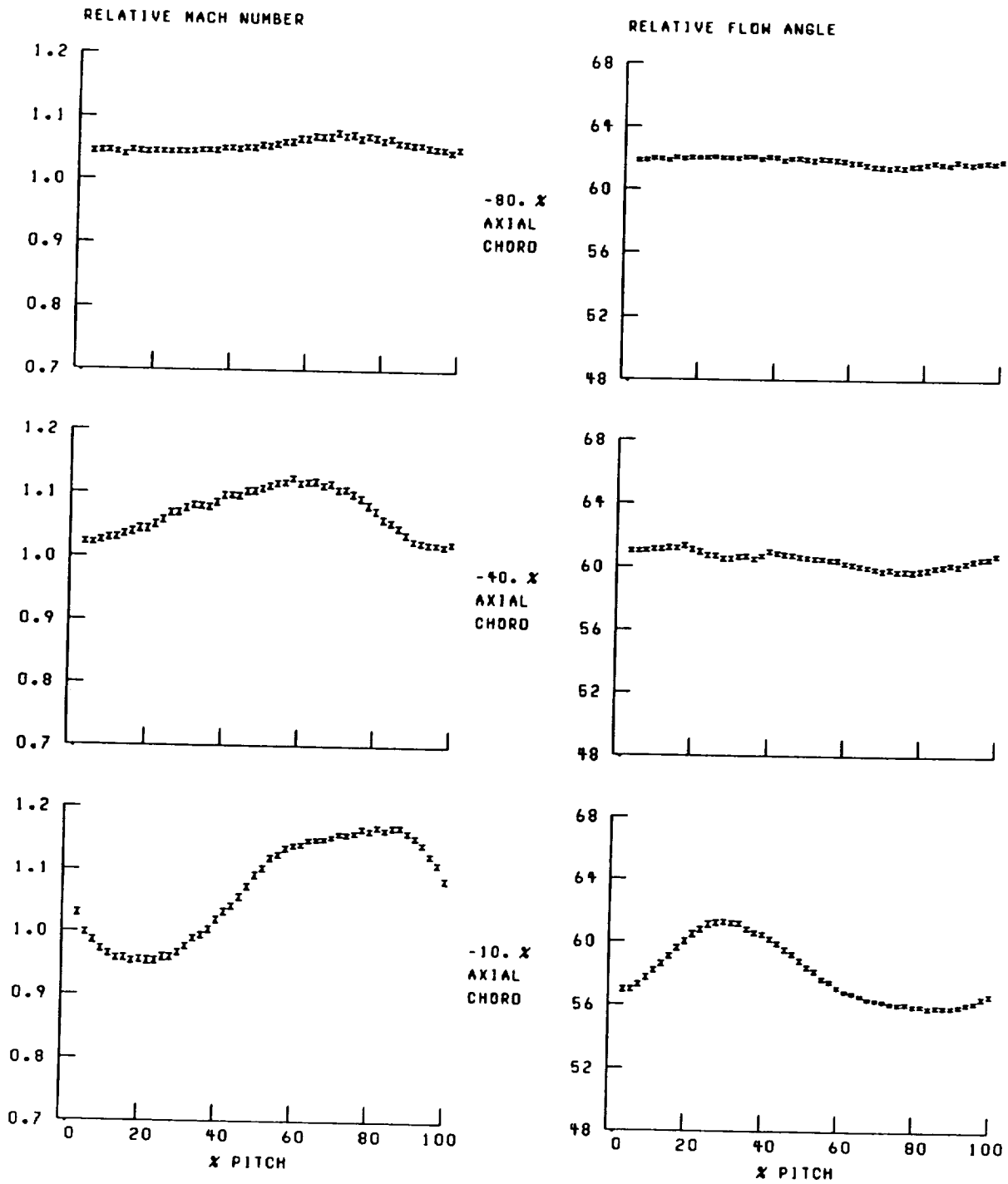


Figure 43.—Blade-to-blade distribution of relative Mach number and flow angle at 50-percent span and near stall.

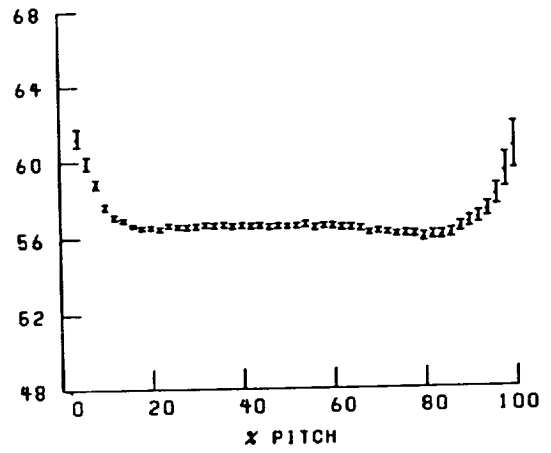
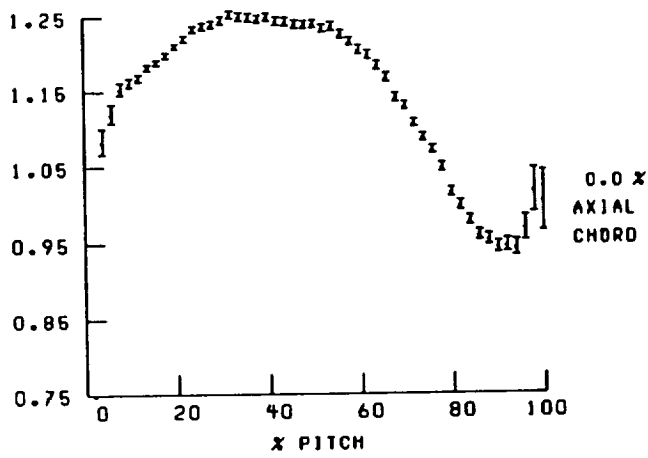
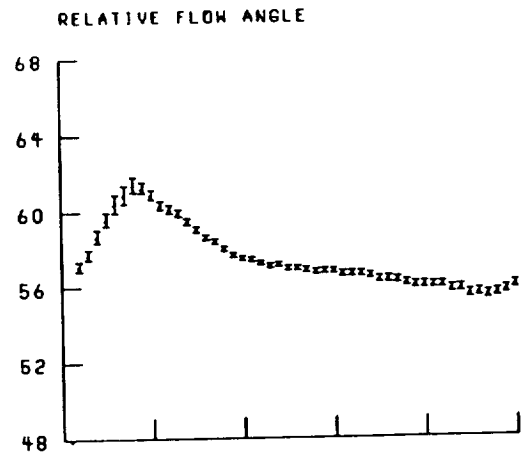
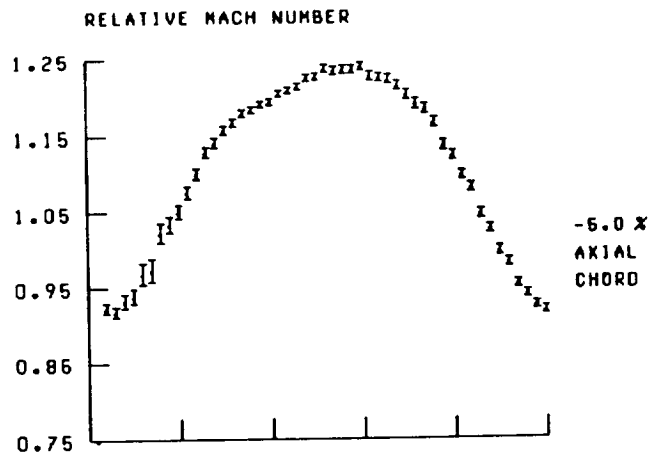


Figure 43.—Continued.

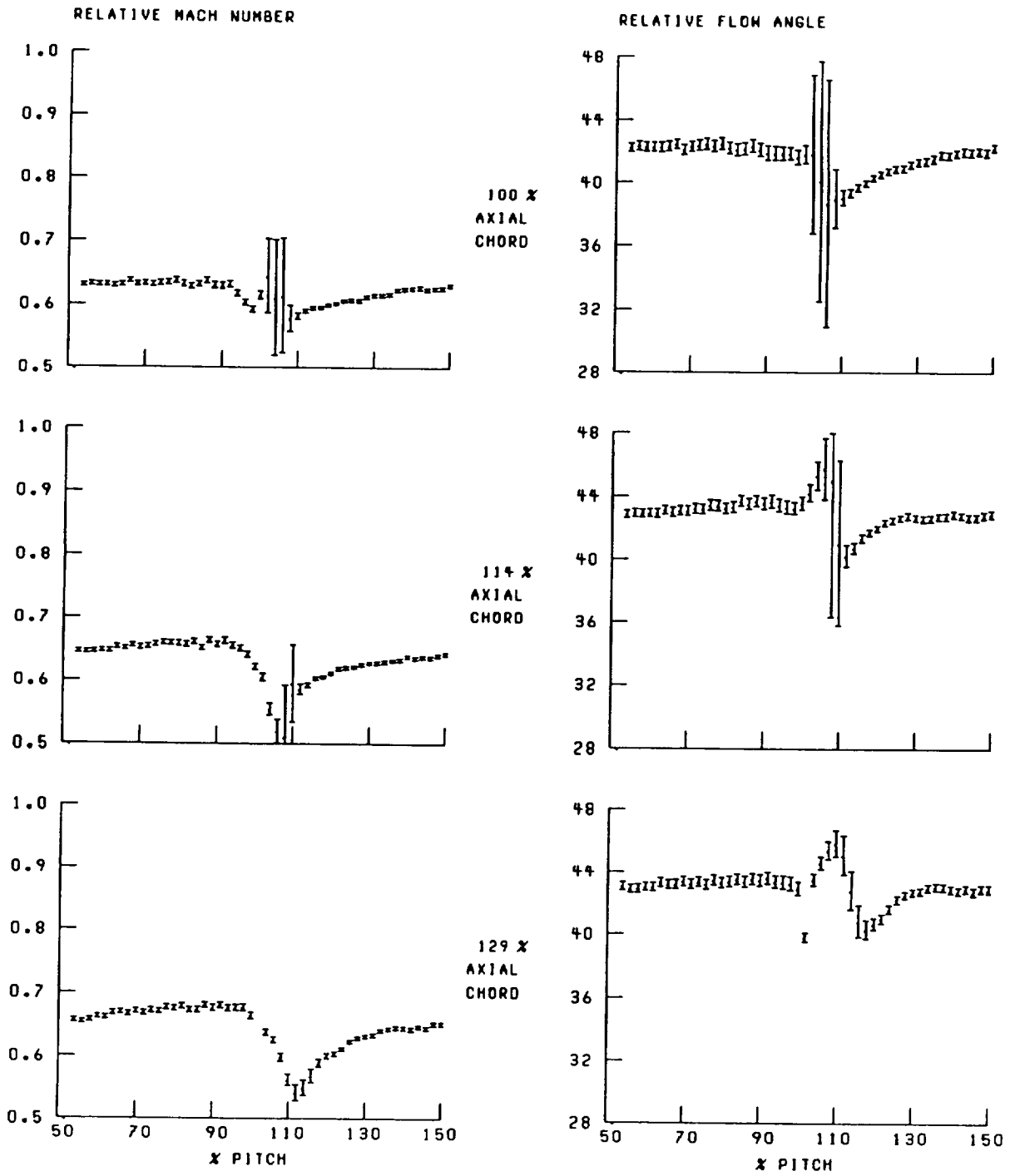


Figure 43.—Continued.

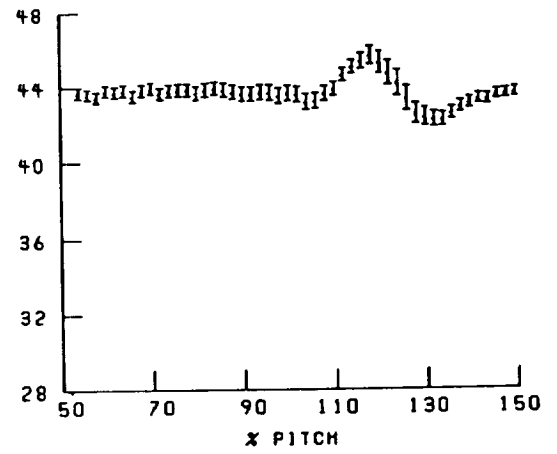
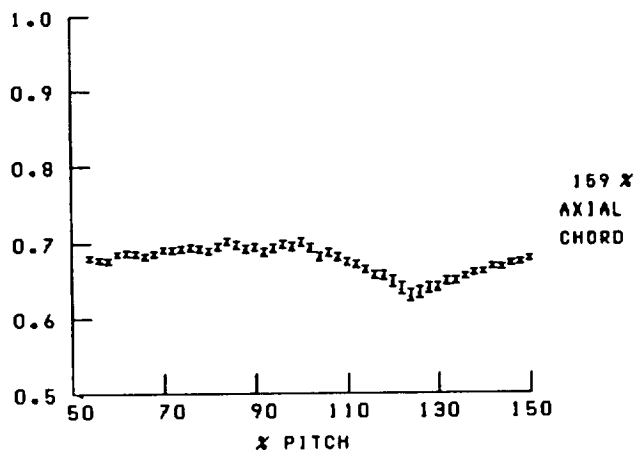
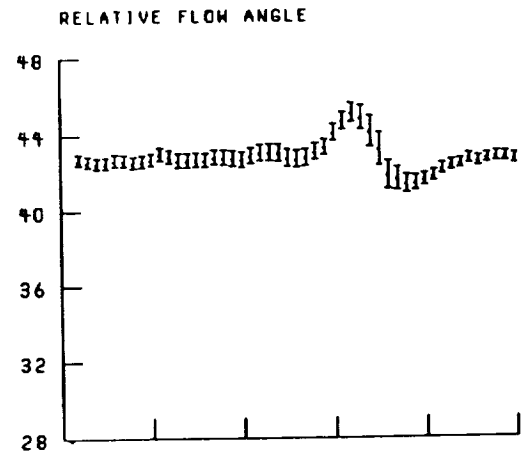
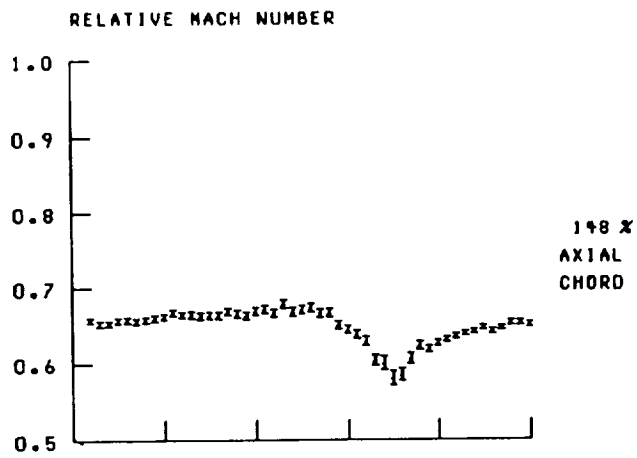


Figure 43.—Concluded.

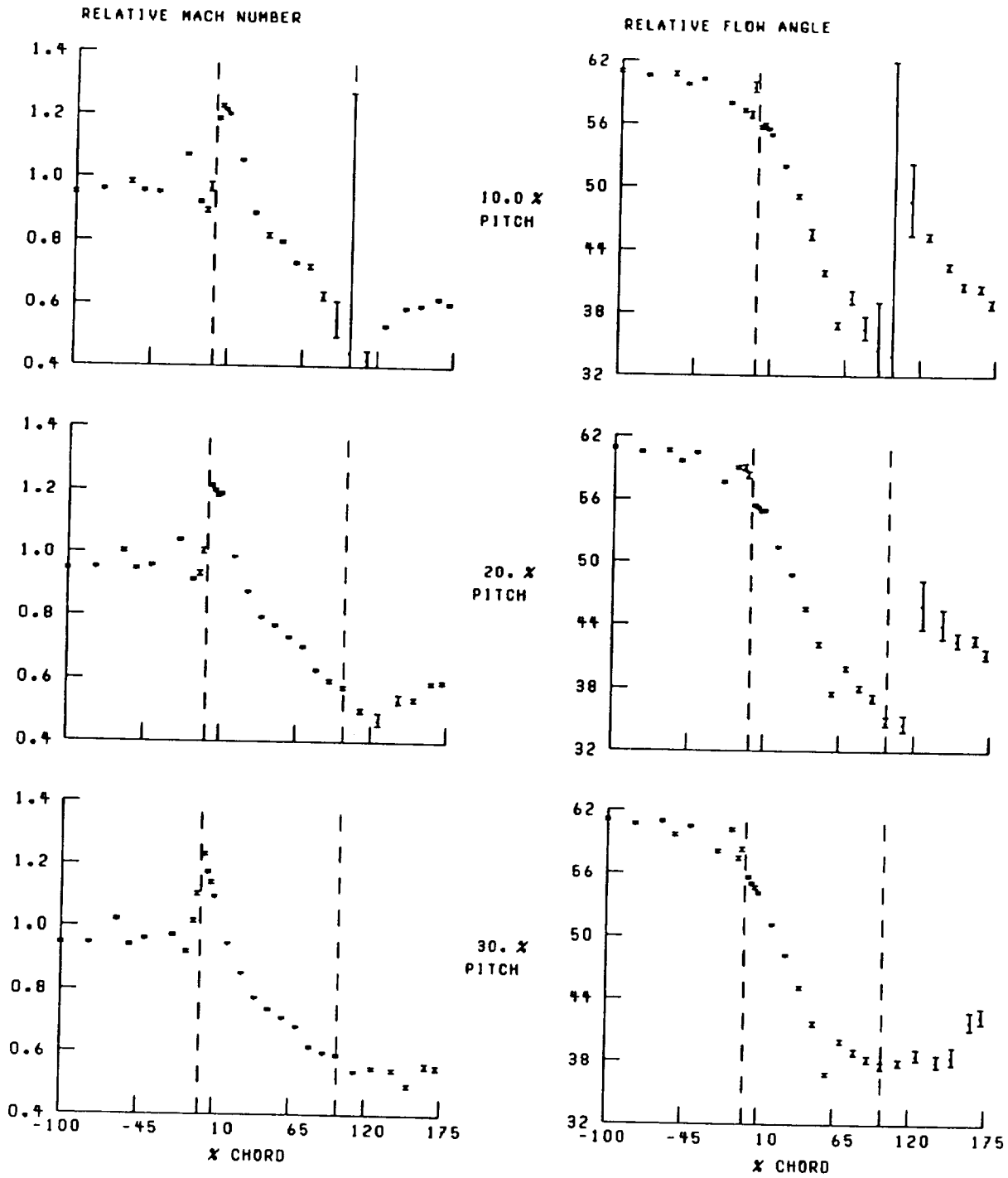


Figure 44.—Streamwise distribution of relative Mach number and flow angle at 60-percent span and near stall. Broken lines denote location of blade leading and trailing edges.

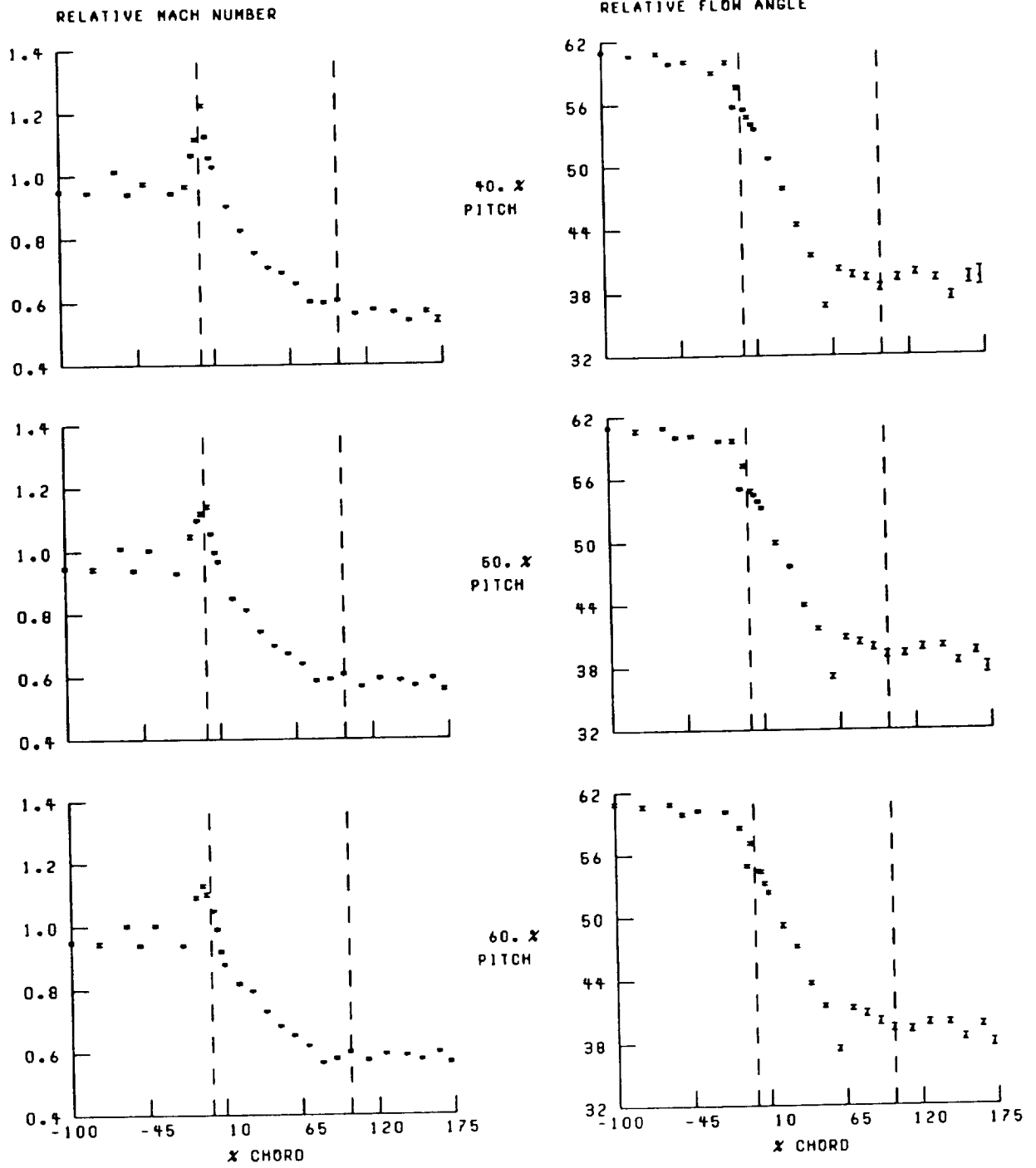


Figure 44.—Continued.

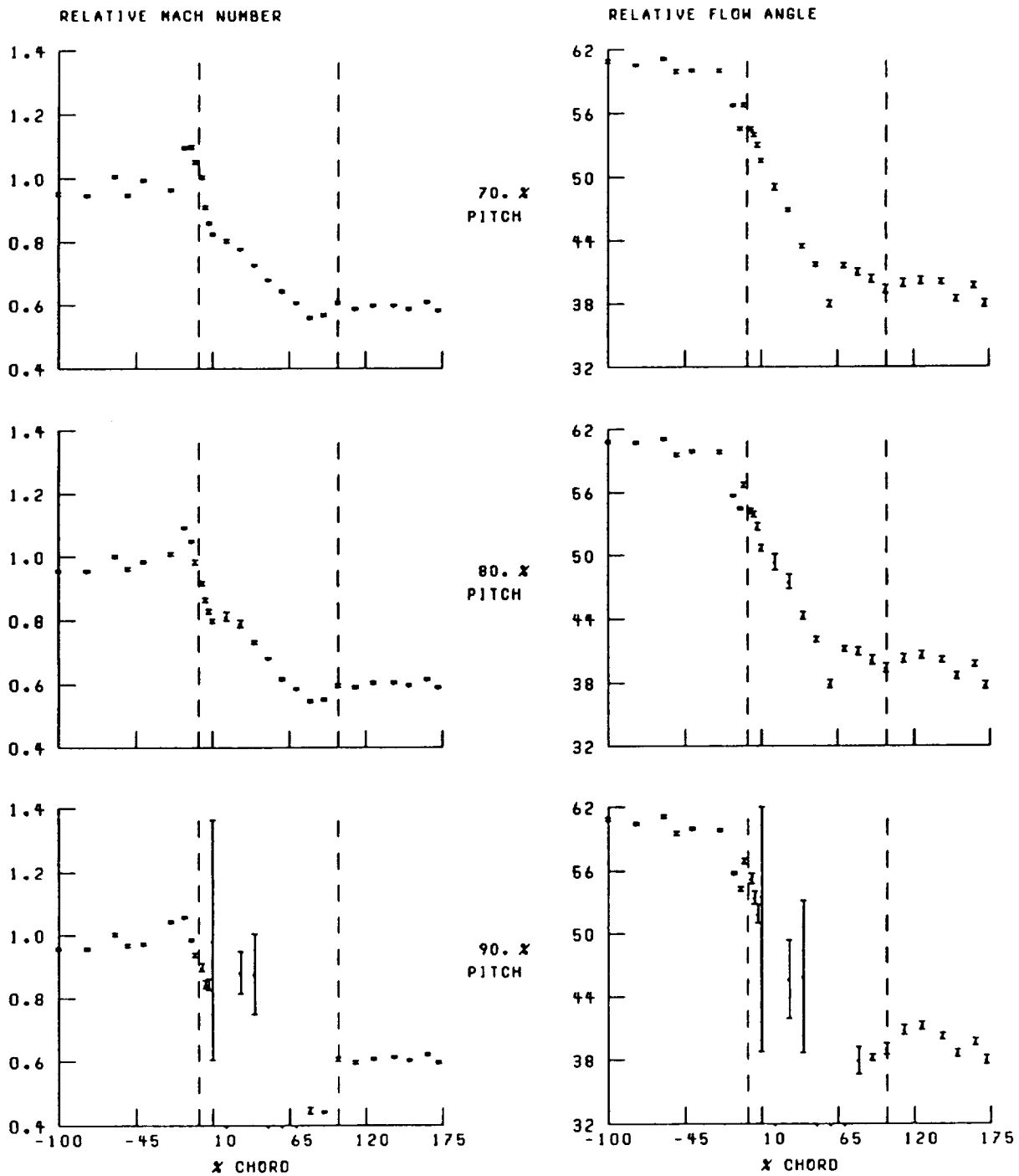


Figure 44.—Concluded.

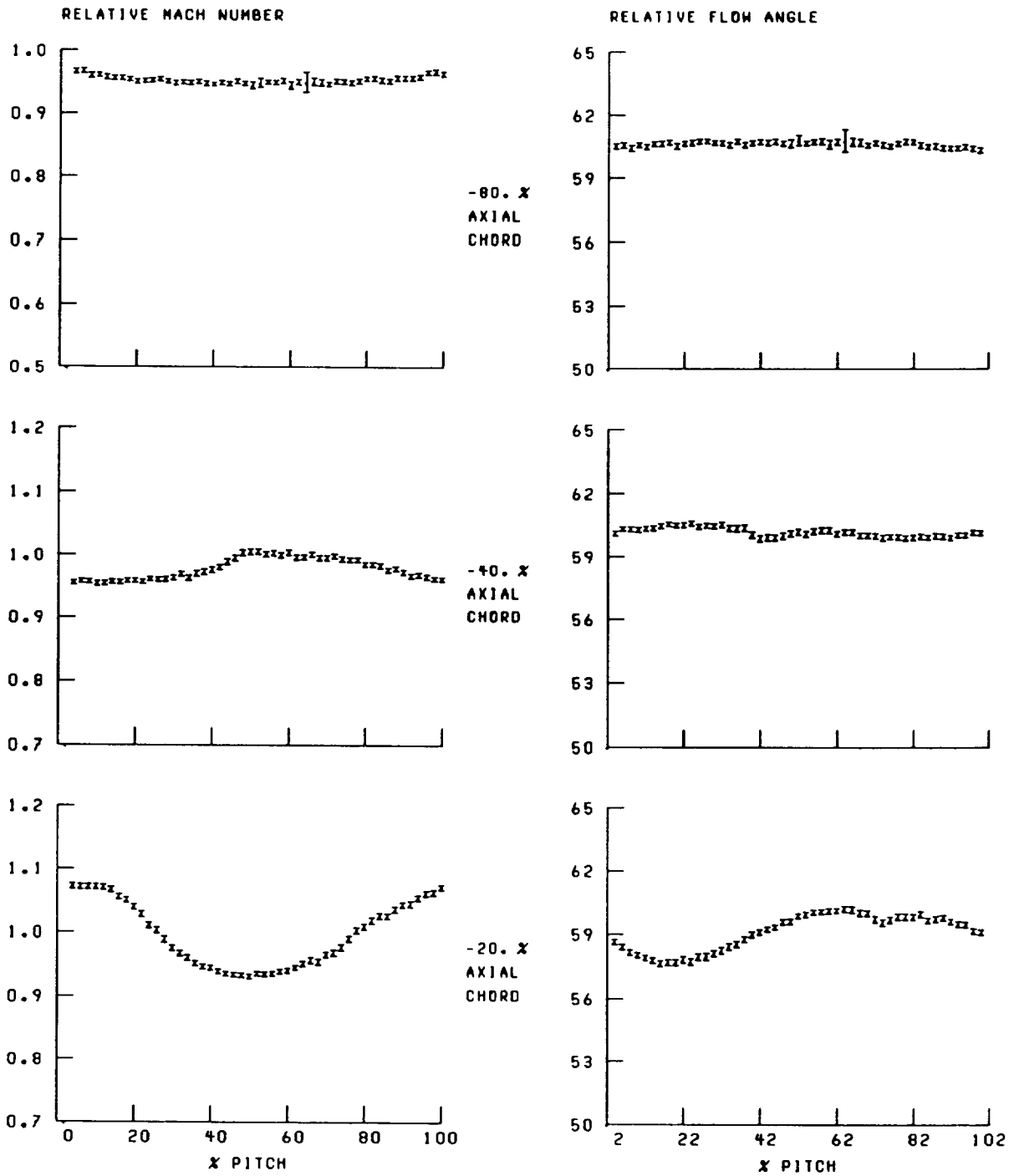


Figure 45.—Blade-to-blade distribution of relative Mach number and flow angle at 60-percent span and near stall.

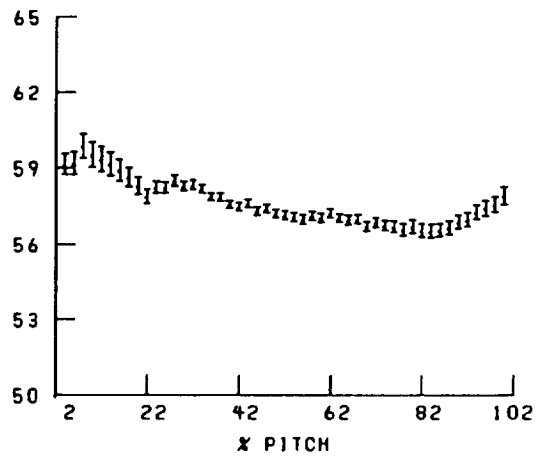
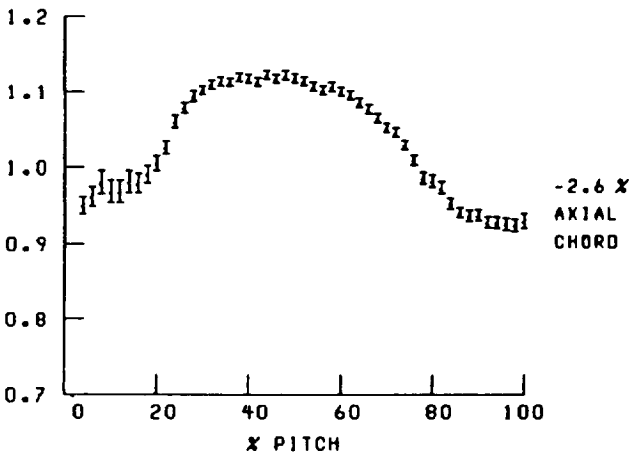
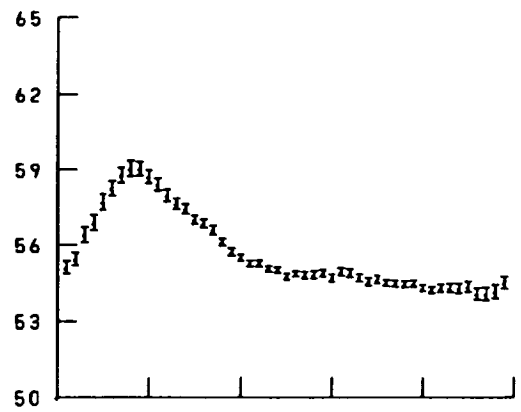
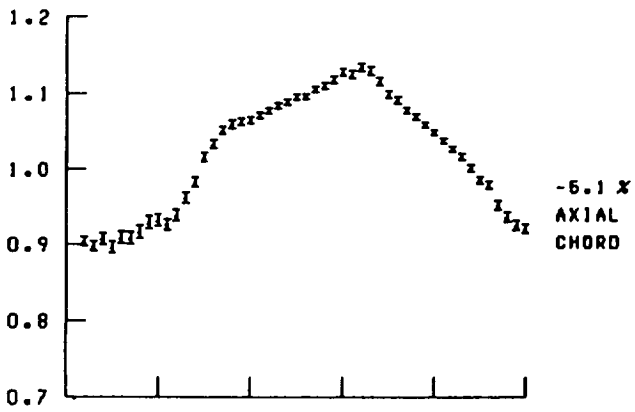
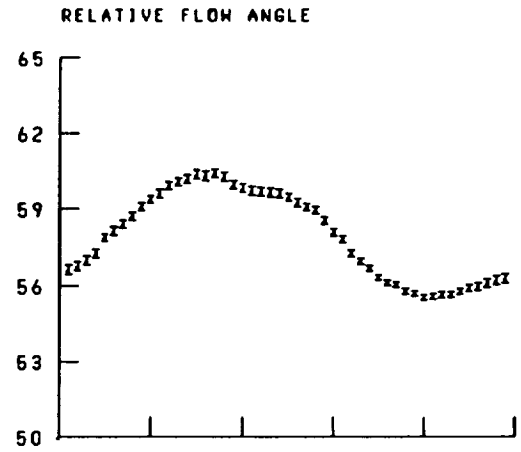
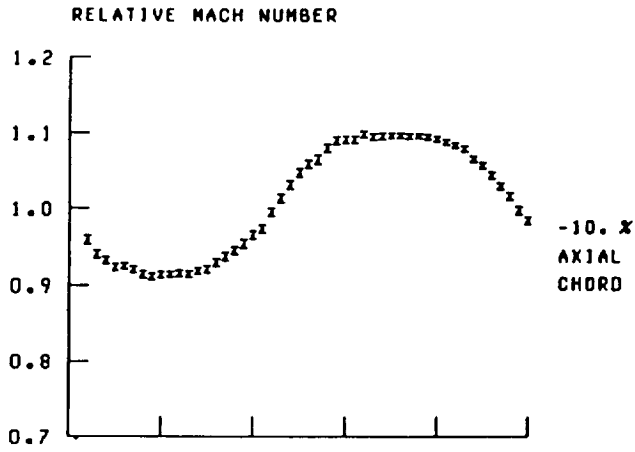


Figure 45.—Continued.

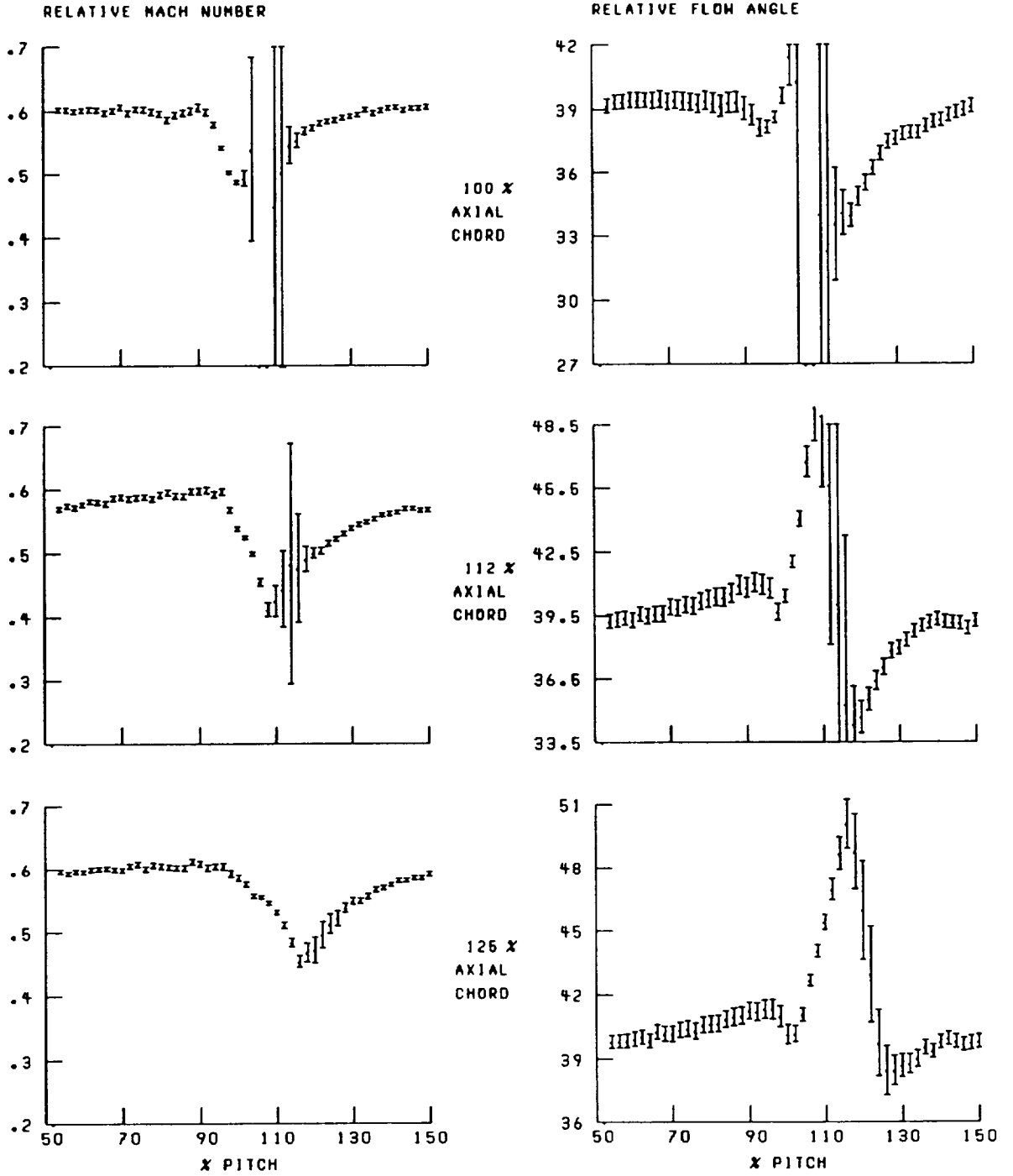


Figure 45.—Continued.

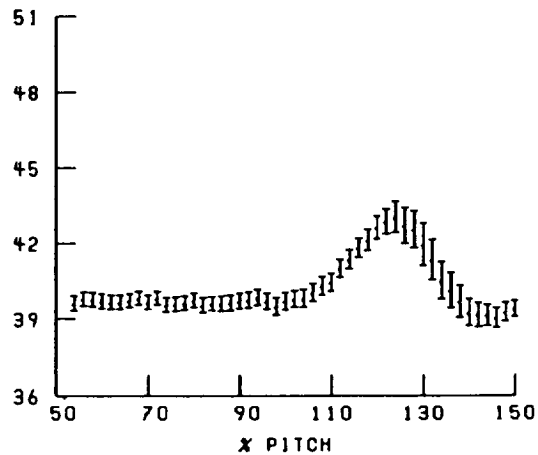
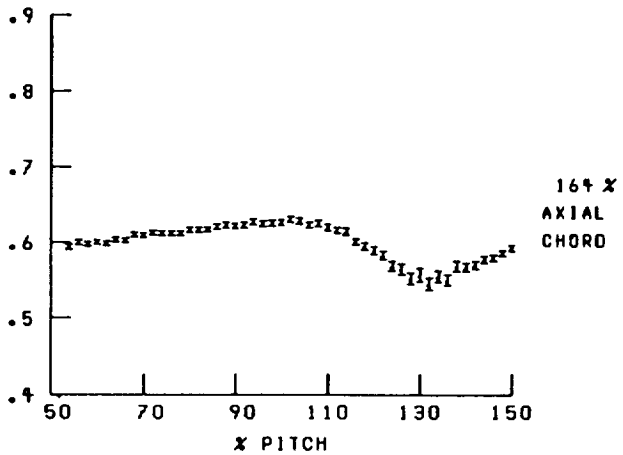
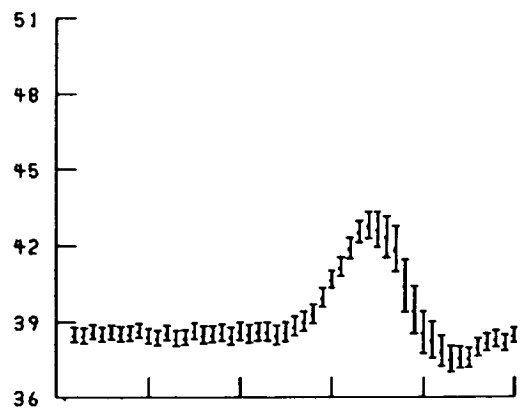
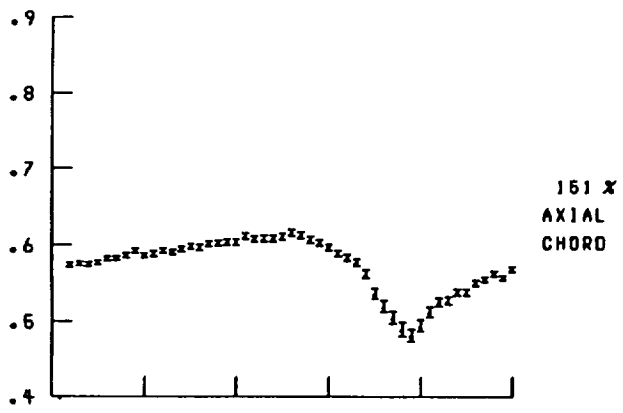
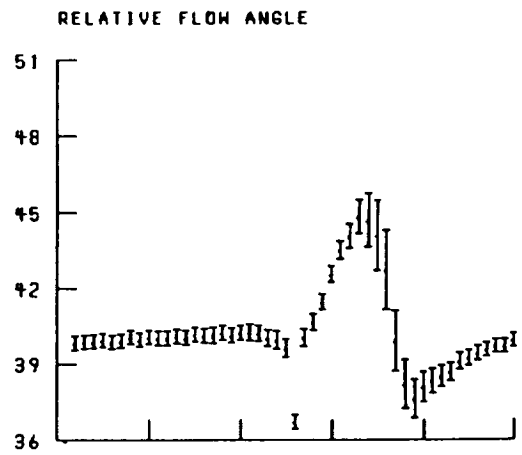
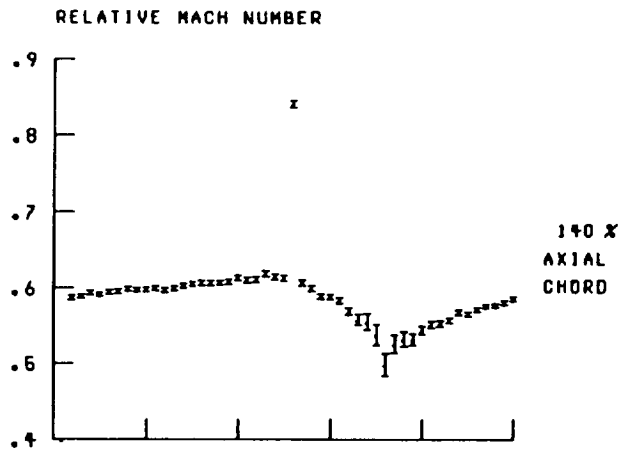


Figure 45.—Concluded.

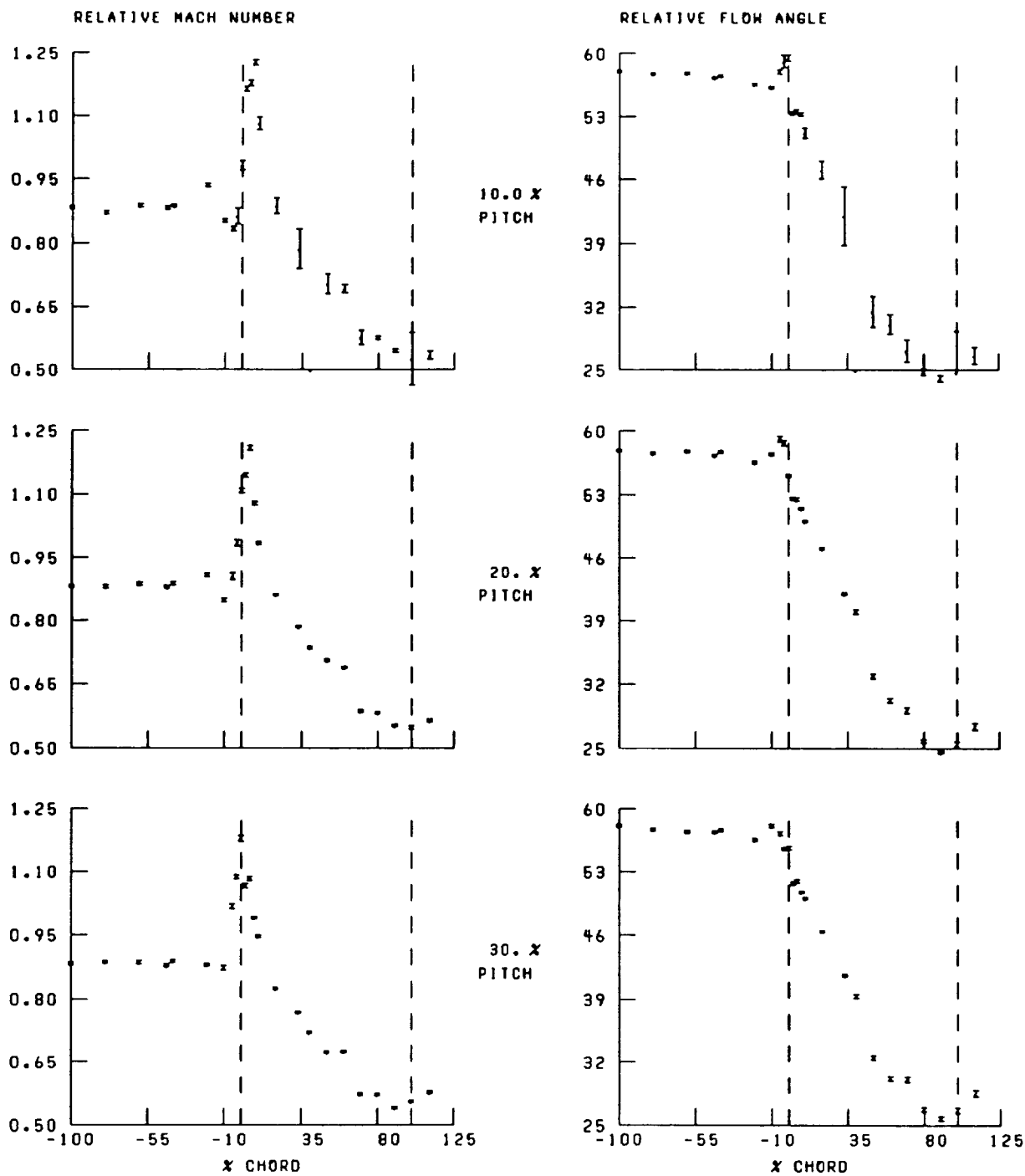


Figure 46.—Streamwise distribution of relative Mach number and flow angle at 70-percent span and near stall. Broken lines denote location of blade leading and trailing edges.

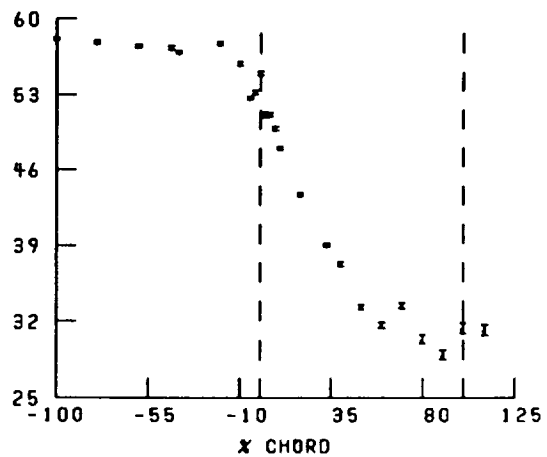
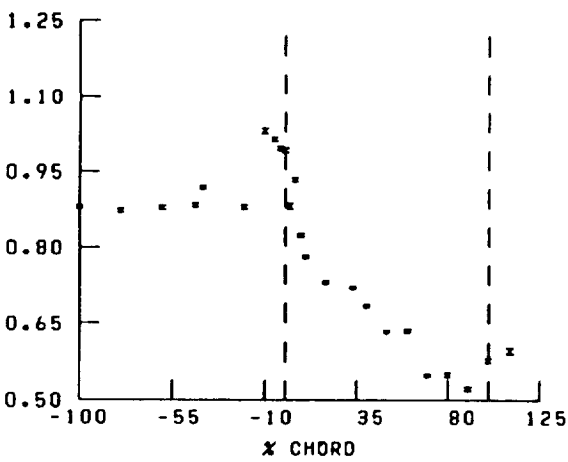
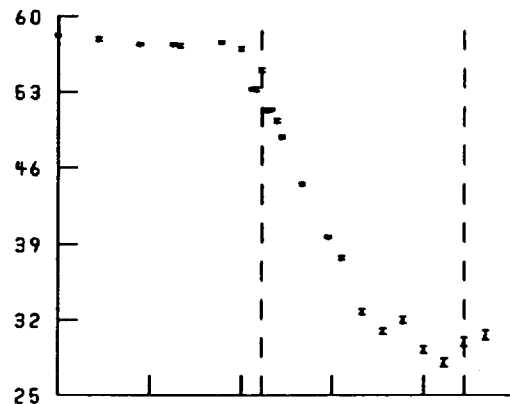
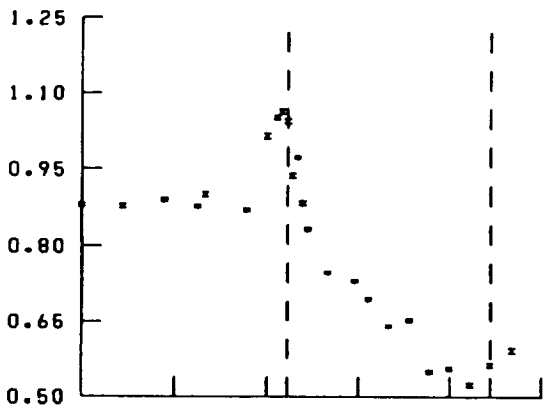
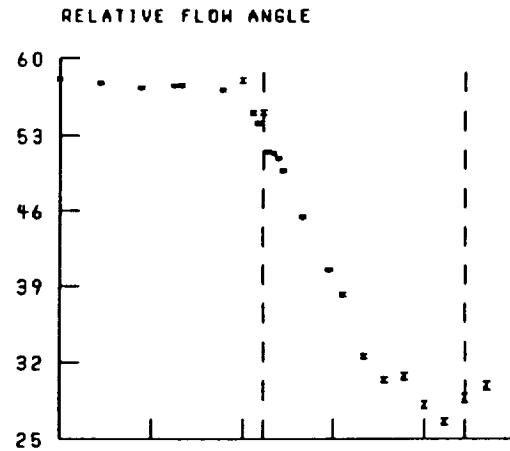
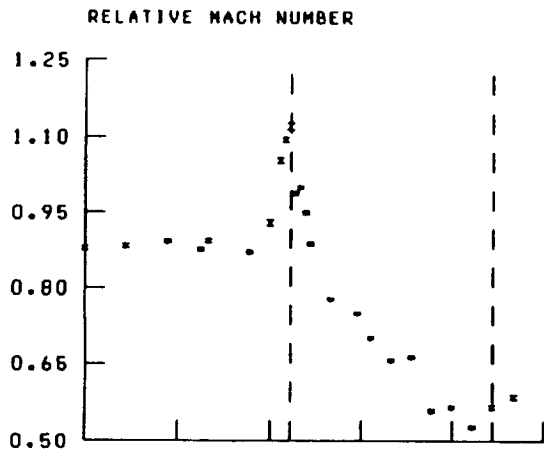


Figure 46.—Continued.

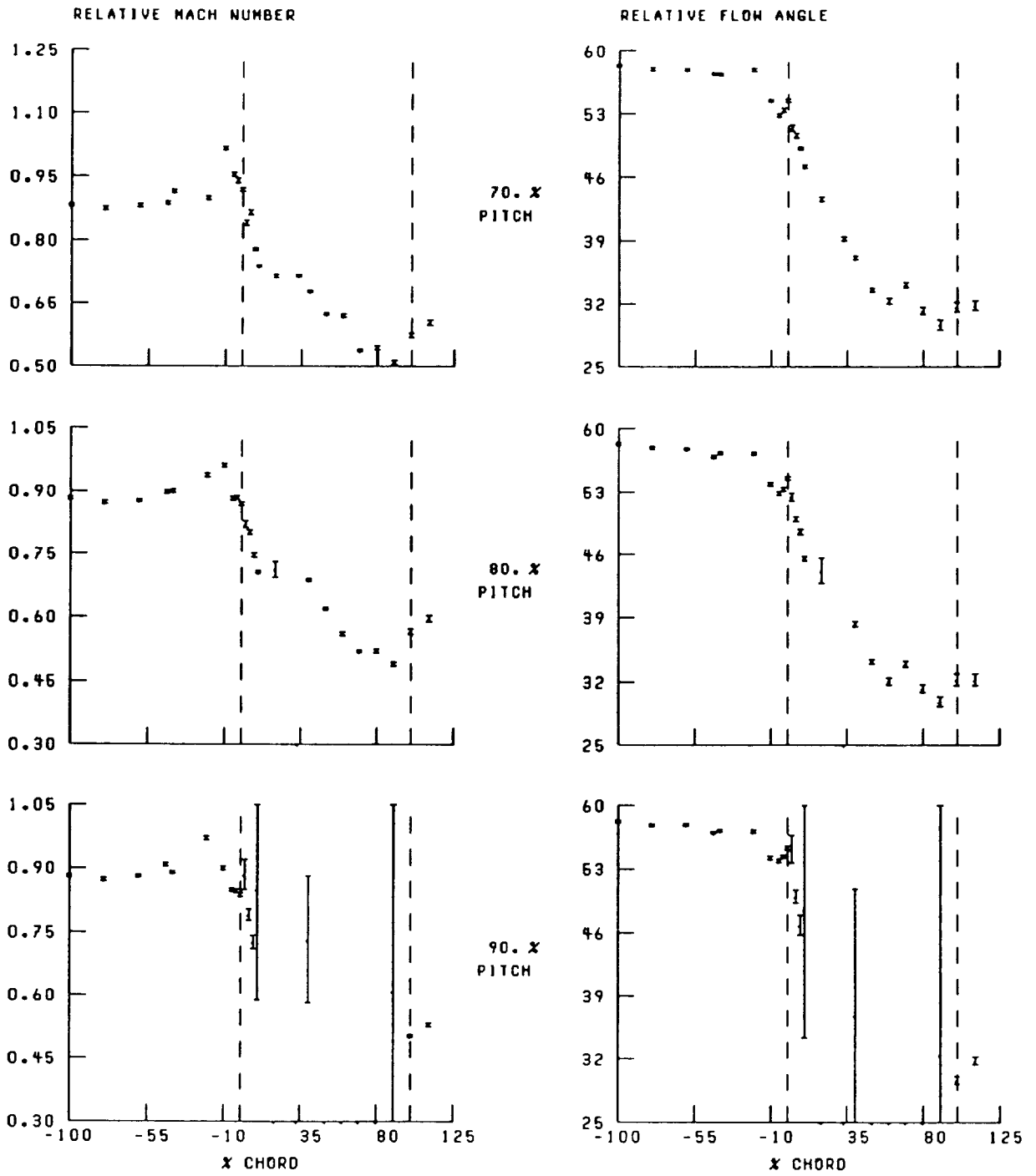


Figure 46.—Concluded.

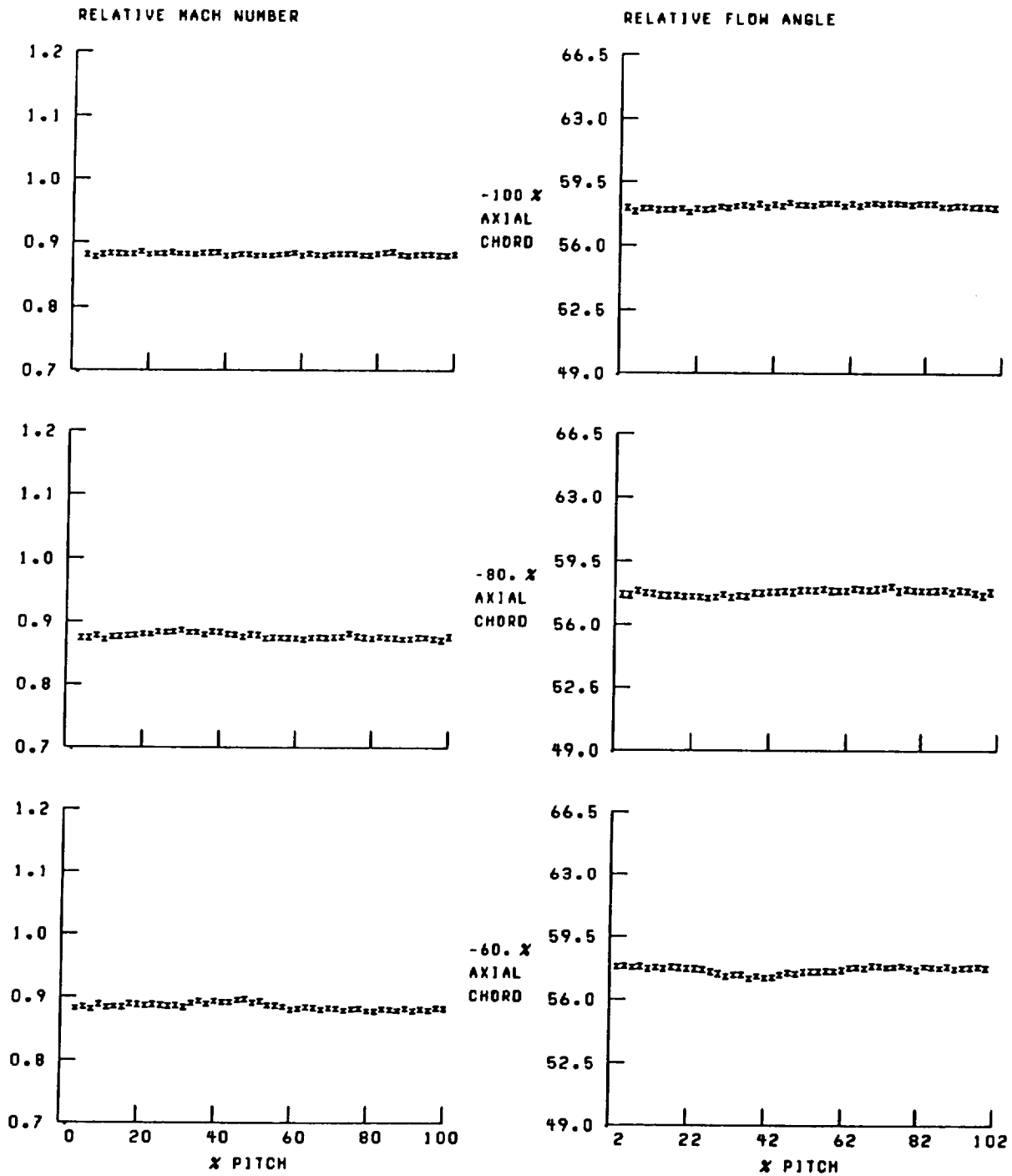


Figure 47.—Blade-to-blade distribution of relative Mach number and flow angle at 70-percent span and near stall.

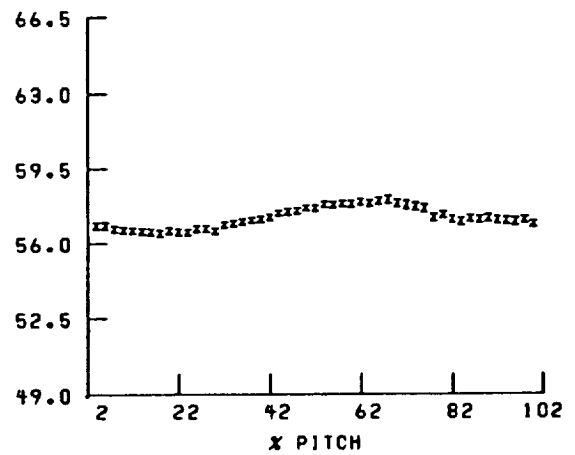
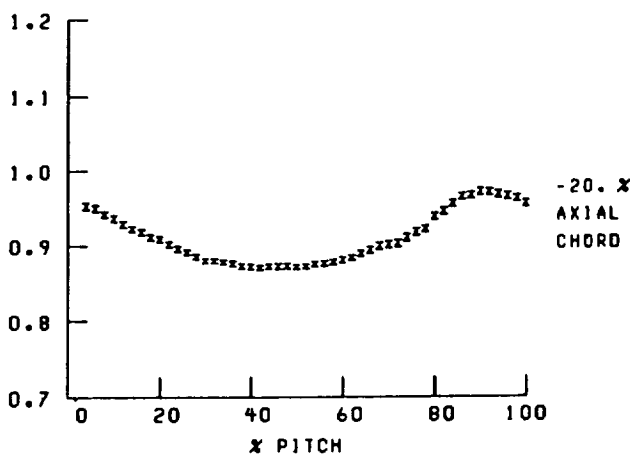
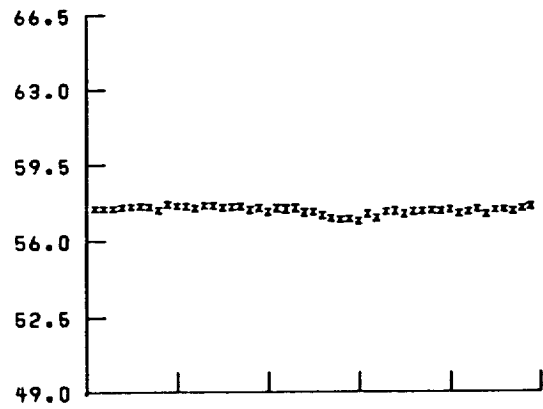
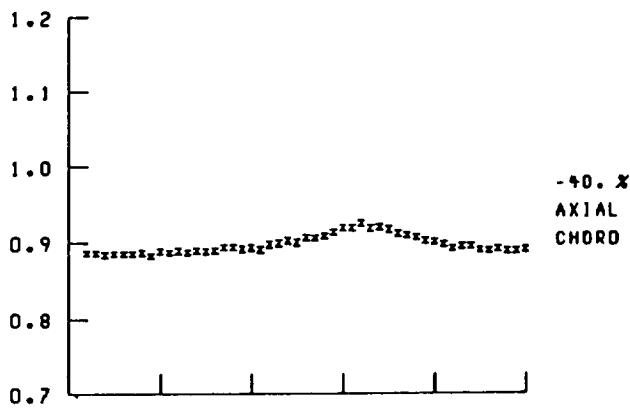
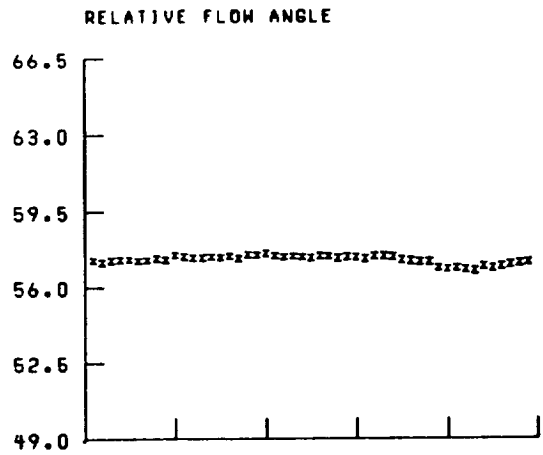
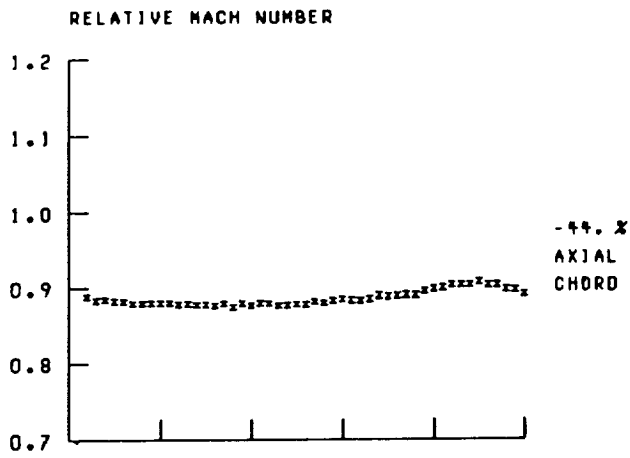


Figure 47.—Continued.

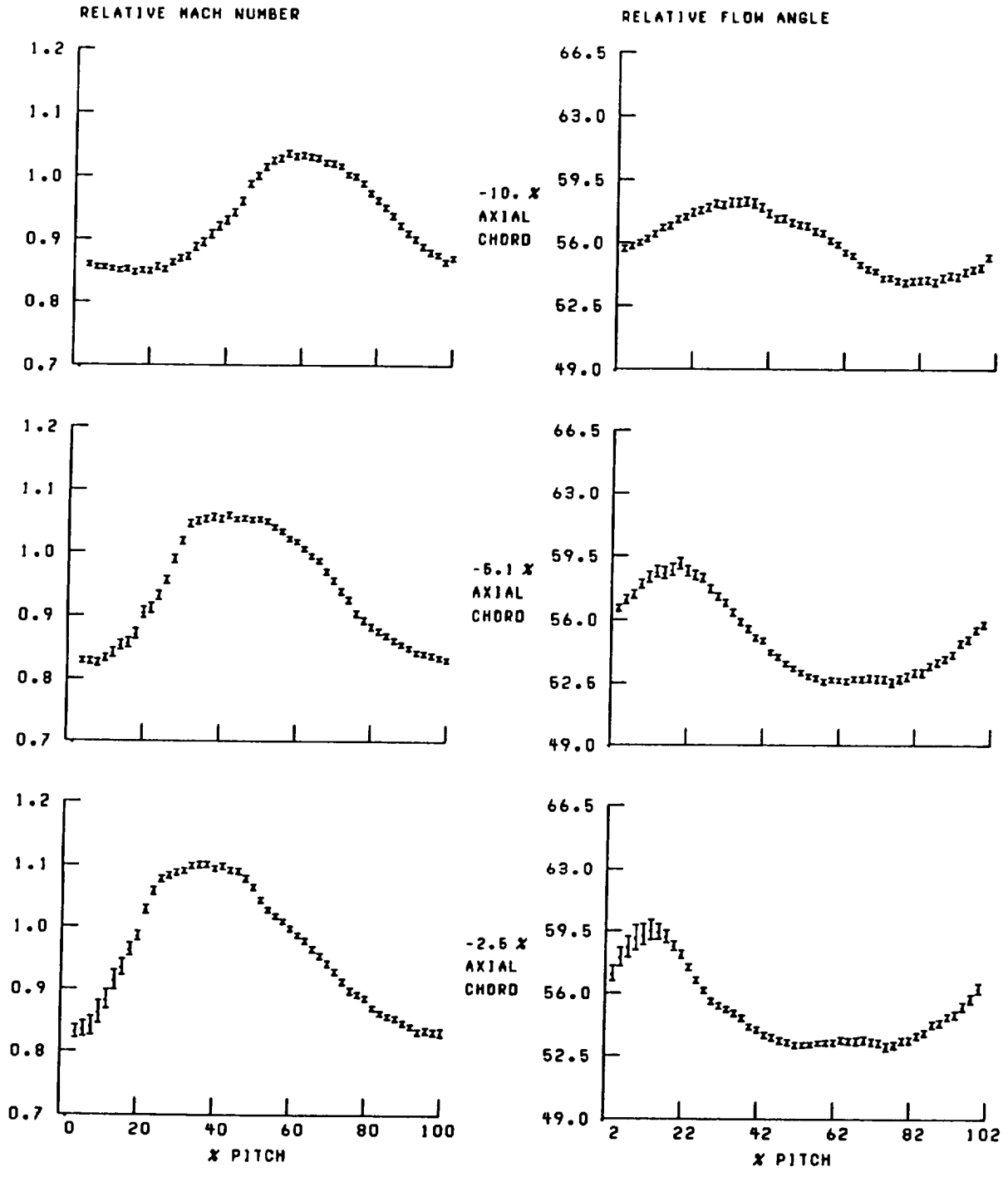


Figure 47.—Continued.

0-3

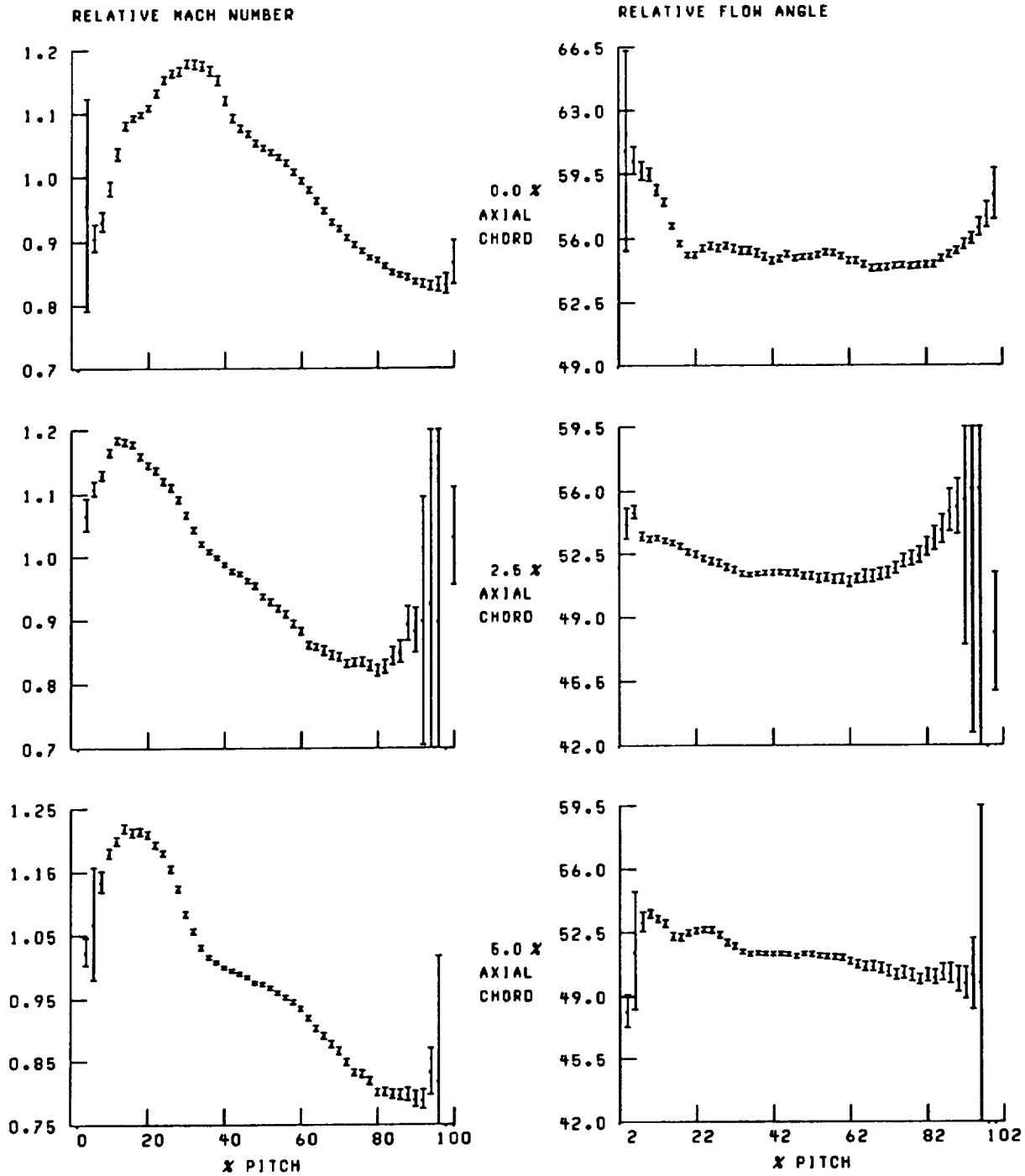


Figure 47.—Continued.

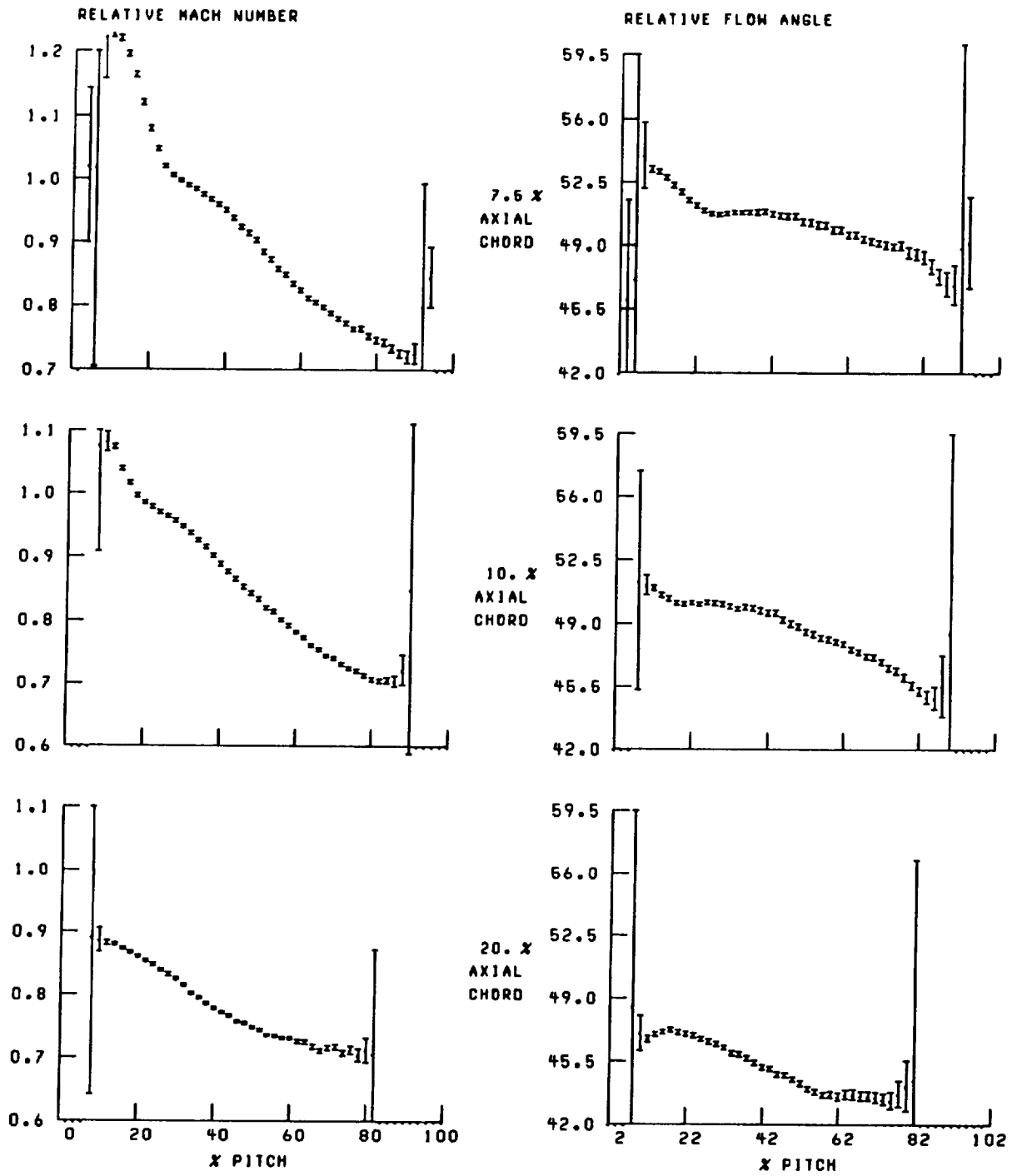


Figure 47.—Continued.

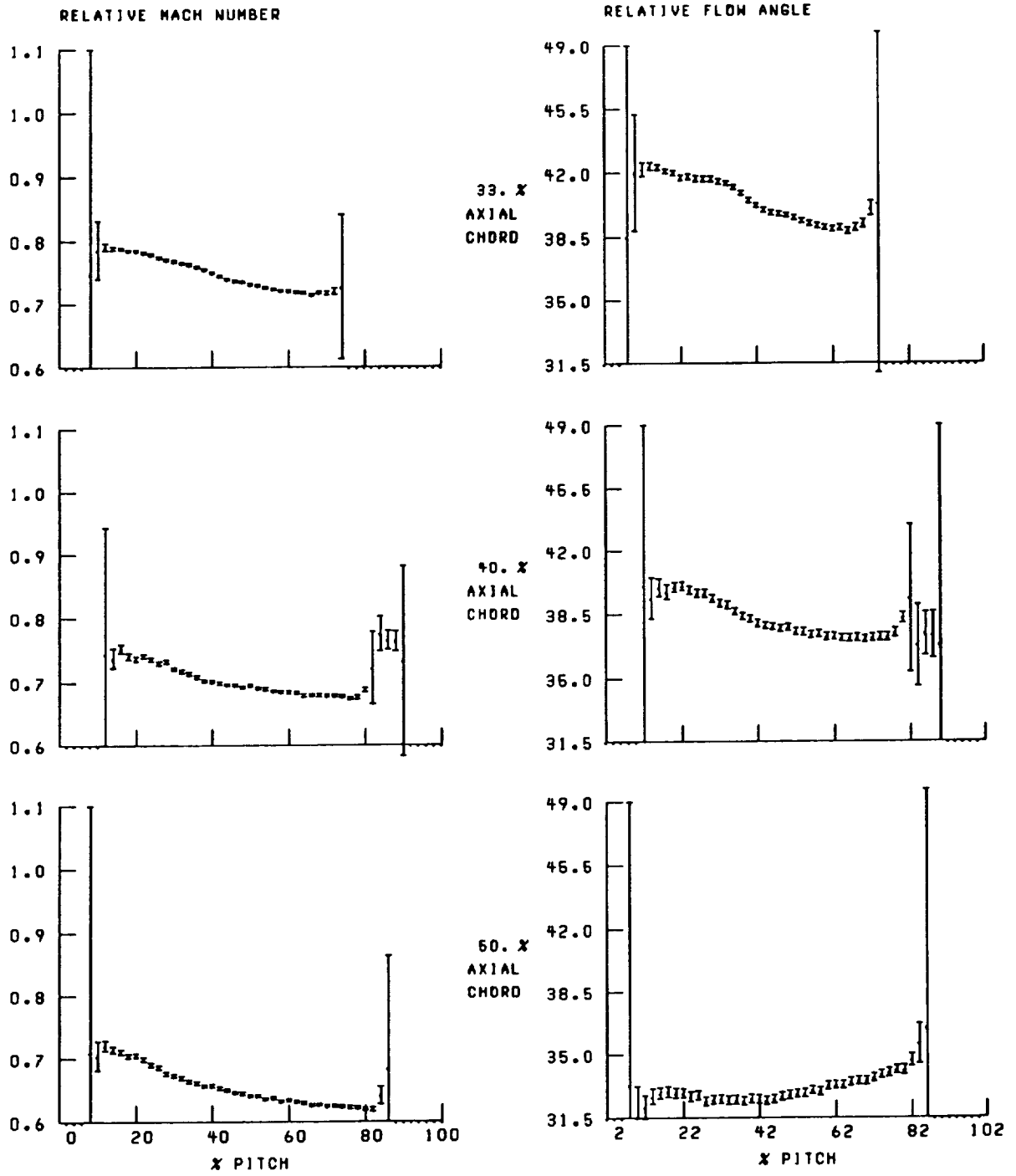


Figure 47.—Continued.

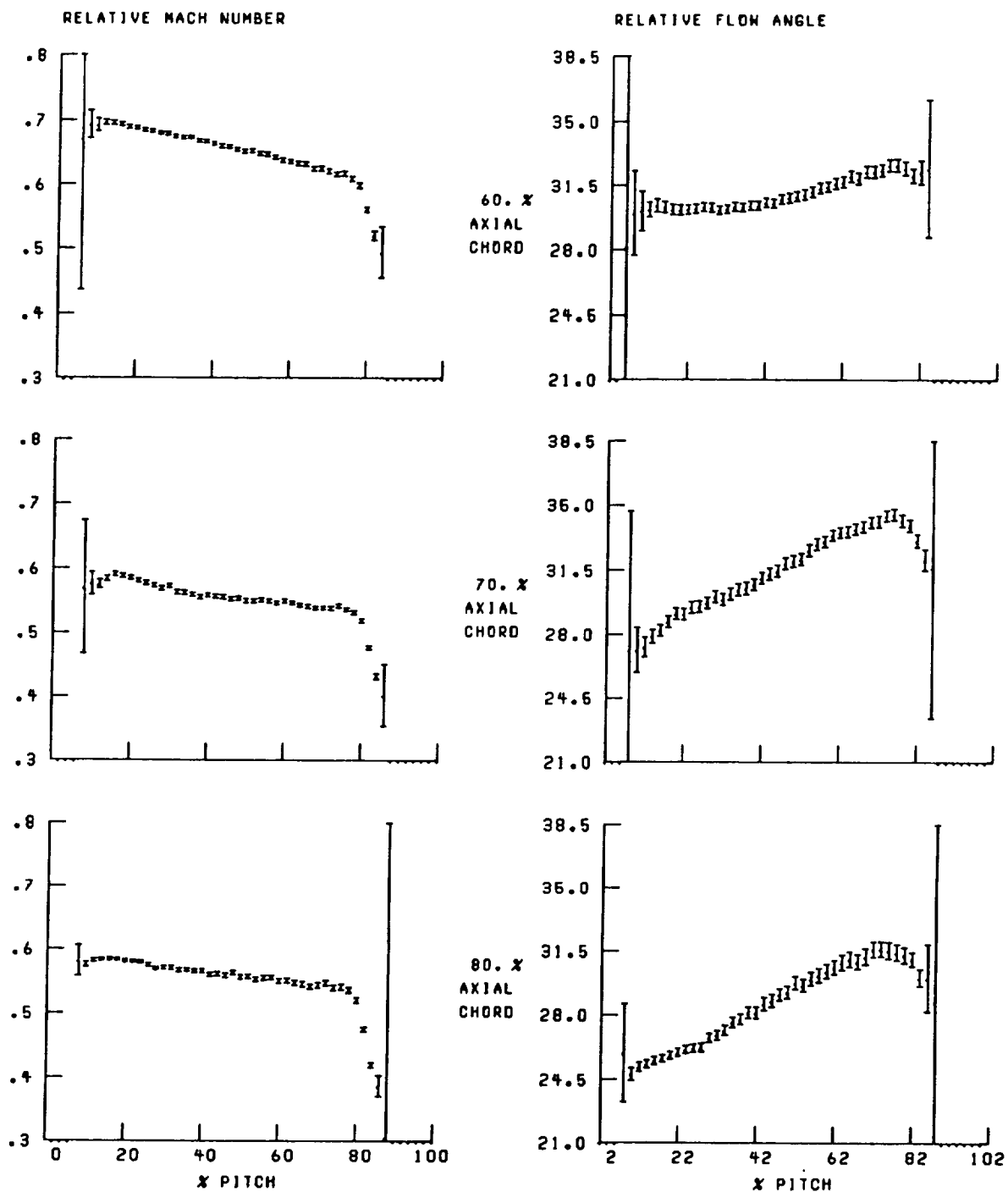


Figure 47.—Continued.

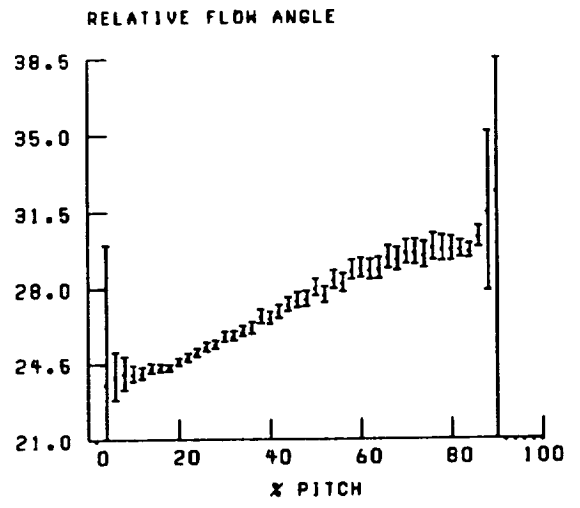
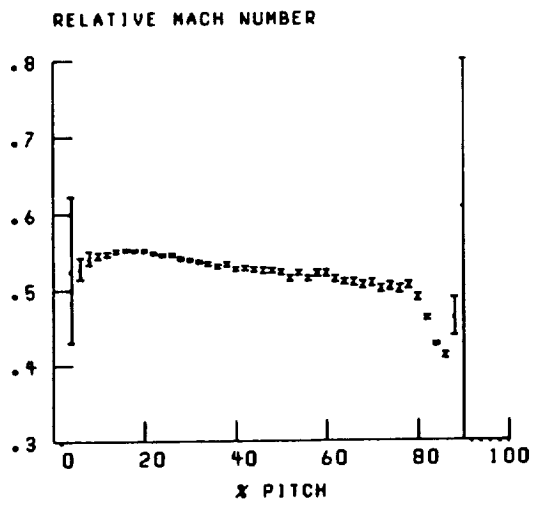


Figure 47.—Continued.

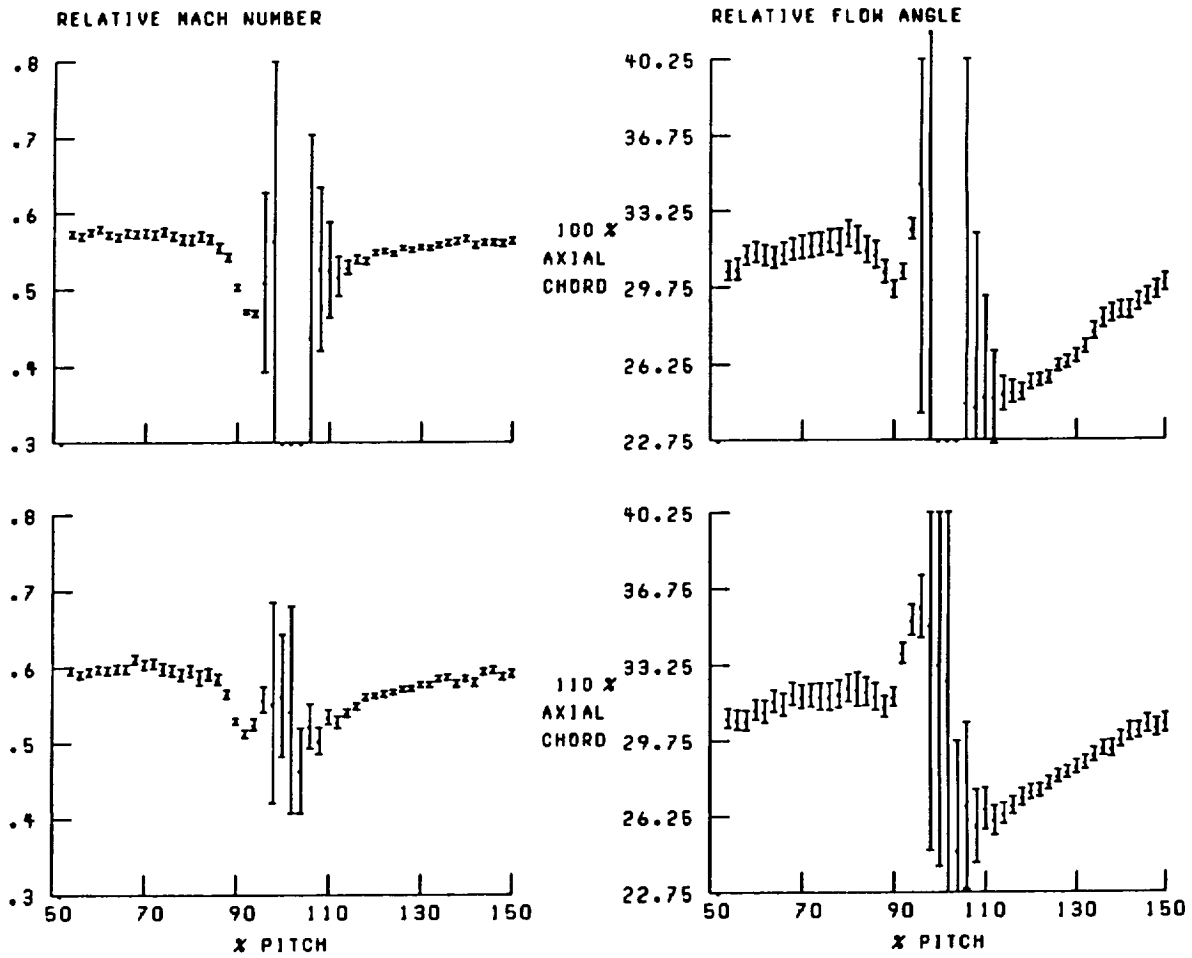


Figure 47.—Concluded.

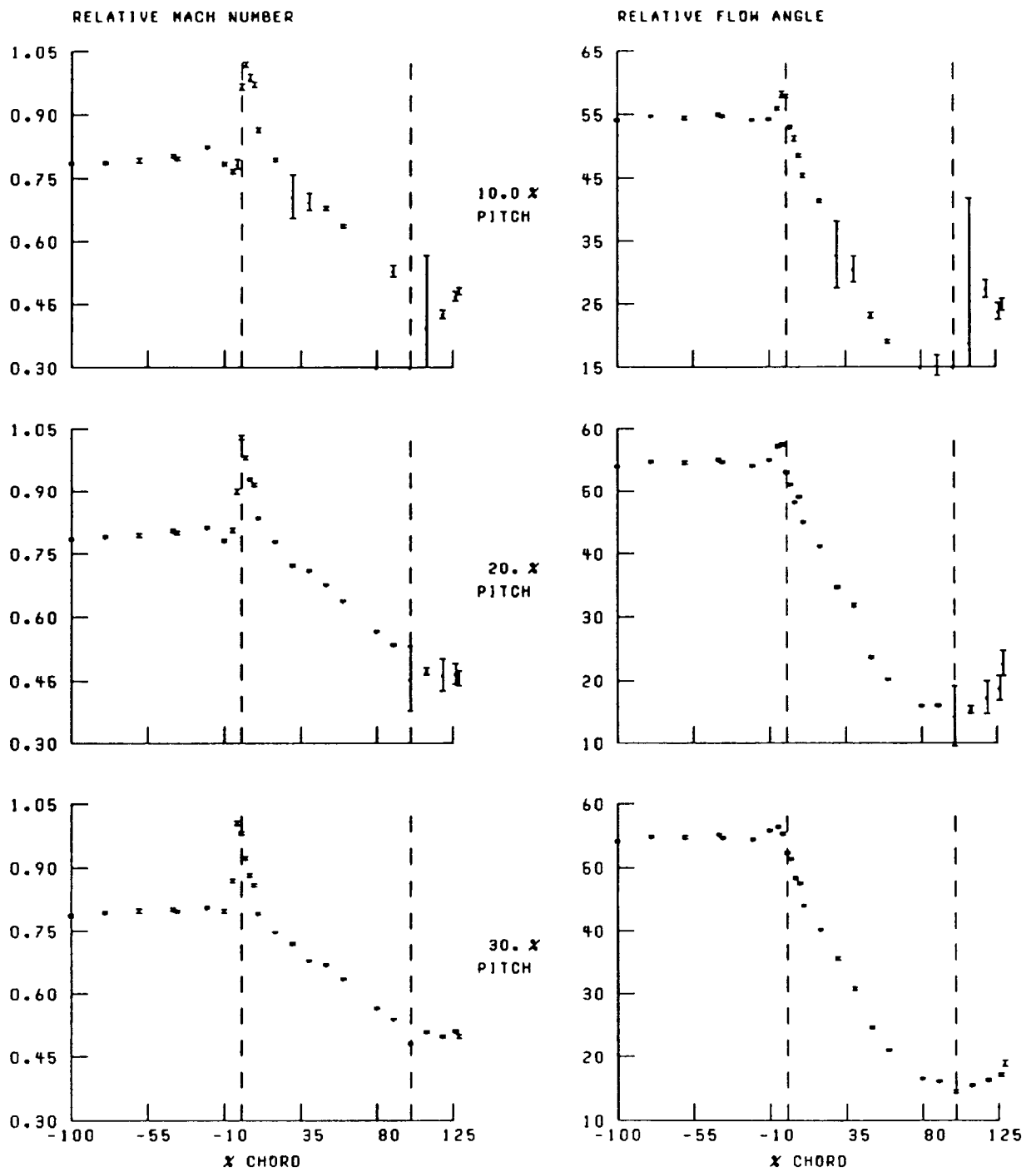


Figure 48.—Streamwise distribution of relative Mach number and flow angle at 80-percent span and near stall. Broken lines denote location of blade leading and trailing edges.

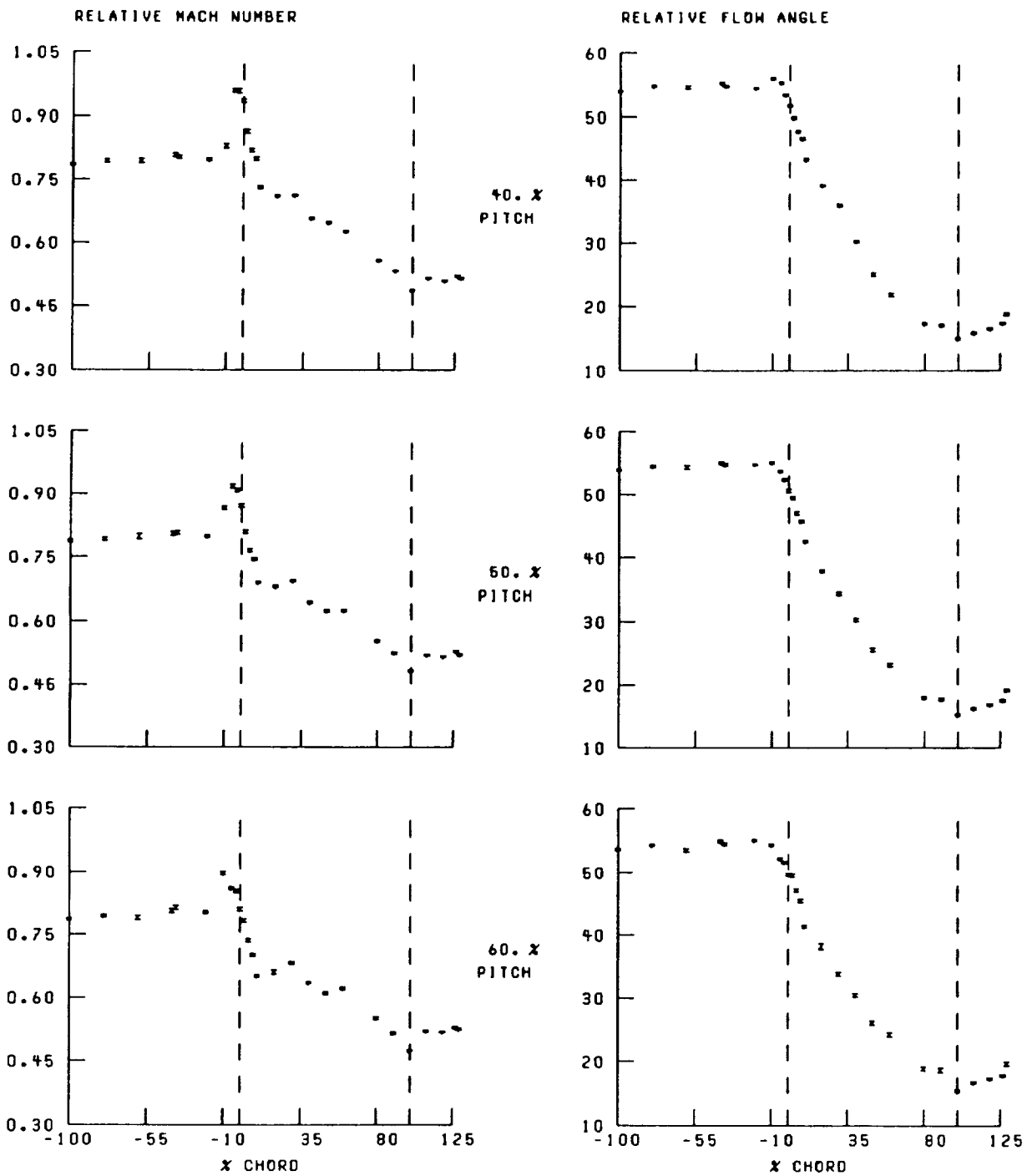


Figure 48.—Continued.

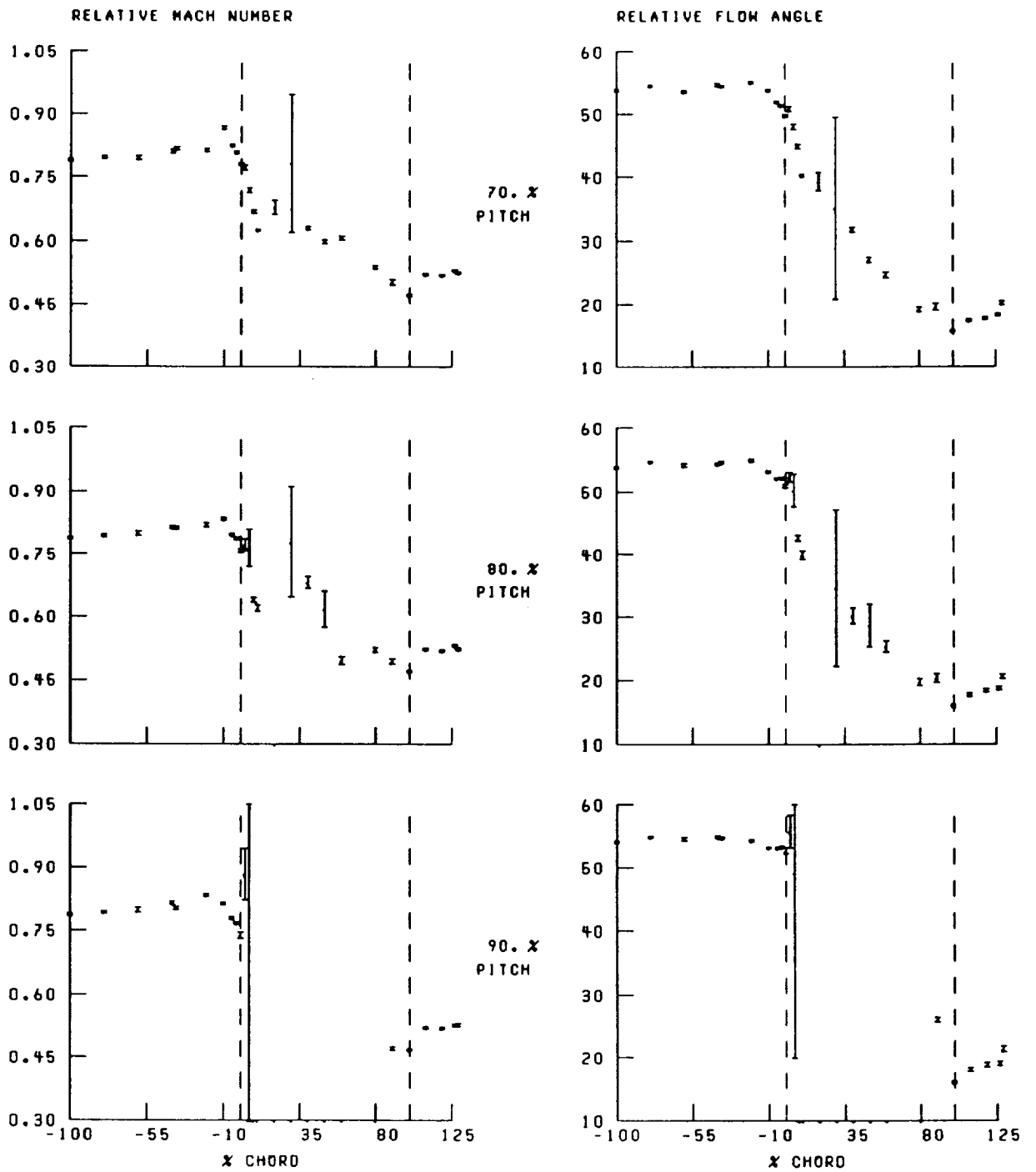


Figure 48.—Concluded.

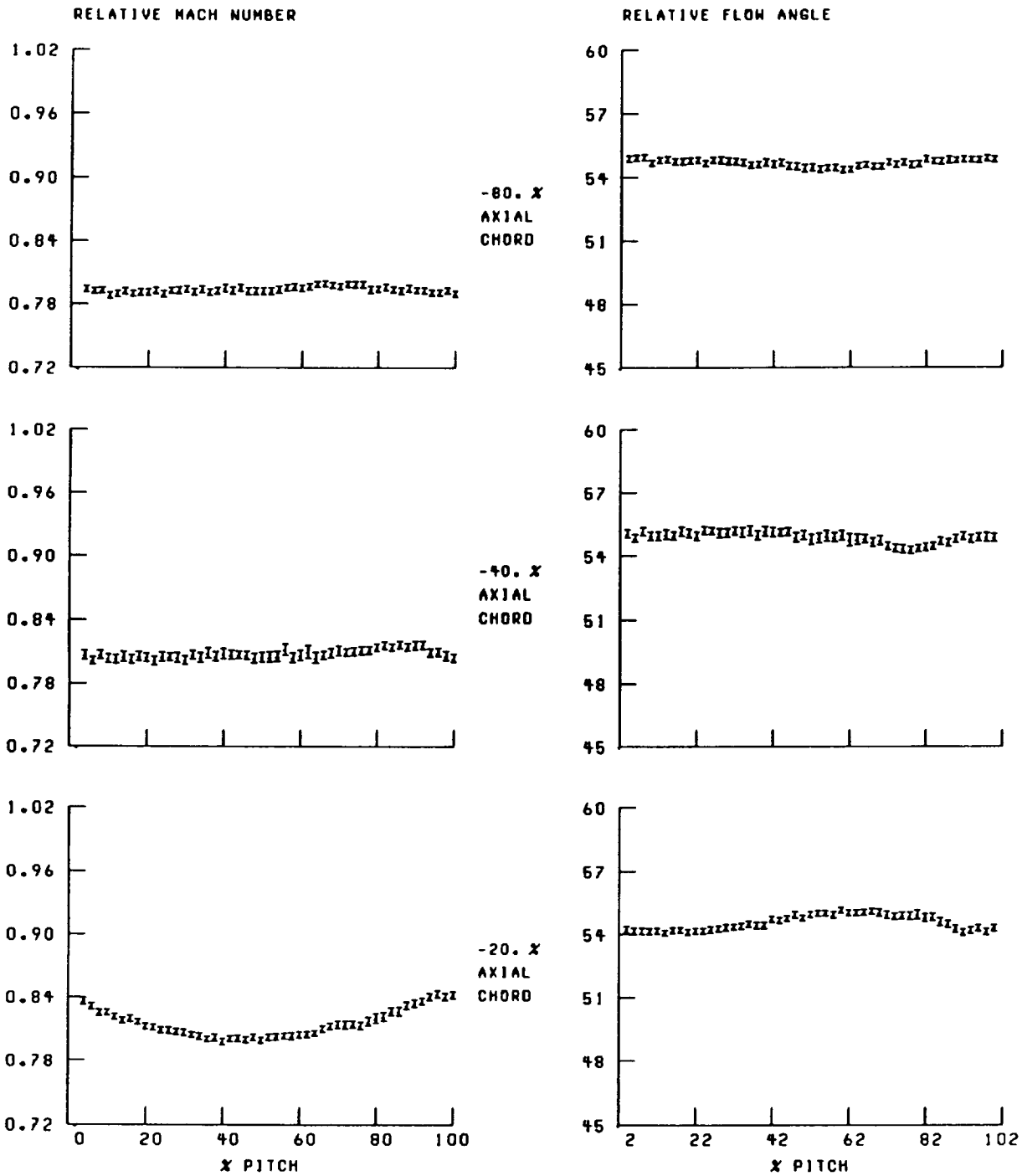


Figure 49.—Blade-to-blade distribution of relative Mach number and flow angle at 80-percent span and near stall.

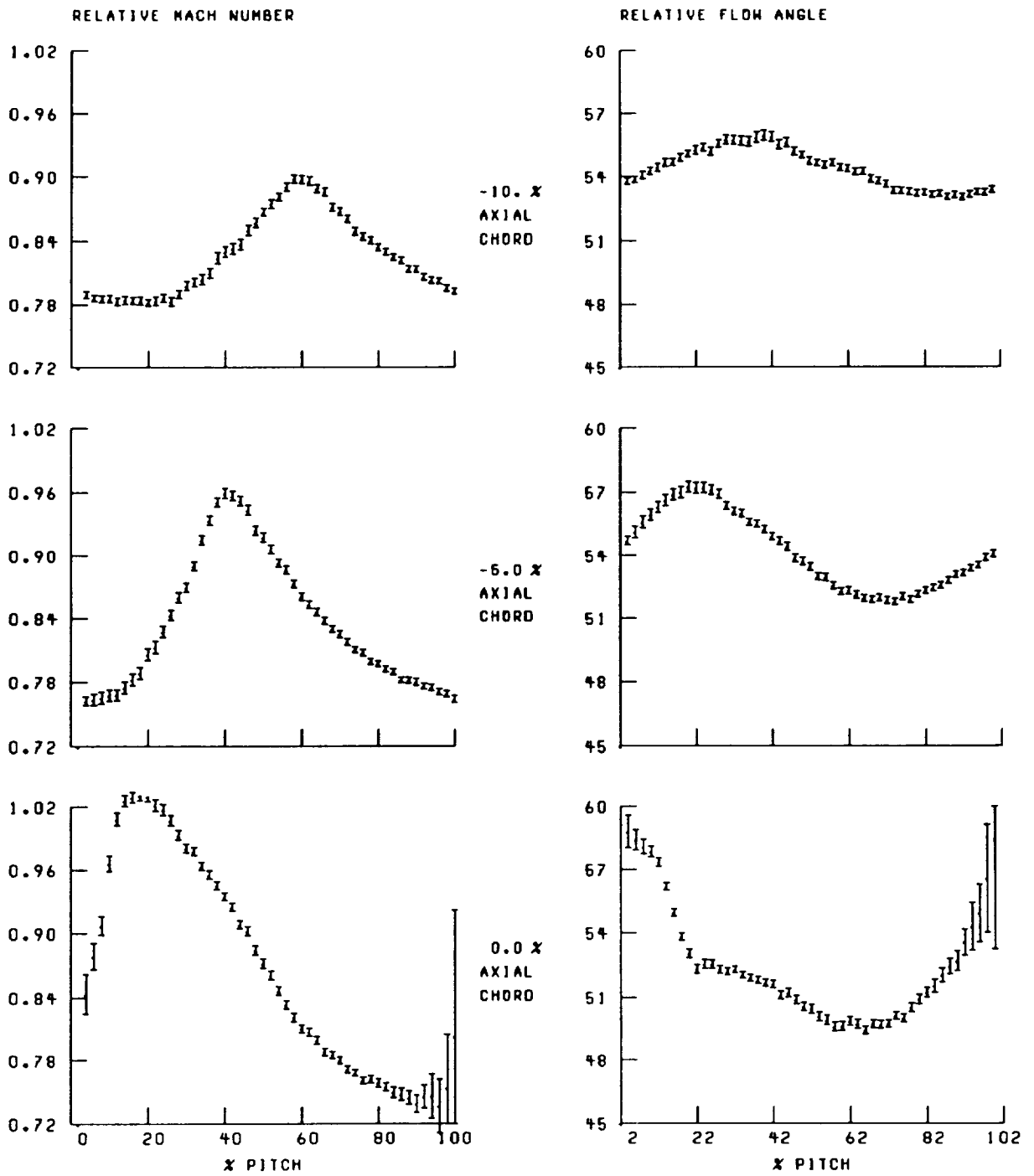


Figure 49.—Continued.

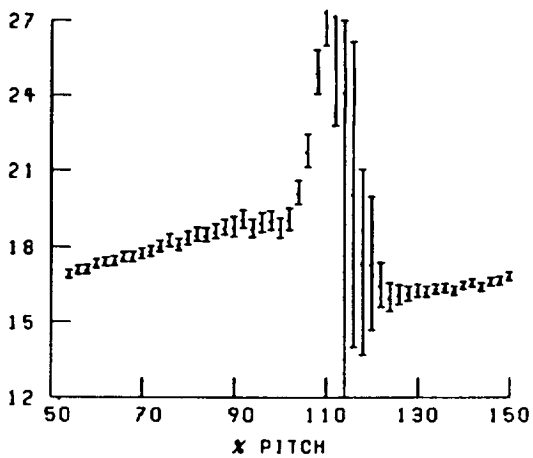
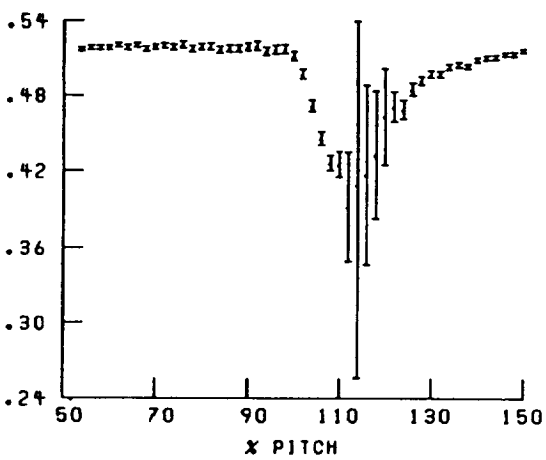
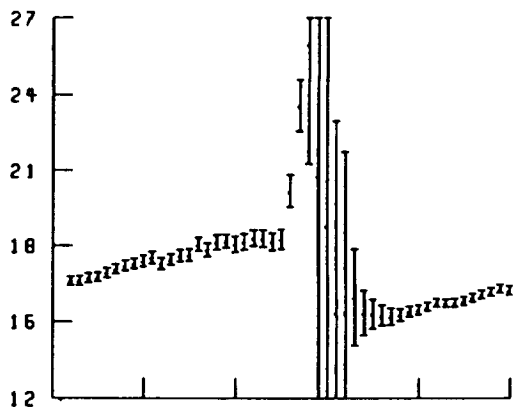
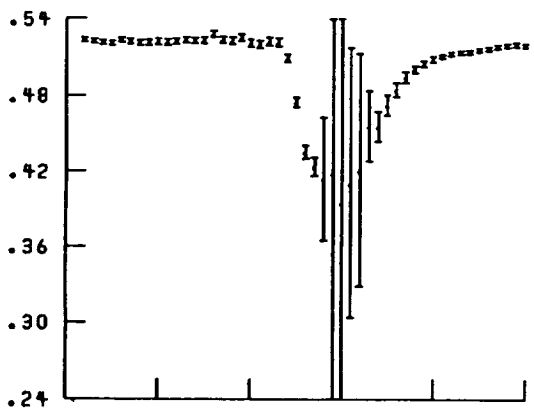
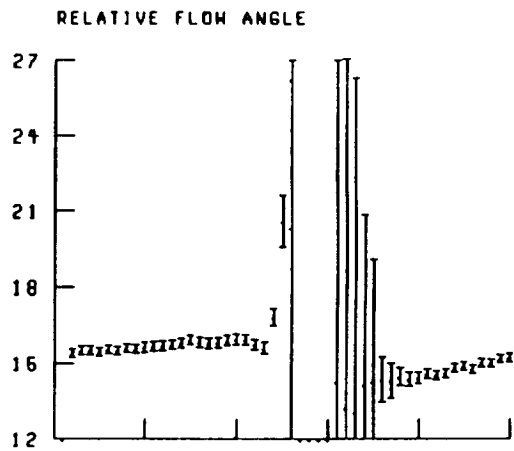
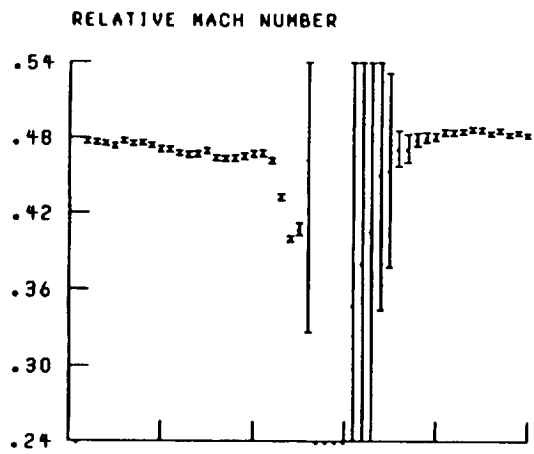


Figure 49.—Continued.

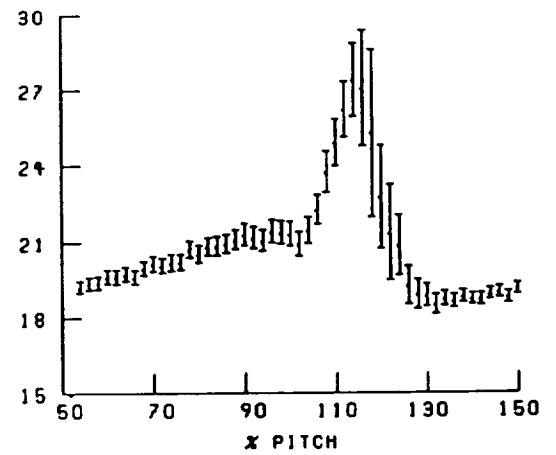
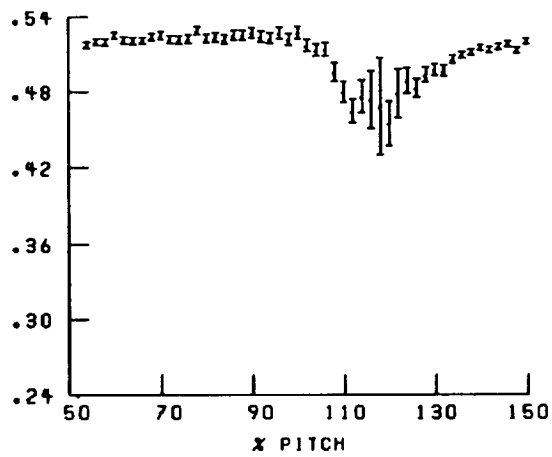
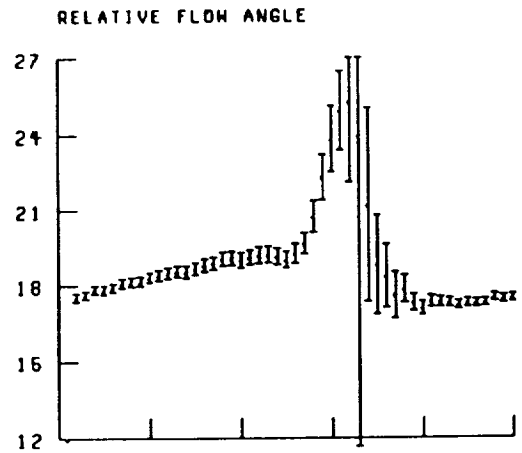
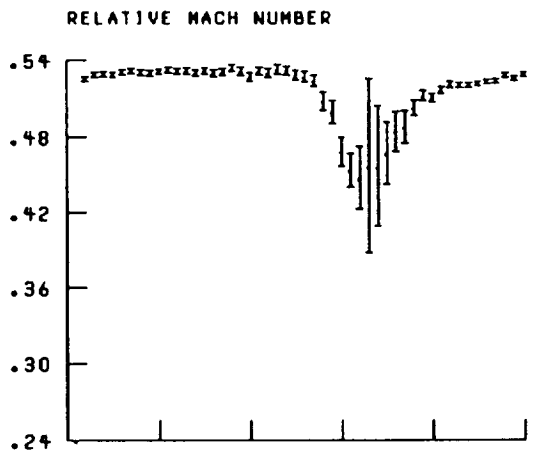


Figure 49.—Concluded.

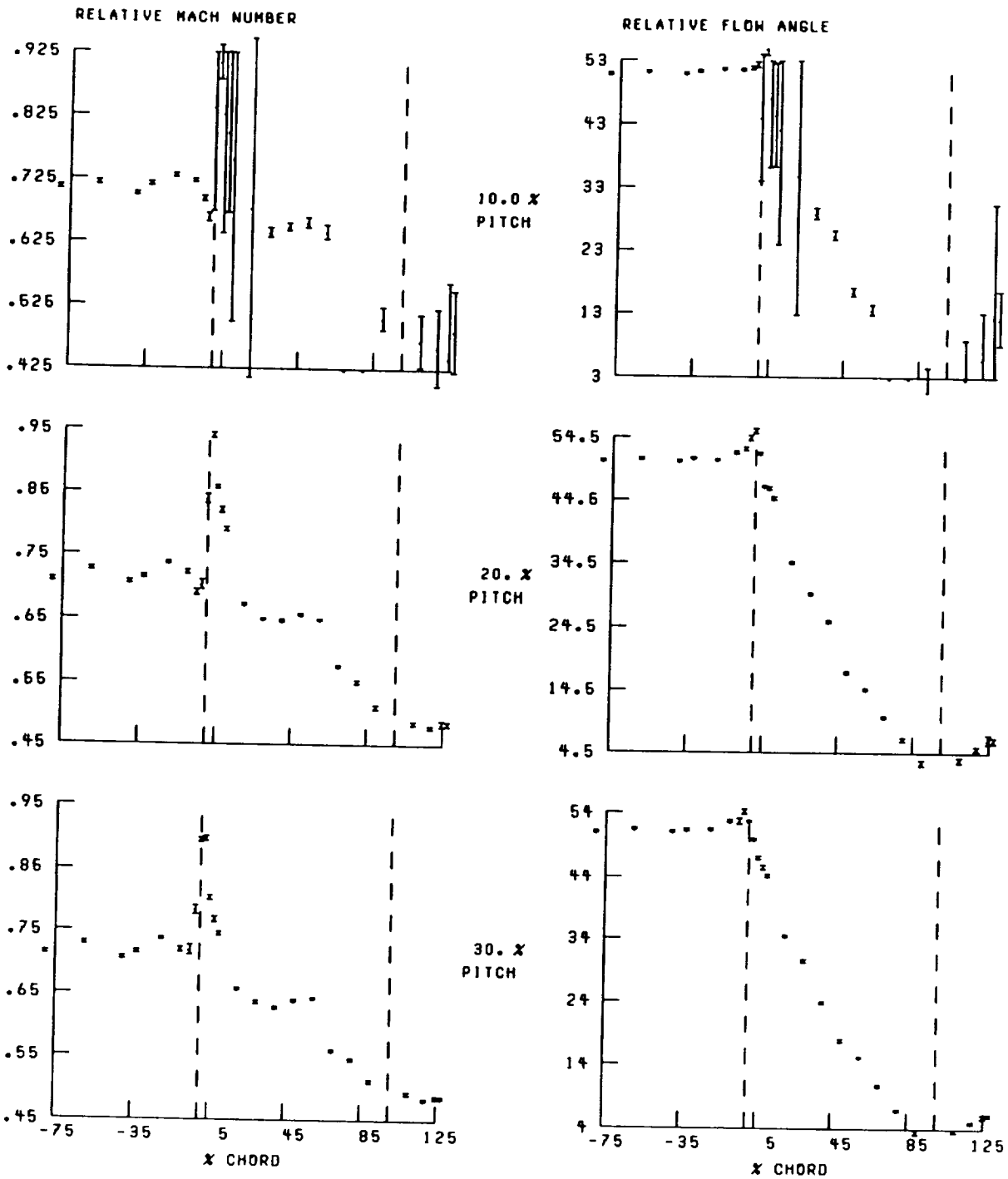


Figure 50.—Streamwise distribution of relative Mach number and flow angle at 90-percent span and near stall. Broken lines denote location of blade leading and trailing edges.

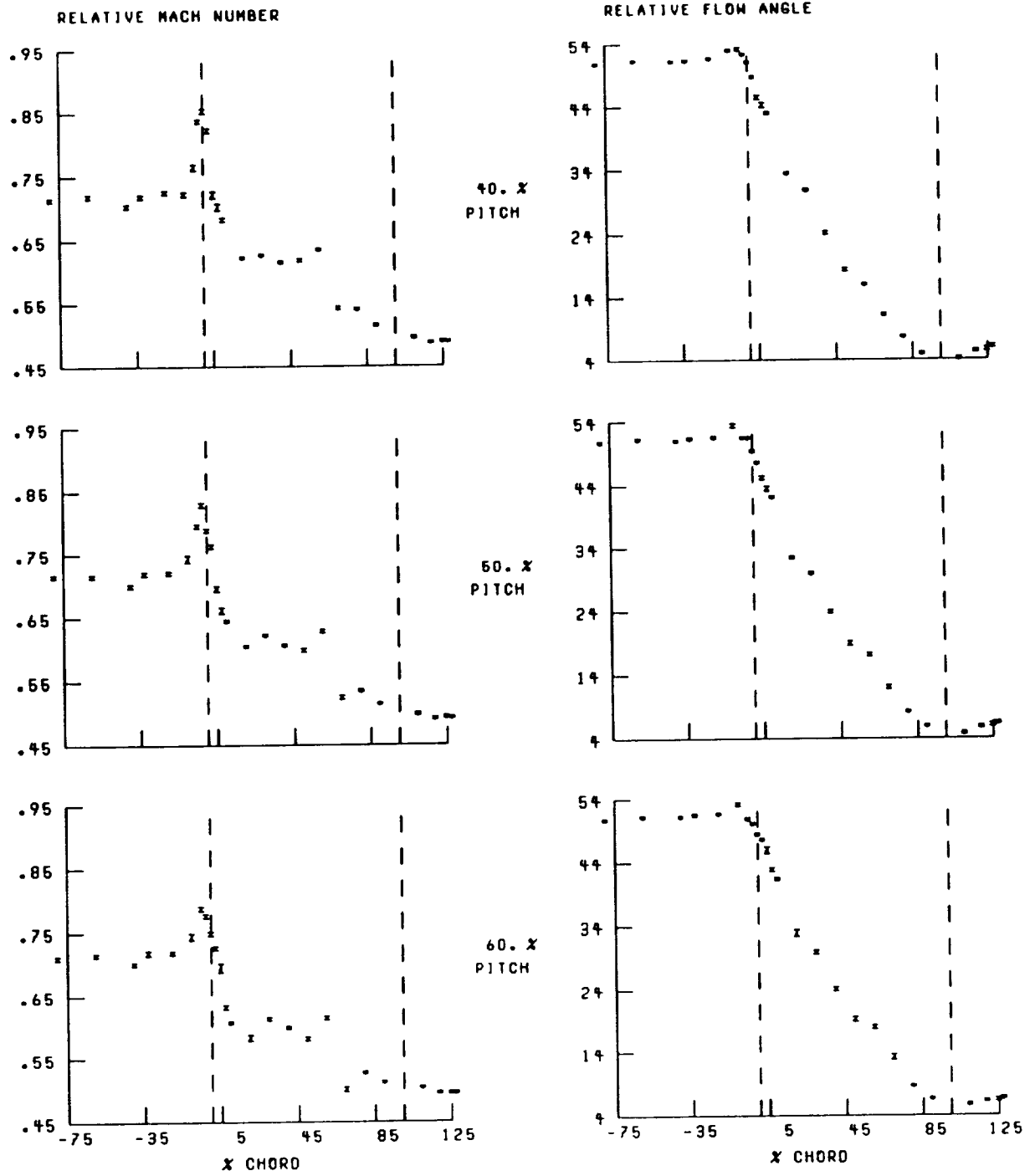


Figure 50.—Continued.

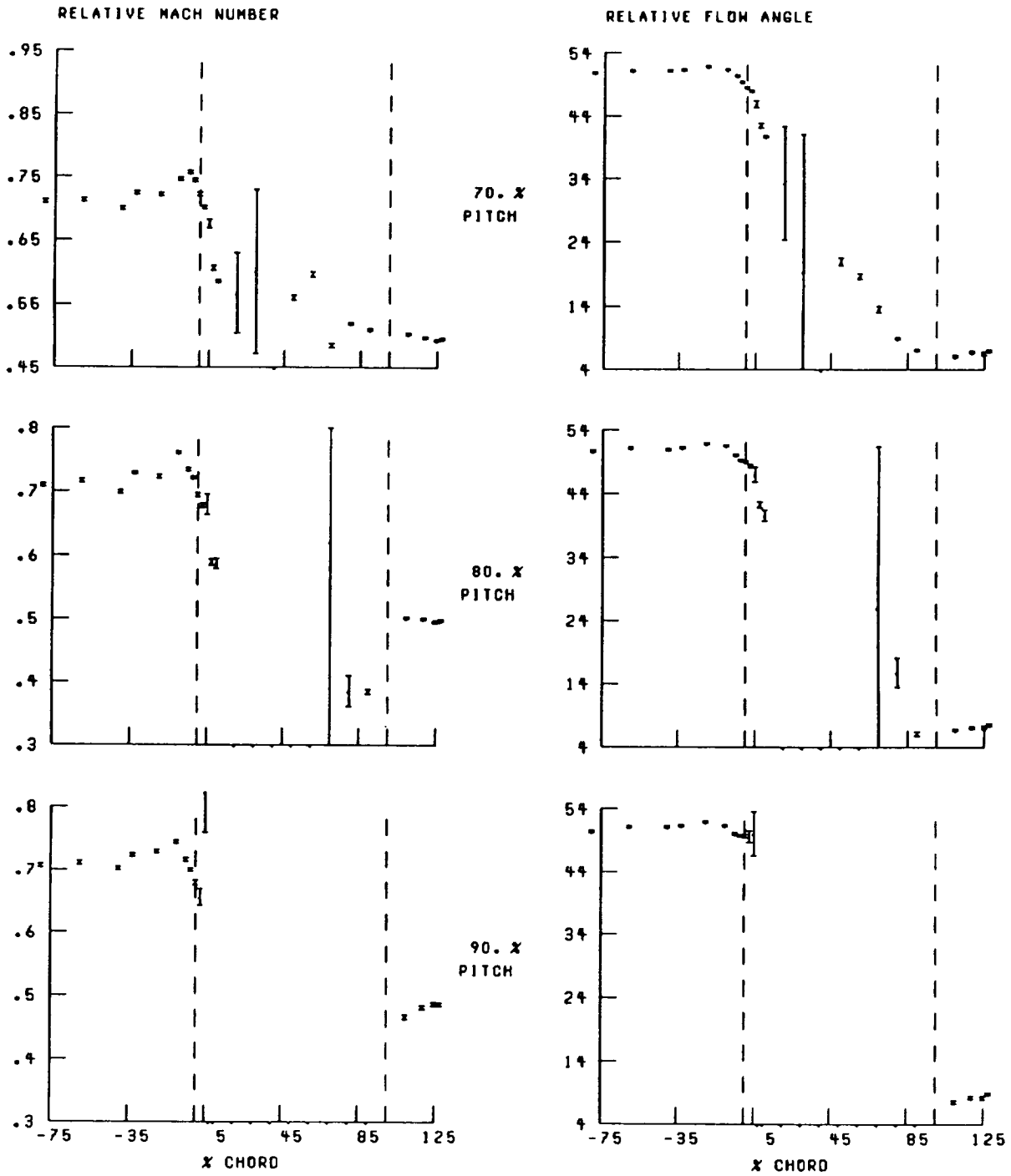


Figure 50.—Concluded.

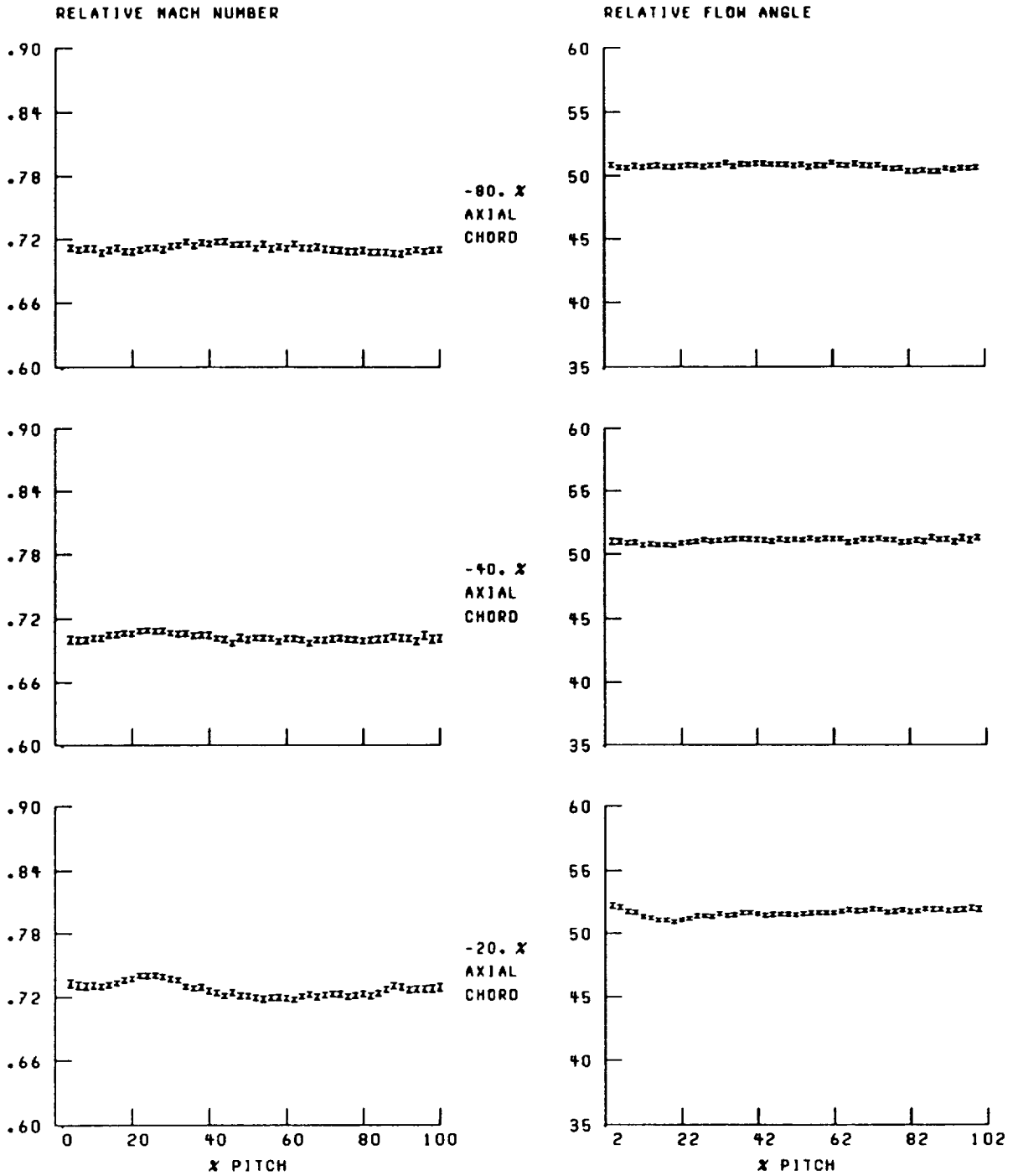


Figure 51.—Blade-to-blade distribution of relative Mach number and flow angle at 90-percent span and near stall.

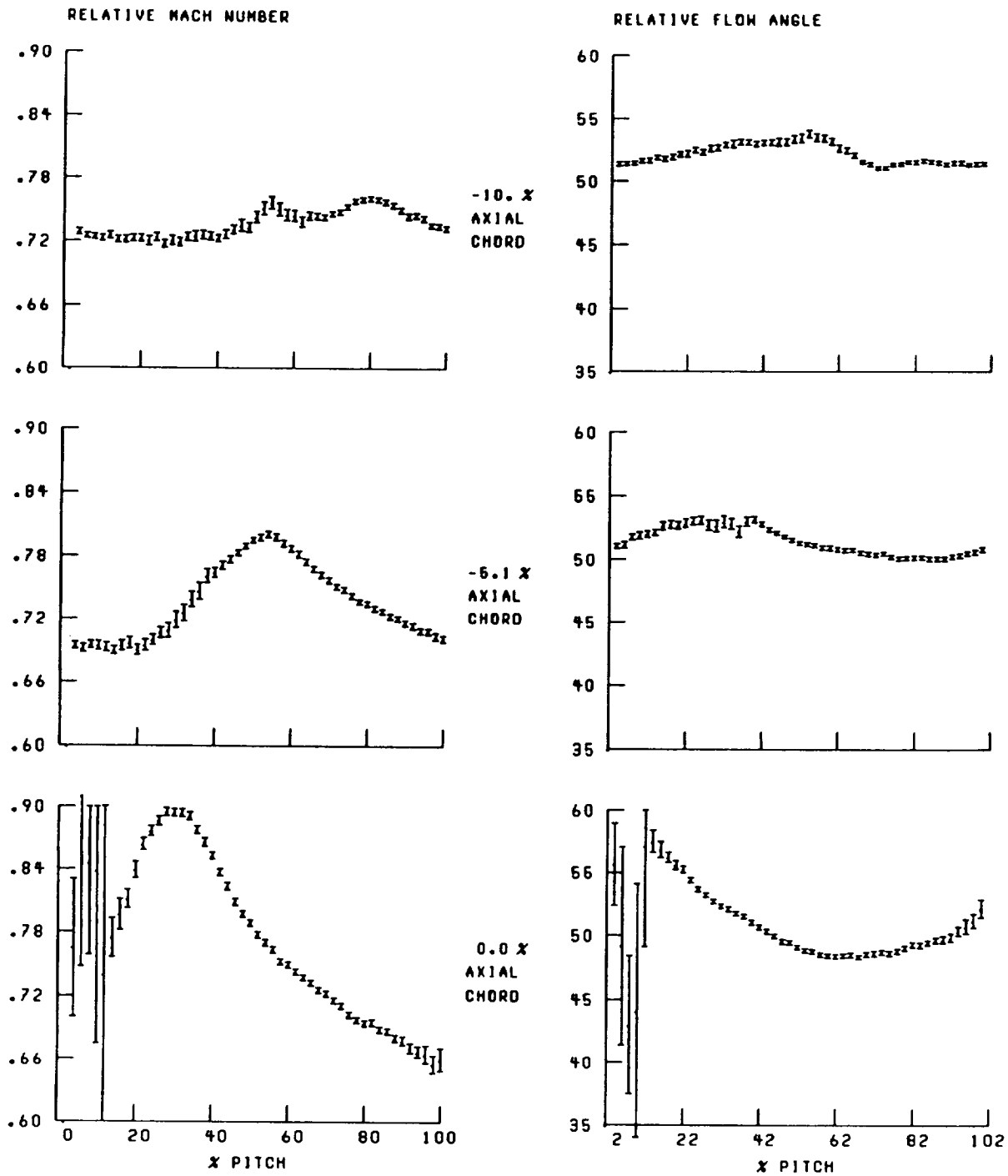


Figure 51.—Continued.

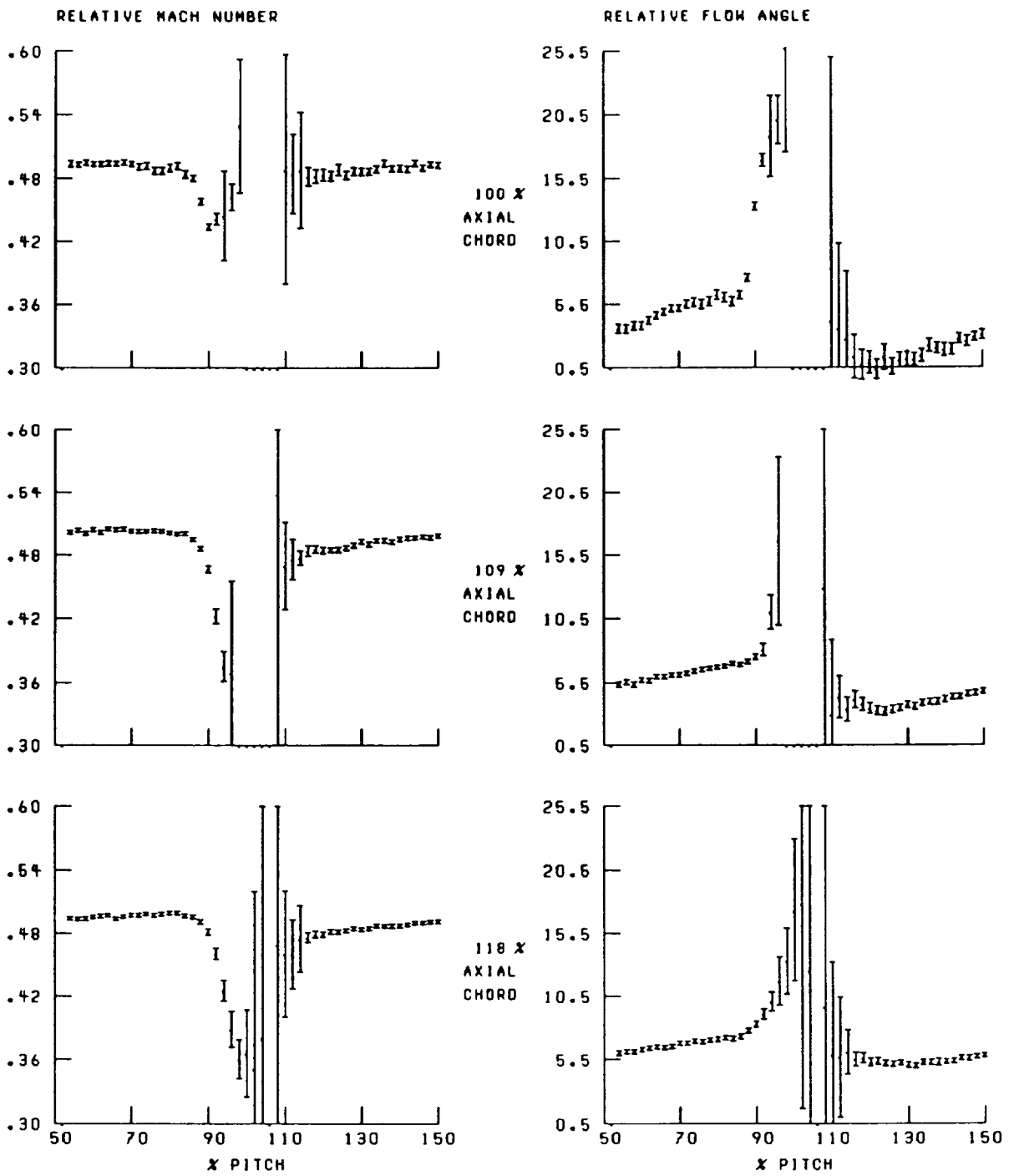


Figure 51.—Continued.

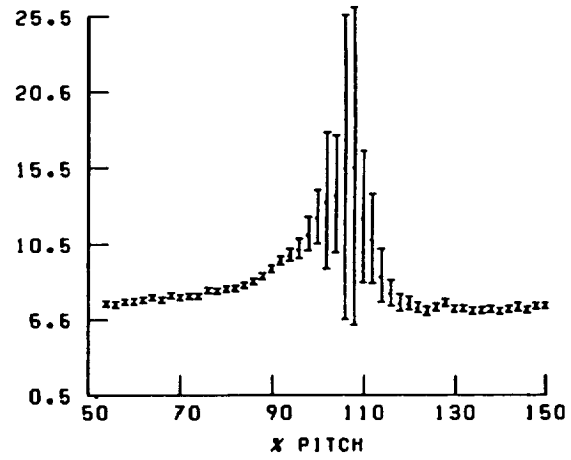
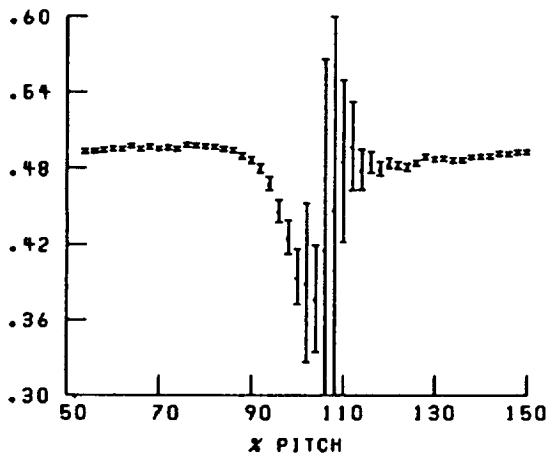
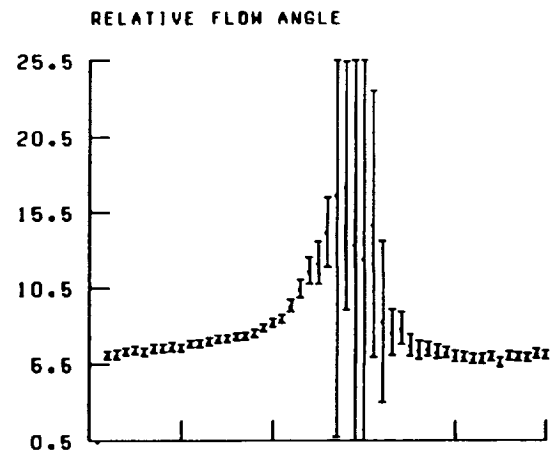
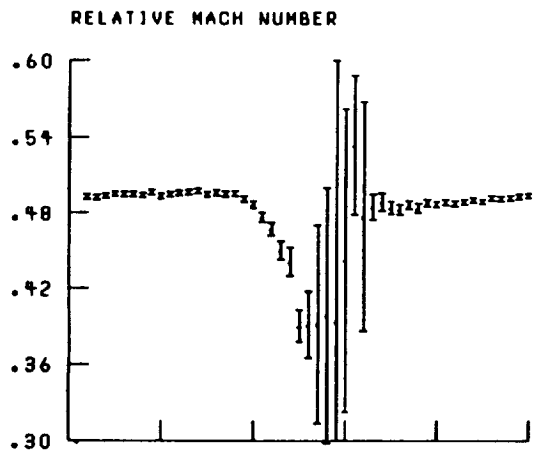


Figure 51.—Concluded.



Report Documentation Page

1. Report No. NASA TP-2879		2. Government Accession No.		3. Recipient's Catalog No.	
4. Title and Subtitle Laser Anemometer Measurements in a Transonic Axial-Flow Fan Rotor				5. Report Date November 1989	
				6. Performing Organization Code	
7. Author(s) Anthony J. Strazisar, Jerry R. Wood, Michael D. Hathaway, and Kenneth L. Suder				8. Performing Organization Report No. E-4480	
				10. Work Unit No. 505-62-61	
9. Performing Organization Name and Address National Aeronautics and Space Administration Lewis Research Center Cleveland, Ohio 44135-3191				11. Contract or Grant No.	
				13. Type of Report and Period Covered Technical Paper	
12. Sponsoring Agency Name and Address National Aeronautics and Space Administration Washington, D.C. 20546-0001				14. Sponsoring Agency Code	
				15. Supplementary Notes	
16. Abstract <p>Laser anemometer surveys were made of the three-dimensional flowfield in NASA rotor 67, a low-aspect-ratio transonic axial-flow fan rotor. The test rotor has a tip relative Mach number of 1.38. The flowfield was surveyed at design speed for operating conditions near peak efficiency and near stall. Data are presented in the form of relative Mach number and relative flow angle distributions on surfaces of revolution at nine spanwise locations evenly spaced from hub to tip. At each spanwise location data were acquired upstream, within, and downstream of the rotor. Aerodynamic performance measurements and detailed rotor blade and annulus geometry are also presented so that the experimental results can be used as a test case for three-dimensional turbomachinery flow analysis codes.</p>					
17. Key Words (Suggested by Author(s)) Turbomachinery Compressors Laser anemometry Computational fluid dynamics			18. Distribution Statement Unclassified - Unlimited Subject Category 07		
19. Security Classif. (of this report) Unclassified		20. Security Classif. (of this page) Unclassified		21. No of pages 214	22. Price* A10